This electronic thesis or dissertation has been downloaded from Explore Bristol Research, http://research-information.bristol.ac.uk

Author:
Sutcliffe, Katy

Title:
Molecular dynamics simulations and mutagenesis to identify the mechanisms of ligand efficacy and bias at the opioid receptor

General rights
Access to the thesis is subject to the Creative Commons Attribution - NonCommercial-No Derivatives 4.0 International Public License. A copy of this may be found at https://creativecommons.org/licenses/by-nc-nd/4.0/legalcode This license sets out your rights and the restrictions that apply to your access to the thesis so it is important you read this before proceeding.

Take down policy
Some pages of this thesis may have been removed for copyright restrictions prior to having it been deposited in Explore Bristol Research. However, if you have discovered material within the thesis that you consider to be unlawful e.g. breaches of copyright (either yours or that of a third party) or any other law, including but not limited to those relating to patent, trademark, confidentiality, data protection, obscenity, defamation, libel, then please contact collections-metadata@bristol.ac.uk and include the following information in your message:

- Your contact details
- Bibliographic details for the item, including a URL
- An outline nature of the complaint

Your claim will be investigated and, where appropriate, the item in question will be removed from public view as soon as possible.

Molecular dynamics simulations and mutagenesis to identify the mechanisms of ligand efficacy and bias at the μ opioid receptor

Katherine Judith Sutcliffe

A dissertation submitted to the University of Bristol in accordance with the requirements for award of the degree of Doctor of Philosophy in the Faculty of Life Sciences

School of Physiology, Pharmacology & Neuroscience

September 2019

Word count: 43,427

Abstract

There is a resurgence of interest in G protein-coupled receptor (GPCR) structure-guided drug design due to the rapid increase in high-resolution structures of these biologically important proteins. The μ opioid receptor (MOPr) is an important GPCR, both therapeutically for analgesia and in drug abuse. There are opportunities to develop new opioids which exhibit distinct efficacies for different signalling pathways, a phenomenon known as agonist bias. This could represent a strategy to fine-tune MOPr activation, directing signalling towards analgesia whilst avoiding adverse effects. However, the mechanisms underlying ligand efficacy and agonist bias at the MOPr remain poorly understood. With this in mind, we employed molecular dynamics (MD) simulations of ligand-MOPr complexes to identify potential structural signatures of MOPr activation and biased agonism. Small molecules and peptides were selected for their differing efficacies and bias profiles, docked to the inactive MOPr and 1 μs MD simulations performed. On a residue-level, these MD simulations predicted that opioids adopt distinct binding poses and therefore interact with different subsets of residues. Specifically, high efficacy agonists induced conformational changes in the W293$^{6.48}$ microswitch. Mutagenesis of this residue resulted in a receptor which did not respond to agonists, indicating that W293$^{6.48}$ is essential for MOPr activation. Comparison of the arrestin-biased peptide, endomorphin-2, with the novel G protein-biased peptide, bilorphin, revealed that interaction with the MOPr extracellular loops may indicate bias towards arrestin recruitment. On the level of the transmembrane domains, the MOPr adopted distinct conformations which differentiated high efficacy ligands from those of lower efficacy, as well as agonists of opposing bias. Conformational changes in the MOPr helices were prevented by an allosteric sodium ion or the W293$^{6.48}$A mutation. This work builds on evidence that GPCRs occupy multiple conformations dependent on the bound ligand. Moreover, this thesis identifies key residues which may be important in conferring ligand efficacy and agonist bias at the MOPr.

Acknowledgements

Firstly, I must thank my supervisors Eamonn Kelly and Richard “Sesh” Sessions for their guidance, expertise and nurturing a self-confidence I didn’t know I had. Neither of you have ever been too busy to spend time discussing ideas, working through problems, or to patiently explain torsion angles (again!). Also, Graeme Henderson for his enthusiasm for this project, constructive criticism along the way, and cluttering my desk with old copies of TGO magazine.

I feel very lucky to be part of the Sessions Office and I’m so glad that I can spend another year in your company. Particularly, I must thank Amaurys Avila Ibarra for his help using BUDE, putting on his superhero cape to fix my computer and keeping me nourished with an endless supply of sweet treats and eye-wateringly strong coffee. Also, Debbie Shoemark for being my work-mum, Peter Wilson for helping me use the thermocycler, and Sofia Oliveira and Sukhee Bancroft for their friendship.

Thank you to all the past and present members of the Kelly-Henderson lab; particularly Rob Hill and Alex Conibear for their invaluable knowledge, insightful ideas, and generally being my go-to people. Gerda Gasiunaite - thank you for my crash course in the lab, without which I’d have been totally lost, and particularly for all your help with BRET assays.

I must acknowledge the SWBio DTP for my funding and training, especially in statistics and public speaking. Also, my fellow SWBio-ers: Clara Montgomery, Em Stevens, Travis Bacon and Arne Scott. Sharing this experience with you all has made these 4 years a lot of fun. Thank you especially to Em for giving up your free time to help me with PCR, and Clara for being the best friend a PhD student could ask for.

My family have always encouraged me to do what I love and supported me, so thank you to my mum and sister who have proudly put every publication up on the fridge! Finally, thank you Dave, for being my rock, listening to my problems, cheering my successes, and your occasional much needed perspective; “it’s only a PhD”.

Author’s declaration

I declare that the work in this dissertation was carried out in accordance with the requirements of the University's Regulations and Code of Practice for Research Degree Programmes and that it has not been submitted for any other academic award. Except where indicated by specific reference in the text, the work is the candidate's own work. Work done in collaboration with, or with the assistance of, others, is indicated as such. Any views expressed in the dissertation are those of the author.

SIGNED: .... DATE:..........................

Abbreviations

5HT	5-hydroxytryptamine
AC	adenylyl cyclase
aMD	accelerated molecular dynamics
AMP	adenosine monophosphate
ANOVA	analysis of variance
BRET	bioluminescence resonance energy transfer
BRIL	cytochrome b562RIL
BSA	bovine serum albumin
BUDE	Bristol University Docking Engine
CaMKII	calcium/calmodulin-dependent protein kinase II
cryoEM	cryogenic electron microscopy
DADLE	[D-Ala^2, D-Leu^5]-enkephalin
DAMGO	[D-Ala^2, N-MePhe^4, Gly-ol]-enkephalin
DEER	double electron-electron resonance
DMEM	Dulbecco's Modified Eagle's Medium
DMSO	dimethyl sulfoxide
DOPr	delta opioid receptor
ECL	extracellular loop
ELISA	enzyme-linked immunosorbent assay
ERK	extracellular signal-regulated kinase
FBS	foetal bovine serum
FDA	Food and Drug Administration
FRET	fluorescence resonance energy transfer
GAFF	General Amber ForceField
GDP	guanosine-5'-diphosphate
GFP	green fluorescent protein

GIRK	G protein-coupled inwardly-rectifying potassium channel
GLP	glucagon-like peptide
GPCR	G protein-coupled receptor
GRK	G protein-coupled receptor kinase
GTP	guanosine-5'-triphosphate
HA	human influenza hemagglutinin
HEK 293	human embryonic kidney 293
HPLC	high performance liquid chromatography
ICL	intracellular loop
IPTG	isopropyl β-D-1-thiogalactopyranoside
JNK	c-Jun N-terminal kinase
KOPr	kappa opioid receptor
LB	lysogeny broth
LC	locus coeruleus
LSD	lysergic acid diethylamide
MD	molecular dynamics
MOPr	mu opioid receptor
NMR	nuclear magnetic resonance
NOPr	nociceptin opioid receptor
PAG	periaqueductal gray
PAR	protease activated receptor
PBS	phosphate-buffered saline
PC	principal component
PCA	principal component analysis
PCR	polymerase chain reaction
PDB	Protein Data Bank
PFA	paraformaldehyde

PKC	protein kinase C
POPC	palmitoyl-oleoyl-phosphatidyl-choline
POPE	palmitoyl-oleoyl-phosphatidyl-ethanolamine
RLucII	renilla luciferase
RMSD	root mean square deviation
RMSF	root mean square fluctuation
RVM	rostral ventromedial medulla
SEM	standard error of the mean
SNP	single-nucleotide polymorphism
SOC	super optimal broth with catabolite repression
TBS	Tris-buffered saline
TM	transmembrane domain
VTA	ventral tegmental area
WT	wildtype
X-gal	5-bromo-4-chloro-3-indolyl-β-D-galactopyranoside
YFP	yellow fluorescent protein
β-FNA	beta-funaltrexamine

Publications

Z. Dekan, S. Sianati, A. Yousuf, **K.J. Sutcliffe**, A. Gillis, C. Mallet, P. Singh, A.H. Jin, A.M. Wang, S.A. Mohammadi, M. Stewart, R. Ratnayake, F. Fontaine, E. Lacey, A. Piggott, Y.P. Du, M. Canals, R.B. Sessions, E. Kelly, R.J. Capon, P.F. Alewood, M.J. Christie (2019). A tetrapeptide class of biased analgesics from an Australian fungus targets the µ-opioid receptor. *PNAS* **166**(44):22353-22358.

R. Hill, A. Disney, A. Conibear, **K. J. Sutcliffe**, W. Dewey, S. Husbands, C. Bailey, E. Kelly, G. Henderson (2018). The novel µ-opioid receptor agonist PZM21 depresses respiration and induces tolerance to antinociception. *Br J Pharmacol* **175**(13):2653-2661.

K. J. Sutcliffe, G. Henderson, E. Kelly, R. B. Sessions (2017). Drug Binding Poses Relate Structure with Efficacy in the µ Opioid Receptor. *J Mol Biol* **429**(12):1840-1851.

Table of Contents

List of Figures

List of Tables

Chapter 1: General Introduction

1.1 The μ opioid receptor

Opioid drugs, such as morphine, are widely considered the gold standard for treating all types of severe pain, from acute, post-operative pain to on-going, chronic cancer pain. However, although opioids are frequently used in the clinic (a recent report in The Lancet showed a 34 % increase in opioid prescriptions in England between 1998 and 2016 (1)), they are not without drawbacks. Adverse effects such as constipation, nausea, respiratory depression, addiction and the development of tolerance limit their use (2). Furthermore, the rise of the opioid addiction and overdose epidemic in the United States (3) has increased the drive to develop better analgesics and understand the molecular nature of opioid agonist efficacy. As such, the task of discriminating the desirable therapeutic effects of opioid ligands from their undesirable adverse effects has long been the goal of opioid pharmacologists and the pharmaceutical industry (4, 5). Morphine, and other opioids, exert their biological effects through activation of the μ opioid receptor (MOPr) (6).

1.1.1 The opioid receptor family

The MOPr belongs to the opioid receptor family, which also includes the delta (DOPr), kappa (KOPr) and nociceptin (NOPr) receptors (7). All four opioid receptors exhibit high sequence homology, but the NOPr displays distinct pharmacology from the other three opioid receptors and is therefore often referred to as “opioid-like” (8). Opioid receptors are members of the G protein-coupled receptor (GPCR) superfamily of membrane proteins (see Section 1.2).

Opioid receptors are widely expressed pre- and postsynaptically in both the central and peripheral nervous system, as well as in some non-neuronal tissues. The MOPr shows the highest levels of expression in the thalamus, periaqueductal gray (PAG), locus coeruleus (LC), rostral ventromedial medulla (RVM), and dorsal horn of the spinal cord (9). In general, opioid receptors function as inhibitors of neuronal excitability, though the ultimate effect of opioid receptor activation may be excitation of a neuronal pathway due to “disinhibition” of inhibitory interneurons (10). Activation of the MOPr results in a range of physiological effects including analgesia, euphoria, respiratory depression and inhibition of the gastrointestinal tract. Although the MOPr is thought to generally signal from the plasma membrane, a recent study by *Stoeber et al.,* has suggested that MOPr signalling can also occur within endosomes and the Golgi, potentially leading to different signalling outcomes (11). The existence of heterodimers within the opioid receptor family adds further complexity to opioid signalling, with studies of the DOPr-MOPr dimer in particular reporting novel signalling and modulation of ligand binding affinities (12-14).

1.1.2 Pharmacology

Studies of MOPr knockout mice showed that the MOPr mediates all the analgesic and euphoric actions of morphine (15), indicating that the MOPr is the primary target of the opioid analgesics.

Morphine, the prototypical opioid agonist derived from the opium poppy, is an alkaloid possessing a rigid ring structure with a protonatable amine. The majority of opioid ligands are also based on this “morphinan” structure, although there are notable exceptions such as methadone and fentanyl, both synthetically derived opioid agonists. Structure-activity relationship studies have demonstrated that most opioid ligands bind to the MOPr via an interaction between the protonated amine and an aspartate residue in the receptor orthosteric site (see Section 1.2.3.2).

The first endogenous opioid peptides to be described were the enkephalins (16), later followed by the endorphins and dynorphins (17, 18), none of which are selective for the MOPr over other opioid receptors. Putative endogenous agonists of the MOPr include the endomorphins, endomorphin-1 and endomorphin-2, both tetrapeptides highly selective for the MOPr (19). The most commonly used peptide agonist in *in vitro* studies of the MOPr is the pentapeptide, DAMGO, a full agonist for both G protein-mediated signalling and phosphorylation, arrestin recruitment and internalisation of the receptor (20, 21). So far, all peptide agonists of the MOPr comprise an N terminal protonated tyrosine residue, or similar, which fulfils the equivalent function of the protonated amine in small molecule opioids (7).

1.1.3 Intracellular signalling from the MOPr

Activation of the MOPr by an opioid agonist results in conformational changes in the receptor (see Section 1.2.3) allowing the intracellular portion of the protein to adopt an open conformation able to couple to a G protein (22, 23), the predominant subtype coupling to the MOPr being the $G_{i/o}$ family (24-26). As depicted in Figure 1.1, through this G protein-dependent signalling, opioids decrease neuronal excitability by promoting the opening of G protein-coupled inwardly rectifying potassium (GIRK) channels (27-31) and inhibiting voltage gated calcium channels (32, 33), resulting in hyperpolarisation of the cell to inhibit action potential firing, and the suppression of neurotransmitter release. Activation of the $G_{i/o}$ G protein also causes inhibition of adenylyl cyclase and thus a reduction in cyclic AMP levels (26, 34, 35). The MOPr can also initiate signalling through the ERK pathway, as well as other kinases including PKC and JNK (36-39).

To produce analgesia, this inhibitory effect of MOPr activation results in reduced neuronal firing in the ascending pain pathway from the dorsal horn of the spinal cord to the thalamus, and disinhibition of the descending pain pathway from the PAG and RVM to the spinal cord (10). Also inhibition of rhythm-generating neurons in the pre-Bötzinger complex, or related nuclei, is thought to result in respiratory depression (40). The euphoric actions of MOPr agonists are produced in the mesolimbic reward pathway, where disinhibition of neurones in the ventral tegmental area (VTA) causes increased dopamine release in the nucleus accumbens (41).

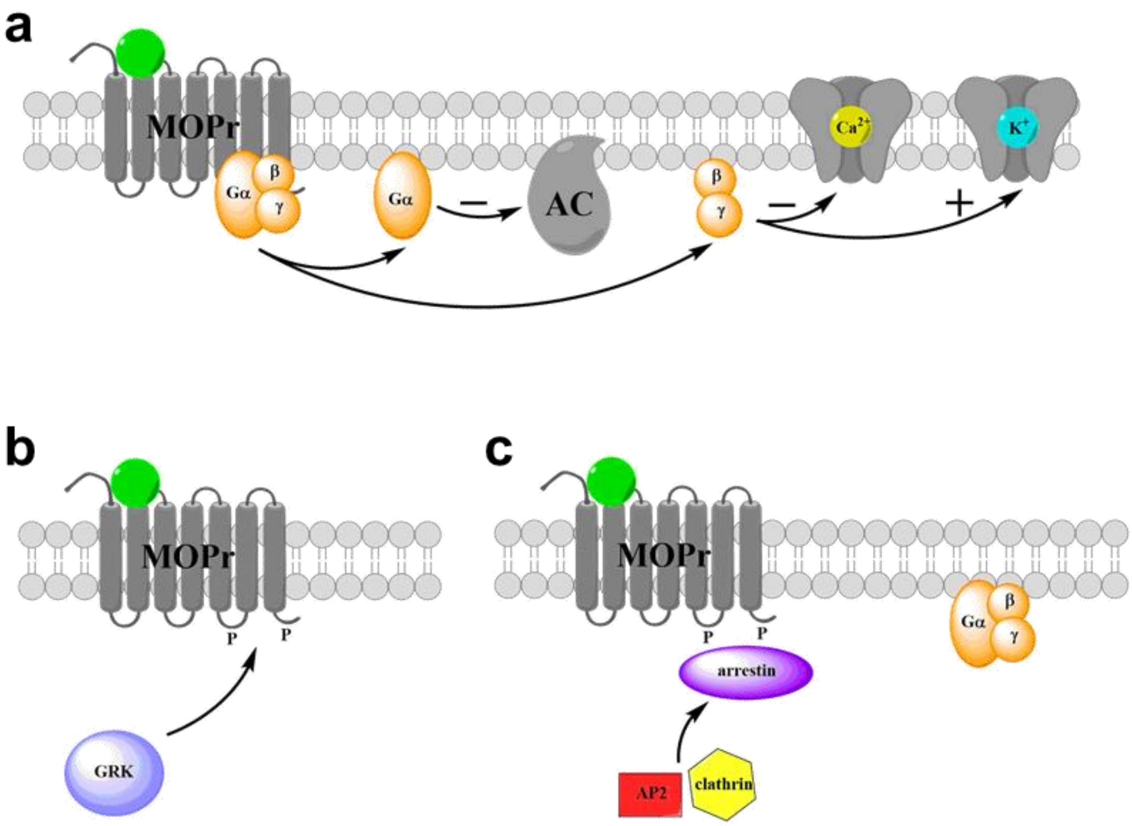

Figure 1.1 Intracellular signalling from the MOPr

a) Upon activation by an extracellular agonist (green), the MOPr activates $G_{i/o}$ G proteins (orange), resulting in dissociation of the Gα unit from the Gβγ subunits. Gα inhibits adenylyl cyclase (AC), whilst the Gβγ subunits open GIRK channels and close calcium channels. b) Following agonist activation, MOPr is phosphorylated on the intracellular loops and C tail by GRK (violet). c) Phosphorylation leads to the recruitment of arrestin (purple), termination of G protein signalling and initiation of arrestin-dependent signalling and receptor internalisation.

1.1.4 Regulation

Residues in the MOPr intracellular loops and C tail are subject to phosphorylation by kinases, both in the basal state and in response to agonist application (42, 43). Phosphorylation of the MOPr promotes recruitment of arrestin and subsequent receptor desensitisation and internalisation; there is a strong correlation between the ability of an agonist to induce phosphorylation and endocytosis of the MOPr (21).

The primary site of MOPr phosphorylation is the unstructured intracellular C terminal tail where a cluster of serine and threonine residues, the “^{370}TREHPSTANT^{379}” motif, undergo agonist-mediated phosphorylation (42). Another serine residue, S363, is constitutively phosphorylated in the absence of opioid agonist (44-46). Within the “^{370}TREHPSTANT^{379}” motif phosphorylation appears to be hierarchical, where all opioid agonists induce phosphorylation of S375, but ligands differ in their ability to induce multi-site phosphorylation (44, 47). In general, high efficacy agonists such as DAMGO induce phosphorylation of all sites in the “^{370}TREHPSTANT^{379}” motif, whereas lower efficacy agonists such as morphine can only induce significant phosphorylation of S375 (44, 48). Moreover, S375 appears to act as the initiator of MOPr C tail phosphorylation, as a S375A mutation resulted in decreased phosphorylation of other residues within the ^{370}TREHPSTANT^{379} motif (49). In the same study, the authors showed that phosphorylation of the ^{370}TREHPSTANT^{379} motif is necessary for sustained interaction with arrestin and consequent MOPr internalisation (49).

The MOPr, like other GPCRs, is primarily phosphorylated by G protein-coupled receptor kinases (GRKs), of which there are seven isoforms (50). Studies in HEK 293 cells and LC neurons have shown that for high efficacy agonists, MOPr phosphorylation and desensitisation is GRK2/3-dependent, whereas morphine desensitisation has a PKC component (39, 46, 47, 51-54). There is also evidence of opioid receptor phosphorylation and desensitisation mediated by other kinases, including ERK, JNK and CaMKII (55-60).

Tolerance to opioids is defined as a reduction in responsiveness after prolonged treatment with an agonist (6). The molecular mechanisms of opioid tolerance are contentious and still under investigation (6). However, receptor desensitisation, along with longer term adaptive changes in the cell, are believed to play a role. Parallel to studies of MOPr desensitisation *in vitro*, *in vivo* tolerance to high efficacy opioids appears to be GRK-dependent (61, 62), whereas tolerance to low efficacy opioids (morphine and oxycodone) can be reversed by PKC inhibition (63, 64). Although there are clear parallels between the kinases involved in MOPr desensitisation and *in vivo* opioid tolerance, it is not yet clear how far desensitisation of the receptor contributes to tolerance (6). In a seminal paper, tolerance to morphine was reported to be abolished in unconditional arrestin-3 knock out mice, suggesting that arrestin-mediated receptor desensitisation is required for opioid tolerance (65). Interestingly, a more recent report by *Kliewer et al.,* showed that in knock-in mice expressing a phosphorylation-deficient MOPr, analgesic tolerance was attenuated, though not completely abolished, suggesting that phosphorylation of the receptor along with other components are involved in opioid tolerance (66). Moreover, morphine tolerance did not develop in LC neurons from animals expressing phosphorylation-deficient MOPr (67).

In summary, the MOPr is an important drug target, both therapeutically in analgesia and in drug abuse, with complex pharmacology and regulation. A better understanding of how the receptor structure relates to the function of this clinically important GPCR may aid the development of more effective opioid drugs.

1.2 Structure and function of G protein-coupled receptors

1.2.1 GPCR signalling

G protein-coupled receptors (GPCRs) serve as cell sensors to external stimuli, translating extracellular inputs to intracellular signalling events. GPCRs are the largest superfamily of membrane proteins, comprising over 800 different receptors (68), with important roles in all tissue types, from the cardiovascular system to the central nervous system, regulating a vast array of physiological processes. These diverse roles of GPCRs necessitate that they can respond to a wide range of stimuli, from small molecules and peptides, to ions (69), photons and even mechanical force (70).

Upon activation by an agonist, GPCRs undergo conformational changes to facilitate coupling to intracellular heterotrimeric G proteins. G proteins are composed of Gα, Gβ and Gγ subunits, with the type of Gα subunit dictating the G protein subtype (G_s, $G_{i/o}$, $G_{q/11}$ or $G_{12/13}$). Binding of the G protein to the activated GPCR induces the exchange of GDP for GTP within the Gα subunit, and dissociation of the complex into separate Gα subunits and Gβγ dimers. The dissociated subunits regulate second messenger proteins and modulate ion channels to initiate cellular signalling.

After activation, residues on the GPCR intracellular loops and C tail are phosphorylated, primarily by GRKs but also other kinases as discussed for the MOPr in Section 1.1.4, which promotes the recruitment of arrestins. Arrestin, as the name suggests, terminates G protein signalling causing desensitisation of the receptor. Arrestins can also act as scaffolds to recruit the cellular machinery required for receptor internalisation, and initiate arrestin-dependent, G protein-independent signalling (71). There are four arrestin isoforms, subdivided into two families; the visual arrestins (arrestin-1 and arrestin-4) and the non-visual arrestins (arrestin-2 and arrestin-3). The predominant arrestin isoform involved in the regulation of the MOPr is probably arrestin-3 (72). Note that arrestin-2 and arrestin-3 are also termed β-arrestin1 and β-arrestin2, respectively. However, the systematic names arrestin-2 and arrestin-3 will be used throughout this thesis.

1.2.2 GPCR structure

Due to their wide role in physiology and disease and intrinsically high druggability, GPCRs represent the largest family of protein targets for FDA (USA Food and Drug Administration) approved drugs, with approximately 35 % of medicines acting on this superfamily (73). Revolutionary technological developments in structural biology over the last few decades have made possible the determination of high resolution structures of these dynamic membrane proteins (74), and have thus led to the increasing use of structure-based drug discovery to rationally design new therapeutics.

Figure 1.2 shows the dramatic rise in the number of available GPCR structures since the first structure of bovine rhodopsin was resolved in the year 2000 (75). The inactive, antagonist-bound x-ray crystal structure of the MOPr was resolved in 2012 (76), followed by the agonist and G protein-mimetic nanobody-bound structure in 2015 (22). Most recently, developments in the field of cryo-electron microscopy (cryoEM) (77) have led to many reported structures of GPCRs in complex with intracellular proteins; the agonist-bound MOPr-G_i complex was released in 2018 (23).

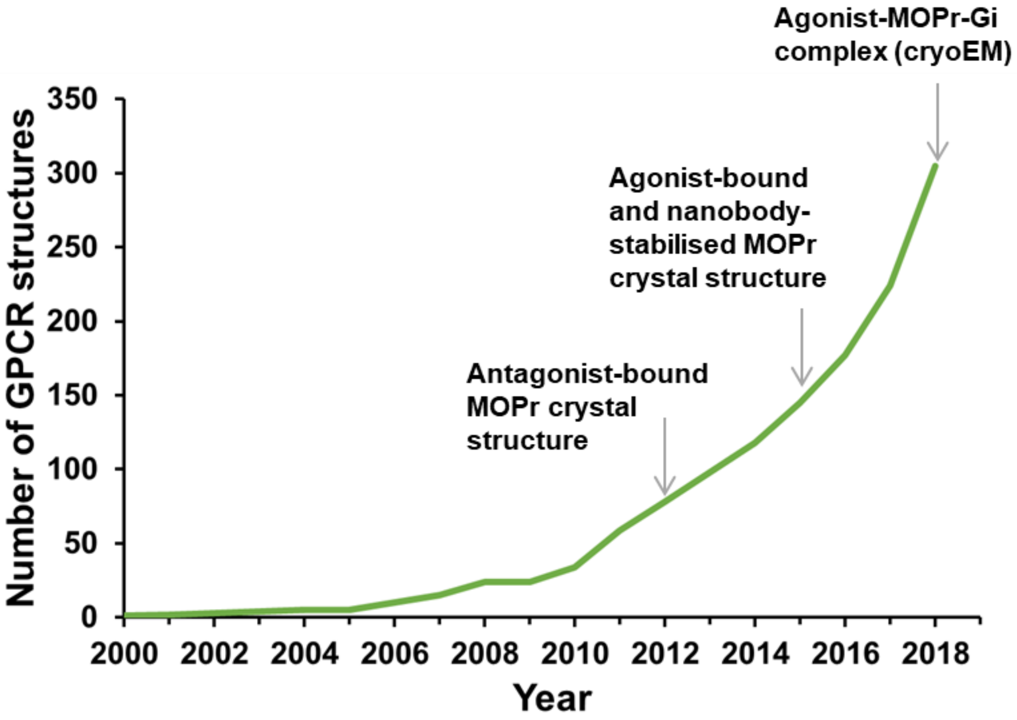

Figure 1.2 Exponential increase in GPCR structures

The cumulative number of GPCR structures available on the Protein Data Bank since the year 2000. Data obtained from the GPCRdb (78).

This plethora of new GPCR structures has provided unprecedented insight into how receptor structure relates to function, and yet the precise molecular determinants of drug specificity and efficacy have not been fully elucidated. A better understanding of how ligand-receptor interactions translate to activation of a GPCR will aid future drug design for these important biological targets.

GPCRs can be classified by sequence homology into the following subfamilies; Class A (Rhodopsin-like), Class B1 (secretin receptor-like), Class B2 (adhesion receptors), Class C (metabotropic glutamate receptor-like) and Class F (frizzled-like) (79). Class A is by far the most populated class, both in receptor number (around 80 % of the GPCRome are Class A receptors (80)) and as drug targets, with the vast majority of GPCR-targeting compounds acting on this class (68). The MOPr is a Class A GPCR.

The general architecture of GPCRs encompasses an extracellular N terminus, seven hydrophobic α-helical transmembrane domains (TMs) connected by three extracellular and three intracellular loops, and an intracellular C tail important for receptor trafficking and regulation. Within the Class A GPCR subfamily (and to a large extent, Class B1 and B2) there is significant conservation of the structural motifs which appear to underlie receptor activation, the key components of which are discussed below.

In order to make comparisons between different receptors, residues in Class A GPCRs can be numbered according to the system developed by *Ballesteros and Weinstein* (81). In this system, residues in the GPCR transmembrane domains are given the notation “X.Y”, where “X” is the helix number (1 to 7), and “Y” is the position along the helix; the most conserved residue in each helix is numbered “50” and all others are numbered by their position relative to this residue. Ballesteros-Weinstein numbering will be used throughout this thesis.

1.2.3 Key motifs for Class A GPCR activation

Although this large superfamily of GPCRs vary in sequence and the type of ligand they respond to, incredibly the activation-related conformational changes converge around the intracellular region (82) so that over 800 different receptors couple to only four G protein families and four subtypes of arrestin.

Key motifs throughout the GPCR architecture are conserved within GPCR subfamilies and are responsible for transmitting the binding of an agonist ligand to the orthosteric pocket in the extracellular portion of the helix bundle, to large conformational changes on the intracellular side of the protein. Comparison of the available x-ray crystal structures, cryoEM structures and other biophysical data, has identified conformations of groups of residues and whole helices which hallmark the active state.

Activation of the MOPr, and all currently resolved active-state Class A GPCRs, is associated with large conformational changes in the receptor transmembrane domains on the intracellular side of the protein (Figure 1.3). TM5 and TM7 move in towards the helix bundle, whilst a large outswing of TM6 results in an “open” receptor conformation to accommodate interaction with a G protein (22, 83-87). For the receptor to adopt the fully active state, characterised by this large outward movement of TM6, agonist binding is insufficient and the interaction with a G protein or mimetic nanobody is also required (88-91). An NMR study of the MOPr revealed that although the conformational changes in TMs 5 and 6 required the presence of a G protein, smaller conformational changes in intracellular loop (ICL) 1 and helix 8 were observed in the presence of an agonist alone, suggesting that these more subtle movements may precede G protein coupling (92).

On the residue level, Figure 1.4 depicts the important signal transduction motifs in Class A GPCRs, comparing the positions of these groups of residues in the inactive state antagonist-bound MOPr crystal structure with the fully active agonist- and G protein bound-MOPr cryoEM structure. The following sections will describe these motifs and their importance in conveying agonist efficacy.

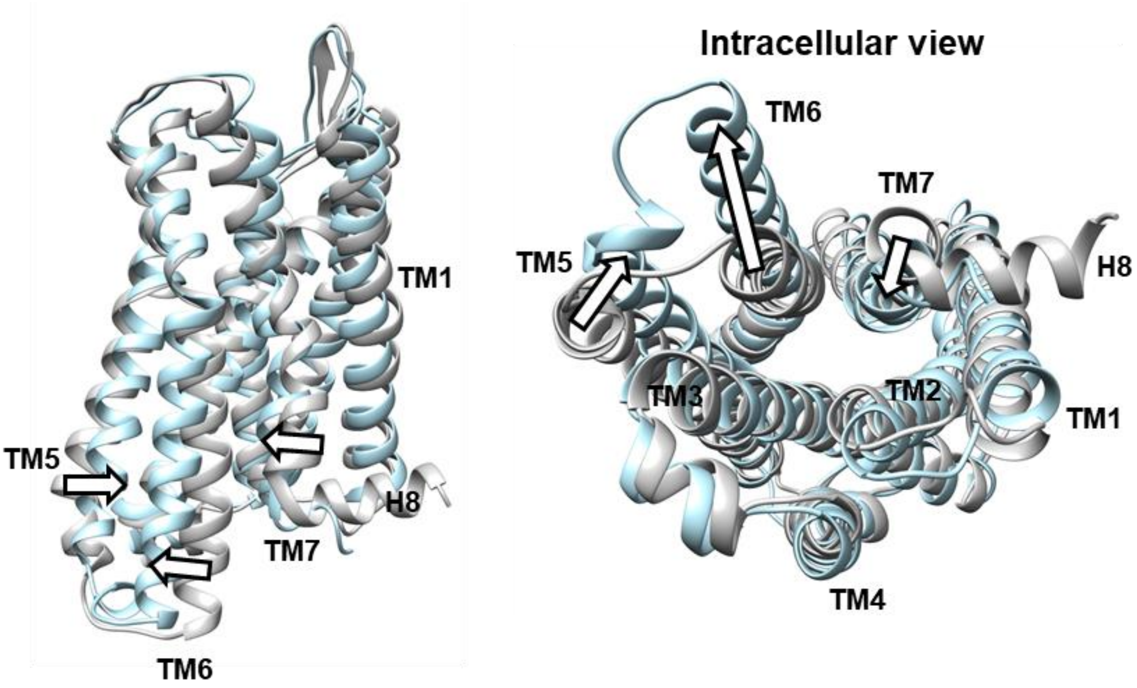

Figure 1.3 Transmembrane domain movements associated with MOPr activation

Activation of the MOPr is characterised by large scale movements of the intracellular ends of TMs 5, 6 and 7. Arrows depict the helix movements between the β-FNA bound inactive MOPr crystal structure (PDB: 4DKL, (76)) (grey), and the DAMGO and G_i bound active MOPr cryoEM structure (PDB: 6DDE (23)) (teal).

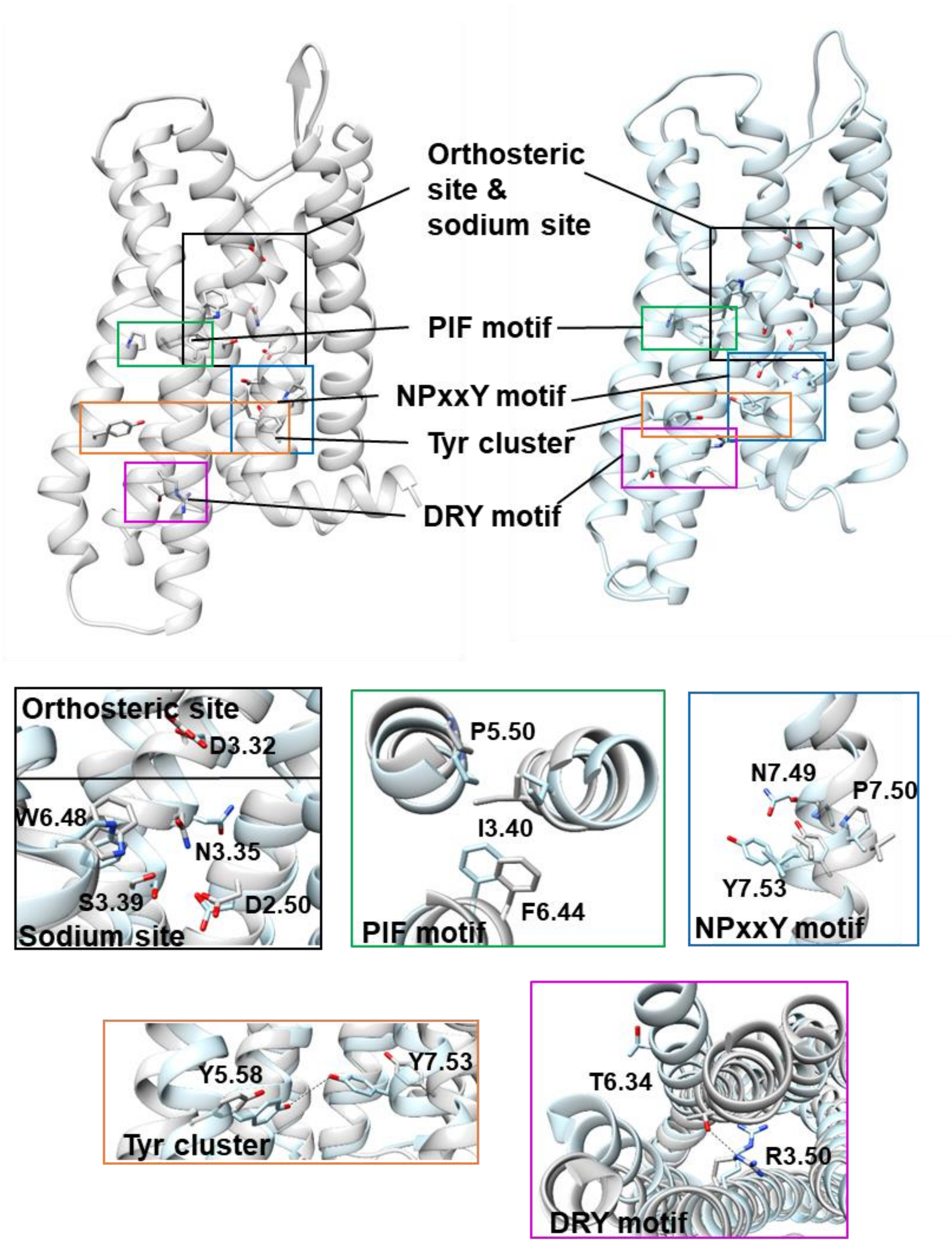

Figure 1.4 Important motifs in Class A GPCRs

Residues considered to be important in signal transduction from the orthosteric ligand binding site to the intracellular domain are shown for the β-FNA bound inactive MOPr crystal structure (PDB: 4DKL, (76)) (grey), and the DAMGO and G_i bound active MOPr cryoEM structure (PDB: 6DDE (23)) (teal).

1.2.3.1 DRY motif and the ionic lock

The E/DRY motif is a conserved group of residues on the third transmembrane domain (TM3) which have been shown to play important roles in GPCR signal transduction, as mutations of this site can enhance GPCR constitutive activity (93-96), abolish G protein coupling (97, 98), whilst naturally occurring mutations in this region cause disease (99). In the inactive state, E/D3.49 forms a salt bridge with R3.50 (100).

Importantly, the DRY motif also interacts with TM6, for which the most striking difference between the inactive and active MOPr is the large outward swing of this helix (Figures 1.3 and 1.4), opening a crevice on the intracellular side of the receptor allowing coupling to a G protein or arrestin (22). This large domain movement of TM6 is common across GPCRs, serving as a hallmark of the active state (101, 102). This TM6 outswing was first characterised in a study of rhodopsin which used spin labelling to show that a large movement of TM6 was coupled to receptor activation, well before any crystal structures were available (103). In the inactive state, an interaction termed the “ionic lock” between R3.50 of the DRY motif on TM3 and an acidic residue in position 6.30 on TM6 stabilises the receptor in the closed inactive conformation. The MOPr, and other opioid receptors, lack an acidic residue in position 6.30, but instead a threonine in position 6.34 participates in the inactive state interaction with R3.50, so that in opioid receptors this “ionic lock” is in fact a hydrogen bond. However, the interaction appears to serve the same purpose (76). Disruption of the ionic lock by mutation of either residue to alanine resulted in increased constitutive activity of the β_2 adrenoceptor (93, 100). Furthermore, mutation of T6.34 in the MOPr resulted in a constitutively active receptor in the case of a T6.34K mutation, whilst the T6.34D receptor was inactive (104). These studies suggest that this TM3 – TM6 interaction, whether through a salt bridge or hydrogen bond, is indeed important in maintaining the inactive state of the GPCR.

Recently, cryoEM structures of a series of Class A and Class B GPCRs have revealed that the size of this TM6 outswing varies between receptors (23, 105-108). It has been suggested that this discrepancy relates to the G protein coupling specificity of the GPCR, with receptors primarily coupled to the G_s subtype of G protein favouring a greater movement of TM6 than $G_{i/o}$ coupled receptors (23, 109, 110). In the cryoEM structure of the MOPr-G_i complex, TM6 is displaced by 10 Å compared to the inactive structure, whereas in the β_2 adrenoceptor, TM6 is displaced by a further 9 Å (23).

1.2.3.2 Orthosteric ligand binding site

For Class A GPCRs the orthosteric ligand binding site is located towards the extracellular side of the receptor, comprising a solvent-accessible pocket surrounded by TMs 3, 5, 6 and 7. Compared to other crystallised Class A GPCRs, perhaps because it is fundamentally a peptide-sensing receptor, the MOPr has a remarkably deep orthosteric binding pocket extending into the helix bundle (76). Mutagenesis studies, later corroborated by crystallographic data, have shown that D3.32 and H6.52 in particular are essential residues for opioid ligand binding, recognising the protonated amine and the phenol groups of the opioid, respectively (22, 76, 95, 111-114).

Due to the wide diversity in the type of ligands recognised by the GPCR family, the precise movements and ligand-residue interactions within the orthosteric ligand binding site vary between receptors. However, these agonist-related changes quickly converge to stabilise common side chain movements in key motifs at the base of the orthosteric pocket (101). Indeed, this region of the GPCR helix bundle below the orthosteric site serves as a hub of signal transduction activity and is discussed in sections 1.2.3.3 to 1.2.3.5 below.

For the MOPr, which has so far been crystallised with a covalently bound antagonist (76) and an unusually high affinity agonist (22), the understanding of how clinically relevant opioids and endogenous agonists interact with the MOPr orthosteric pocket is incomplete.

1.2.3.3 Allosteric sodium ion binding site

Immediately below the orthosteric site sits a highly conserved allosteric binding pocket for a sodium ion (Figure 1.4). The term “allosteric” refers to any modulatory binding site on a protein outside of the “orthosteric” site to which the endogenous ligand binds.

For over 40 years, sodium has been known to modulate agonist binding and GPCR signalling within a physiological range of concentrations in many Class A GPCRs, including the MOPr (115-121). More recently, high resolution x-ray crystal structures were able to detect the binding of sodium in the helix bundle (122-125). Notably, a sodium ion was resolved in the inactive state structure of the DOPr (124). In this site, the sodium ion is directly coordinated by the conserved residues D2.50, N3.35 and S3.39, as well as water molecules. A second coordination shell includes the conserved tryptophan microswitch in position 6.48 (see Section 1.2.3.4). As these residues are conserved in the MOPr, it is generally assumed that the configuration of the allosteric sodium site is similar in the MOPr, however the available crystal structures of the MOPr are not at high enough resolution to detect a bound sodium ion.

Mutations of this allosteric sodium ion binding site have striking effects on both ligand binding affinity and signal transduction (126-131). Sodium generally functions as a negative allosteric modulator of GPCR function, reducing the binding affinities of agonists, whilst enhancing that of antagonists, and inhibiting downstream signalling (115, 116, 120, 121, 132). Compellingly, ^{19}F-NMR experiments reported sodium stabilising the inactive state ensemble of the adenosine A_{2A} receptor, providing biophysical evidence of the negative modulatory effect of sodium on this GPCR (133). Interestingly, there are also reports of biased modulation by the allosteric sodium site, whereby mutations to the allosteric sodium site in the neurokinin-1 receptor altered the balance between G protein and arrestin signalling (134). Together, these data clearly identify sodium and the allosteric pocket in which it resides, as important regulators of GPCR function.

The positive allosteric modulator of the MOPr, BMS-986122, may exert its modulatory effect via the allosteric sodium ion binding pocket, as BMS-986122 inhibited the ability of sodium to reduce agonist binding (135). Positive allosteric modulators of the MOPr have therapeutic merit if they can be developed to specifically enhance the activity of endogenous opioid peptides to alleviate pain, whilst avoiding adverse effects in non-analgesic pathways (136). Probe dependence here would be key, as compounds capable of enhancing the euphoric effects of abused opioids would have considerable abuse liability. The allosteric sodium pocket therefore provides an interesting novel target for MOPr allosteric modulators.

Moreover, *White et al.,* obtained crystal structures of D2.50N and S3.39A mutant adenosine A_{2A} receptors, showing that mutations in the allosteric sodium site did not affect the conformation of residues in the orthosteric binding site, but did modulate the conformation of the distant NPxxY motif (see Section 1.2.3.6), highlighting the role of the allosteric sodium site in transmitting conformational changes between the extracellular and intracellular domains of the GPCR (137).

Importantly, GPCR activation involves structural rearrangements which collapse the allosteric sodium pocket and presumably disrupt sodium binding (138, 139). These dramatic changes in the sodium pocket have been used as evidence that sodium is an important regulator of receptor activation (138). One hypothesis proposes that the sodium ion occupies the allosteric pocket in the inactive state until, upon agonist binding, structural changes in the extracellular region around the orthosteric site lead to relocation of the sodium ion from the allosteric pocket to the cytoplasm, and this facilitates the GPCR transitioning to an active state. However, the precise molecular mechanism and physiological role of sodium modulation of GPCR function is still unknown.

Finally, it has been suggested (140) that translocation of sodium ions through the receptor from the extracellular to intracellular side may provide a mechanism for the observed voltage sensitivity of some GPCRs, such as the α_{2A} adrenoceptor (141), M_1, M_2, M_3 and M_5 muscarinic receptors (142-144) and the P2Y receptor family (145). This may indeed be important for opioid receptors, which are expressed in excitable tissue, and deserves further exploration.

1.2.3.4 W6.48 rotamer toggle switch

A highly conserved tryptophan in position 6.48 resides in the second coordination shell of the allosteric sodium ion binding pocket (Figure 1.4) at the base of the orthosteric ligand binding site. Spectroscopic and computational studies identified conformational changes in this residue which corresponded to agonist stimulation of the receptor, leading to the hypothesis that W6.48 may act as an important microswitch for GPCR activation (146-152). Indeed, subsequent crystal and cryoEM structures, including that of the MOPr, revealed rotameric changes in the W6.48 indole ring between inactive and active state structures (22, 23, 76, 153, 154). As depicted in Figure 1.4, rotation around the Cβ-Cγ axis allows the indole ring to adopt different conformations; orientated perpendicular to the lipid bilayer (the inactive antagonist-bound MOPr), parallel to the bilayer (the fully active agonist- and G protein-bound MOPr), or a position in between. Mutagenesis of this residue drastically alters ligand-induced signalling in a range of GPCRs, in some cases reducing ligand binding affinity (155-157), abolishing downstream signalling (158-160), or even altering the bias profile for some receptors (158, 161). However, functional assays with a W6.48 mutant have not been reported for the MOPr.

Together, these data suggest that W6.48 functions as an important link between the orthosteric agonist binding site and the activation state of the GPCR.

1.2.3.5 PIF motif

Also close to the allosteric sodium site resides the PIF motif (alternatively termed the “core triad” (22)) comprising P5.50 of TM5, I3.40 of TM3 and F6.44 of TM6. Comparison of the available inactive and active state structures of the MOPr (22, 76), and other Class A GPCRs (86, 162-164), revealed concerted movements of these residue side chains such that P5.50 moves inwards, whilst the side chain of I3.40 undergoes a rotameric change and the phenyl ring of F6.44 swings towards TM5 (Figure 1.4). It has been suggested that these movements serve to alter the hydrogen bonding network between side chains within the helix bundle to connect changes in the orthosteric site to the intracellular domain of the GPCR (22). Indeed, mutations of the PIF motif in the $5HT_{2C}$ receptor abolished the inverse agonist profile of ritanserin for G_q activation (165).

1.2.3.6 NPxxY motif

On the intracellular side, the NPxxY motif has also been identified as undergoing conformational changes during receptor activation (166, 167). Similar to the DRY motif stabilising the inactive state, the GPCR active state appears to be stabilised by a water-mediated interaction between Y7.53 of the NPxxY motif and Y5.58 in TM5; sometimes termed the “tyrosine cluster”. This is supported by numerous studies across many GPCRs showing that single or double mutations of Y5.58 and Y7.53 result in disruption to receptor signalling and destabilisation of the active state (168-172). Moreover, conformational changes around the NPxxY motif have been used in computational studies to reliably assign the activation state of the GPCR (173). Finally, disease-causing mutations at this site have been identified in humans, again highlighting the critical role of this motif in normal GPCR function (174-176).

1.2.3.7 Intracellular loops

The three intracellular loops, particularly ICL3, are highly dynamic and therefore often replaced with a T4 lysozyme, or other stabilising protein, in GPCR crystal structures. ICL3 connects the intracellular ends of TM5 and TM6 and therefore undergoes a large conformational change on receptor activation due to the outward movement of TM6 (see Section 1.2.3.1). Both ICL2 and ICL3 also have important roles in coupling to intracellular G proteins and arrestin, as residues in these loops are found at the interface between the GPCR and its binding partner in crystal structures of GPCR-G protein and GPCR-arrestin complexes (177). Interestingly, in the only current structure of a GPCR-arrestin complex, that of rhodopsin and visual arrestin (178), ICL1 is also found at this interface, whereas it does not appear to be involved in G protein coupling in structures of GPCR-G protein complexes (23, 105).

1.2.3.8 Extracellular loops

It is becoming increasingly appreciated that the extracellular loops play an important role in GPCR function. ECL2 is the longest extracellular loop in Class A GPCRs and has been implicated in ligand recognition (179-183), GPCR activation (181, 184, 185), agonist bias (186, 187) and as the binding site for allosteric modulators (87, 188, 189). Studies of the muscarinic and endothelin receptors, along with rhodopsin, have suggested that ECL2 forms a “lid” over the orthosteric binding site, effectively trapping the ligand in the binding pocket and possibly controlling ligand dissociation rate (75, 190, 191). Similarly, ECL2 forms an intermediate binding site during ligand association and dissociation from β-adrenoceptors (192, 193).

For the MOPr, studies using chimeric receptors have implicated the ECLs in determining ligand selectivity between different opioid receptor subtypes and other Class A GPCRs (194-197). Furthermore, the cryoEM structure of the DAMGO-MOPr-G_i complex (23), as well as computational studies docking fentanyl (198) and herkinorin (199) to the MOPr, all revealed interactions between the ligands and the ECLs.

1.3 Biased agonism

1.3.1 Definition

The previously held simplistic view of GPCR pharmacology was that GPCRs function as binary switches, residing in either an inactive state or an agonist-bound active state. However, it is now appreciated that GPCRs can occupy a variety of functional states, stabilised by different ligands, with different affinities for coupling to intracellular signalling partners. This idea that an agonist can stabilise a distinct conformational state of the receptor with higher affinity for one intracellular signalling protein over another leads to the concept of biased agonism (also known as ligand bias, functional selectivity and ligand directed signalling) (200).

Biased agonism is defined as a ligand inducing preferential signalling through one pathway over another, via stabilisation of different active conformations of the GPCR (Figure 1.5). Ligand bias is always described relative to a reference agonist, usually the endogenous ligand, taken to be “unbiased” or “balanced”. In Figure 1.5a, the reference agonist (green) stabilises a conformation of the GPCR capable of engaging a G protein or an arrestin, whereas, the G protein-biased agonist (blue) stabilises a conformation which favours G protein activation over arrestin recruitment. This preferentially directs signalling through the G protein pathway. Conversely, the arrestin-biased agonist (red) has the opposite bias profile; promoting a receptor conformation which preferentially recruits arrestin over G protein activation.

Agonist bias can be measured and quantified by comparison of concentration-response curves in the relevant cell signalling assays. In the example in Figure 1.5b, the G protein-biased ligand (blue curve) is left-shifted compared to the reference agonist (green) in the G protein assay, but in the arrestin assay the G protein-biased agonist has a reduced maximum response and right-shifted curve, relative to the reference agonist. *Vice versa*, the arrestin-biased ligand has lower potency in the G protein assay (red curve), but a left-shifted curve in the arrestin assay, compared to the reference agonist. In practice, agonist bias is not always this obvious, necessitating the use of bias calculations and statistics to determine relative bias between compounds (201).

Classically, the term ligand bias is often used to describe bias between G protein or arrestin-mediated signalling. However, bias can also occur between different G protein subtypes (202-204), different arrestin isoforms (205), and other signalling proteins, for instance the kinases responsible for receptor regulation (206).

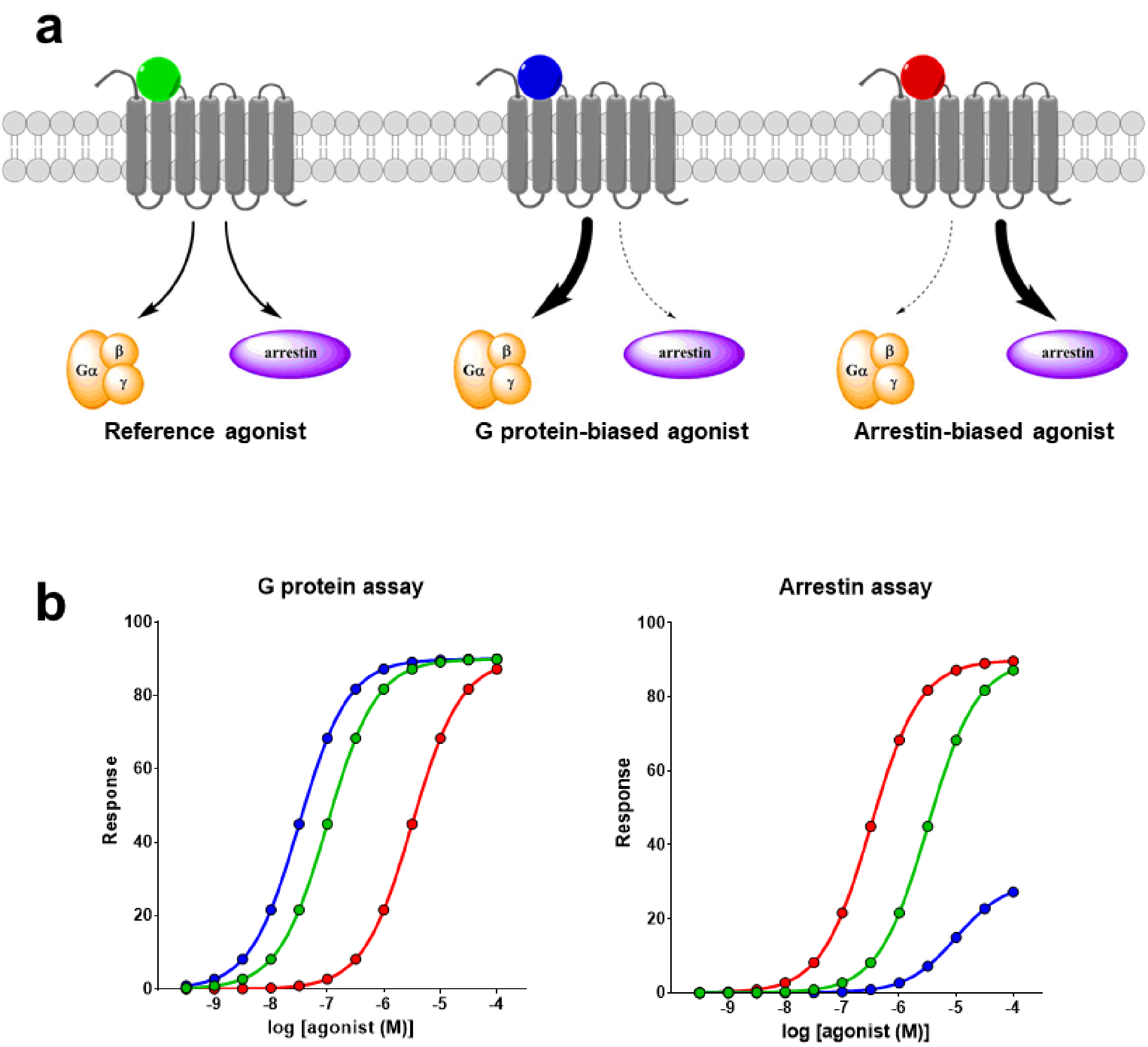

Figure 1.5 Biased agonism

a) An unbiased ligand (green) stabilises an active receptor conformation capable of engaging all the downstream signalling pathways, G protein (orange) and arrestin (purple). A G protein-biased ligand (blue) will stabilise an active conformation which preferentially activates G protein signalling, whereas an arrestin-biased ligand (red) will preferentially recruit arrestin. b) In cell signalling assays, compared to the reference agonist (green), the G protein-biased agonist (blue) has a left-shifted curve in the G protein assay, but a reduced response in the arrestin assay. In contrast, the arrestin-biased agonist (red) switches from being less potent than the reference agonist in the G protein assay, to more potent in the arrestin assay.

1.3.2 Biased compounds in the clinic

The possibility of a ligand being able to bias downstream signalling towards one particular intracellular outcome potentially has huge implications for drug design. Clinically, a biased ligand could avoid adverse effects by directing signalling away from a pathway known to cause side effects, whilst simultaneously enhancing the beneficial effect by displaying increased efficacy for the therapeutic signalling pathway.

Although the rational design of biased compounds is still in the early stages, some clinically used compounds have retrospectively been identified as biased agonists. For instance, the β_2 adrenoceptor antagonist, carvedilol, used to treat heart failure, has been since shown to be arrestin-biased, as it stimulates recruitment of arrestin to the β_2 adrenoceptor whilst acting as an antagonist for G protein activation (207). This arrestin-biased nature of carvedilol may contribute to improved survival statistics in heart failure patients treated with carvedilol over other β-blockers (208), as arrestin signalling from the β_2 adrenoceptor appears to be cardio-protective (209).

In the opioid field, although various G protein-biased MOPr compounds are under development (see Section 1.3.4), none have yet reached the clinic. Biased agonism is also under investigation as a therapeutic strategy for other opioid receptor subtypes (210, 211). For example, the KOPr agonist, nalfurafine, which is currently licenced in Japan as an anti-pruritic, was recently reported to be G protein-biased (212). This finding may provide an explanation for its reduced dysphoric effects compared to other KOPr agonists (213, 214).

As yet, no newly developed biased agonist for any GPCR has reached the clinic. For instance, TRV-027, an arrestin-biased ligand at the angiotensin II type 1 receptor, was efficacious in *in vivo* models of congestive heart failure, reducing blood pressure but improving cardiac performance (215-217). However, a Phase 2 clinical trial reported that TRV-027 failed to perform better than placebo, and development of this compound has since halted (218).

The reason for this attrition is unclear, though it remains challenging to translate biased signalling observed at the cellular level to efficacy in whole animal systems (219, 220).

1.3.3 Molecular mechanisms of ligand bias

The molecular mechanism of biased agonism at the MOPr, and indeed any GPCR, is yet to be fully elucidated. The current favoured hypothesis is that the underlying conformational heterogeneity of a GPCR allows the receptor to occupy multiple distinct active conformations, dependent on the bound ligand (221). If agonists are capable of stabilising unique active conformations of a receptor, it follows that these distinct active states would have different affinities for intracellular effector proteins, and therefore drive signalling through one coupling partner over another.

There is a body of evidence from spectroscopic studies supporting the presence of multiple GPCR functional states. For instance, using a quantitative mass spectrometry technique labelling residues at multiple sites along the protein, *Kahsai et al.,* showed that the β_2 adrenoceptor adopts different conformations in the presence of 9 functionally distinct ligands (222). Indeed, an NMR study of the same receptor showed the β_2 adrenoceptor existing in multiple inactive, active and intermediate conformations (91). A similar approach also reported the presence of at least two inactive and two active states of the adenosine A_{2A} receptor, with the relative population of each state determined by the bound ligand (223). More recently, study by *Wingler et al*., used DEER spectroscopy to probe the conformational state of the angiotensin II type I receptor in the presence of a panel of differently biased ligands (224). They showed not only that in the apo state the receptor exists in a conformationally heterogenous population, but that agonist binding caused large conformational changes in the intracellular regions of the receptor. Importantly, in the presence of G protein-biased agonists the receptor favoured an “open” state, whereas arrestin-biased agonists shifted the ensemble to an “occluded” conformation, which was less capable of interacting with a G protein.

The lack of a cell membrane and unusual detergent environment in the above studies may impact the conformations favoured by the GPCR. The development of biosensors using FlAsH-BRET constructs may allow monitoring of receptor conformations in an intact cell. FlAsH-BRET utilises a tetracysteine motif incorporated into the intracellular domain of the GPCR to bind a fluorescent biarsenical hairpin (FlAsH) tag, which acts as an acceptor for bioluminescence resonance energy transfer (BRET) from a luciferase enzyme fused to the GPCR C tail. Conformational changes in the GPCR intracellular domains are detected as a change in the BRET signal. Such sensors have already been reported for the β_2 adrenoceptor, angiotensin II type I receptor, and prostaglandin F2α receptor (225, 226).

The last year has seen the rapid appearance of many cryoEM-resolved structures of GPCR-G protein complexes (23, 105, 106, 108, 227-230). The speed at which this field is moving suggests that we shall surely see many more complexes resolved in the near future, including that of GPCR-arrestin complexes and GPCRs bound to biased agonists, allowing comparison of the activated receptor conformations. At the time of writing, the only GPCR-arrestin structures available are that of the rhodopsin-visual arrestin complex (178, 231, 232). Comparison of the rhodopsin-arrestin interface with that of GPCR-G protein complexes suggests that in general, a shared interface involving TMs 3, 5 and 6 exists for G proteins and arrestins, however the extent of the outswing of TM6 is greater for the G protein-bound receptor than arrestin (177, 233), in agreement with the “occluded” state described by *Wingler et al., (224)*. Moreover, coupling to arrestin may involve more extensive interactions at the TM7 / helix 8 interface (177). This is supported by a study of the angiotensin II type 1 receptor which used molecular dynamics simulations (see Section 1.4) to investigate the conformational states of both the wildtype and G protein- and arrestin-biased mutants (234). Simulations of the G protein-biased mutant were associated with a change in the conformation of TM7, whereas the arrestin-biased mutant exhibited increased stability of the same helix. The authors therefore suggest that in the angiotensin II type I receptor, destabilisation of TM7 is involved in G protein activation, whilst stabilisation facilitates arrestin signalling.

A cryoEM resolved structure of the Class B GLP-1 receptor in complex with the G_s G protein and the G protein-biased agonist ExP5, revealed a possible structural mechanism for biased agonism at this peptide-sensing receptor (108). Unlike the GLP-1 bound receptor (235), ExP5 engaged in interactions with the extracellular end of TM1, causing this helix to rotate towards TM2, whereas with GLP-1 bound TM1 was positioned closer to TM7. Alanine mutagenesis of residues in TM1 confirmed their importance in ExP5 G protein-mediated signalling, but not for GLP-1. In addition, the conformation of ECL3 was different between the two agonist-bound structures, with mutation of ECL3 residues hindering the binding affinity of GLP-1, but not ExP5. This suggests that at the GLP-1 receptor, biased ligands stabilise different conformations on the extracellular side of the protein which translates to an allosteric effect on effector coupling of the intracellular domain.

In order to facilitate the rational structure-guided design of biased ligands, work is also underway to identify specific residues and motifs important for encoding agonist bias. For example, comparison of the crystal structures of ergotamine bound to the $5HT_{2B}$ (162) and $5HT_{1B}$ (236) receptors, at which it is an arrestin-biased and unbiased ligand respectively, revealed structural differences in the PIF and NPxxY motifs (see Sections 1.2.3.5 and 1.2.3.6). In these structures, the PIF motif was stabilised in an active conformation in the $5HT_{1B}$ receptor, but not in the $5HT_{2B}$ receptor, whereas NPxxY was in an active conformation in the $5HT_{2B}$ receptor, suggesting that these residues may be important in specifying the bias profile of ergotamine (162). Residues in the allosteric sodium ion binding site (Section 1.2.3.3) have also been implicated in biased agonism as mutation of N3.35 to alanine or valine in the DOPr enhanced constitutive arrestin recruitment, but not G protein signalling (124). A series of studies of aminergic receptors have also identified a conserved hydrophobic residue in position 45.52 of ECL2 (numbering for loops follows the nomenclature described in (237)), along with position 7.35 in TM7 and residues in TM5, as predictors for biased agonism at this receptor family (186, 187, 238, 239).

Together, these studies point to a mechanism whereby biased ligands stabilise distinct receptor conformations via their interactions with residues in the binding pocket and stabilisation of specific conformations of key activation motifs. However, the precise nature of these interactions and whether there is a general mechanism for bias across the Class A GPCR family is unknown.

1.3.4 Biased agonism at the MOPr

There is abundant evidence that agonist bias exists at the MOPr. A thorough study of a variety of opioid ligands by *McPherson et al.,* correlated the agonist intrinsic efficacy for GTPγS binding with arrestin-3 recruitment, showing that the endomorphins, along with etorphine and alfentanil, were notable outliers (21). A subsequent analysis revealed endomorphin-2 to be biased towards arrestin recruitment (240). Similarly, *Thompson et al.,* characterised a series of opioid peptides across a range of signalling pathways, revealing that endomorphin-1, loperamide and α-neoendorphin displayed unique bias profiles compared to the other ligands (241). Bioluminescence or fluorescence resonance energy transfer (BRET or FRET) assays are widely used to interrogate ligand-induced G protein activation and arrestin recruitment, and both techniques have been utilised to demonstrate the differential bias of morphinan small molecule MOPr agonists (242, 243).

There are increasing efforts to develop G protein-biased agonists at the MOPr, based on the observation by *Bohn et al.,* that arrestin-3 knockout mice displayed enhanced analgesia in response to morphine, but with a reduction in side effects such as respiratory depression, abuse liability and GI disturbance (244, 245). The widely accepted conclusion from these genetic studies is that arrestin recruitment to the MOPr mediates most (if not all) of the adverse effects seen with MOPr agonists. Moreover, a study by *Schmid et al*., correlated increasing bias towards G protein activation with a greater therapeutic window between efficacy in inducing anti-nociception and the dose limiting adverse effect of respiratory depression, adding weight to the G protein bias hypothesis (246).

This is contradicted however, by the recent paper by *Kliewer et al.,* reporting that mice expressing a phosphorylation-deficient MOPr exhibited a similar, or in some cases enhanced, side effect profile in response to morphine compared to wildtype-expressing mice (66). Furthermore, *Montandon et al.,* used genetically modified mice to show that when GIRK channel subunits are knocked out, opioid agonists induce very little respiratory depression, providing evidence that GIRK channels mediate, at least in part, the inhibition of respiration by opioids (29). As GIRK channel activation is mediated by G proteins, this suggests that respiratory depression may not be avoided by a G protein-biased agonist, and the complete deconvolution of analgesic properties over all adverse side effects by opioids may not be possible.

Although the clinical usefulness of biased opioid ligands is still under debate, the development of G protein-biased MOPr agonists has nevertheless continued. Oliceridine (or TRV-130) (247), is currently in Phase 3 clinical trials for use in acute pain, with the latest published results of the Phase 2b trial showing modest improvement over morphine; oliceridine produced similar levels of analgesia, but with rapid onset and reduced gastrointestinal side effects compared to morphine (248). However, oliceridine appears to still retain abuse potential (249, 250), suggesting that G protein-biased opioids will not overcome the problem of opioid addiction (251).

A computational screen for new MOPr ligands with novel scaffolds fortuitously hit upon a G protein-biased agonist, PZM21, structurally distinct from other small molecule opioids (252). In the same paper, PZM21 was reported to induce antinociception in mice in the hot plate test, but minimal respiratory depression, constipation and reinforcement in conditioned place preference. However, a study carried out in our laboratory failed to replicate these findings, showing instead that PZM21 caused respiratory depression at a similar level to morphine, casting doubt onto the findings of the original paper (253).

Although oliceridine and PZM21 receive the most attention, several groups have reported the discovery of biased agonists at the MOPr. For instance, mitragynine pseudoindoxyl was identified as a mixed DOPr antagonist, MOPr G protein-biased agonist with efficacy in anti-nociception assays but reduced onset of tolerance and other opioid side effects (254). The salvinorin A derivative, herkinorin, is a MOPr agonist which does not recruit arrestin nor induce receptor internalisation (255) (although conversely, *Manglik et al.,* reported that herkinorin does robustly recruit arrestin, with a maximum response comparable to DAMGO (252)). In *in vivo* studies, whilst herkinorin dose-dependently induced anti-nociception, it produced minimal tolerance under chronic administration (256). More recently, a cyclic MOPr peptide was reported as the first G protein-biased MOPr agonist with a “peptide-like” structure (257).

However, it is often the case, particularly for G protein-biased MOPr agonists, that these compounds are partial agonists for G protein activation, making the quantitative assessment of ligand bias difficult (258, 259). Indeed, oliceridine and PZM21 have been shown to act as low efficacy partial agonists for G protein signalling, both in BRET assays directly measuring G protein activation (253), and on downstream ion channel targets (260). Moreover, deconvoluting the relative contributions of bias versus efficacy in mediating the different *in vitro* and *in vivo* profiles of these agonists is problematic. For instance, in a recent study of agonist bias in native neurons, buprenorphine was identified as a G protein-biased agonist, which may in part explain its clinical usefulness as an effective analgesic and opioid-abuse treatment with low abuse liability and tolerance development (220, 261). However, buprenorphine is a partial agonist at the MOPr, so some of its therapeutic effects may also be attributable to its lower efficacy.

1.3.5 Structural basis of MOPr biased agonism

There is limited structural data on the molecular mechanism of biased agonism at the MOPr, partly due to the lack of strongly biased MOPr agonists (see Section 1.3.4, above).

Insights from NMR spectroscopy suggest that, like other GPCRs, the MOPr can exist in multiple ligand-bound conformations, with unbiased or oppositely biased agonists stabilising distinct states (262). The authors proposed a model whereby in the antagonist-bound state the MOPr favours a closed conformation, but the agonist-bound receptor exists in an equilibrium between the closed state and multiple “open” active states, with biased ligands favouring one active state over another (262). This model has been recently supported by a similar study of the angiotensin II type I receptor showing again that the receptor existed in a heterogenous population of closed and open states, stabilised by different biased ligands (224). Furthermore, both independent studies agree that the arrestin-biased conformation is likely to have a more occluded intracellular cavity than the G protein-coupled state (224, 262).

Molecular dynamics simulations by *Schneider et al.,* modelling the binding and subsequent ligand-MOPr interactions of the G protein-biased ligand oliceridine versus morphine, showed different subsets of residues participated in information transfer between the orthosteric ligand binding site and the intracellular domain of the MOPr (263). Specifically, residues in TMs 1, 3 and 7 and helix 8 contributed to the allosteric networks only in the oliceridine-MOPr complex, whereas residues in TMs 2, 4 and 6 were unique to the morphine-MOPr complex (263). Interestingly, one of these residues highlighted in the molecular dynamics study, W7.35, when mutated to alanine altered the bias profiles of the MOPr peptide agonists, DAMGO and endomorphin-2 (264).

Together, these studies suggest that bias at the MOPr has a molecular basis in that the distinct pattern of ligand-residue interactions influences the overall conformation of the receptor, which then drives differential effector coupling. However, specific pharmacophores and ligand-residue interactions responsible for dictating G protein or arrestin bias, or even overall agonist intrinsic efficacy, are yet to be discovered.

The DAMGO-MOPr-G_i complex has recently been resolved by cryoEM (23). With the current rate of technological development in the field of high-resolution cryoEM (77), along with the increasing number of reported MOPr biased agonists, it is surely only a matter of time before further unbiased and biased ligand-MOPr structures are resolved in complex with other intracellular proteins, such as arrestins or GRKs. Ultimately, comparison of multiple MOPr-effector and MOPr-ligand complexes may well reveal the molecular mechanism of how different ligands direct receptor coupling to distinct effector proteins.

Until such structures are available, however, computational techniques such as molecular dynamics simulations, are invaluable as a tool to predict the behaviour of yet unsolved ligand-receptor complexes, based on the currently available crystallographic data. Molecular dynamics, and its application to the study of GPCRs, will be discussed in the section below.

1.4 Molecular dynamics simulations

1.4.1 Definition

Molecular dynamics (MD) simulations are a computational approach to capture the dynamic behaviour of biological molecules. Using a crystal structure or homology model as a starting point, an MD “trajectory” is generated to simulate the thermally induced movement of the structure. Trajectories are calculated using Newtonian mechanics to determine the atomic positions and velocities at each time step, governed by the temperature, pressure and energetics of the system.

MD simulations can be “atomistic”, whereby each atom in the system is represented explicitly and individually, or “coarse-grained”, where atoms are grouped together into beads with an overall property to reduce the degrees of freedom and therefore reduce the computational effort required so that long timescale simulations can be performed. However, in coarse-grained MD what you gain in simulation time you lose in resolution, so detailed side chain movements and ligand-residue interactions cannot be explored. In atomistic MD, although the achievable simulation timescales are much shorter, the behaviour of individual atoms is modelled, allowing much more detailed interpretation of the results. To investigate the detailed ligand-residue interactions and behaviour of key signalling motifs in the MOPr, this thesis will therefore use atomistic MD simulations.

1.4.2 Advantages and limitations

There are a number of advantages in using MD simulations to explore the behaviour of protein-ligand complexes. Firstly, as mentioned in Section 1.3.5, currently available protein structures can be utilised to model how other, yet unsolved, ligand-protein complexes may interact and behave. In the case of the MOPr, neither of the high resolution x-ray crystal structures currently available show the receptor bound to a clinically used opioid drug (22, 76).

Secondly, whilst x-ray and cryoEM structures of GPCRs have given much insight into ligand binding poses and structural differences between inactive and active states, they are static snapshots in time of highly dynamic proteins, and under non-physiological conditions. In order to obtain highly purified and stable samples, GPCRs are usually modified with thermo-stabilising mutations (265), engineered to contain fusion partners such as a T4 lysozyme or BRIL (266), stabilised by the addition of an antibody or nanobody (267, 268), and truncated at the N and C termini, so that the resulting receptor may be quite different from that found *in vivo.* Furthermore, structures of ligand-GPCR complexes are often determined using ligands with unusual properties, such as very slow dissociation rates, picomolar affinity (22, 269), or covalent binding (76) in order to further stabilise the GPCR in a single conformation. In preparing a GPCR structure to model using MD simulations, fusion proteins, antibodies and mutations are removed in order to model the receptor in a more native-like state. In addition, any number of biologically interesting or clinically important ligands can be docked to the receptor and subsequently simulated.

MD simulations also capture the dynamic behaviour of a protein; information which is lost in a static structure, and is particularly important when studying GPCRs which are known to exist in a heterogeneous ensemble of different conformational states (270).

Finally, compared to traditional *in vitro* experiments, molecular docking and MD simulations are a relatively high-throughput method to study different receptors, variants, and compounds. *In silico* screening is now routinely performed in drug discovery to narrow down the number of lead compounds subsequently used in *in vitro* studies (271-273).

Of course, it must be remembered that *in silico* approaches are only models of biological systems. MD simulations are inherently limited by the accuracy of the available forcefields (the algorithms and equations providing the parameters for calculating each MD trajectory step).

Although advances in computing power have vastly increased the possible simulation time from picoseconds to microseconds, except on the most highly specialised machines (274), the timescales for membrane-embedded GPCR MD simulations are still limited to between nanoseconds and microseconds. This is in contrast to physiological GPCR signalling which occurs over milliseconds to hours. Even where longer timescale simulations are achievable, there may still be incomplete sampling of the conformational landscape due to energy minima (275). Both of these issues can (in part) be overcome by the use of enhanced sampling methods, such as accelerated MD and meta-dynamics (275).

Finally, it is not possible to model all aspects of the environment of the native cell, for example the exact membrane composition around the receptor, interactions with other proteins (other than G proteins and arrestins) and interactions with the cytoskeleton. All of these factors may have important impacts on GPCR function (140, 144, 276-278).

1.4.3 Application to the study of GPCRs

In spite of the limitations described above, the application of MD simulations to the study of GPCRs, and indeed the MOPr, have yielded some important findings.

Using the specially designed supercomputer, Anton in the D. E. Shaw laboratory (274), *Dror et al.,* were able to model the binding pathway of small molecule ligands to the β_1 and β_2 adrenoceptor, showing that the ligands all interacted with a common extracellular vestibule before transitioning to the orthosteric binding pocket (192). Similarly, MD simulations of the M_3 muscarinic receptor showed the inverse agonist, tiotropium, also interacted transiently with an extracellular vestibule on dissociation from the receptor (279). Combined with previously reported mutagenesis data (280), the authors proposed this extracellular vestibule may represent an allosteric site on muscarinic receptors. This allosteric site has since been successfully exploited in the structure aided design of muscarinic receptor allosteric modulators (281).

In the opioid receptor family, a putative binding site for allosteric modulators of the DOPr has been discovered using MD simulations (282). The *in silico* experiments resolved a binding site between TMs 1, 2 and 7 above the orthosteric binding pocket, which was validated by *in vitro* mutagenesis in the same study. Similarly, docking and MD simulations of the methadone-bound MOPr in the presence of the positive allosteric modulator, BMS-986122, revealed a similar allosteric pocket in an extracellular vestibule composed of TMs 2 and 7. This revealed a possible molecular mechanism for the modulatory effect of this compound, whereby binding of BMS-986122 disrupted sodium binding (283), which is in line with the experimental data on these compounds, discussed in Section 1.2.3.3.

MD simulations have also been utilised to predict unusual binding modes of some GPCR ligands. Notably, in both the cannabinoid CB2 and PAR1 receptors, MD simulations have revealed that lipophilic ligands for these receptors can enter the orthosteric site via a pathway through the phospholipid bilayer (284, 285). *Chan et al.,* recently reported a hitherto unknown binding site for the endogenous muscarinic agonist acetylcholine, much deeper in the receptor pore than the orthosteric site (286). Moreover, insight from crystallographic and MD data was successfully used by *McCorvy et al.,* to rationally design biased compounds at the dopamine D_2 receptor (187), providing proof of concept that agonist bias can be reliably predicted using key ligand-residue interactions highlighted in MD simulations.

The mechanism of GPCR activation and deactivation has also been explored using very long timescale simulations of the β_2 adrenoceptor. Starting from the active-state crystal structure, after removal of the agonist and G protein mimetic nanobody, the receptor was observed to relax back to an inactive conformation, revealing several intermediate conformations along this deactivation pathway (287).

Molecular modelling is perhaps most powerful when used in parallel with experimental studies. In many of the examples above, the novel predicted binding sites were validated by mutagenesis and signalling assays in cell lines. As discussed above in Section 1.3.3, DEER spectroscopy of the angiotensin II type I receptor was used to identify unique receptor conformations stabilised by biased agonists (224). In the same paper, MD simulations of the angiotensin II type I receptor were also performed showing that the positions of the transmembrane domains in the MD simulations overlapped with the spin densities from the DEER measurements, showing that the receptor indeed sampled a range of conformations different to that observed in the static crystal structure. In addition, *Landin et al.,* combined MD simulations with NMR studies of the adenosine A_{2A} receptor to show a unique conformation of TM5 stabilised by the antagonist, compound 1, again highlighting the use of *in silico* techniques to corroborate experimental data (288).

To summarise, MD simulations of GPCRs have revealed unique ligand binding sites and receptor conformations which are not captured in x-ray or cryoEM structures. Along with experimental data, these studies have provided important insights into the structure and function of these important drug targets and allowed the rational design of novel therapeutics.

1.5 Outstanding questions

There are a number of outstanding questions relating to the molecular mechanisms of opioid ligand efficacy and bias;

1. *How do the interactions of an opioid with the MOPr binding pocket dictate efficacy?*

Much of our understanding of the nature of agonist efficacy is based on the "canonical" Class A GPCR, the β_2 adrenoceptor (166). However, the molecular mechanisms governing ligand efficacy at the MOPr may be very different.

Firstly, the MOPr is primarily $G_{i/o}$ coupled, whereas the β_2 adrenoceptor couples to G_s. The recently reported cryoEM structures of GPCR-G protein complexes have revealed important differences in the conformation of the intracellular domain between G_s and $G_{i/o}$ coupled receptors (23).

Secondly, although the clinically used opioid drugs are small molecules, the MOPr is a peptide receptor. It therefore has a much deeper binding pocket than the β_2 adrenoceptor (76) and has evolved to respond to large peptide molecules. The adrenoceptors, on the other hand, recognise small molecule catecholamines. The important interactions between the respective ligands and the orthosteric pocket are therefore likely to be very different. Although it is generally appreciated that Class A GPCR activation mechanisms converge around the intracellular, G protein-coupling domain, the conformational changes around the orthosteric site are divergent across different receptors and receptor families (82, 101). It cannot be assumed that the ligand-residue interactions identified in one receptor are conserved in another.

Finally, at the time of writing, the only available high resolution x-ray crystal structures of the MOPr are in complex with either a covalently bound antagonist (β-FNA) or a very high affinity, slowly dissociating, experimental agonist (BU72) (22, 76). Neither of these compounds are clinically-used opiates. Therefore, we do not know how these ligands compare with medically important opioids, such as morphine, buprenorphine and methadone. Data on the interactions between the MOPr and its endogenous peptide ligands are also lacking; in the cryoEM-resolved structure of the MOPr-G_i complex, DAMGO is not the endogenous agonist and there is low resolution in the binding pocket (23).

2. *Do different MOPr ligands stabilise distinct receptor conformations?*

Spectroscopic data suggest the presence of multiple active conformations for other GPCRs (222, 224). However, there is limited literature on this phenomenon for the MOPr, although *Okude et al*., reported the existence of an equilibrium between open and closed conformations of the intracellular domain of the MOPr (262).

3. *How do the ligand-receptor interactions and MOPr conformations differ for biased agonists?*

There are currently no structures of the MOPr bound to biased ligands. Therefore, as discussed in Section 1.3.5, there is limited data on the structural basis of opioid ligand bias. Computational studies have so far largely focussed on oliceridine (173, 263, 289), which may not be strongly biased (260), and there are few studies which describe arrestin-biased MOPr agonists (240, 246).

1.6 Thesis aims

Given the therapeutic potential of developing MOPr ligands with distinct signalling profiles (Section 1.3.4), along with the gap in current scientific knowledge around the molecular mechanisms governing ligand efficacy and bias at this clinically important receptor (Section 1.5), this thesis will aim to use a combination of *in silico* and *in vitro* approaches to identify possible molecular mechanisms for opioid ligand efficacy and bias.

The aims are: -

i) Using *in silico* MD simulations:

- Characterise the interactions of biased and unbiased opioid ligands with the MOPr orthosteric binding pocket
- Determine how the binding of a sodium ion modulates opioid ligand binding and receptor conformation
- Explore receptor conformational changes induced by biased and unbiased ligands
- Identify key residues in conveying efficacy and/or bias at the MOPr

ii) Using *in vitro* cell signalling assays:

- Characterise the signalling profiles of biased and unbiased MOPr ligands
- Validate hypotheses based on MD simulation data by expressing the relevant MOPr mutants in HEK 293 cells and determining the effect on ligand-induced signalling

Chapter 2: Materials & Methods

2.1 Molecular modelling studies

2.1.1 Molecular mechanics

Molecular dynamics (MD) simulations model the dynamic behaviour of a biological system, using a molecular mechanics forcefield to define the energy of each atom and hence the potential energy of the whole system.

In a molecular mechanics forcefield, the system energy is broken down into bonded and non-bonded interactions between the atoms (Equation 1).

[Equation 1] $\Delta E = \Delta E_{bonded} + \Delta E_{non-bonded}$

Bonded (or covalent) interactions are described by energy terms for bond length and stretching, bond angle bending, and torsion angle rotation (Equation 2).

[Equation 2] $\Delta E_{bonded} = \Delta E_{bonds} + \Delta E_{angles} + \Delta E_{torsions}$

All molecular mechanics have this general form but may differ in some of the details of the functions used. Next, I will outline the functions used in the Amber-ff14SB forcefield (290), which are typical of most modern forcefields.

The energy term for bond length equates two covalently bonded atoms to balls connected by a spring, with the energy required to stretch or compress the bond described by Hooke's Law (Equation 3).

[Equation 3] $\Delta E_{bonds} = \frac{k_b}{2}(l - l_0)^2$

Where k_b is the force constant, specific to the pair of bonded atoms, l is the bond length and l_0 is the equilibrium bond length. This function follows a harmonic potential, whereby stretching or compressing the bond requires increasing energy.

Similarly, the energy term for bond angle bending also follows a harmonic potential (Equation 4).

[Equation 4] $\Delta E_{angles} = \frac{k_a}{2}(\theta - \theta_0)^2$

Where k_a is the force constant (smaller than the force constant for bond length k_b), θ is the angle between 3 bonded atoms, and θ_0 is the equilibrium angle. The smaller force constant for angle bending ensures that the energy required to distort a bond angle is lower than to distort bond length.

Torsion angle rotation (the angle made between the 2 planes of 4 sequentially bonded atoms) is described by trigonometric functions to model the favoured, low energy torsional states such as *trans*, *gauche*$^+$ and *gauche*$^-$ conformations for tetrahedral atoms (n=3), and E and Z (*cis* and *trans*) for trigonal atoms (n=2) (Equation 5).

[Equation 5] $\Delta E_{torsions} = \frac{V_n}{2}[1 + cos(n\omega - \gamma)]$

Where V_n is the force constant for torsion rotation, ω is the torsion angle and γ is the phase shift.

Non-bonded interactions are described by energy terms for van der Waals interactions and electrostatic (Coulombic) interactions (Equation 6).

[Equation 6] $\Delta E_{non-bonded} = \Delta E_{VDW} + \Delta E_{Coulombic}$

Van der Waals interactions between 2 atoms are described by the Lennard-Jones equation (Equation 7), whereby very short range contacts are repulsive (modelling orbital overlap), the optimal interaction distance is weakly attractive, and longer distances give energy values towards zero.

[Equation 7] $\Delta E_{VDW} = 4\epsilon\left[\left(\frac{\sigma}{r}\right)^{12} - \left(\frac{\sigma}{r}\right)^{6}\right]$

Where ϵ and σ are atom-specific parameters, and r is the distance between the 2 atoms.

Electrostatic interactions between 2 atoms are described by Coulomb's Law (Equation 8). When the 2 atoms have the same sign (e.g. both positive) the force will be increasingly repulsive with decreasing distance. When the 2 atoms have the opposite charge, the force will be attractive.

[Equation 8] $\Delta E_{Coulombic} = k_e \frac{q_1 q_2}{r^2}$

Where k_e is Coulomb's constant, q_1 and q_2 are the partial charges of atoms 1 and 2, and r is the distance between atoms 1 and 2.

The total potential energy of the modelled system is therefore equal to the sum of all the energy terms described above, plus any "improper" terms for bonds not adequately described by the bond length and bond angle functions, such as out-of-plane bending of planar arrangements of atoms like carbonyl and amide groups. Hence:

[Equation 9]

$$\Delta E_{total} = \Delta E_{bonds} + \Delta E_{angles} + \Delta E_{torsions} + \Delta E_{improper} + \Delta E_{VDW} + \Delta E_{Coulombic}$$

In an MD simulation, the time-dependent movement of all the atoms in the system are resolved using the above equations. Firstly, energy minimisation is performed to allow the system to "relax" to the nearest local energy minimum. For the MD simulations presented in this thesis, the steepest descent method of energy minimisation was employed. Following minimisation, the system is slowly heated to the desired production temperature and then an equilibration simulation performed to equilibrate the system's density and dimensions. Finally, production MD can be performed; each atom is assigned an initial velocity, according to the system temperature (usually 300 or 310 K), and then moved for one time step (usually 2 fs). The forces acting on each atom are then recalculated, and the process repeated until the desired simulation time is reached. Formally, this is a numerical integration of Newton's equations of motion.

The production simulations in this thesis were all performed under constant temperature and pressure (NPT ensembles), using the Langevin thermostat and the anisotropic Berendsen barostat. These methods control the average temperature and pressure of the system, whilst allowing small fluctuations so that the kinetic energy of the system is not fixed.

The MD simulations were conducted under periodic boundary conditions. This approach eliminates edge effects in a simulation and long-range Coulombic interactions can be efficiently calculated using the Particle Mesh Ewalds method. Briefly, the system is modelled in a box, but the atoms are free to diffuse around and out of the box. The system is surrounded by an infinite number of identical replicate boxes in all directions to form a lattice, with all the replicate molecules in each of the boxes moving in the same way. This means that any atom that leaves the system box will immediately re-enter from the opposite side and atoms can interact with other atoms in the replicate boxes, thus removing any surface effect.

Water was simulated using the TIP3P water model (291). This models water as a rigid molecule of fixed geometry, which can participate in non-bonded interactions.

2.1.2 Making the MOPr models from crystal structures

The initial starting structures and the final structures used in MD simulations are shown in Figure 2.1. X-ray crystal structures of the inactive β-FNA bound MOPr (PDB:4DKL) (76) (Figure 2.1a) and the active BU72 bound MOPr (PDB:5C1M) (22) (Figure 2.1b) were obtained from the Protein Data Bank. The co-crystallised bound ligands were removed so that both receptors were in their unliganded, apo form. The inactive structure contains a T4 lysozyme (Figure 2.1a, orange) in place of intracellular loop 3 (ICL3). Using Insight II the lysozyme was removed, and a loop search performed to find a homologous loop which aligned well with the intracellular ends of TMs 5 and 6. A loop was selected by visual inspection and the residues changed to the correct mouse MOPr sequence (Figure 2.1a, blue-green). The side chains were inspected for clashes and bonds rotated where necessary. For the active MOPr model, the G protein-mimetic nanobody, Nb39, was removed from the active structure (Figure 2.1b, green). In order to compare the inactive and active structures during the MD simulation, both proteins were adjusted to be the same length. The inactive structure retained a longer portion of the C terminal helix 8, so this was spliced onto the active structure (Figure 2.1b, grey), assuming that the active state MOPr retains this α helix. The N terminus of the active structure (Figure 2.1b, purple) has been shown to fold over the ligand binding pocket during activation (22, 92) and so deemed inappropriate to splice onto the inactive structure. The active protein was therefore truncated at M65$^{1.29}$ to match the inactive structure.

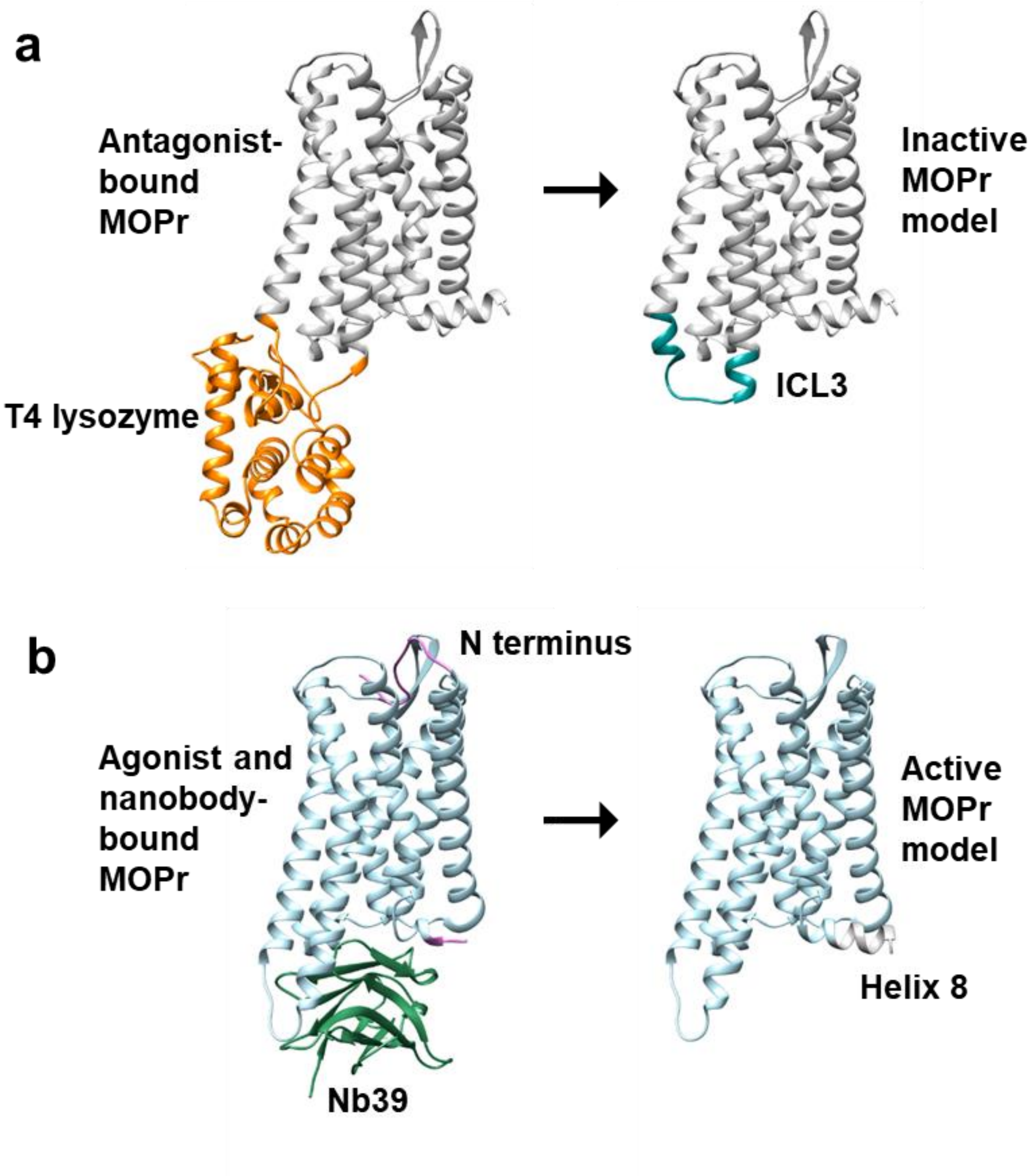

Figure 2.1 Modification of the MOPr crystal structures

a) Crystal structure of the antagonist-bound MOPr-T4 lysozyme chimera (PDB: 4DKL (76)), with the MOPr shown in grey and the lysozyme in orange. To make the inactive MOPr model, the lysozyme was removed and intracellular loop 3 (ICL3, blue-green) was modelled as described in Section 2.1.2. b) Crystal structure of the agonist and G protein-mimetic nanobody bound MOPr (PDB: 5C1M (22)), with the MOPr shown in teal, the nanobody in green and the N and C termini in purple. To make the active MOPr model, the nanobody and the N and C termini of the MOPr were removed, and helix 8 from the inactive model spliced onto the C terminus (grey).

2.1.3 Ligand docking

The full molecular docking and molecular dynamics protocol is outlined in Figure 2.2.

The co-crystallised ligand β-FNA in the inactive MOPr crystal structure shares a morphinan scaffold with all the morphinan ligands used in this study (morphine, norbuprenorphine, buprenorphine and diprenorphine). Therefore, the binding pose of β-FNA in the crystal structure was used as a template to determine the initial orientation of the morphinan ligands for MD simulation (76, 152). Ligands were protonated at the amine and parameterised with the Antechamber package and the general Amber force field (GAFF) (292). The GAFF is a molecular mechanics forcefield (see Section 2.1.1), specialised for pharmaceutical molecules, and is used by the Antechamber software to generate parameter files for drug molecules by assigning atom types and charges. Amber parameter topology and coordinate files were then prepared using the LEaP software.

For the non-morphinan ligands (methadone, DAMGO, endomorphin-2 and bilorphin), the conformer generation and subsequent docking protocol described below and summarised in Figure 2.2, was used to find a binding pose before simulation of the full ligand-MOPr complex.

2.1.3.1 Generation of ligand conformations

The 3D conformers of methadone and endomorphin-2 were downloaded from PubChem (CID: 22267 and 5311081), and the structures of DAMGO and the novel peptide bilorphin were built in the molecular modelling program, Chimera (293). Peptide bonds are generally in the *trans* conformation (Figure 2.3a), however, the Tyr^1-Pro^2 peptide bond of endomorphin-2 can adopt either a *cis* or *trans* conformation, with conflicting evidence in the literature as to which is the bioactive conformation of endomorphin-2 (294-299). The two different 3D conformers of endomorphin-2 were therefore built in Chimera and treated as separate ligands for MD simulation and docking (Figure 2.3b). The ligand protonation state was set consistent with pH 7, hence peptides were protonated at the backbone N terminus, methadone at the tertiary amine, and parameterised with Antechamber and the GAFF (292). Amber parameter topology and coordinate files were prepared in LEaP such that each ligand was solvated with TIP3P water and 0.15 M NaCl, in a simulation box with initial dimensions 45, 50, 45 Å. The system was minimised in two steps; initially the water and ions were minimised over 1000 steps with the ligand restrained, then the whole system was minimised over a further 2500 steps. The system was heated under constant volume and pressure from 0 K to 310 K over 20 ps, and then equilibrated under constant pressure for 100 ps. Simulations were run for 1 µs per ligand under the Amber ff14SB force field (290). Temperature and pressure were controlled with the Langevin thermostat and the anisotropic Berendsen barostat, with a 2 fs time step and trajectories written every 100 ps. Trajectory data were analysed with the Amber analysis software, cpptraj (300), to extract 10,000 conformations for each ligand to use in molecular docking.

2.1.3.2 Molecular docking

Molecular docking was performed with the Bristol University Docking Engine (BUDE) (301). Ligands were docked to the inactive MOPr model (Section 2.1.2) independently. The following describes the docking procedure for one ligand. Multi-conformer docking was run such that the 10,000 conformations of the ligand were treated as independent molecules. A box of size 15, 15, 15 Å centred on the orthosteric binding site was designated as the search space. BUDE's genetic algorithm was used to search the available pose space for the best energy poses. A total of 105,000 poses were sampled for each of the 10,000 ligand conformers. The total possible number of poses was 1.57×10^8 for each conformer, corresponding to x,y,z translation within the box and 360° rotation in all axes in 10° increments. The 50 lowest energy binding poses were inspected visually and subjected to a distance constraint between the protonated amine of the ligand and $D147^{3.32}$ of less than 3 Å. The obtained ligand-MOPr complexes were then used in MD simulations.

2.1.4 System set-up

Each unliganded receptor or ligand-MOPr complex were modelled as separate systems. The receptors were embedded in phospholipid bilayers using the replacement method, and the simulation box (initial dimensions: 90, 110, 90 Å) solvated with TIP3P water and 0.15 M NaCl, using the CHARMM-GUI software for generating membrane models (302). The box size was chosen to ensure the receptor was always at least 90 Å away from its images and therefore outside of interaction distance. The N terminus and C terminus of each receptor were acetylated or amidated, respectively, and a disulphide bond formed between $C140^{3.25}$ and $C217^{ECL2}$. Hydrogen atoms were added to the receptor consistent with pH 7. The lipid composition of the bilayer contained palmitoyl-oleoyl-phosphatidyl-choline (POPC) and palmitoyl-oleoyl-phosphatidyl-ethanolamine (POPE), as well as cholesterol at a level comparable to that in mammalian cells (303-305). The ratio of POPC:POPE:cholesterol was approximately 5:5:1, with the final membrane-embedded MOPr systems each containing 103 POPC lipids, 100 POPE lipids and 20 cholesterol molecules. The total number of atoms was approximately 85,000 in each system. Amber parameter topology and coordinate files were prepared in LEaP.

2.1.5 Molecular dynamics simulations

Structures were minimised over 10,000 steps, then the system was heated under constant volume and pressure with lipids restrained, from 0 K to 100 K over 5 ps, and then from 100 K to 310 K over 100 ps. 10 rounds of 500 ps equilibration was performed under constant pressure to equilibrate the periodic box dimensions. Each production simulation was run for 125 ns under the Amber ff14SB and Lipid14 force fields (290, 306). Temperature and pressure were controlled using the Langevin thermostat and the anisotropic Berendsen barostat, with a 2 fs time step and trajectories written every 100 ps.

To increase sampling, after the initial 125 ns production simulation 7 structures from this short trajectory were extracted. These structures were minimised, heated, equilibrated and 125 ns production simulations were run as described above. This resulted in a total of 1 μs MD data for each receptor model in a series of 8 x 125 ns parallel steps, with newly minimised structures and new random velocities for each simulation.

Accelerated MD (aMD) uses an external boost potential to accelerate conformational changes, with the aim of increasing sampling over the same amount of computation time as conventional MD. The aim is for protein conformational changes to be investigated which would otherwise not be accessible over the short computing time available. Parameters for the aMD were calculated as described in *Kappel et al.,* (307), using the Equations 10 - 13 below. Values for the average total potential energy ($V_{\text{average total}}$) and average dihedral energy ($V_{\text{average dihedral}}$) were obtained from the conventional MD simulations. N_{atoms} is the total number of atoms in the system.

[Equation 10] $E_{dihedral} = V_{average\ dihedral} + 0.3 \times V_{average\ dihedral}$

[Equation 11] $\alpha_{dihedral} = 0.3 \times V_{average\ dihedral} \times 0.2 \times N_{atoms}$

[Equation 12] $E_{total} = V_{average\ total} + 0.2 \times N_{atoms}$

[Equation 13] $\alpha_{total} = 0.2 \times N_{atoms}$

2.1.6 Computational resources

All simulations were performed on either BlueCrystal phase 3 (Advanced Computing Research Centre, University of Bristol), or on a local workstation with Nvidia GTX 1080. 125 ns of production MD takes approximately 7 days using BlueCrystal, or 4 days on the local workstation.

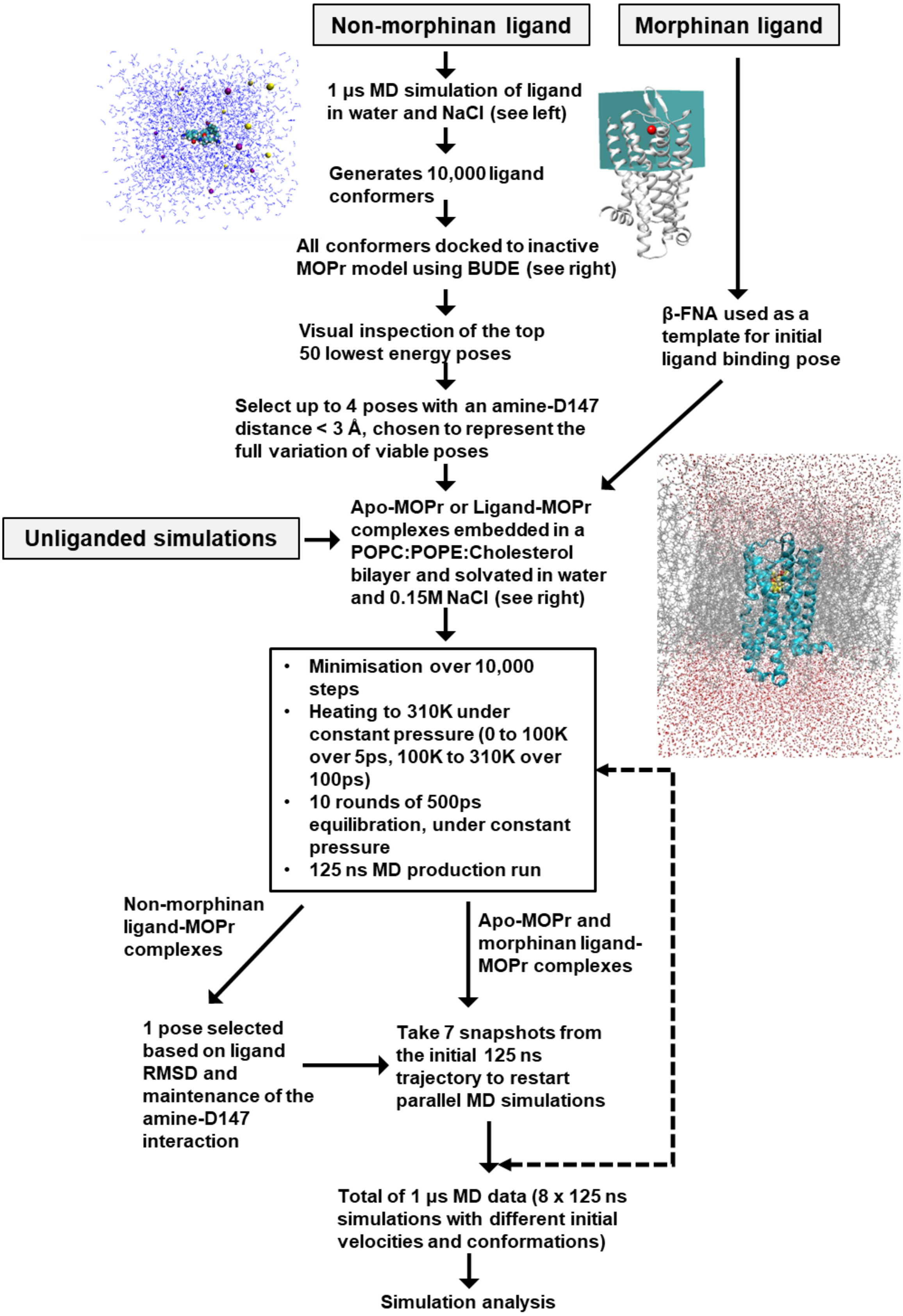

Figure 2.2 Molecular docking and molecular dynamics protocol

Starting with either a morphinan ligand, non-morphinan ligand, or unliganded simulation (grey boxes), docking poses are decided, receptors are embedded in a bilayer, and MD simulations performed to produce a total of 1 µs MD data for analysis.

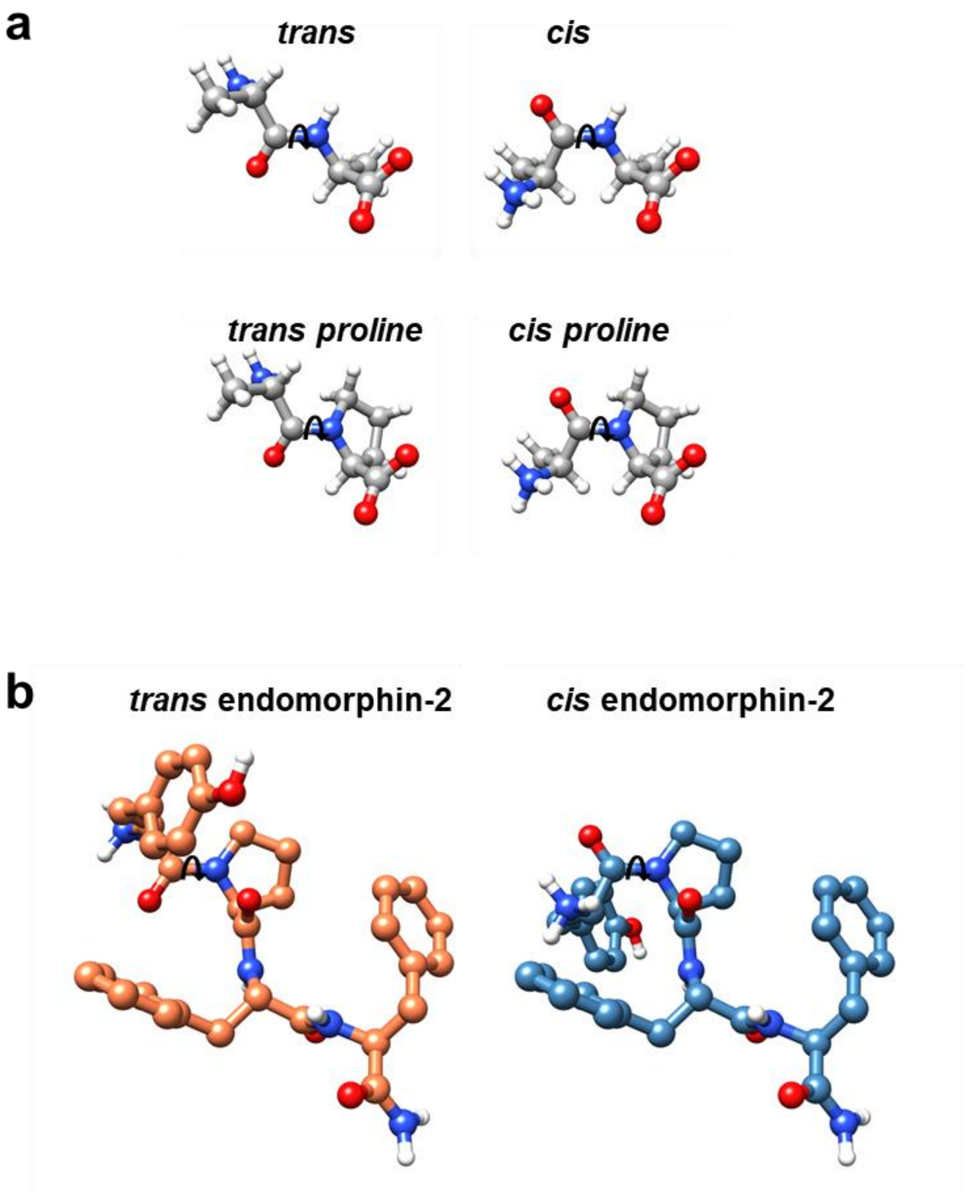

Figure 2.3 *Trans* and *cis* peptide bonds

a) Rotation around the peptide bond allows the formation of *trans* or *cis* isomers. For non-proline residues, *trans* isomers are the predominant form due to steric hinderance in the *cis* conformation. For peptide bonds involving proline, *cis* isomers can also form as the proline side chain offers less steric hinderance. b) Endomorphin-2 contains a proline residue and can exist in either *trans* (orange) or *cis* (blue) conformations.

2.1.7 Analysis

Trajectories were visualised in the molecular visualisation program, VMD (308) and analyses were performed using cpptraj (300). All images relating to molecular modelling were made in Chimera (293). Before any further processing, trajectories were fitted to the inactive MOPr model to remove translation and rotation of the receptor. For all figures illustrating trajectories, the parallel simulations were concatenated to a trajectory totalling 1 µs, and the individual simulations indicated on the plots by light grey vertical lines at 125 ns intervals.

Root mean square deviation (RMSD) measurements were taken to determine the stability of both the receptor and the docked ligands. For RMSD calculations on the receptor, calculations were performed on just the alpha carbons of the transmembrane domains (Figure 2.4a) to avoid including the highly flexible loops and residue side chains in the analysis, which would mask more subtle movements of the receptor helices. Atomic coordinates were compared to the first frame of the production simulation. For RMSD calculations on the ligands, calculations were performed using the heavy (non-hydrogen) atoms of the ligand and comparing the atomic positions to the initial docked pose of the ligand, and to the final binding pose after 1 µs MD simulation.

Principal component analyses on the alpha carbons of the receptor transmembrane domains (Figure 2.4a) was performed to extract the first two principal components (PC) of motion. Trajectories were aligned by the alpha carbon atoms of a set of “core residues” (Figure 2.4b) which showed the least amount of movement through the simulation (determined by per residue RMS fluctuations). This avoided translation and rotation of the receptor and anchored the protein around a core area so movement of the rest of the structure could be determined. The covariance matrix was calculated and diagonalised using cpptraj, and the PCs obtained by mapping the alpha carbons of all structures’ trajectories. Each frame of the simulated trajectories was mapped onto PC1 and PC2, to produce a plot visualising the conformational space occupied by the receptor at each time point. Pseudo-trajectories for each PC were generated in cpptraj to visualise the helix movements contributing to the PC.

Interactions between the bound ligand and receptor residues were determined using a 4.5 Å distance cut-off, and calculated as the percentage of simulation time the contact was present.

The angle of the W293$^{6.48}$ "rotamer toggle switch" was determined by measuring the χ2 dihedral between the Cα, Cβ, Cγ and Cδ1 atoms of the tryptophan residue (Figure 2.5).

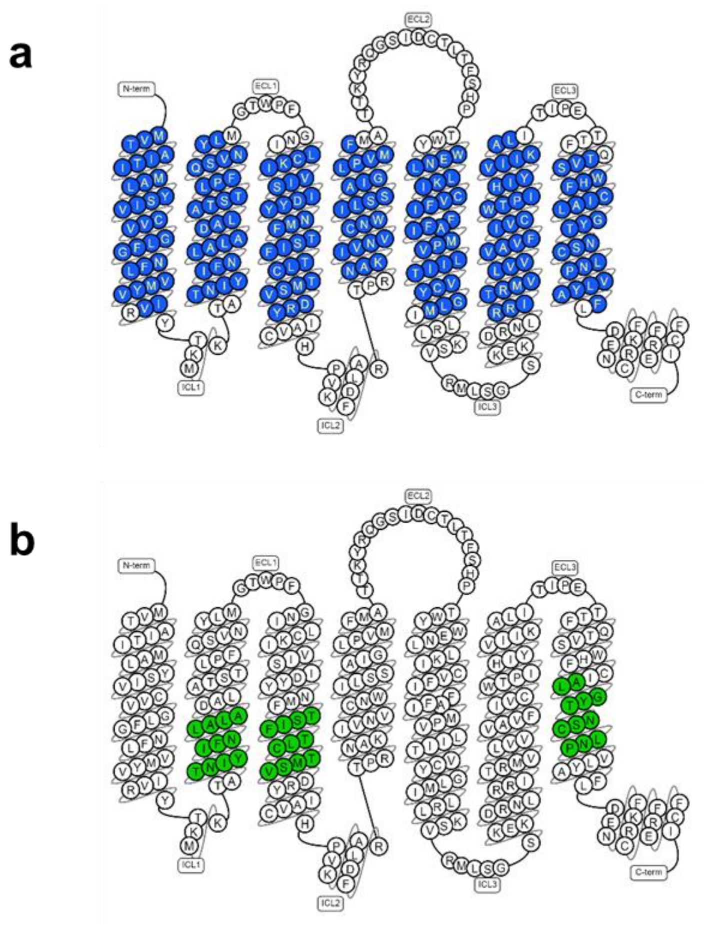

Figure 2.4 Snake plots of the murine MOPr used in the molecular modelling

a) The MOPr transmembrane region is shown in blue. The coordinates of these residues were used for the RMSD calculations and the PCA. b) The core residues to which trajectories were aligned prior to PCA are shown in green.

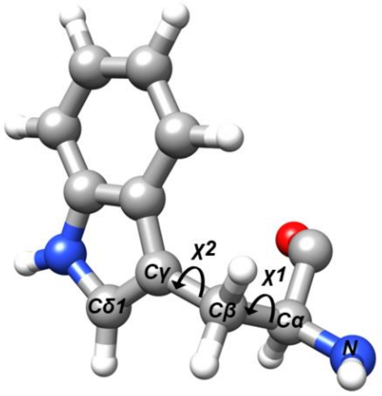

Figure 2.5 Torsion angles in tryptophan

χ1 and χ2 torsion angles in the tryptophan side chain. χ1 is angle of the Cα – Cβ axis. χ2 is the angle of the Cβ – Cγ axis.

2.2 *In vitro* cell signalling studies

2.2.1 Compounds

The novel peptide, bilorphin, was synthesised in the laboratories of Prof. Rob Capon and Prof. Paul Alewood, University of Queensland, and provided to us as a gift. DAMGO (Sigma-Aldrich), endomorphin-2 (Sigma-Aldrich), morphine (MacFarlan Smith) and methadone (Sigma-Aldrich) were dissolved in sterile, de-ionised water. Diprenorphine (Sigma-Aldrich), norbuprenorphine (NIDA Drug Supply Program), buprenorphine (Tocris) and bilorphin were dissolved in dimethyl sulfoxide (DMSO) (Sigma-Aldrich). High concentration drug stocks (10 - 30 mM) were stored as frozen, small volume aliquots (10 - 20 µl). Prior to use, all drug stocks were diluted in clear, serum-free media (ThermoFisher) to the desired concentration prior to assay. Unless otherwise stated, the vehicle control in all experiments was 0.01 % DMSO in serum-free media.

2.2.2 Plasmid preparation

The pQCXIN-hMOPR-RLucII and pQCXIH-Arr3-GFP10 constructs were a gift from Dr Tomasso Costa, Istituto Superiore di Sanita. The pcDNA3.1-Gαi-RLucII and pcDNA3.1-Gγ-GFP plasmids were a gift from Dr Michel Bouvier, University of Montreal. The pcDNA3-Arr3-RLuc construct was a gift from Dr Nick Holliday, University of Nottingham. The pcDNA3-HA-rMOPR and pcDNA3-rMOPR-YFP constructs were from Dr Helen Sanderson, University of Bristol. The plasmids containing the W293A and L219A MOPr point mutations were generated by myself using the QuikChange site directed mutagenesis kit as detailed in Section 2.2.6. For all the plasmids used in this thesis, the methods for obtaining purified DNA from bacteria were as follows;

20 µl aliquots of DH5α competent cells (Invitrogen), stored at -80 ˚C, were thawed on ice. 2 – 4 µl of plasmid DNA was added to the competent cells and the mixture incubated on ice for 30 minutes. Plasmids were transformed into the bacteria by heat shock at 42 ˚C for 45 seconds. The bacteria were then incubated on ice for a further

2 minutes. 200 µl of pre-warmed SOC media (Invitrogen) was added to each tube of competent cells / DNA and incubated at 37 ˚C for 1 hour with shaking, to improve recovery of the competent cells. Following incubation, bacteria were streaked onto Luria-Bertani (LB) agar plates containing 100 µg/mL ampicillin (ThermoFisher) for selection of only bacteria containing the transformed plasmid, and incubated overnight at 37 ˚C.

The following day (at least 16 hours post-transformation) single, well-separated colonies were picked from the agar plates and added to separate tubes of 3 ml LB broth containing 100 µg/mL ampicillin. Selection of a single colony with no surrounding satellite colonies is important to ensure selection of a single clone. The tubes of LB broth were incubated at 37 ˚C overnight with shaking. The following day, the bacterial cultures were expanded in 200 ml flasks of LB broth and 100 µg/mL ampicillin. Flasks were incubated for 24 hours at 37 ˚C with shaking.

Plasmid DNA was purified from the bacterial culture using the HighSpeed Plasmid Preparation Kit (Qiagen), based on alkaline lysis. Unless specified, all buffers and reagents were provided in the kit. Bacteria were pelleted by centrifugation at 4500 x g for 20 minutes at 4 ˚C, and the supernatant discarded. Pellets were resuspended in resuspension buffer containing 100 µg/mL RNase A. Cells were then lysed by addition of lysis buffer and incubated at room temperature for 5 minutes, before termination of the lysis reaction by addition of the neutralisation buffer. The lysate was cleared by filtration through the QIAfilter cartridge. The cleared lysate was added to the HighSpeed Tip containing an anion exchange resin which binds the negatively charged phosphates on the plasmid DNA. The column was washed with wash buffer, and then the DNA eluted using a high salt buffer. DNA was precipitated by incubation with isopropanol (Sigma-Aldrich) for 5 minutes. The precipitated DNA was collected by filtration through the QIAprecipitator, washed with 70 % ethanol (Sigma-Aldrich) and then eluted with TE buffer.

The obtained DNA was quantified by UV spectrophotometry at 260 nm (Nanodrop 2000, Thermo Scientific), and purity determined by the 260 / 280 nm absorbance ratio. DNA was sequenced by Source Bioscience to confirm the correct DNA sequence of each insert.

2.2.3 Cell culture and transfection

Human embryonic kidney (HEK) 293 cells were maintained at 37 ˚C in high glucose Dulbecco's Modified Eagle's Medium (DMEM) containing L-Glutamine (ThermoFisher) and supplemented with 10 % foetal bovine serum (FBS) (Life Technologies) and 100 U /ml penicillin and 0.1 mg/ml streptomycin (Invitrogen). Cells were seeded onto 10 cm dishes and grown to 80 % confluence before sub-culture or transfection.

HEK 293 cells were transfected with the required plasmids by lipofectamine 2000 transfection (Invitrogen). 48 hours prior to assay, cells were washed with phosphate-buffered saline (PBS) and the DMEM growth media replaced with OptiMEM media (ThermoFisher). The required DNA were diluted in OptiMEM media to a total volume of 500 µl. Separately, the lipofectamine reagent (at a DNA (µg) to lipofectamine (µl) ratio of 1:2.7) was diluted in OptiMEM to a total volume of 500 µl. After a 5 minute incubation, the lipofectamine dilution was added dropwise to the DNA dilution and incubated at room temperature for 20 minutes. The DNA-lipofectamine complex was then added dropwise to the dish of HEK 293 cells. The cells were incubated with the DNA-lipofectamine overnight, and then the OptiMEM media was replaced with DMEM + 10 % FBS the following morning. Cells were allowed to grow for a further 24 - 36 hours before assay.

2.2.4 Bioluminescence Resonance Energy Transfer (BRET) assay

Bioluminescence resonance energy transfer (BRET) assays were used to measure the recruitment of arrestin-3 to the MOPr, and the dissociation of the Gαi and Gγ protein subunits upon activation by a ligand. These assays were originally optimised in our laboratory by Dr Gerda Gasiunaite, showing the optimal ratio of donor:acceptor DNA and the absence of a BRET signal from cells transfected with pcDNA alone (309).

The principle of the BRET assay is shown diagrammatically in Figure 2.6a. BRET relies on the energy transfer between a bioluminescent donor, renilla luciferase (Rluc) and a fluorescent acceptor, such as yellow fluorescent protein (YFP) or green fluorescent protein (GFP). Rluc catalyses the oxidation of the substrate coelenterazine to coelenteramide, emitting light with a peak at wavelength 475 nm (coelenterazine h) or 410 nm (coelenterazine 400a), depending on the coelenterazine analogue used. The light is captured by the YFP or GFP, which then emits at a longer wavelength, with peaks at approximately 535 nm for YFP or 515 nm for GFP. As the efficiency of this energy transfer is highly dependent on distance, it will only occur when the donor and acceptor come into close range, approximately 10 - 100 Å. Conjugating the Rluc and the YFP or GFP onto different proteins therefore allows detection of when the two cellular proteins come into close proximity or move further apart.

This energy transfer can be quantified by calculation of the BRET ratio; the ratio between the acceptor and donor peak emissions (Equation 14).

[Equation 14] $$BRET\ ratio = \frac{YFP\ or\ GFP\ emisson}{RLuc\ emission}\ x\ 1000$$

An increase in the BRET ratio indicates that the proteins are in closer proximity, whilst a decrease indicates that the distance between donor and acceptor has increased.

For the G_i activation assay, HEK 293 cells were transfected with 3 µg HA-rat MOPr, 3 µg $G\alpha i_1$-RlucII and 3 µg $G\gamma_2$-GFP, to measure BRET between the RlucII and GFP ($BRET^2$). Two different BRET configurations were used to measure arrestin-3 recruitment to the MOPr. Initially the $BRET^1$ configuration was used; HEK 293 cells were transfected with 5 µg MOPr-YFP and 5 µg arrestin-3-RLuc. This BRET configuration results in a high background and low signal due to the poor spectral resolution as the donor and acceptor emission peaks differ by only ~50 nm (Figure 2.6b). To improve the signal the constructs were switched to the BRET^2 configuration; cells were transfected with 5 µg MOPr-RlucII and 5 µg arrestin-3-GFP10. This gives a larger wavelength shift between the donor and acceptor emission peaks, a lower background, and a higher signal to noise ratio (Figure 2.6b).

For all BRET configurations, immediately prior to assay the transfected HEK 293 cells were resuspended in clear, serum-free DMEM (ThermoFisher) and then transferred to a flat-bottom 96 well Corning plate at 90 µl per well. Drugs were dissolved in water or DMSO and then diluted in DMEM media to the required concentration. The final DMSO concentration never exceeded 0.01 %. The BRET assay was performed on the FLUOstar Omega microplate reader (BMG Labtech) at 37 ˚C. Coelenterazine h (Insight Biotechnology) was used as the substrate for the BRET^1 configuration. Coelenterazine 400a (Insight Biotechnology) was used as the substrate for the BRET^2 configuration. Both substrates were dissolved in methanol and DMEM and added to the plate at a final concentration of 5 µM and 1 % methanol. Each substrate was injected 5 seconds prior to reading the plate. For G protein activation, BRET measurements were taken 2 minutes after drug application. For arrestin-3 recruitment, BRET measurements were taken after a 10 minute incubation with the drugs. The ratio of the light emitted by the BRET acceptor (YFP or GFP) to the light emitted by the BRET donor (Rluc) was used to calculate the BRET ratio (Equation 14). For assays using the BRET^1 configuration, signals were recorded via 475-30 nm (RLuc) and 535-30 nm (YFP) emission filters (Figure 2.6b). For assays in the BRET^2 configuration, signals were recorded via 410-80 nm (RLuc) and 515-30 nm (GFP) emission filters (Figure 2.6b). All treatments were performed in duplicate and the average response taken. Each assay condition was repeated in 3 - 5 independent experiments. For the G_i activation assay, data were expressed as the percentage decrease in the BRET ratio from transfected cells treated with media or media +

DMSO. A decrease in the BRET ratio is indicative of dissociation of the Gαi and Gβγ subunits upon activation (note that only the Gγ subunit contains the GFP tag, but it is assumed that the Gβ and Gγ subunits remain associated). For the arrestin-3 recruitment assay, data were expressed as BRET ratio minus background from transfected cells treated with media or media + DMSO. An increase in the BRET ratio is indicative of arrestin-3 being recruited to the receptor. Analyses and curve fitting were performed in GraphPad Prism version 7. All ligands were compared to DAMGO, as the standard high efficacy agonist at the MOPr.

Detection time points were chosen based on previously described G protein activation and arrestin translocation assays in the literature (243, 310-313), and the previous assay optimisation performed in our laboratory by Dr Gerda Gasiunaite (309). In addition, time course experiments were performed for each BRET configuration when cells were stimulated with 10 µM DAMGO.

Figure 2.7a shows the time course for DAMGO-induced dissociation of the Gαi and Gβγ subunits, measured by BRET. Baseline recordings were taken for 1 minute and then the cells were stimulated with 10 µM DAMGO. DAMGO caused a decrease in the BRET ratio, consistent with the dissociation or rearrangement of the G protein subunits, which was maximal within 2 minutes of drug administration, and remained for the duration of the assay time. For all future experiments measuring G_i activation, 2 minutes post-drug was taken as the detection time point for maximal signal.

The time courses for DAMGO-induced arrestin-3 recruitment to the MOPr with the two different BRET configurations are plotted in Figures 2.7b and 2.7c. The overall kinetics with the two pairs of BRET constructs are very similar, with a steep rising phase over the first 2 minutes, and a plateau between 6 and 12 minutes. The signal from the $BRET^2$ constructs (Figure 2.7c) is ~100 fold higher than for the $BRET^1$ constructs (Figure 2.7b), reflecting the enhanced detection in this configuration. From these time courses the time point chosen for maximal recruitment was 10 minutes and was used in all further arrestin-3 recruitment assays.

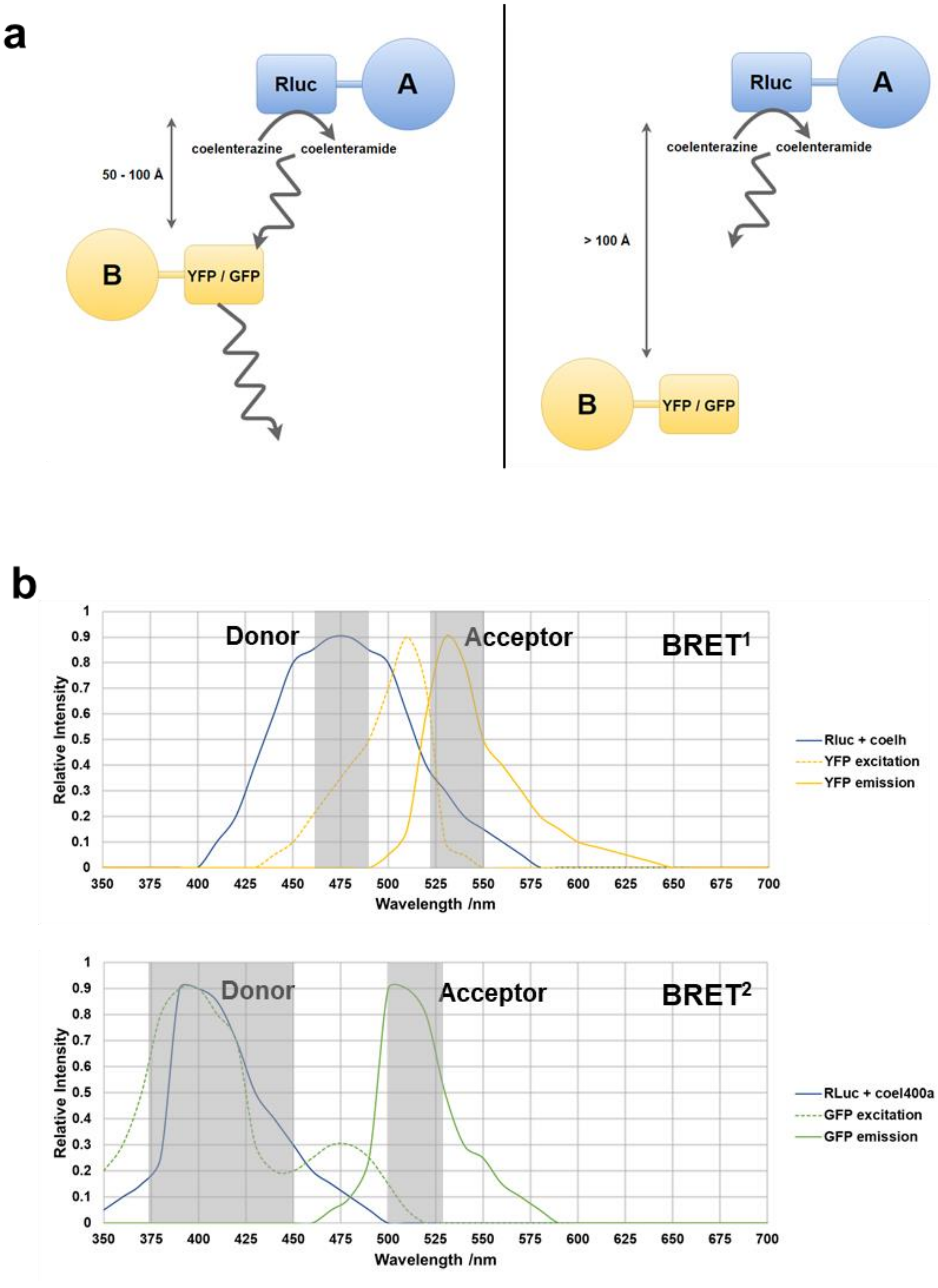

Figure 2.6 The principle of the BRET assay

a) The breakdown of coelenterazine is catalysed by renilla luciferase (RLuc), emitting light. When proteins A and B are in close proximity, YFP or GFP is excited by the light emitted by the breakdown of coelenterazine and emits light of a longer wavelength. When protein A and B are not in close range, YFP or GFP is not excited. b) Diagram of the approximate excitation and emission spectra for different BRET configurations. BRET^2 gives a greater separation between donor and acceptor peaks than BRET^1. The emission filters used for each assay are displayed as grey shaded areas.

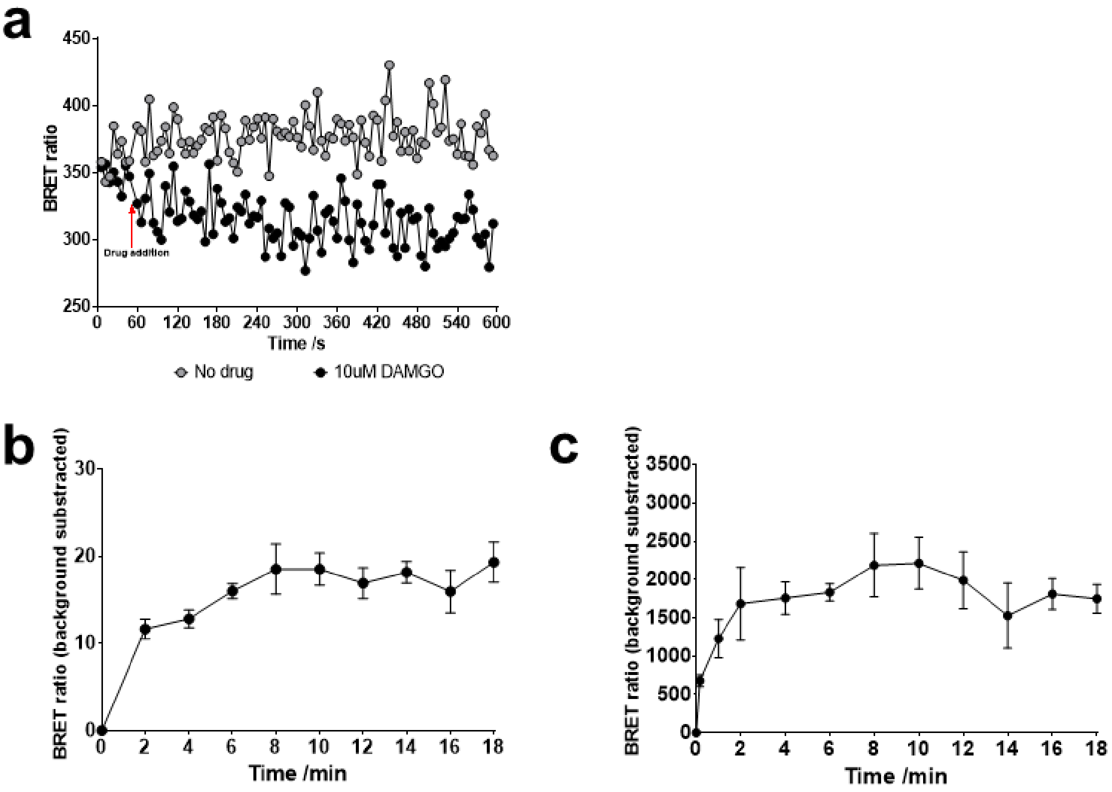

Figure 2.7 Time courses for different BRET configurations

a) Time course for dissociation of Gαi and βγ subunits induced by 10 μM DAMGO applied after 60 seconds, in cells transfected with HA-tagged rat MOPr, Gαi-RlucII and Gγ-GFP; n=1. Time courses for arrestin-3 recruitment to the MOPr induced by 10 μM DAMGO applied at time 0, using b) the MOPr-YFP/arr3-RLuc BRET^1 constructs or c) the MOPr-RLucII/arr3-GFP BRET^2 constructs. Data plotted as mean of 4 experiments ± SEM.

2.2.5 Quantification of ligand bias

Ligand bias between G_i protein activation and arrestin-3 recruitment was quantified using the Black and Leff operational model of agonism (201, 314) employing the method described in *van der Westhuizen et al.,* (315).

The operational model (Equation 15) describes the response of an experimental system to a given concentration of agonist.

[Equation 15] $$\mathrm{E} = \mathrm{basal} + \frac{(\mathrm{E_{max}} - \mathrm{basal})\tau^{\mathrm{n}}[\mathrm{A}]^{\mathrm{n}}}{\tau^{\mathrm{n}}[\mathrm{A}]^{\mathrm{n}} + ([\mathrm{A}] + \mathrm{K_A})^{\mathrm{n}}}$$

Where E is the agonist-induced response, basal is the response in the absence of agonist, $\mathrm{E_{max}}$ is the maximal possible tissue response, $[\mathrm{A}]$ is the agonist concentration, $\mathrm{K_A}$ is the functional equilibrium dissociation constant, τ is the operational efficacy (a composite of intrinsic agonist efficacy, receptor density and effector coupling), and n is the slope of transducer function.

The transduction ratio $\left(\frac{\tau}{\mathrm{K_A}}\right)$ was taken as a parameter of agonist activity at a particular signalling pathway. To allow curve fitting, the transduction ratio was expressed as a single parameter, R. To obtain the transduction ratio (R) for each ligand at each pathway, baseline-subtracted concentration – response data for each ligand was fit to the operational model in Equation 16, which was derived from Equation 15 by dividing through by $\mathrm{K_A}$ and $\mathrm{R}^n[A]^n$ and expressing $\mathrm{K_A}$ and R as logarithms.

[Equation 16] $$\mathrm{E} = \mathrm{basal} + \frac{(\mathrm{E_{max}} - \mathrm{basal})}{1 + \left(\frac{\left(\frac{[\mathrm{A}]}{10^{\log \mathrm{K_A}}} + 1\right)}{10^{\log \mathrm{R}}[\mathrm{A}]}\right)^{\mathrm{n}}}$$

$\mathrm{E_{max}}$ was constrained to the maximum response of the reference full agonist, DAMGO, in each assay. The slope, n, was constrained to 1, and the basal response to 0. The value of $\log \mathrm{K_A}$ was constrained to zero for full agonists and derived from the curve fitting for partial agonists, as suggested by *van der Westhuizen et al.,* (315).

To remove any influence of system and observational bias, all agonists were compared to the reference ligand DAMGO (Equation 17).

[Equation 17] $$\Delta\log\left(\frac{\tau}{K_A}\right) = \log\left(\frac{\tau}{K_A}\right)_{\text{LIGAND}} - \log\left(\frac{\tau}{K_A}\right)_{\text{DAMGO}}$$

Ligand bias between G protein activation and arrestin-3 recruitment for each agonist was calculated from Equation 18, expressed as $\Delta\Delta\log\left(\frac{\tau}{K_A}\right)$ or the “Bias Factor”.

[Equation 18] $$\Delta\Delta\log\left(\frac{\tau}{K_A}\right) = \Delta\log\left(\frac{\tau}{K_A}\right)_{\text{G protein}} - \Delta\log\left(\frac{\tau}{K_A}\right)_{\text{arrestin}}$$

The standard error for each ligand’s $\Delta\log\left(\frac{\tau}{K_A}\right)$ was calculated from Equation 19. The standard error for the Bias Factor was calculated using Equation 20.

[Equation 19] $$\text{S.E.}_{\Delta\log\left(\frac{\tau}{K_A}\right)} = \sqrt{(\text{S.E.M}_{\text{LIGAND}})^2 + (\text{S.E.M}_{\text{DAMGO}})^2}$$

[Equation 20]

$$\text{S.E.}_{\left(\Delta\Delta\log\left(\frac{\tau}{K_A}\right)\right)} = \sqrt{\left(\text{S.E.}_{\left(\Delta\log\left(\frac{\tau}{K_A}\right)\right)_{\text{G protein}}}\right)^2 + \left(\text{S.E.}_{\left(\Delta\log\left(\frac{\tau}{K_A}\right)\right)_{\text{arrestin}}}\right)^2}$$

The resulting Bias Factors were compared by one-way ANOVA with Tukey’s post-test to determine statistical significance.

2.2.6 Site-directed mutagenesis

The desired point mutations were introduced to the pcDNA3-HA-rMOPR and pQCXIN-Myc-hMOPR-RlucII plasmids using the QuikChange-XL site-directed mutagenesis kit according to the manufacturer’s instructions (Agilent). The protocol relies on mutagenesis by polymerase chain reaction (PCR) and is summarised in Figure 2.8. Forward and reverse primers containing the desired mutation (Table 2.1) were designed using the Agilent QuikChange Primer Design tool (available at: https://www.genomics.agilent.com/primerDesignProgram.jsp), and synthesised and

HPLC purified by ThermoFisher. In each primer the mismatched bases containing the mutation are flanked by at least 11 base pairs of complementary sequence, to allow annealing of the primer to the template DNA.

All buffers and reagents were provided with the kit, unless otherwise specified. The PCR reactions were set up in thin-walled PCR tubes as follows; 5 µl reaction buffer, 50 ng of template pcDNA3-HA-rMOPR or 100 ng of template pQCXIN-Myc-hMOPR-RlucII plasmid, 125 ng mutagenic primer #1, 125 ng mutagenic primer #2, 1 µl dNTP mix, 3 µl QuikSolution (containing DMSO to improve product amplification and reduce secondary structure formation) and double-distilled water added to a final reaction volume of 50 µl. 1 µl of PfuTurbo DNA polymerase was added last. Reactions were kept on ice until the tubes were transferred to the thermocycler (Biometra TRobot). The reactions were cycled according to the times and temperatures in Table 2.2. Samples were heated to 95 °C to denature the double-stranded template DNA. The reaction was then cooled to 60 °C to allow the primers to anneal, before heating to 68 °C; the optimum temperature for DNA polymerase activity to synthesise the new DNA strand. This was repeated 18 times to amplify the product. An extra 7 minute extension time was added to the end of the PCR protocol to ensure full amplification of these relatively large plasmids.

Plasmid	Primer name	Sequence 5’ to 3’
pcDNA3-HA-rMOPR	W293A Primer #1	CGTAGATGTGGATGGGGGTGGCGCAGACGATAAATACAGCC
	W293A Primer #2	GGCTGTATTTATCGTCTGCGCCACCCCCATCCACATCTACG
	L219A Primer #1	TTGGGTGGGAGAACGTGGCGGTGCAATCTATGGAC
	L219A Primer #2	GTCCATAGATTGCACCGCCACGTTCTCCCACCCAA
pQCXIN-Myc-hMOPR-RLucII	W293A Primer #1	CGTAAATGTGAATGGGAGTGGCGCAGACGATGAACACAGCC
	W293A Primer #2	GGCTGTGTTCATCGTCTGCGCCACTCCCATTCACATTTACG
	L219A Primer #1	CAGGTTGGATGAGAGAATGTGGCTGTACAATCTATGGAACCTTGCCT
	L219A Primer #2	AGGCAAGGTTCCATAGATTGTACAGCCACATTCTCTCATCCAACCTG

Table 2.1 Primers for site-directed mutagenesis

Primers were synthesised by ThermoFisher. Mutagenic regions are highlighted in red.

	Segment	Cycles	Temperature /°C	Time
pcDNA3-HA-rMOPR	1	1	95	1 min
	2	18	95	50 s
			60	50 s
			68	7 min (1 min per kb)
	3	1	68	7 min
pQCXIN-Myc-hMOPR-RLucII	1	1	95	1 min 30s
	2	18	95	1 min
			60	50 s
			68	20 min (2 min per kb)
	3	1	68	7 min

Table 2.2 Parameters for site-directed mutagenesis by PCR (adapted from the QuikChange XL protocol)

After PCR, the reaction tubes were cooled on ice for 2 minutes to terminate the DNA polymerase activity. Samples were then incubated with Dpn I restriction enzyme to digest the non-mutated template plasmid. The Dpn I enzyme recognises methylated DNA, which is only present on the template plasmid isolated from E.coli as there are no methylases present in the PCR reaction to methylate the PCR product. This digestion step ensures that only the mutated plasmid is left over in the PCR product mix to be transformed into the bacteria.

4 µl of each PCR product was transformed into separate aliquots of XL10-Gold Ultracompetent cells, pre-treated with β-mercaptoethanol, by heat shock, and the rest of the reaction used to check for the presence of a band at ~7 kb (pcDNA3) or ~10 kb (pQCXIN), by electrophoresis on a 1 % agarose gel. After transformation and incubation for 1 hour in SOC media, the bacteria were plated on LB agar plates containing 100 µg/mL ampicillin. Agar plates were incubated at 37 °C overnight and colonies picked the following day. Colonies were grown in LB broth and plasmid preparation carried out as detailed in Section 2.2.2. The obtained plasmid DNA was sequenced by Source Bioscience to determine if the desired mutations had been incorporated (see Appendix I and II for sequencing results).

Both mutagenic and transformation controls were included in the experiment. The mutagenic control was a pWhitescript template plasmid, which after successful mutation by PCR with the control mutagenic primers, will cause transformed bacterial colonies to appear blue on LB agar plates containing isopropyl β-D-1-thiogalactopyranoside (IPTG) (Sigma-Aldrich) and X-gal (Invitrogen). Bacterial colonies expressing the unmutated plasmid will appear white. To check for transformation efficiency, a separate aliquot of XL10-Gold Ultracompetent cells were transformed with pUC18 plasmid, which will also cause the bacterial colonies to appear blue on IPTG and X-gal agar plates.

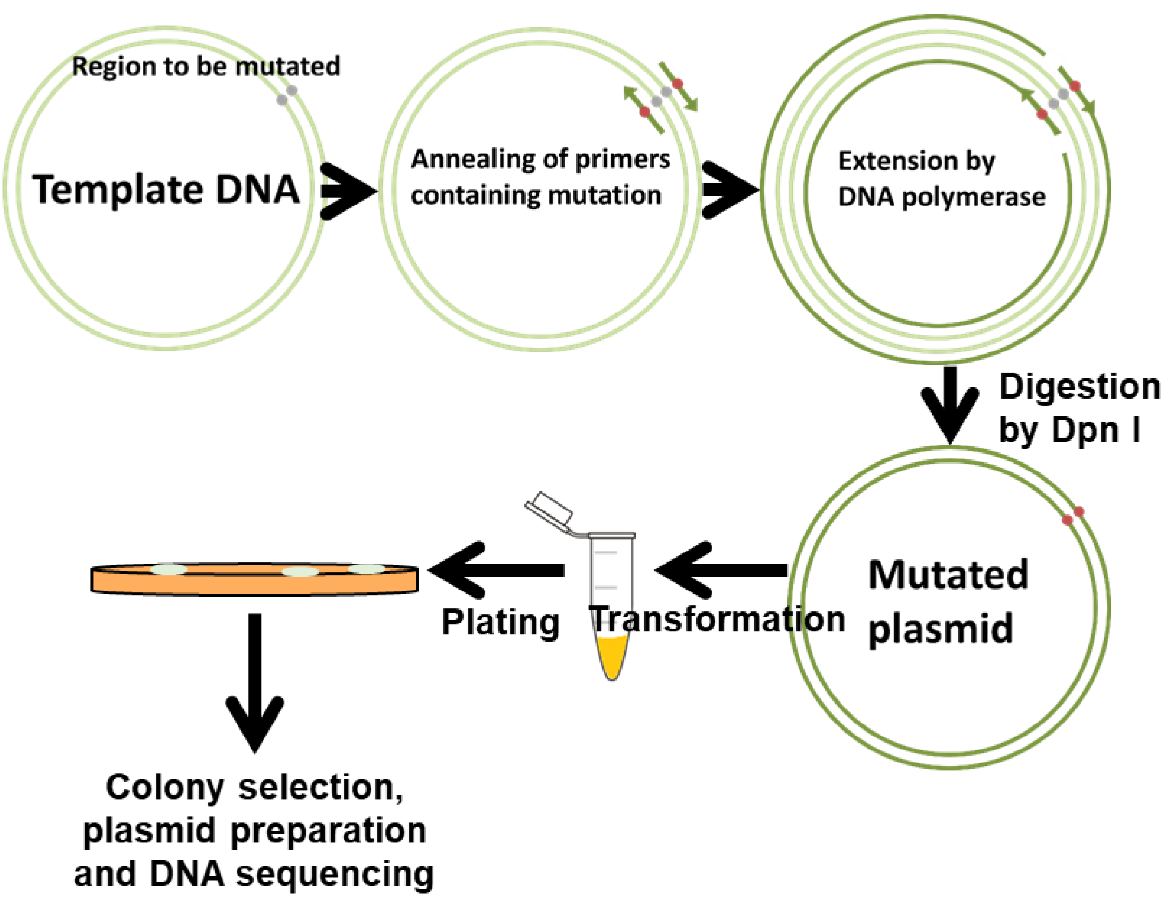

Figure 2.8 Site-directed mutagenesis by PCR

Schematic representation of the PCR protocol and subsequent transformation of E.coli. The single point mutations were generated by annealing of primers (dark green) to the template strand (light green) containing the region to be mutated (wildtype region in grey, mutated region in red). After primer annealing, DNA strands were extended by DNA polymerase. Reactions were cycled multiple times to amplify the DNA product. PCR product was then digested with Dpn I restriction enzyme to leave just the mutagenized DNA. This was transformed into bacteria, which were then plated on agar containing ampicillin for colony selection.

2.2.7 Surface receptor enzyme-linked immunosorbent assay (ELISA)

The surface expression of the HA-rMOPR construct and the W293A and L219A point mutants was confirmed using surface receptor enzyme-linked immunosorbent assay (ELISA), based on the methods described by *Daunt et al.,* (316). HEK 293 cells were transfected by lipofectamine transfection (see Section 2.2.3). The following day, cells were counted and plated equally at 250,000 cells per well in a 24-well plate coated with poly-L-lysine (Sigma-Aldrich) and grown overnight in DMEM media supplemented with 10 % FBS and penicillin/streptomycin. Untransfected HEK 293 cells were also plated as background controls.

The following morning, approximately 36 hours post-transfection, the cell media was replaced with serum-free DMEM and incubated at 37 ˚C for 10 minutes. Cells were then fixed with 4% paraformaldehyde (PFA) (VWR International) for 5 minutes. This time was chosen as sufficient time for fixation but short enough to prevent membrane permeabilisation (316). Cells were washed three times in Tris-buffered saline (TBS) to remove the PFA, and then incubated with 1% bovine serum albumin (BSA) (Sigma-Aldrich) for 45 minutes to block non-specific binding sites. After blocking, cells were incubated with the primary antibody, mouse anti-HA monoclonal (#MMS-101R, BioLegend), for 1 hour at 1 in 1000 dilution. Cells were washed three times with TBS to remove any unbound antibody, and then blocked with 1% BSA for 15 minutes. After blocking, cells were incubated with the secondary antibody, goat anti-mouse IgG alkaline phosphatase conjugate (#A5153, Sigma), at 1 in 1000 dilution for 1 hour. Cells were then washed three times with TBS to remove any unbound antibody and incubated at 37 ˚C for 40 minutes with alkaline phosphatase substrate (Bio-Rad Laboratories) to detect the signal. Once colour change had occurred, the reaction was stopped by transferring the substrate to wells containing 0.4 M NaOH, at a 1:1 ratio. Absorbance at 405 nm was read on a Tecan Infinite plate reader (Tecan), and values expressed as absorbance minus the background untransfected cells. All experiments were performed in triplicate wells and an average taken. Data were analysed in GraphPad Prism version 7.

2.2.8 Receptor internalisation assay (ELISA)

Agonist-induced receptor internalisation was also measured by ELISA, as described by *Cooke et al.,* (317). In order to measure receptor internalisation without the confounding factor of subsequent recycling of receptors to the surface, receptor internalisation in response to opioid agonists was measured by pre-labelling surface receptors prior to incubation with drugs. As described in Section 2.2.7, HEK 293 cells were transiently transfected with HA-rMOPR or the W293A or L219A point mutants and the following day plated in poly-L-lysine coated 24-well plates.

The following day, 36 hours post-transfection, media was replaced with serum-free DMEM and the plates incubated at 37 ˚C for 10 minutes. Cell surface receptors were labelled by incubation with the anti-HA primary antibody ((#MMS-101R, BioLegend) for 1 hour at 4 ˚C. This lower temperature reduced any constitutive receptor internalisation. Cells were washed three times with TBS to remove unbound antibody, and then incubated with opioid agonists diluted in 0.5 % BSA at 37 ˚C for 30 minutes. This time point was chosen as sufficient time for maximum receptor internalisation to have occurred (21, 47, 318). Cells were fixed with 4 % PFA for 5 minutes and then washed three times with TBS, before blocking in 1 % BSA for 15 minutes. After blocking, cells were incubated with the secondary antibody for 1 hour and detection performed as described in Section 2.2.7, using alkaline phosphatase substrate (Thermo Fisher).

All experiments were performed in triplicate and an average taken. Data were analysed in GraphPad Prism version 7. After subtraction of the background absorbance from untransfected cells, receptor internalisation was expressed as the percentage decrease in absorbance from vehicle-treated wells.

Chapter 3: MD simulations of the unliganded MOPr capture the binding of sodium to the allosteric site

3.1 Introduction

With the technological advances in structural biology over the last two decades, determination of membrane protein structures at high resolution has become possible (167, 319-322). To date, there are two x-ray crystal structures of the MOPr (22, 76). The first, resolved by *Manglik et al.,* comprises the antagonist-bound receptor with intracellular loop 3 (ICL3) replaced with a T4 lysozyme (76), thus representing an inactive conformation of the MOPr. More recently, an active state MOPr structure was resolved with the receptor bound to an agonist and a G protein mimetic nanobody (22). Whilst these structures provide important insight into the receptor conformation at the beginning and end of the activation process, these static snapshots cannot explain the dynamic nature of the MOPr and how this is modulated by the cellular environment.

Radioligand binding studies conducted over 40 years ago identified sodium as a negative allosteric modulator of the MOPr, as binding of antagonists was enhanced in the presence of sodium whilst the affinity of agonists was diminished (115). A similar negative modulatory effect of sodium was also reported for other GPCRs (116-119). It was not until a very high resolution crystal structure of the adenosine A_{2A} receptor was reported that a molecular mechanism for this sodium modulation was identified (122). In this high resolution structure, a sodium ion was found bound within the transmembrane helix bundle below the orthosteric ligand binding site. A sodium ion was later resolved in structures of the DOPr, β_1 adrenoceptor and PAR1 receptor (123-125), suggesting that this conserved sodium binding site is a mechanism for sodium-dependent modulation of agonist activity across a range of Class A GPCRs. However, although the earliest *in vitro* studies described the effect of sodium at the MOPr (115, 120, 121), neither of the available crystal structures of the MOPr are at a high enough resolution to determine if a sodium ion is present in the allosteric site.

Molecular dynamics (MD) simulations allow exploration of the conformational landscape of the MOPr in a native-like membrane, capturing some of the innate conformational heterogeneity of the receptor which is lost in static crystal structures. Importantly, MD simulations can also model how water and ions interact with the MOPr, information which is often beyond the resolution routinely achievable by crystallographic and spectroscopic techniques.

Therefore, in this chapter I use the inactive- (76) and active-state (22) MOPr crystal structures to develop models of the membrane-embedded unliganded (apo) MOPr. I perform all-atom MD simulations of each MOPr model, sampling 1 µs of MD data, in order to study the binding of sodium to the receptor.

3.2 Materials & Methods

Two models of the unliganded (apo) MOPr were generated from the available x-ray crystal structures. The model made from the agonist- and nanobody-bound crystal structure (22) (PDB: 5C1M), and the model made from the antagonist-bound crystal structure (76) (PDB: 4DKL), were termed the active MOPr model and the inactive MOPr model, respectively. The crystal structures were downloaded from the Protein Data Bank and modified as described in Chapter 2 Section 2.1.2. In brief, all ligands and interacting proteins were removed and the missing ICL3 was modelled in to the inactive MOPr structure using Insight II. The two models were each embedded in phospholipid and cholesterol bilayers and solvated in water and NaCl.

Molecular dynamics (MD) simulations of the membrane-embedded apo MOPr structures were performed as described in Chapter 2 Section 2.1.5, to produce 1 µs of MD data for each MOPr model. Additionally, 1 µs of accelerated MD was performed as described in Chapter 2 Section 2.1.5. All analyses were performed using cpptraj (see Chapter 2 Section 2.1.7).

3.3 Results

Separate systems of the membrane-embedded MOPr using either the inactive or active model, were each subjected to up to 1 μs of MD simulation. The interactions between the receptor and sodium ions in the solvent were monitored to determine if our computational model could capture the binding of a sodium ion to the allosteric site.

During the MD simulations, sodium moved from the bulk solvent on the extracellular side of the membrane to bind within the transmembrane domains of both apo MOPr models. The position of an individual sodium ion during each frame of the trajectories is mapped in Figure 3.1. The clusters of these positions of the sodium ion at each time point indicate that for the inactive MOPr model, sodium interacted with the receptor at three distinct sites, whereas for the active MOPr model, sodium only accessed two of these sites. In both cases, only one sodium ion was observed to enter the MOPr helix bundle at any given time.

For both the inactive and active MOPr models, a sodium ion entered from the extracellular side of the receptor, first interacting with polar and acidic residues at the extracellular end of TM2 and ECL2 (“Site 1”); N127$^{2.63}$, S214^{ECL2} and D216^{ECL2}. The next cluster was found around the orthosteric ligand binding site, “Site 2”, where a sodium ion interacted with D147$^{3.32}$ in both the inactive and active MOPr models. The final cluster, “Site 3”, was only populated in the inactive MOPr model, and was identified as the conserved allosteric sodium ion binding site by comparison with the position of the sodium ion in the related crystal structures (the DOPr and adenosine A$_{2A}$ receptor (122, 124)). Here, the sodium ion was coordinated by residues in TM2 and 3; D114$^{2.50}$, N150$^{3.35}$ and S154$^{3.39}$.

To measure the movement of the sodium ion along this pathway visualised in Figure 3.1, the distance between the interacting sodium ion and D114$^{2.50}$ in the allosteric site (Site 3) was monitored and plotted in Figure 3.2. During the conventional MD simulations of the inactive MOPr model, a sodium ion interacted with Site 1 on the extracellular side of the receptor at multiple points during the simulation (Figure 3.2a). On all but one occasion, the sodium ion then moved further into the receptor helix bundle to interact with D147$^{3.32}$ in Site 2. From here, the sodium ion then bound to the allosteric binding site, Site 3. In conventional MD simulations of the active MOPr model, whilst sodium did interact with Site 1 at the extracellular side of the receptor and Site 2 in the orthosteric pocket, it did not bind to the allosteric sodium site (Figure 3.2b).

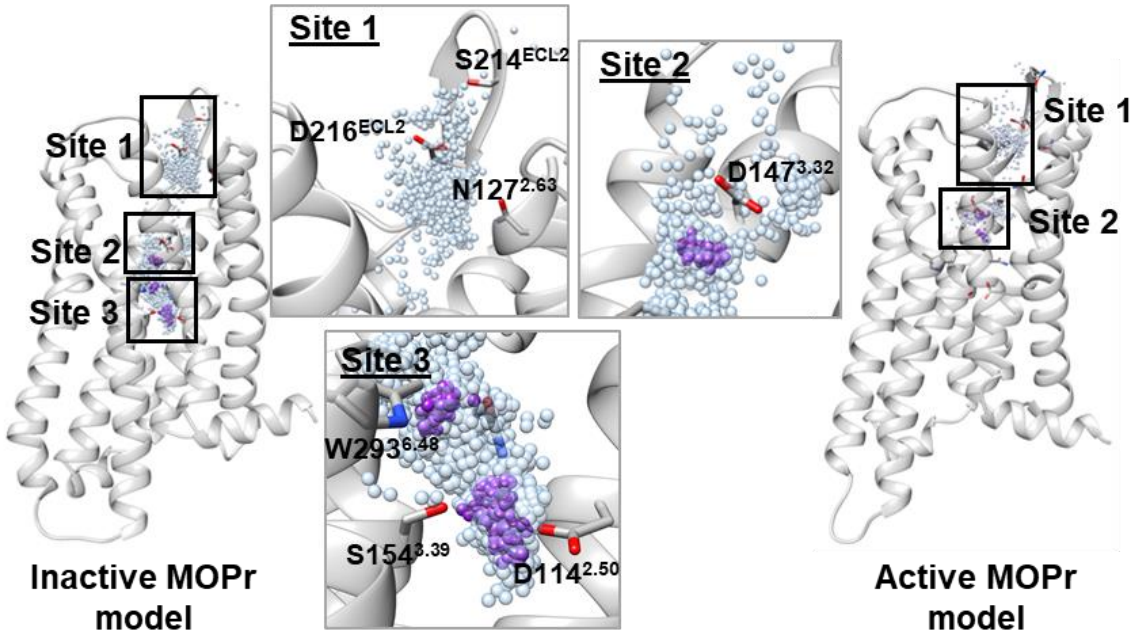

Figure 3.1 Entry of sodium into the allosteric site from the bulk solvent

The route taken of sodium from the bulk solvent into the receptor pore during 1 µs conventional MD simulations of the unliganded MOPr models, revealing 3 distinct sites. Sodium ions at each frame of the trajectory are depicted as light blue beads, with interacting residues as sticks. Sodium ions from the final 10 ns of each 125 ns simulation are coloured purple. In the inactive MOPr model (left) the sodium ion binds to all 3 sites, whereas in the active MOPr model (right) sodium only accesses Sites 1 and 2.

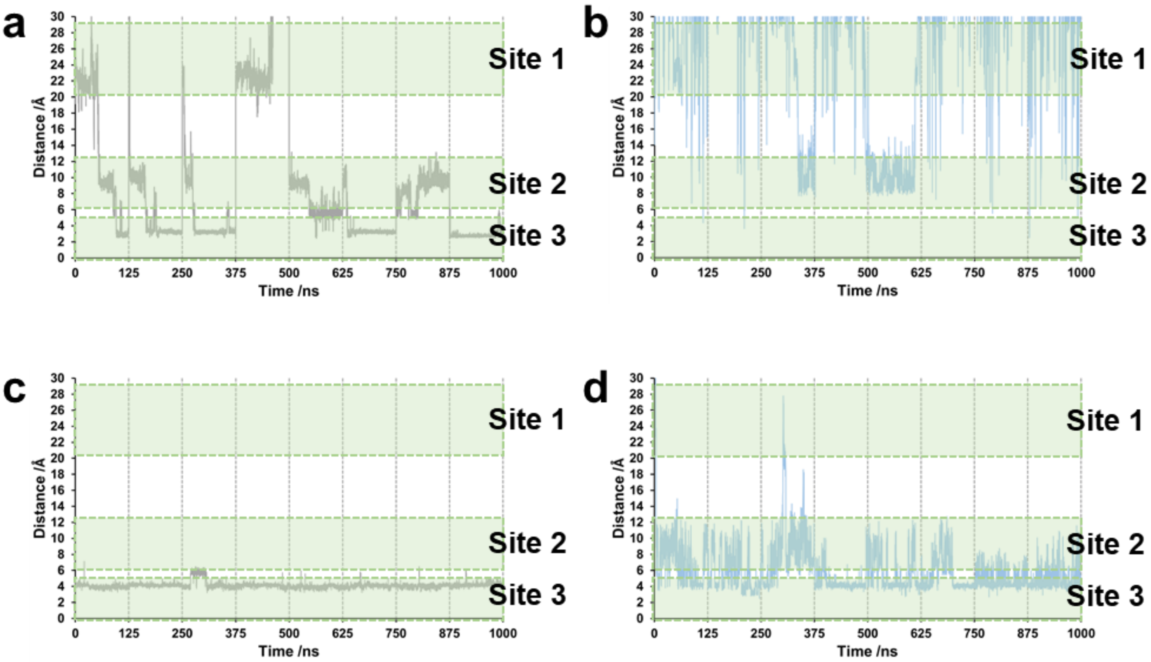

Figure 3.2 Movement of sodium through the 3 sites

Data plotted as the distance between the sodium ion and D114$^{2.50}$ of the allosteric sodium binding site (Site 3) during conventional MD simulations of a) the inactive MOPr model and b) the active MOPr model or accelerated MD simulations of c) the inactive MOPr model and d) the active MOPr model.

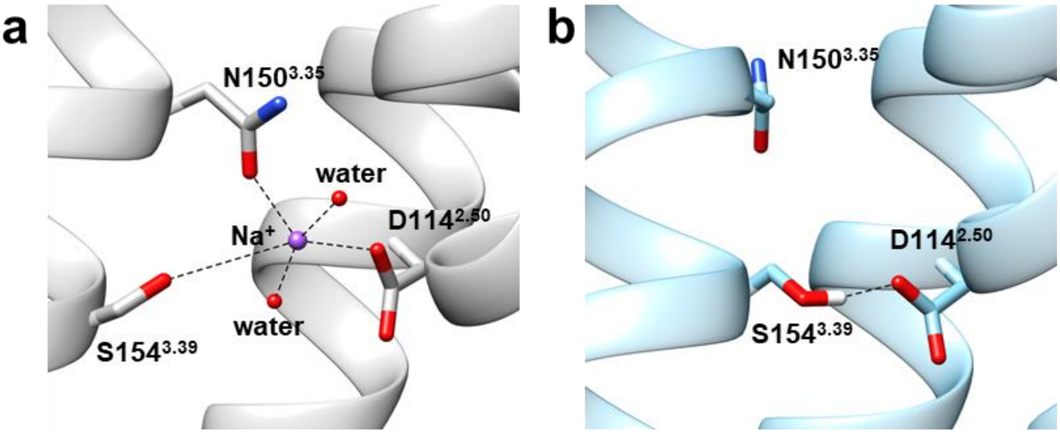

Figure 3.3 The allosteric sodium ion binding site ("Site 3")

a) A sodium ion (purple) occupies the allosteric sodium site during MD simulations of the unliganded inactive MOPr model. The sodium ion is coordinated by D114$^{2.50}$, N150$^{3.35}$, S154$^{3.39}$ and two water molecules. b) In the active MOPr model this binding pocket is collapsed, with a hydrogen bond formed between S154$^{3.39}$ and D114$^{2.50}$.

Accelerated MD simulations were employed to enhance the sampling of the receptor conformational space (see Chapter 2 Section 2.1.5). During the accelerated MD simulations of the inactive MOPr model, a sodium ion very rapidly moved from the bulk solution to bind in the allosteric site (Site 3) and remained bound for the entire simulation (Figure 3.2c). In contrast, in accelerated MD simulations of the active MOPr model, although a sodium ion entered the helix bundle more readily than in the conventional MD simulations, the ion oscillated between Sites 2 and 3, and did not bind stably to the allosteric sodium site (Figure 3.2d).

Closer inspection of the conformation of the residues comprising the allosteric sodium site suggests that the lack of interaction of sodium with this site in the active MOPr model is probably due to the alternative conformation of these residues (Figure 3.3). In the inactive MOPr model (Figure 3.3a), the sodium ion was coordinated by two water molecules, D114$^{2.50}$, N150$^{3.35}$ and S154$^{3.39}$, in agreement with the crystal structure of the DOPr (124). However, in the active MOPr model the binding pocket collapsed due to an inward movement of TM7 above the NPxxY motif, the inward movement of TM3 such that S154$^{3.39}$ formed a hydrogen bond with D114$^{2.50}$, and the side chain of N150$^{3.35}$ rotated to point away from the helix bundle (Figure 3.3b). This binding pocket collapse thus prevented the binding of a sodium ion.

These data suggest that sodium will readily bind to the conserved allosteric site in the inactive MOPr model, and transitions between two other binding sites on route; first interacting with a cluster of polar and acidic residues on the extracellular surface of the MOPr, then the orthosteric binding site and finally reaching the allosteric pocket. However, for the active MOPr model, although sodium can interact with the other two sites in the receptor, a sodium ion will only interact with residues in the allosteric site under accelerated MD conditions but will not bind in a stable manner.

3.4 Discussion

In this chapter, MD simulations of the unliganded (apo) MOPr successfully modelled the binding of a sodium ion to the receptor. The resolution of the currently available MOPr crystal structures was not able to detect a sodium ion bound to the allosteric site, therefore the observations described here demonstrate the power of using MD simulations to visualise the dynamic nature of important interactions between the protein and ions which are not captured in crystal structures.

Moreover, the position of the sodium ion when occupying “Site 3” in the inactive MOPr model agreed with that resolved in the x-ray crystal structure of the inactive DOPr (124). In this allosteric site, the sodium was coordinated by residues highly conserved in Class A GPCRs (D114$^{2.50}$ and S154$^{3.39}$), as well as the N150$^{3.35}$ residue specifically conserved in opioid receptors (78, 138). In Chapter 4, I will use these coordinates of the sodium ion in the allosteric site to investigate the effect of sodium on the ligand-MOPr complex.

In addition, we were able to model the binding pathway of sodium to the inactive MOPr, showing that the sodium ion was first captured by a site on the extracellular surface of the MOPr, before transitioning into the helix bundle; first binding to D147$^{3.32}$ of the orthosteric ligand binding site, and finally binding in the allosteric pocket. These MD data are similar to that reported in other computational studies modelling sodium binding to opioid receptors, where sodium first interacts with extracellular residues and the orthosteric site (323-325).

Interestingly, although sodium could readily bind to the inactive MOPr model under either conventional or accelerated MD conditions, the same was not true for the active MOPr model. Under conventional MD we did not observe sodium binding to the allosteric site in the active state receptor, and even using accelerated MD the sodium ion was unable to bind stably to the allosteric pocket due to a collapsed conformation of this site. This suggests that coordination of a sodium ion is characteristic of the inactive state MOPr; agreeing with the experimentally observed negative modulatory effect of sodium (115, 121). Similarly, a recent study by *Hu et al.,* reported that sodium binding to the inactive MOPr is more energetically favourable than active-state binding (326). Furthermore, in MD simulations of the DOPr, the presence of an allosteric sodium ion stabilised the inactive conformation of the W6.48 rotamer toggle switch (see Chapter 1 Section 1.2.3.4), and constrained the movement of TM6; both hallmarks of the GPCR inactive state (161, 166).

Finally, the lack of sodium interaction with the allosteric site in these MD simulations of the active MOPr model indicates that the active MOPr model remained in the active state even in the absence of the co-crystallised agonist BU72 and the G protein-mimetic nanobody, and under accelerated MD conditions. This suggests that the active conformation captured in the crystal structure is in a very low energy conformation and/or would require very long timescale MD simulations to revert to an inactive conformation, beyond what is achievable with our available computational resources. Therefore, I will use the inactive MOPr model for further ligand-bound MD experiments in order to capture the changes in the MOPr conformation induced by the ligand of interest, rather than that already stabilised by BU72 and the Nb39 nanobody (22).

3.5 Conclusions

Using MD simulations of the unliganded MOPr, in this chapter I have shown that a sodium ion can spontaneously bind to the conserved allosteric sodium binding site in the inactive state receptor. However, the collapse of this site in the active state prevents sodium binding. These data agree with radioligand binding, crystallographic and computational data showing that sodium is a negative allosteric modulator of the MOPr, stabilising the inactive state, and provides confidence that our MD simulation protocol is able to model physiologically relevant MOPr states.

Chapter 4: The binding poses of small molecule opioids relates structure with efficacy

4.1 Introduction

Crystal structures of the MOPr bound to both an antagonist and an agonist have been resolved at high resolution (22, 76). The co-crystallised antagonist β-FNA is unusual in that it forms a covalent bond with the receptor, whilst the co-crystallised agonist BU72 is an experimental compound, not used in the clinic, and may have super-agonist properties (92, 327). There is therefore little structural information on how more typical and clinically important small molecule opioid ligands bind to the MOPr. In this chapter, I perform molecular docking and molecular dynamics simulations with 5 such small molecule opioids, in order to identify how they bind to the MOPr, and how ligand binding translates to receptor activation. I show that small molecules sharing the same chemical scaffold adopt distinct binding poses in the MOPr orthosteric site, correlating with ligand intrinsic efficacy.

The majority of small molecule opioids are morphinan derivatives with a common ring scaffold, but different substituents on the amine and carbons 3, 6 and 7 (Figure 4.1a). The aim of this study was to utilise ligands sharing the same core morphinan scaffold, but with different efficacies at the MOPr, to understand the nature of drug efficacy at this clinically important GPCR. The chosen ligands were; norbuprenorphine, a high efficacy agonist, buprenorphine, a low efficacy agonist, and diprenorphine, an antagonist. I first confirmed the expected signalling characteristics of these compounds in bioluminescence resonance energy transfer (BRET) assays measuring G protein activation and arrestin-3 recruitment. Molecular dynamics (MD) simulations of the membrane-embedded MOPr bound to each ligand were performed and ligand binding poses, residue interactions, and induced receptor protein conformations compared for these compounds of widely varying efficacy. In addition, through further MD simulations I investigated the role of an allosteric sodium ion in determining the binding positions of these drugs. Sodium is a negative allosteric modulator of Class A GPCRs, binding to a conserved site in the receptor transmembrane domains (122-125, 138). However, the molecular mechanism of sodium modulation of agonist action has yet to be fully elucidated. The work in this chapter was published in the Journal of Molecular Biology (DOI: 10.1016/j.jmb.2017.05.009).

In order to widen the conclusions of this morphinan study (152) to a greater test set of small molecule ligands and to include important clinically used opioids, I also performed MD simulations with the MOPr bound to methadone and morphine.

Buprenorphine (Figure 4.1e) is an opioid ligand derived from oripavine. It has mixed activity at opioid receptors; behaving as a partial agonist at the MOPr and KOPr, and as an antagonist at the DOPr (21, 328, 329). Buprenorphine is a clinically important opioid, used both as an analgesic and as a maintenance therapy in heroin addiction. Norbuprenorphine (Figure 4.1d) is a major metabolite of buprenorphine and a potent agonist at the MOPr, KOPr and DOPr (21, 329, 330). As a metabolite, norbuprenorphine shares the same chemical scaffold as buprenorphine but lacks the cyclopropylmethyl ring group on the amine. Although norbuprenorphine is pharmacologically active at opioid receptors, it has limited *in vivo* effects due to poor brain exposure because it is a substrate for the efflux transporter P-glycoprotein (331). Diprenorphine (Figure 4.1f) is a MOPr antagonist (328), with a similar chemical structure to buprenorphine, including the cyclopropylmethyl ring on the amine, but with a smaller substituent group on carbon 7. Morphine (Figure 4.1b), the prototypical opioid, is also based on the morphinan scaffold. It is a partial agonist at the MOPr and the gold standard of pain relief. Methadone is the only small molecule used in this chapter which is not based on the morphinan scaffold (Figure 4.1c), though it retains a protonatable amine group, which is an important structural feature for opioid action (332).

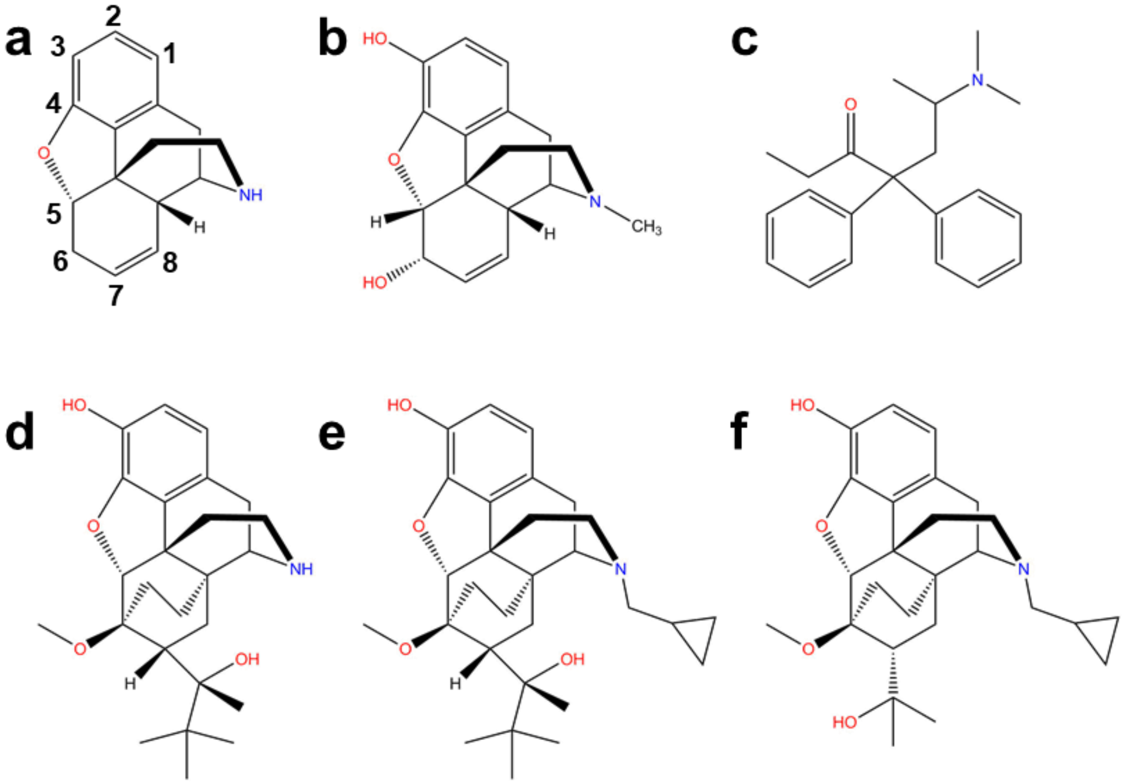

Figure 4.1 Structures of the small molecules

a) Many opioid ligands are based on a morphinan scaffold. 2D structures of the small molecules used in this chapter; b) morphine, c) methadone, d) norbuprenorphine, e) buprenorphine, and f) diprenorphine.

4.2 Materials and Methods

4.2.1 BRET assays

Ligand-induced G_i activation and arrestin-3 recruitment were measured by BRET assay, as described in Chapter 2 Section 2.2.4. DAMGO was included in all experiments as the reference full agonist.

For norbuprenorphine, buprenorphine and diprenorphine, the $BRET^1$ configuration was used to measure arrestin-3 recruitment in HEK 293 cells expressing rat MOPr-YFP and arrestin-3-RLuc. Diprenorphine antagonism was determined by incubation of the HEK 293 cells with 1 μM diprenorphine for 10 minutes, prior to addition of 10 μM DAMGO and measurement of the BRET signal.

After experiments with the buprenorphine-series had been completed, the arrestin BRET assay was switched to the $BRET^2$ configuration as it produced a higher signal than $BRET^1$ (see Chapter 2 Figure 2.7). Therefore, for morphine and methadone the $BRET^2$ configuration was used to measure arrestin-3 recruitment in HEK 293 cells expressing human MOPr-RlucII and arrestin-3-GFP. For this reason, drugs cannot be compared across the two arrestin-recruitment assays, but can instead be compared to the reference agonist DAMGO included in all experiments.

Data analysis and curve fitting was performed in GraphPad Prism v7. For the G_i activation assay, BRET ratios were expressed as the percentage decrease from vehicle-treated control wells. For the arrestin-3 recruitment assays, data were expressed as the BRET ratio minus background from vehicle-treated control wells. Data were then fitted to log concentration – response curves with a Hill Slope of 1.0, and the minimum constrained to zero. The EC_{50} and maximum response (E_{Max}) values for each ligand were compared to DAMGO using one-way ANOVA with Dunnett’s post-test.

4.2.2 Molecular modelling

Molecular docking was performed as described in Chapter 2 Section 2.1.3. The position of β-FNA in the crystal structure of the MOPr (76) was used to determine the initial binding pose of the morphinan ligands (morphine, norbuprenorphine, buprenorphine and diprenorphine). For the non-morphinan ligand, methadone, conformer generation and molecular docking with BUDE was carried out as detailed in Section 2.1.3. The initial docked poses for all 5 ligands are shown in Figure 4.2. 1 µs MD simulations of all 5 membrane-embedded ligand-MOPr complexes were performed as described in Chapter 2 Section 2.1.5. In addition, 1 µs of accelerated MD was performed on the norbuprenorphine-, buprenorphine- and diprenorphine-bound MOPr, as described in Chapter 2 Section 2.1.5.

4.2.3 MD simulations with an allosteric sodium ion

For the MD experiments in the presence of an allosteric sodium ion, the ion was placed in the allosteric site in the position it occupied spontaneously in MD simulations of the unliganded inactive MOPr model (Chapter 3). A total of 250 ns of MD simulation was performed with norbuprenorphine or buprenorphine in the same initial binding poses as in Figure 4.2, and with the sodium ion occupying the allosteric site. In addition, 250 ns of accelerated MD was also performed from the same initial coordinates.

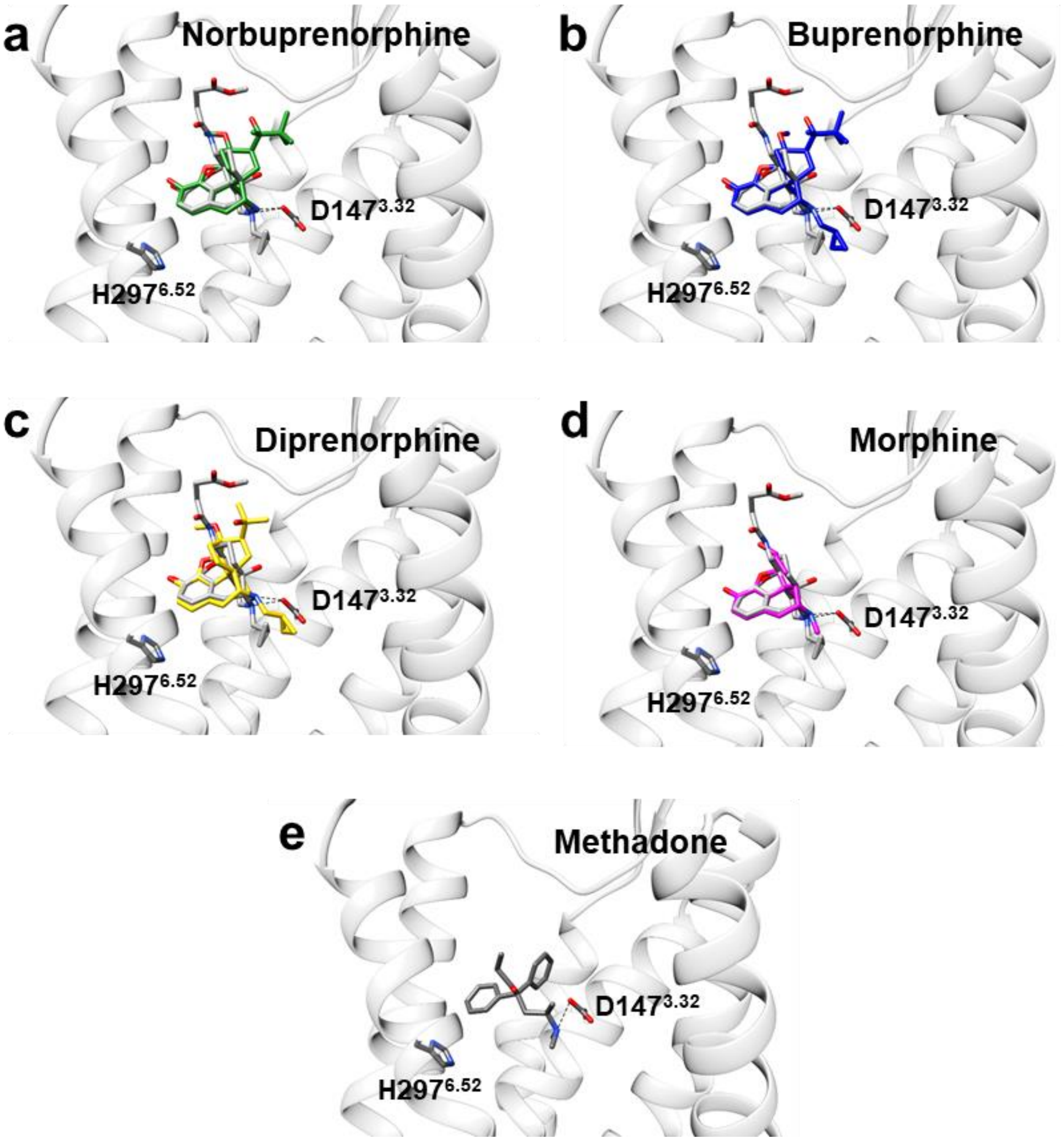

Figure 4.2 Initial docked poses of the small molecules

a-d) The co-crystallised morphinan antagonist β-FNA (grey sticks) was used to determine the initial starting poses for morphinan small molecules: a) norbuprenorphine, b) buprenorphine, c) diprenorphine, and d) morphine. e) For methadone, 10,000 conformers were docked using BUDE as outlined in Chapter 2 Section 2.1.3. The pose selected for MD simulations is shown above. The essential opioid binding residues, D147$^{3.32}$ and H297$^{6.52}$, were used to choose the best docked poses and are depicted as dark grey sticks.

4.3 Results

4.3.1 Ligand-induced G protein activation and arrestin recruitment

Dissociation of the Gαi and Gβγ subunits upon activation of the MOPr was measured in HEK 293 cells expressing HA-rat MOPr, Gαi-RlucII and Gγ-GFP. A ligand-induced decrease in the BRET ratio compared to untreated cells was indicative of this subunit rearrangement or dissociation. Recruitment of arrestin-3 to the MOPr was measured in HEK 293 cells expressing rat MOPr-YFP and arrestin-3-Rluc (BRET^1), or in HEK 293 cells expressing human MOPr-RlucII and arrestin-3-GFP (BRET^2). In both cases, a ligand-induced increase in the BRET ratio compared to untreated cells was indicative of the arrestin and receptor coming into closer proximity. Concentration-response curves for G_i activation and arrestin-3 recruitment are shown in Figure 4.3.

DAMGO behaved as a potent full agonist for both G_i activation and arrestin-3 recruitment, with an EC_{50} ranging between 0.05 – 0.5 µM for G_i activation, and 2.5 ± 0.6 µM (Table 4.1) and 1.6 ± 0.5 µM (Table 4.2) for arrestin-3 recruitment in the BRET^1 and BRET^2 assays, respectively. There is a slight discrepancy between the calculated EC_{50} values for DAMGO in the G_i activation assays performed months apart (Tables 4.1 and 4.2), however the values are not significantly different (Welch’s t-test, $p > 0.05$). Compared to DAMGO, norbuprenorphine was a full agonist for G_i activation (Figure 4.3a), with an EC_{50} of 0.18 ± 0.1 µM (Table 4.1). In the arrestin recruitment assay (Figure 4.3b), norbuprenorphine was a potent partial agonist, with an EC_{50} of 0.2 ± 0.05 µM and an E_{max} approximately 68 % of the DAMGO response (Table 4.1). Buprenorphine was a partial agonist for G_i activation, producing a response approximately 48 % of that due to DAMGO (Figure 4.3a, Table 4.1). In the arrestin recruitment assay, buprenorphine produced a very weak response, barely above the levels of detection (Figure 4.3b). 1 µM diprenorphine failed to produce a response in either the G_i activation or arrestin-3 recruitment assays (yellow filled circles in Figures 4.1a and 4.1b). Furthermore, incubation of cells with 1 µM diprenorphine prior to stimulation with 10 µM DAMGO completely abolished the DAMGO response in both the G protein and arrestin assays (purple filled circles in Figures 4.1a and 4.1b), therefore confirming diprenorphine's antagonist activity.

Morphine behaved as a partial agonist for both G_i activation (Figure 4.3c) and arrestin-3 recruitment (Figure 4.3d). The EC_{50} and E_{max} for morphine in the G protein assay was 0.96 ± 0.4 µM and 74 % that of DAMGO, respectively (Table 4.2). In the arrestin-3 assay morphine had an EC_{50} of 1.2 ± 0.6 µM and an E_{max} of 32 % of the DAMGO response (Table 4.2).

Methadone was a full agonist in both assays (Figures 4.3c and 4.3d), with an EC_{50} of 0.39 ± 0.1 µM for G_i activation and 3.1 ± 1.2 µM for arrestin-3 recruitment (Table 4.2).

These results are in agreement with the previously reported signalling characteristics of these ligands (21).

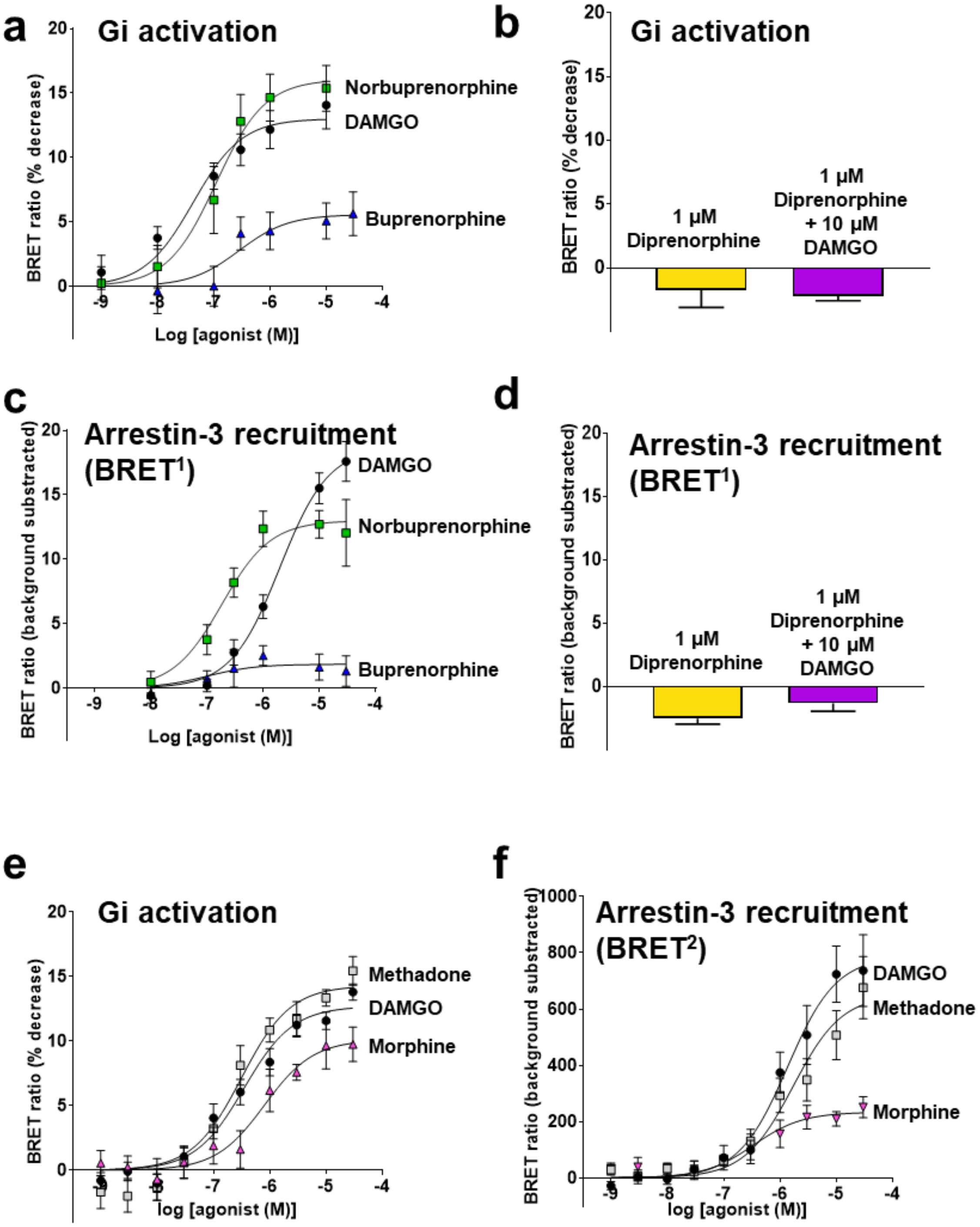

Figure 4.3 Ligand-induced G protein activation and arrestin recruitment

a) In HEK 293 cells expressing HA-MOPr, Gαi-RLucII and Gγ-GFP, DAMGO (black circles), norbuprenorphine (green squares) and buprenorphine (blue triangles) induced concentration-dependent activation of G_i, measured as a decrease in the BRET signal. b) 1 µM diprenorphine alone (yellow) did not activate G_i. In the presence of 1 µM diprenorphine, 10 µM DAMGO did not activate G_i (purple). c) In HEK 293 cells expressing HA-MOPr-YFP and arrestin-3-RLuc ($BRET^1$), DAMGO (black circles) and norbuprenorphine (green squares) induced concentration-dependent recruitment of arrestin-3 to the MOPr, measured as an increase in the BRET signal. Buprenorphine (blue triangles) induced a much lower response. d) 1 µM diprenorphine alone (yellow) did not recruit arrestin-3. In the presence of 1 µM

[continued overleaf]

diprenorphine, 10 µM DAMGO did not recruit arrestin-3 (purple). e) In HEK 293 cells expressing HA-MOPr, Gαi-RLucII and Gγ-GFP, DAMGO (black circles), methadone (grey squares) and morphine (magenta triangles) induced concentration-dependent activation of G_i, measured as a decrease in the BRET signal. f) In HEK 293 cells expressing MOPr-RLucII and arrestin-3-GFP ($BRET^2$), DAMGO (black circles), methadone (grey squares) and morphine (magenta triangles) induced concentration-dependent recruitment of arrestin-3 to the MOPr, measured as an increase in the BRET signal. All values are mean ± SEM for 5 independent experiments.

	Gi activation			Arrestin-3 recruitment (BRET[1])		
Agonist	**EC$_{50}$ (M)**	**E$_{max}$ (BRET ratio)**	**E$_{max}$ (% of DAMGO)**	**EC$_{50}$ (M)**	**E$_{max}$ (BRET ratio)**	**E$_{max}$ (% of DAMGO)**
DAMGO	$4.5 \times 10^{-8} \pm 1.2 \times 10^{-8}$	13.0 ± 1.6	100	$2.5 \times 10^{-6} \pm 0.6 \times 10^{-6}$	19.2 ± 1.6	100
Norbuprenorphine	$1.8 \times 10^{-7} \pm 1.0 \times 10^{-7}$	16.0 ± 1.6	123	$2.0 \times 10^{-7} \pm 0.5 \times 10^{-7}$ *	13.0 ± 1.7 *	68
Buprenorphine	$4.6 \times 10^{-6} \pm 3.2 \times 10^{-6}$	6.3 ± 1.6 *	48	–	2.7 ± 0.8 *	14

Table 4.1 EC$_{50}$ and maximum response values for DAMGO, norbuprenorphine and buprenorphine in the G$_i$ activation and arrestin-3 recruitment assays

Data are expressed as mean ± SEM, of 5 independent experiments. * $p < 0.05$, significantly different from the respective DAMGO value (one-way ANOVA with post-hoc Dunnett's test).

	Gi activation			Arrestin-3 recruitment (BRET[2])		
Agonist	**EC$_{50}$ (M)**	**E$_{max}$ (BRET ratio)**	**E$_{max}$ (% of DAMGO)**	**EC$_{50}$ (M)**	**E$_{max}$ (BRET ratio)**	**E$_{max}$ (% of DAMGO)**
DAMGO	$4.8 \times 10^{-7} \pm 1.6 \times 10^{-7}$	12.9 ± 0.4	100	$1.6 \times 10^{-6} \pm 0.5 \times 10^{-6}$	792 ± 111	100
Methadone	$3.9 \times 10^{-7} \pm 1.0 \times 10^{-7}$	14.4 ± 0.8	112	$3.1 \times 10^{-6} \pm 1.2 \times 10^{-6}$	706 ± 101	89
Morphine	$9.6 \times 10^{-7} \pm 3.6 \times 10^{-7}$	9.6 ± 0.8 *	74	$1.2 \times 10^{-6} \pm 0.6 \times 10^{-6}$	255 ± 25 *	32

Table 4.2 EC$_{50}$ and maximum response values for DAMGO, methadone and morphine in the G$_i$ activation and arrestin-3 recruitment assays

Data are expressed as mean ± SEM, of 5 independent experiments. * $p < 0.05$, significantly different from the respective DAMGO value (one-way ANOVA with post-hoc Dunnett's test).

4.3.2 Ligand binding poses and residue interactions

MD simulations were performed with the inactive MOPr model embedded in a lipid bilayer and bound to each of the 5 small molecule ligands; norbuprenorphine, buprenorphine, diprenorphine, morphine and methadone. A total of 1 µs MD data was collected for each ligand-MOPr complex.

Root mean square deviation (RMSD) calculations were performed to determine how far the MOPr changed from the initial inactive conformation and the stability of the bound pose of the ligand (Figure 4.4). For the receptor, RMSD calculations were performed on the alpha carbons of the transmembrane domains to avoid the high fluctuations of the loop regions and residue side chains masking important helix movements (light grey in Figures 4.4a-e). For the ligands, the heavy atoms of each ligand were compared to the initial docked pose to determine how far the ligand moved from this position, and to the final frame of the simulation to provide a measure of the stability of the final binding pose.

For all ligand-MOPr complexes, the RMSD calculations performed on the receptor transmembrane domains quickly reached a plateau. The norbuprenorphine-MOPr complex deviated the most from the initial helix positions, plateauing at approximately 2 Å (light grey in Figure 4.4a). The methadone-MOPr complex deviated from the initial conformation by approximately 1.5 Å (light grey in Figure 4.4e), whilst the buprenorphine-, diprenorphine- and morphine-bound MOPr helices reached a plateau at approximately 1 Å RMSD (light grey in Figures 4.4b-d). The higher RMSD values for the norbuprenorphine- and methadone-bound MOPr complexes suggests that these higher efficacy ligands induced a greater conformational change in the MOPr helices compared to the inactive MOPr model, than did the lower efficacy ligands.

For the ligands, norbuprenorphine deviated the most from its initial docked position, with an RMSD value of approximately 4 Å (green in Figure 4.4a). In contrast, buprenorphine (dark blue in Figure 4.4b) and morphine (magenta in Figure 4.4d) deviated very little from the initial docked pose. For the majority of the simulation time diprenorphine (yellow in Figure 4.4c) remained close to the initial docked position, but it did occasionally sample an alternative binding position. Methadone (dark grey in Figure 4.4e) reached a plateau at 3 Å from the initial docked pose. Compared to the final binding pose, norbuprenorphine, buprenorphine and morphine were stable in their binding positions (light blue in Figures 4.4a, 4.4b and 4.4d). Again, diprenorphine remained in the same binding pose for the majority of the simulation but did sample the alternative pose (light blue in Figure 4.4c). Methadone had the least stable binding pose, but reached a plateau in the latter portion of the simulation (light blue in Figure 4.4e).

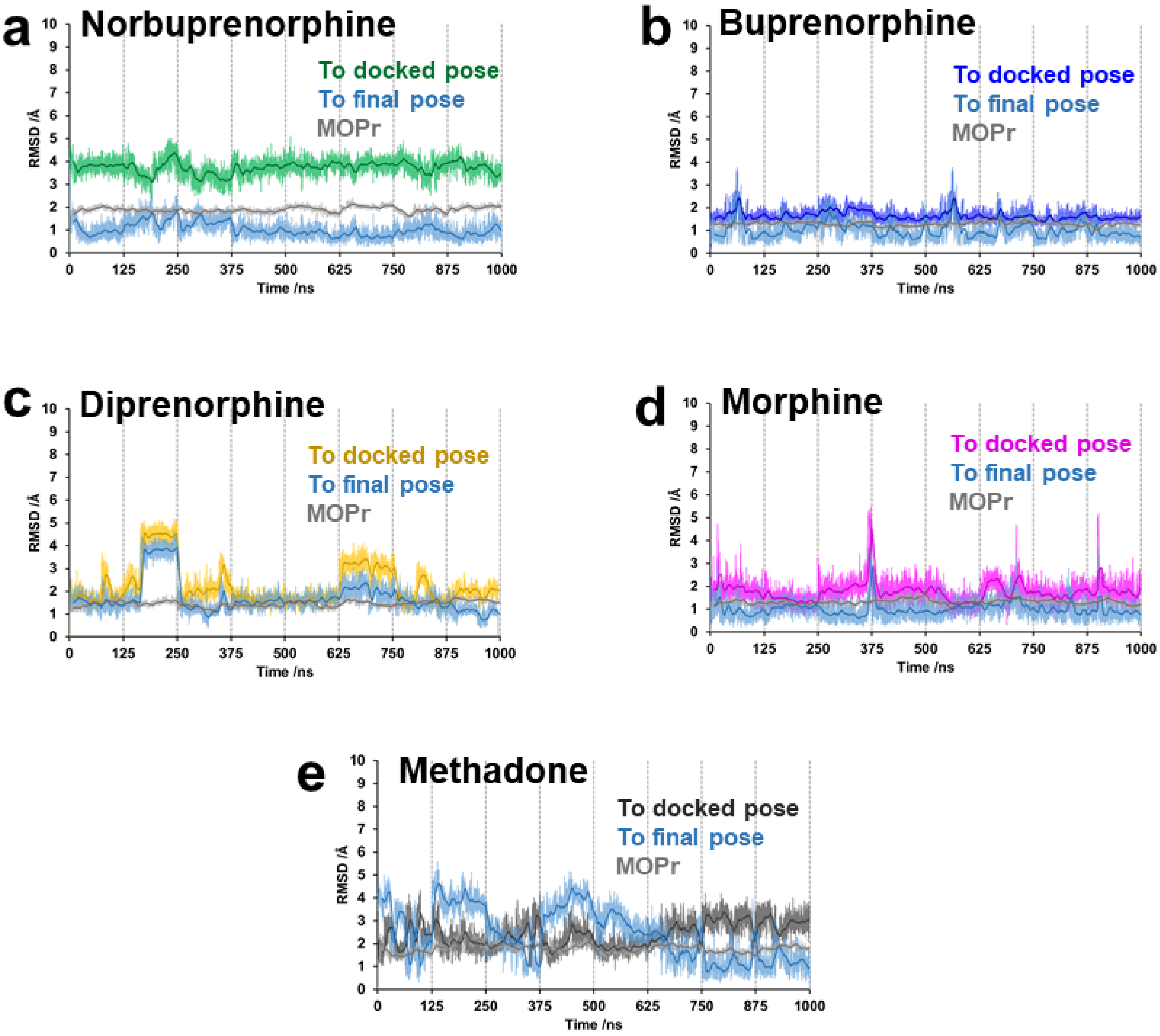

Figure 4.4 RMSD plots for the small molecule ligand-MOPr complexes

a) RMSD calculations performed on the heavy atoms of norbuprenorphine compared to the initial docked position (green) or the final binding pose (light blue). b) RMSD calculations performed on the heavy atoms of buprenorphine compared to the initial docked position (dark blue) or the final binding pose (light blue). c) RMSD calculations performed on the heavy atoms of diprenorphine compared to the initial docked position (yellow) or the final binding pose (light blue). d) RMSD calculations performed on the heavy atoms of morphine compared to the initial docked position (magenta) or the final binding pose (light blue). e) RMSD calculations performed on the heavy atoms of methadone compared to the initial docked position (dark grey) or the final binding pose (light blue). RMSD calculations were also performed on the alpha carbons of the MOPr transmembrane domains, compared to the first frame of the MD simulation (light grey in each plot). Data expressed as raw values (faded line) and moving average over 100 frames (10 ns) (bold line).

The final binding pose for each ligand is shown in Figure 4.5. In simulations with the morphinan ligands (Figures 4.5a-d), the ligand remained in the MOPr orthosteric site, maintaining interactions with the essential opioid ligand binding residues D147$^{3.32}$ and H297$^{6.52}$. The final pose for methadone differed from the initial docked position in that the amine group lost its interaction with D147$^{3.32}$, and instead interacted with its own aromatic ring (Figure 4.5e). In fact, during the 1 µs simulation time, methadone alternated between the canonical ionic interaction between the amine and D147$^{3.32}$, and the amine rotating to interact with the aromatic ring. This instability of the amine-D147$^{3.32}$ interaction may explain why methadone's binding pose fluctuated more so than the other ligands.

The lower efficacy morphinan ligands, morphine, buprenorphine and diprenorphine, remained stably bound in the initial docked pose overlapping with the pose of the co-crystallised antagonist β-FNA (Figures 4.2b-d and 4.5b-d). Unexpectedly, the high efficacy morphinan norbuprenorphine shifted from the initial docked position, pivoting about the amine-D147$^{3.32}$ interaction, to sit deeper in the receptor binding pocket (Figure 4.5a). The presence of the cyclopropylmethyl ring appeared to restrict the ability of buprenorphine and diprenorphine to pivot about this interaction, so despite sharing the same morphinan scaffold as norbuprenorphine, they adopted binding poses higher in the receptor pore. The alternative binding pose of diprenorphine sampled infrequently during the simulation (Figure 4.4c) was due to the ligand switching from a direct interaction between the amine and D147$^{3.32}$, and one mediated via a bridging water molecule.

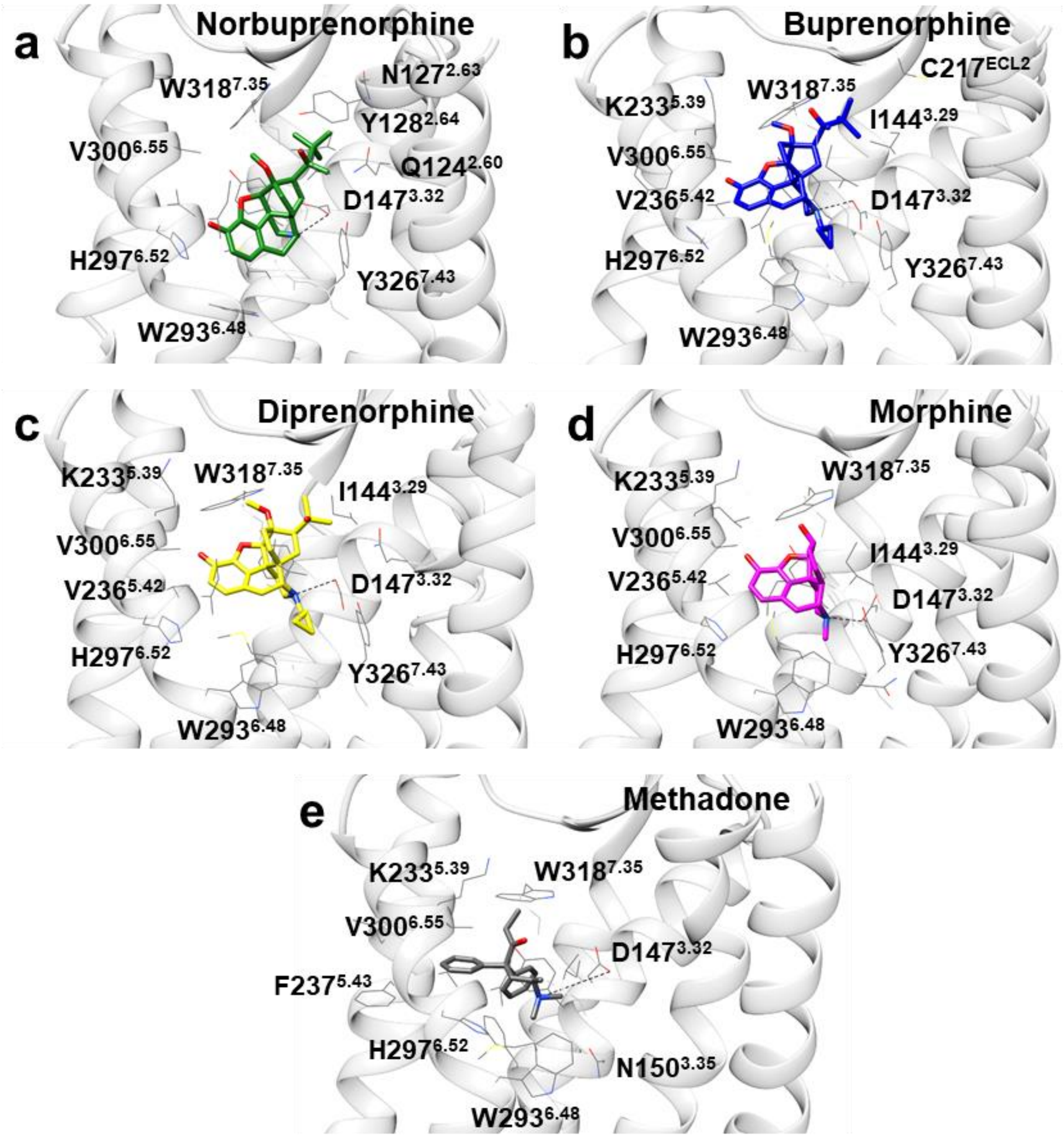

Figure 4.5 Final binding poses for the small molecules

Final binding poses of the small molecule ligands in the MOPr orthosteric site after 1 µs MD simulations (taking the final frame of the concatenated trajectory composed of the 8 individual 125 ns parallel simulations). The MOPr helices are shown in light grey, with residues forming the ligand binding site as sticks. a) norbuprenorphine is depicted in green and sits deeper in the binding pocket than the other morphinan ligands. b) buprenorphine depicted in blue, c) diprenorphine depicted in yellow, d) morphine depicted in magenta, and e) methadone in dark grey.

As these small molecules adopted distinct binding poses in the orthosteric site, they therefore interacted with different subsets of residues. Ligand-residue interaction plots, with a cut-off distance of 4.5 Å, are shown in Figure 4.6. All the small molecules interacted with residues in TM3 and TM6; D147$^{3.32}$, Y148$^{3.33}$ and M151$^{3.36}$ in TM3, and W293$^{6.48}$, I296$^{6.51}$, H297$^{6.52}$ and V300$^{6.55}$ in TM6. Norbuprenorphine alone engaged in interactions with TM2, specifically Q124$^{2.60}$, N127$^{2.63}$ and Y128$^{2.64}$, but was the only ligand not to contact residues in TM5 (Figure 4.6a). Buprenorphine engaged in the most extensive interactions with the orthosteric pocket (Figure 4.6b). This may reflect the unusually slow dissociation rate of this ligand (333).

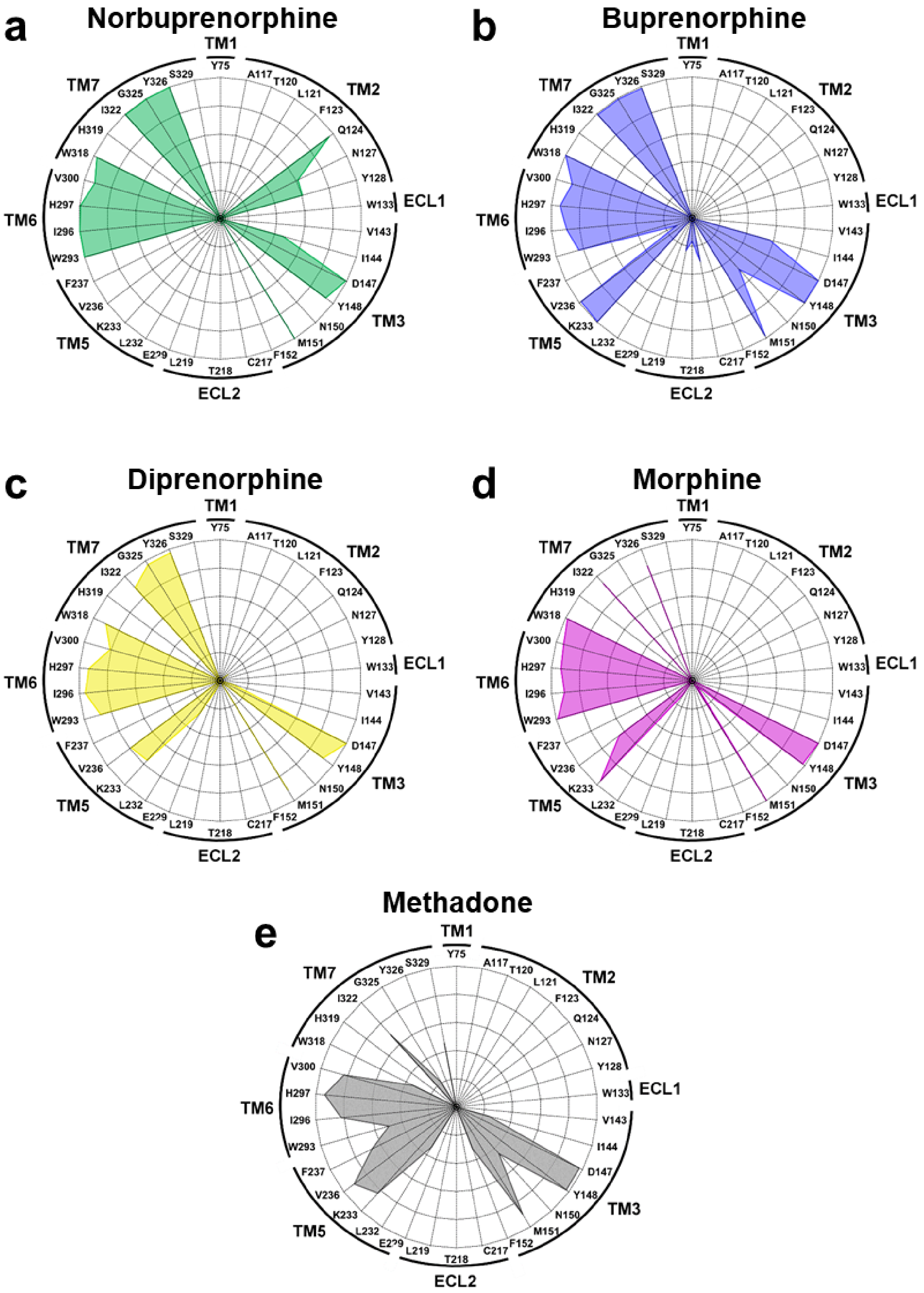

Figure 4.6 Ligand-residue interactions for all small molecule ligand-MOPr complexes

a) Norbuprenorphine, b) buprenorphine, c) diprenorphine, d) morphine, and e) methadone. Ligand-residue interactions are expressed as the percentage of simulation time each residue is within 4.5 Å of the ligand, with points radiating outwards from 0 to 100 % in 20 % increments.

4.3.3 The W293$^{6.48}$ rotamer toggle switch

The highly conserved aromatic residue, W293$^{6.48}$, is positioned at the base of the orthosteric ligand binding pocket (Figure 4.5), and forms part of the second coordination shell of the allosteric sodium ion binding site (see Chapter 1 Sections 1.2.3.3 and 1.2.3.4). Previous studies of other Class A GPCRs have suggested that W293$^{6.48}$ acts as a toggle switch for receptor activation (22, 134, 150, 151, 156, 334). During our MD simulations of ligand-bound MOPr, W293$^{6.48}$ underwent significant changes in the angle of its indole ring side chain. These rotamer changes were monitored by plotting the $\chi 2$ angle, shown in Figure 4.7. With the indole ring positioned perpendicular to the bilayer, viewed as a “vertical” position when looking through the plane of the membrane, the $\chi 2$ dihedral is approximately 120°. Rotation about this dihedral so that the indole ring is positioned parallel to the bilayer (“horizontal” when viewed in the plane of the membrane) results in a $\chi 2$ angle closer to 0°. In the antagonist-bound MOPr crystal structure, W293$^{6.48}$ is in the “vertical” position (76). In the “horizontal” position, observed in the agonist- and G protein-bound fully active MOPr structure (23), the indole ring obstructs the allosteric sodium ion binding site.

The initial conformation for all MD simulations was with W293$^{6.48}$ in the “vertical” position, as seen in the inactive MOPr model. The low efficacy ligands did not significantly alter this initial conformation of the W293$^{6.48}$ indole ring. As shown in the plots in Figure 4.7 with buprenorphine (Figure 4.7b), diprenorphine (Figure 4.7c) or morphine bound (Figure 4.7d), the sidechain of W293$^{6.48}$ largely maintained a “vertical” conformation, with the indole ring of the tryptophan perpendicular to the bilayer, favouring a $\chi 2$ angle between 80 - 120˚ and pointing into the ligand binding pocket. Both buprenorphine- and diprenorphine-bound receptors occasionally sampled the “horizontal” conformation of W293$^{6.48}$; buprenorphine more frequently than diprenorphine, whereas morphine maintained the “vertical” W293$^{6.48}$ position for the entire MD simulation time sampled.

In contrast, in the MD simulations of the MOPr bound to the higher efficacy ligands, W293$^{6.48}$ underwent significant conformational changes. With norbuprenorphine bound, the indole ring of W293$^{6.48}$ favoured the "horizontal" conformation, parallel to the lipid bilayer, maintaining a $\chi 2$ angle of 0 - 60˚ and spanning the base of the ligand binding site (Figure 4.7a). This rotameric change in W293$^{6.48}$ appeared to be due to the deeper binding pose of norbuprenorphine (Figure 4.5a). Steric hinderance between the ligand in its deeper binding pose and the indole ring of W293$^{6.48}$ would prevent W293$^{6.48}$ remaining in the "vertical" conformation. The rotameric change in the W293$^{6.48}$ side chain to the "horizontal" conformation avoided this clash.

The other high efficacy agonist, methadone, also caused W293$^{6.48}$ to favour this "horizontal" conformation, although it also sampled the "vertical" conformation (Figure 4.7e). This may be related to methadone's less stable binding pose in that it did not fully maintain the amine – D147$^{3.32}$ interaction for the entire simulation time, and neither did it induce the W293$^{6.48}$ rotameric change as frequently as norbuprenorphine.

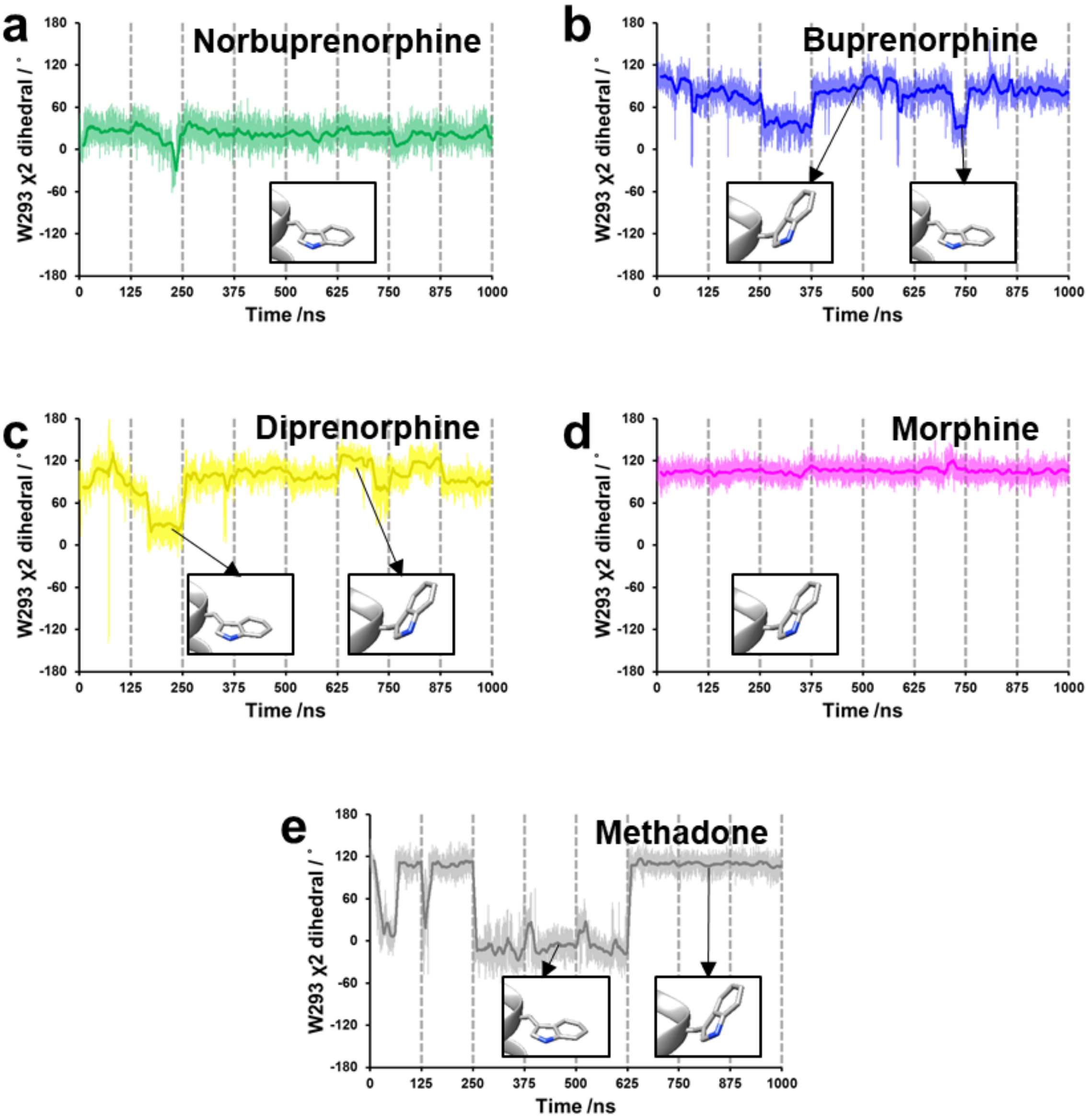

Figure 4.7 W293$^{6.48}$ rotamer toggle switch

The behaviour of the W293$^{6.48}$ rotamer toggle switch plotted as the χ2 dihedral angle during 1 µs MD simulations of the MOPr bound to a) norbuprenorphine, b) buprenorphine, c) diprenorphine, d) morphine, and e) methadone. Insets show how the dihedral angle relates to the conformation of the indole ring. Data expressed as raw values (faded line) and moving average over 100 frames (10 ns) (bold line).

4.3.4 Principal component analysis shows distinct helical arrangements

Large, high-dimensional datasets, such as that obtained by MD, are difficult to analyse by eye or simple statistics. Principal component analysis (PCA) reduces highly dimensional data to the main or 'principal' components which account for the most variation in the data set (335). In the case of these GPCR MD data, these components refer to atomic positions of the receptor helices. PCA was employed to examine the subtle conformational changes in the receptor transmembrane domains, allowing mapping of clusters of conformations sampled by the different ligand-MOPr complexes to determine any differences between the conformations favoured by the MOPr in the presence of the different small molecule ligands.

PCA was performed on the norbuprenorphine-, buprenorphine- and diprenorphine-bound MD simulations to determine what effect small changes in the ligand chemical structure had on the conformation of the MOPr. After fitting to remove global rotation and translation of the system, the covariance matrix was generated from just the alpha carbons of the MOPr transmembrane domains, to avoid including the highly dynamic loops and residue side chains in the analysis. The receptor conformation at each time point was projected onto principal components (PC) 1 and 2 and plotted in Figure 4.8a. This resulted in clusters of receptor conformations which converge if the helical structures are becoming more similar or diverge if the conformations are different.

PC1 and PC2 accounted for 28.2 % and 11.3 % of the variance, respectively. All 3 ligand-MOPr complexes sampled conformations across PC2, but clustered differently based on PC1, with the norbuprenorphine-bound MOPr occupying a distinct cluster (green, Figure 4.8a) to the buprenorphine- (blue, Figure 4.8a) and diprenorphine-bound MOPr (yellow, Figure 4.8a). This indicated different helical arrangements depending on the bound ligand. The diprenorphine-bound MOPr cluster overlapped with the buprenorphine-bound cluster, suggesting that these receptor conformations were similar. Moreover, both the buprenorphine- and diprenorphine-bound clusters overlapped with the conformation of the inactive MOPr model (black, Figure 4.8a), suggesting that with these low efficacy ligands bound, the MOPr favoured a more inactive conformation. The distinct conformational cluster sampled by the norbuprenorphine-bound MOPr did not overlap with the inactive MOPr model, and thus may represent the norbuprenorphine-bound MOPr occupying an intermediate state which may ultimately transition to an active conformation.

By generating a pseudo-trajectory of PC1 and extracting structures from the actual simulations that represent extremes of PC1, we were able to visualise the helix movements contributing to the principal component. An overlay of structures extracted from the norbuprenorphine-bound cluster and the buprenorphine-bound cluster is shown in Figure 4.8b, with the helix movements described by PC1 depicted as white arrows. PC1 primarily described alternative conformations in the extracellular region of the receptor close to the orthosteric binding site, and to a lesser extent differences in the intracellular portions of the helices. Notably, the extracellular ends of TM1, 3 and 7 moved outwards from the helical bundle in the presence of norbuprenorphine, whilst the extracellular ends of TM2 and 6 moved inwards. On the intracellular side of the MOPr, TM5 moved in towards the helix bundle with norbuprenorphine bound, whereas TM6 moved slightly outwards.

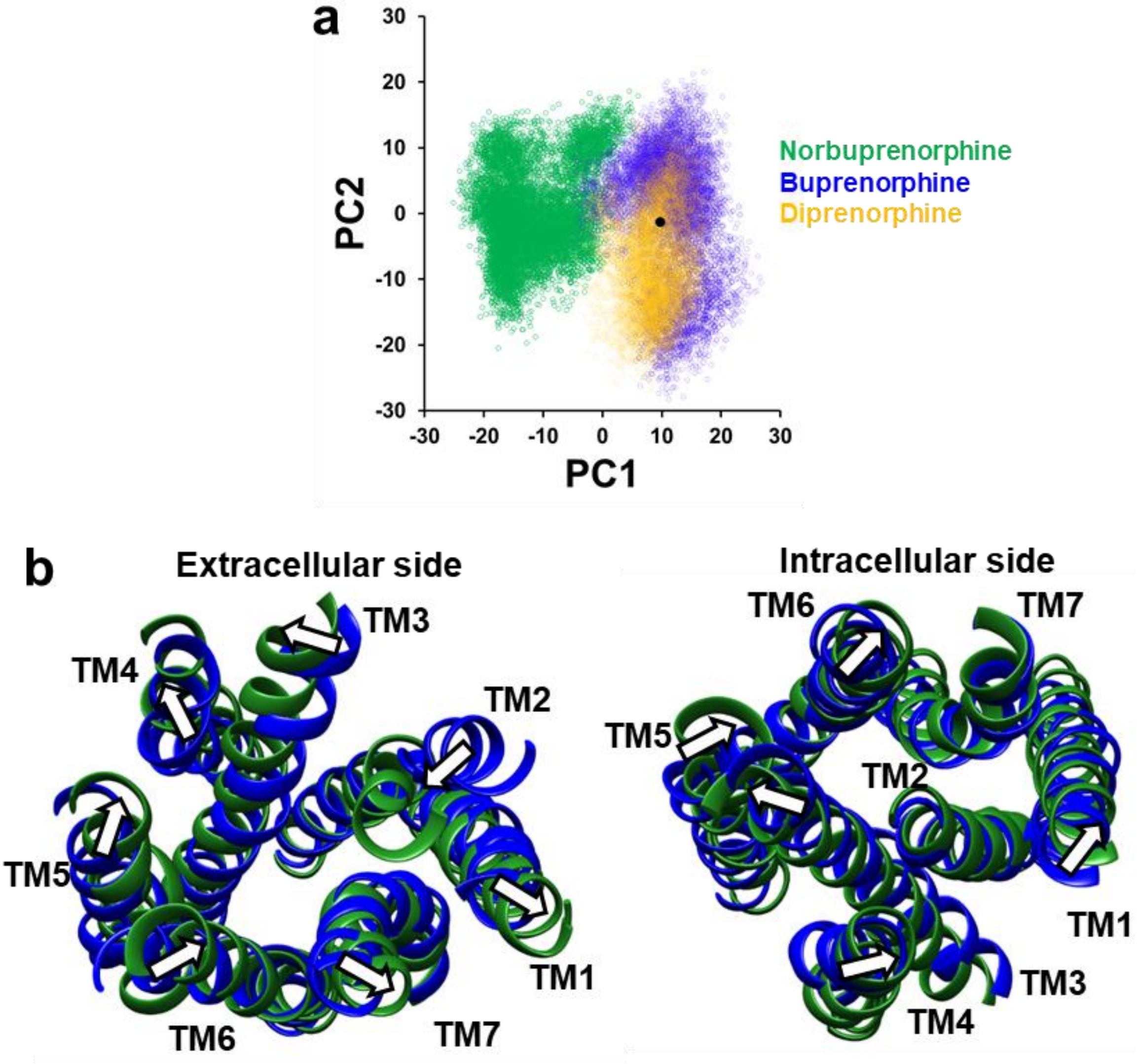

Figure 4.8 Principal Component Analysis reveals distinct MOPr conformations

a) Principal component analysis was performed on the alpha carbons of the receptor transmembrane domains, before projecting the receptor conformations at each simulation time point onto PC1 and PC2. The norbuprenorphine-MOPr complex is in green, the buprenorphine-MOPr complex in blue, the diprenorphine-MOPr complex in yellow, and the black point indicates the conformation of the inactive MOPr model.

b) Extracted structures representing the extremes of PC1 demonstrate the conformational differences between the norbuprenorphine-MOPr complex (green) and the buprenorphine-MOPr complex (blue). Loops have been removed from the image to depict only the part of the receptor the principal component analysis was performed on. White arrows indicate conformational changes in the helices moving from buprenorphine-bound to norbuprenorphine-bound MOPr.

4.3.5 The effect of an allosteric sodium ion on ligand binding pose, W293$^{6.48}$ conformation and helix positions

During unliganded MOPr simulations a sodium ion was observed to move from the extracellular space into the receptor pore to occupy the allosteric sodium binding site (Chapter 3). Sodium is a negative allosteric modulator of Class A GPCRs, with the first studies showing sodium modulation of agonist binding conducted on opioid receptors (120, 121). This previous literature on receptor modulation by sodium, and our MD data showing divergent effects on the behaviour of the W293$^{6.48}$ in the second coordination shell of the sodium site, led us to investigate the effect of an allosteric sodium ion in our MD simulations of ligand-MOPr complexes. 250 ns simulations of the MOPr bound to norbuprenorphine or buprenorphine, with a sodium ion placed in the allosteric site were performed, with the ligands in the same initial binding poses as before (Figures 4.2a and 4.2b). The sodium ion did not leave the allosteric site during the simulation time for either the norbuprenorphine- or buprenorphine-bound receptor.

The ligand binding poses, the conformation of the W293$^{6.48}$ rotamer, and the MOPr helix conformations in the presence and absence of an allosteric sodium ion are shown in Figure 4.9. In the presence of an allosteric sodium ion, both norbuprenorphine and buprenorphine maintained the shallower binding pose favoured by the low efficacy ligands in the previous simulations (Figure 4.9a). Compared to simulations in the absence of an allosteric sodium ion, norbuprenorphine was shifted upwards in the binding pocket (Figure 4.9b). However, the binding pose of buprenorphine was unchanged in the presence or absence of the sodium ion (Figure 4.9c). This suggests that sodium disrupts the binding pose of high efficacy agonists, more so than low efficacy ligands.

The behaviour of the rotamer toggle switch W293$^{6.48}$ was also different in the presence of an allosteric sodium ion (Figure 4.9e). For the buprenorphine-bound receptor, W293$^{6.48}$ maintained the “vertical” conformation in both the presence and absence of sodium, with a χ2 angle between 60-120°. In contrast, for the norbuprenorphine simulations the rotamer of W293$^{6.48}$ switched from a “horizontal” conformation in the absence of sodium (~ 0°), to the “vertical” conformation with a sodium ion bound in the allosteric site. This “vertical” conformation in the presence of sodium, with a χ2 angle between 80-120°, was comparable to the conformation favoured by the buprenorphine- and diprenorphine-bound receptor, pointing into the ligand binding pocket. These data suggest that the presence of an allosteric sodium ion prevented the high efficacy agonist norbuprenorphine inducing conformational changes in the rotamer toggle switch.

PCA was performed as described in Section 4.3.4 on the norbuprenorphine and buprenorphine-bound simulations in the presence and absence of an allosteric sodium ion (Figure 4.9d). As shown in Section 4.3.4, the norbuprenorphine- (green, Figure 4.9d) and buprenorphine-bound (blue, Figure 4.9d) MOPr complexes occupied distinct clusters in the absence of an allosteric sodium ion. With the sodium ion occupying the allosteric site, the conformation of the buprenorphine-bound MOPr was unchanged in terms of PC1 and PC2 (yellow, Figure 4.9d), indicating that the presence of sodium did not significantly alter the conformation of the MOPr helices. In contrast, for the norbuprenorphine-bound receptor the presence of an allosteric sodium ion caused the conformational cluster (black, Figure 4.9d) to shift to overlap with both the sodium-bound and sodium-free buprenorphine-bound clusters. This suggests that the presence of sodium prevented the norbuprenorphine-bound MOPr transitioning to the alternative intermediate state observed in the absence of sodium.

Taken together, the change in norbuprenorphine’s binding pose, the angle of W293$^{6.48}$, and the conformations sampled by the MOPr helices, suggest that the presence of an allosteric sodium ion caused the norbuprenorphine-bound MOPr to favour an inactive conformation, whilst the buprenorphine-bound MOPr was relatively unchanged.

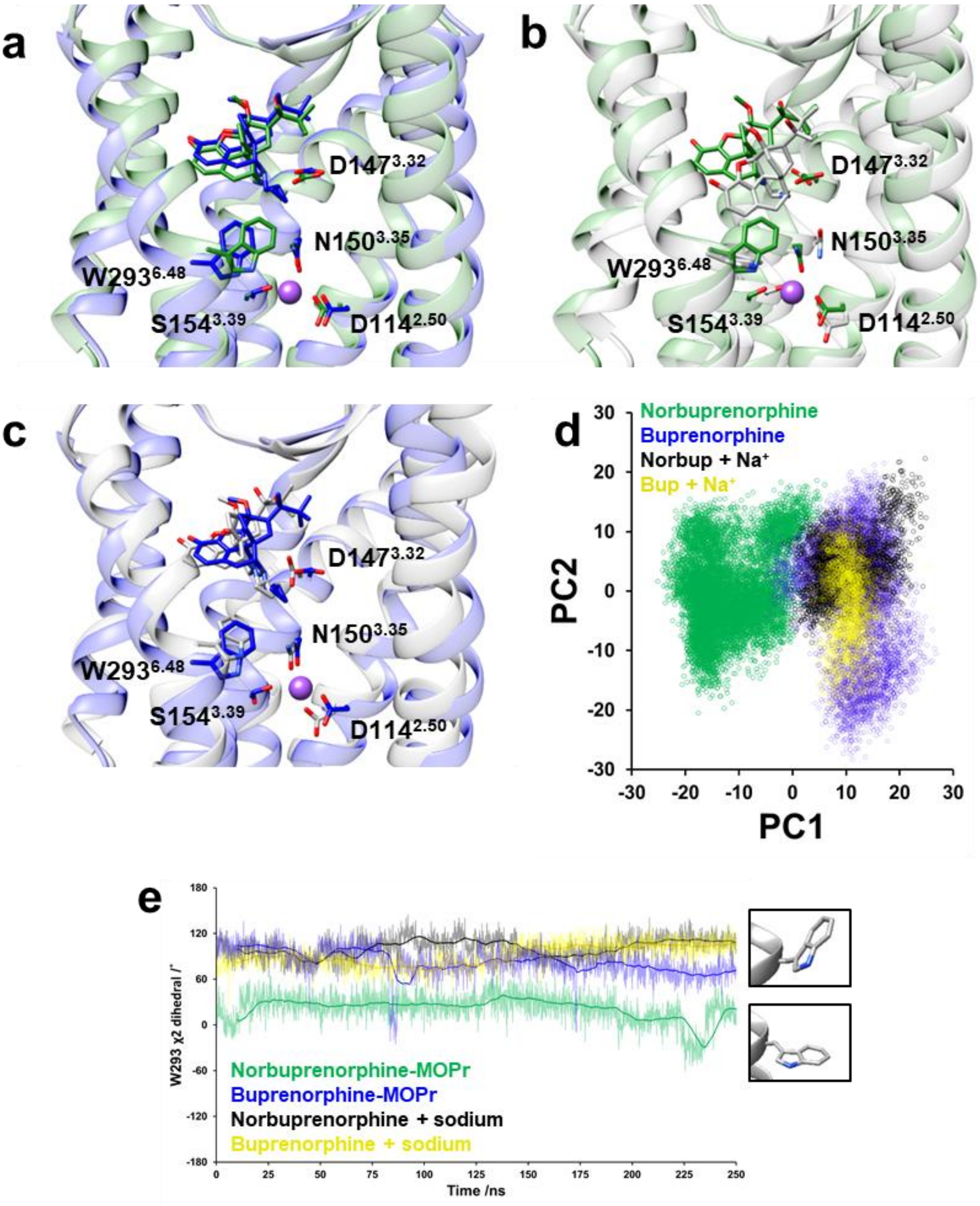

Figure 4.9 Presence of a sodium ion in the allosteric site disrupts high efficacy agonist binding

a) The final frames from 250 ns MD simulations of norbuprenorphine-bound MOPr (green) or buprenorphine-bound MOPr (blue) with a sodium ion in the allosteric site (purple). b) Comparison of norbuprenorphine's binding pose in the absence of an allosteric sodium ion (grey), and in the presence of sodium (green). c) Comparison of buprenorphine's binding pose in the absence of an allosteric sodium ion (grey) and in the presence of sodium (blue). d) Projection of the receptor conformation at each time point onto principal components 1 and 2. The norbuprenorphine-bound receptor in the absence of an allosteric sodium is in green and buprenorphine-bound receptor in the absence of sodium in blue. The norbuprenorphine-bound receptor in the presence of sodium is in black, and the buprenorphine-bound receptor in the presence of sodium is in yellow. e) Rotamer angle of W293$^{6.48}$ over 250 ns MD with norbuprenorphine or buprenorphine bound, in the presence or absence of an allosteric sodium ion. Data expressed as raw values (faded line) and moving average over 100 frames (10 ns) (bold line).

4.3.6 Accelerated MD simulations corroborate the conventional MD findings

Accelerated MD (aMD) is a method of increasing sampling over a short computational time by employing a boost potential to accelerate conformational changes (336). For the norbuprenorphine-, buprenorphine- and diprenorphine-bound MOPr, up to 1 µs of aMD simulation data was collected to determine if this enhanced sampling technique would reveal any further conformational changes in the MOPr in response to each ligand. Each simulation was started with the ligands in the same initial binding pose as in the conventional MD (Figures 4.2a-c).

The aMD results are summarised in Figure 4.10, and broadly agreed with the data from the conventional MD simulations. The binding poses of norbuprenorphine, buprenorphine and diprenorphine were similar in the conventional MD and aMD simulations, with norbuprenorphine adopting a deeper binding position and engaging the W293$^{6.48}$ rotamer (Figure 4.10a), whilst buprenorphine and diprenorphine maintained a shallower binding pose (Figures 4.10b and 4.10c).

PCA was also conducted on the aMD simulations, using the same method as described in Section 4.3.4 for the conventional MD. For the aMD principal components 1 and 2 accounted for 14.2 % and 9.7 % of the variance, respectively. Like in the conventional MD (Figure 4.8a), the norbuprenorphine-bound MOPr formed a distinct cluster of conformations to the buprenorphine or diprenorphine-bound MOPr (Figure 4.10d). The greater spread of the aMD PCA plot, ranging from approximately -40 to 40, showed the conformational space sampled by aMD was greater than that by the conventional MD simulations (ranging from approximately -20 to 20). This highlights the value of this technique in increasing sampling of the conformational landscape of the MOPr over a relatively short computational time. Nevertheless, both approaches gave the same overall result; norbuprenorphine induced the MOPr helices to adopt a distinct conformation to when the lower efficacy ligands were bound.

Furthermore, aMD simulations were also performed on the norbuprenorphine- and buprenorphine-bound MOPr complexes in the presence of an allosteric sodium ion. Again, the aMD data agreed with the conventional MD, with norbuprenorphine adopting the shallower binding pose in the presence of sodium (Figure 4.10e). The W293$^{6.48}$ also reverted to the “vertical” conformation in aMD simulations with an allosteric sodium ion bound. PCA performed on the aMD simulations of the norbuprenorphine- and buprenorphine-bound MOPr in the absence or presence of sodium again showed that in the presence of an allosteric sodium ion the norbuprenorphine-MOPr cluster shifted to occupy the same conformational space as the buprenorphine-bound MOPr (Figure 4.10f).

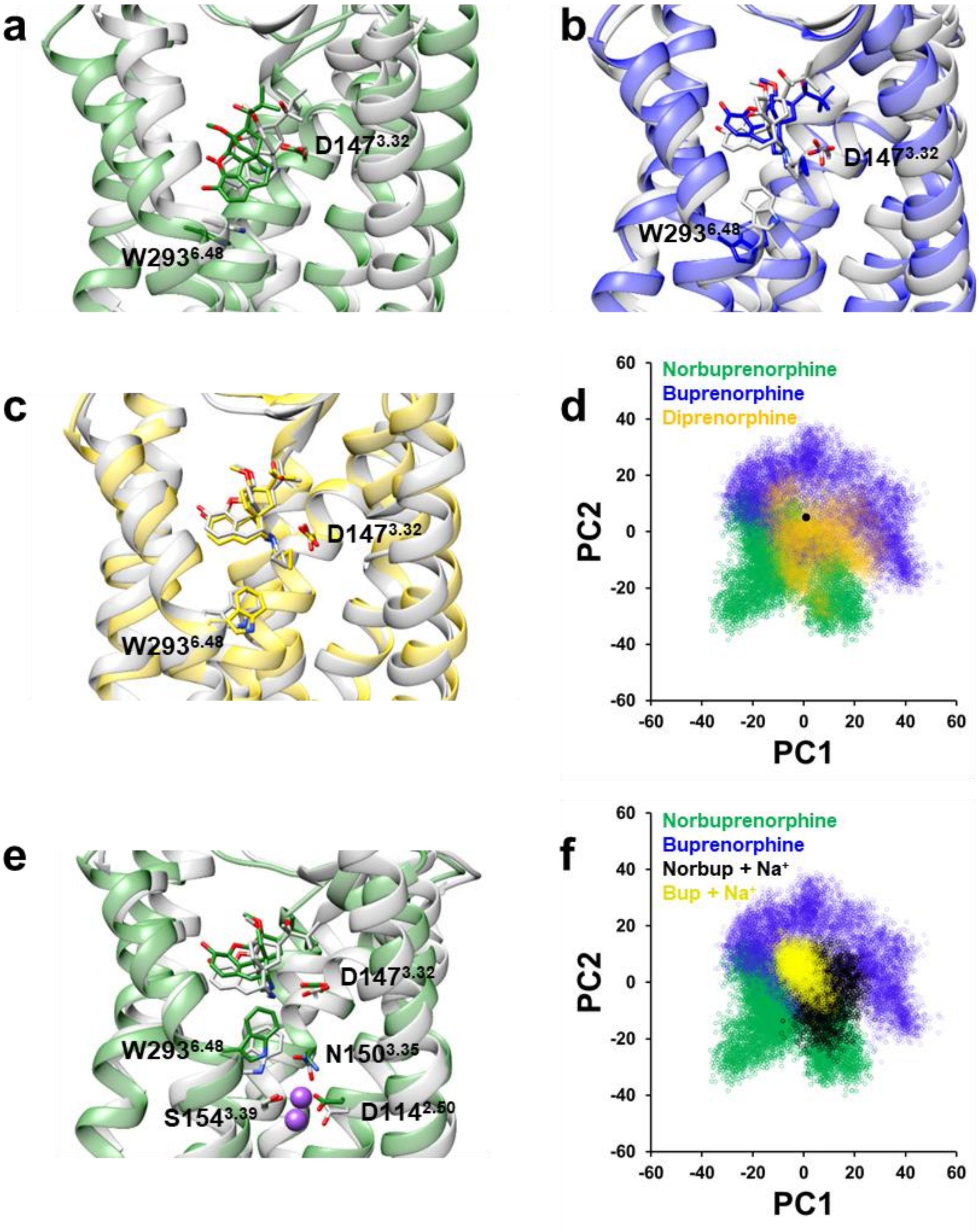

Figure 4.10 Accelerated MD corroborates the conventional MD results

The binding poses of a) norbuprenorphine, b) buprenorphine and c) diprenorphine are similar in conventional MD simulations (grey) and accelerated MD simulations (coloured). d) PCA performed on the aMD simulations. The norbuprenorphine-MOPr complex is in green, the buprenorphine-MOPr complex in blue, the diprenorphine-MOPr complex in yellow, and the black point indicates the conformation of the inactive MOPr model. e) The binding pose of norbuprenorphine and the conformation of W293$^{6.48}$ in the presence of an allosteric sodium ion is similar in the conventional MD (grey) and accelerated MD (green). f) PCA on the sodium-free and sodium-bound aMD simulations. The norbuprenorphine-bound receptor in the absence of an allosteric sodium is in green and buprenorphine-bound receptor in the absence of sodium in blue. The norbuprenorphine-bound receptor in the presence of sodium is in black, and the buprenorphine-bound receptor in the presence of sodium is in yellow.

4.4 Discussion

In this chapter I have used MD simulations to predict the binding poses of a series of small molecule MOPr ligands, which although structurally similar display widely differing signalling profiles.

BRET assays for G_i activation and arrestin-3 recruitment confirmed the reported signalling characteristics of these ligands (21); norbuprenorphine and methadone were both full agonists for G_i activation and robustly recruited arrestin-3, whilst buprenorphine and morphine were partial agonists for G_i activation and with a greatly reduced ability to recruit arrestin-3. Diprenorphine was an antagonist for both G_i activation and arrestin-3 recruitment.

Unexpectedly, comprehensive sampling (1 µs MD simulations) of the ligand-MOPr complexes revealed that these small molecules adopted distinct binding poses within the orthosteric site. We have identified a novel binding pose for norbuprenorphine which may provide a molecular basis for the high efficacy of this ligand compared to its analogues, buprenorphine and diprenorphine. This novel binding pose is deeper in the orthosteric site compared to the other small molecules used in this study and the co-crystallised ligands in the antagonist- and agonist-bound MOPr crystal structures, β-FNA and BU72. This observation that structural analogues can nevertheless bind differently was also recently reported for the $5HT_{2B}$ receptor (186). High resolution crystal structures of the $5HT_{2B}$ receptor bound to ergotamine or LSD showed that although both compounds share the same ergoline moiety, they adopt slightly different poses in the orthosteric site, with ergotamine binding deeper in the pocket than LSD (186). This finding from our study of morphinan ligands (152) highlights the importance for using both molecular docking and molecular dynamics simulations to predict ligand binding poses; it cannot be assumed the molecules derived from the same chemical structure will interact with the receptor in exactly the same way.

The presence of a cyclopropylmethyl ring on morphinan compounds appears to confer a degree of antagonist activity (324, 337, 338), for instance naloxone is an opioid antagonist whereas its derivative oxymorphone, which lacks the cyclopropylmethyl ring on the amine, is an agonist. By performing MD simulations of the active state MOPr crystal structure *Huang et al.,* showed that whilst the binding pose of the agonist BU72 is stable, the cyclopropylmethyl ring-containing analogue, BU74, is unstable when docked into the same pose. They predict that this hydrophobic group cannot interact with residues in the polar cavity at the base of the ligand binding site (22). In the present study, this shared amine substituent in buprenorphine and diprenorphine appeared to reduce the ability of the ligand to pivot about the amine-D147$^{3.32}$ interaction. In contrast, without this bulky ring group norbuprenorphine was able to pivot about the canonical amine-D147$^{3.32}$ interaction to access the deeper binding site. We have therefore provided further molecular evidence for the known activity-modulating properties of this cyclopropylmethyl group in opioid ligands.

Moreover, as well as norbuprenorphine's novel binding pose, we also observed different conformations of the MOPr helices with norbuprenorphine bound compared to the lower efficacy morphinans. We propose that the alternative binding pose of norbuprenorphine translates to these distinct receptor conformations and that this reflects the differing efficacies of the bound ligands. The mechanism is likely due to the distinct ligand-residue interactions caused by the slightly different binding positions of the ligands. Indeed, unique ligand-residue interaction fingerprints which correlated with ligand efficacy were also observed in MD simulations of the β_2 adrenoceptor (339). Furthermore, the recently solved crystal structure of the β_2 adrenoceptor bound to a partial agonist revealed that the partial agonist, salmeterol, interacted with the orthosteric site in a manner different to the full agonist, adrenaline (340).

One such important interaction defined here is with the conserved tryptophan residue, W293$^{6.48}$, at the base of the orthosteric binding pocket. W293$^{6.48}$ has been previously described as a rotamer toggle switch for class A GPCR activation, such as the cannabinoid CB1 and muscarinic M_3 receptors (150, 151, 156, 334). W293$^{6.48}$ also forms part of the allosteric sodium ion binding site in the inactive state of class A GPCRs (122-125). This allosteric pocket collapses upon receptor activation (see Chapter 3 and (138, 139)). Here, we show that this residue behaved differently depending on the bound ligand. When the high efficacy agonists, norbuprenorphine and methadone are bound, W293$^{6.48}$ switched from the "vertical" position of the inactive MOPr model to the "horizontal" position observed in the fully active agonist-MOPr-G_i complex (23). In contrast, with the lower efficacy ligands, morphine, buprenorphine or diprenorphine bound, W293$^{6.48}$ favoured the inactive state "vertical" conformation. This may provide an explanation for the differing efficacies of this panel of small molecules; high efficacy agonists are able to induce the rotameric change in W293$^{6.48}$, causing the allosteric sodium ion binding site to collapse, releasing the brake on receptor activation and transmitting the binding of an agonist to conformational changes in the MOPr helices. Lower efficacy ligands are less able to induce the rotameric change in W293$^{6.48}$, so there is a lower probability of the MOPr transitioning to an active state upon ligand binding than with high efficacy agonists. This role of W293$^{6.48}$ as a microswitch for receptor activation has been described for other class A GPCRs (22, 134, 150, 151, 156, 334), but there is little published data on this phenomenon in the MOPr, particularly in relation to the binding of different ligands.

Although the behaviour of the W293$^{6.48}$ microswitch correlates well with ligand efficacy in our study, it is unlikely to be the sole mechanism of MOPr activation. Indeed, comparison of inactive and active state crystal structures of multiple GPCRs points to diverse mechanisms for the initiation of receptor activation for different ligands and GPCRs (82, 101). These multiple mechanisms of activation around the orthosteric binding pocket converge to a common conformational change at the intracellular G protein coupling region (82, 166); primarily the outward movement of TM6 and concurrent inward movements of TMs 5 and 7. In these MD simulations, neither morphine nor buprenorphine induced the rotameric change in W293$^{6.48}$, but both are MOPr agonists capable of activating the receptor, albeit with reduced responses compared to full agonists. This poses the question of how these lower efficacy opioids activate the MOPr; one possibility is morphine and buprenorphine are able to engage the W293$^{6.48}$ toggle switch but with lower probability than norbuprenorphine and methadone, which we did not sample in our MD simulations. Alternatively, morphine and buprenorphine may activate the MOPr via a different mechanism than the W293$^{6.48}$ rotamer. Supporting this, the principal component analysis showed that the buprenorphine-MOPr complex sampled conformations distinct from both the norbuprenorphine-bound receptor and the inactive state. This may represent a different intermediate state to that stabilised by norbuprenorphine. Furthermore, an MD study comparing the MOPr bound to morphine or the biased compound, oliceridine, revealed different allosteric transduction mechanisms between the ligand binding pocket and the G protein binding site for these two ligands (263). A similar principle may also apply here whereby the subtly different ligand-residue interactions we observed can induce MOPr activation by distinct mechanisms. Moreover, it is important to remember that the MOPr is endogenously a peptide receptor. The mechanism of activation may differ markedly between small molecule and peptide ligands and indeed, unlike GPCRs which evolved to respond to small molecules, the activation mechanisms between different non-peptide opioids may not be as well conserved.

The distinct MOPr conformations captured by the PCA appear to reflect the efficacy of the bound ligand. Certainly, the conformation of the helices with norbuprenorphine bound are consistent with the receptor transitioning towards an active-like intermediate state; TM5 moves inwards towards the helix bundle, the intracellular end of TM6 begins to move outwards, along with rearrangements on the extracellular side. In these MD simulations of the MOPr and agonist alone a fully active state of the receptor was not sampled. Multiple structural studies have suggested that the binding of an agonist is insufficient to stabilise a fully active conformation of the GPCR; the binding of an intracellular G protein or mimetic is also required (83, 88, 89, 92, 166, 177). It is therefore unsurprising that we do not achieve a fully active MOPr conformation here.

If the norbuprenorphine-bound MOPr favours an active-like intermediate state, we would predict that the presence of the negative allosteric modulator, sodium, would disrupt this conformation. Indeed, we found in the presence of a sodium ion the binding pose of norbuprenorphine was disrupted such that it assumed the shallower binding position of the lower efficacy ligands. Moreover, the W293$^{6.48}$ rotamer maintained the inactive “vertical” position, and analysis of the helix conformations by PCA showed the receptor remained in the inactive-like conformation stabilised by the lower efficacy ligands, even in the presence of this high efficacy agonist. Experimentally, the modulatory effect of sodium is dependent on the efficacy of the bound ligand (120, 121). In our MD simulations, the binding pose of the low efficacy ligand buprenorphine was unaffected by sodium. Through these divergent effects on high and low efficacy ligands we provide a molecular basis for the negative modulatory action of sodium on MOPr agonists.

Accelerated MD was employed to enhance the sampling by accelerating conformational changes which could not be accessed by conventional MD in the computing timescales available. Overall the aMD corroborated the conventional MD data, resulting in similar binding poses of the ligands and conformations of the receptor helices. Whilst this provided confidence that the conclusions drawn may be relevant to the physiological situation, it also suggested that the sampling by the conventional MD was sufficient to capture these initial ligand-induced changes, therefore negating the use of aMD in further experiments.

4.5 Conclusions

In conclusion, in this chapter I have identified molecular differences between a series of small molecule opioid ligands which correlate with their different intrinsic efficacies. The high efficacy agonist norbuprenorphine favoured an alternative binding pose to its lower efficacy analogues, which allowed norbuprenorphine to engage the W293$^{6.48}$ rotamer toggle switch. Similarly, the high efficacy non-morphinan agonist methadone also promoted the same conformational change in W293$^{6.48}$, whereas the low efficacy ligands did not. Importantly, these differences at the level of individual residues appeared to translate to divergent conformations of the MOPr helices, with the high efficacy agonist-bound receptor occupying a different state to when bound to the low efficacy ligands. These conformational changes on both a residue and domain-level were abolished by the binding of the negative allosteric modulator sodium. Together, these results suggest that small changes in ligand binding pose and residue interactions are extremely important in determining the global conformation of the MOPr and highlight the potential of using this MD technique to understand how opioid drug efficacy is encoded on a molecular level.

Chapter 5: *In vitro* and *in silico* characterisation of biased MOPr peptide agonists

5.1 Introduction

There are on-going efforts to develop G protein-biased MOPr agonists, based on the suggestion that many opioid-induced side effects may be mediated by arrestin-dependent signalling pathways (244-247, 252). However this topic is controversial; in the original studies arrestin-3 knockout mice exhibited enhanced analgesia in response to morphine with a reduced side effect profile (244, 245), whilst a more recent study of phosphorylation-deficient MOPr knock-in mice showed that many opioid-induced side effects were either unchanged or in some cases exacerbated (66). Moreover, opioid-induced respiratory depression appears to be mediated in part by GIRK channel activation (29), which is a G protein response. Clinical trials of one of the first described G protein-biased compounds, oliceridine, showed only modest improvement over morphine (249, 341), whilst the G protein-biased agonist PZM21 still caused respiratory depression in mice (253). Nevertheless, the development of biased tool compounds would be useful in deconvoluting the role of different signalling pathways downstream of the MOPr in mediating various opioid-driven effects.

The molecular mechanism of biased agonism at the MOPr, and indeed any GPCR, is poorly understood. The current consensus is that biased ligands are able to stabilise a distinct receptor state to unbiased or oppositely biased ligands (222, 224, 262, 342, 343). However, the lack of structural data for biased compounds at the MOPr makes this hypothesis difficult to test. Using the same techniques described in Chapter 4, we have used MD simulations of the MOPr bound to biased and unbiased ligands to attempt to determine any molecular signatures which may underlie biased agonism at the MOPr.

As the MOPr is fundamentally a peptide receptor, it is important to investigate structure-activity relationships for peptide ligands as well as small molecules. We selected three peptide MOPr agonists with different bias profiles; DAMGO, endomorphin-2 and bilorphin (Figure 5.1). DAMGO (D-Ala^2, N-MePhe^4, Gly-ol]-

enkephalin, Figure 5.1a), a pentapeptide highly selective for the MOPr, was chosen as the reference full agonist, as it is widely used as the standard agonist that efficiently activates both G protein and arrestin pathways and is generally assumed to be unbiased. Endomorphin-2 (Tyr-Pro-Phe-Phe-NH_2, Figure 5.1b), a tetrapeptide which also has high selectivity for the MOPr, has been previously shown to be arrestin-biased (21, 240), with sub-maximal efficacy for G protein signalling, but exhibiting robust recruitment of arrestin-3 and inducing MOPr internalisation. Recently, a novel G protein-biased selective MOPr agonist, bilorphin, was developed from an Australian estuarine isolate of *Penicillium bilaii* (344). Bilorphin is composed of an unusual alternating stereochemistry of L and D amino acids ([Dmt]-D-Val-Val-D-Phe-NH_2, Figure 5.1c) and is the first example of a G protein-biased MOPr peptide; all other known MOPr peptide agonists induce arrestin recruitment and receptor internalisation (21, 240, 241, 243).

In this chapter, I confirm the expected signalling characteristics of these peptides in BRET assays for G_i activation and arrestin-3 recruitment. I perform molecular docking and MD simulations of the peptide-MOPr complexes to identify any differences in the binding pose and receptor conformation of the bilorphin-bound receptor compared to that with endomorphin-2 which may reveal a molecular mechanism of biased agonism at the MOPr. I find that bilorphin adopts a distinct binding pose from endomorphin-2 and DAMGO, notably without interaction with the extracellular loops, and induces the MOPr to sample a different cluster of conformations from the endomorphin-2-bound receptor. The *in silico* work described in this chapter was included in the paper reporting the discovery of bilorphin, published in the Proceedings of the National Academy of Sciences of the United States of America (PNAS) (DOI: 10.1073/pnas.1908662116) (344).

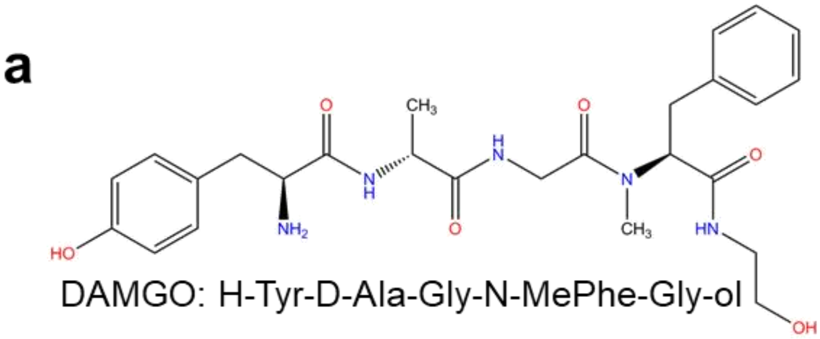

DAMGO: H-Tyr-D-Ala-Gly-N-MePhe-Gly-ol

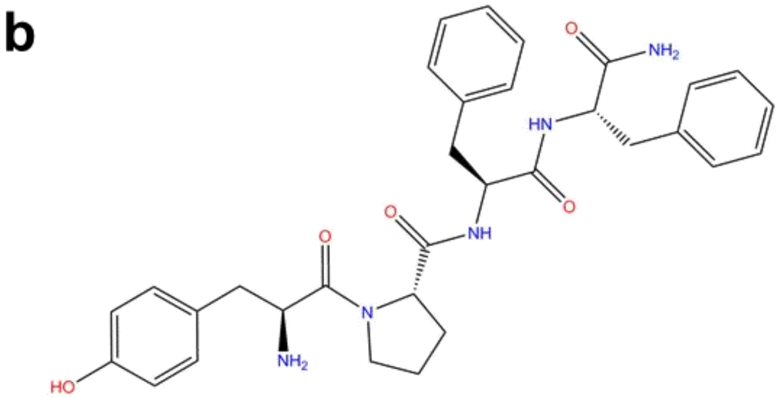

Endomorphin-2: H-Tyr-Pro-Phe-Phe-NH_2

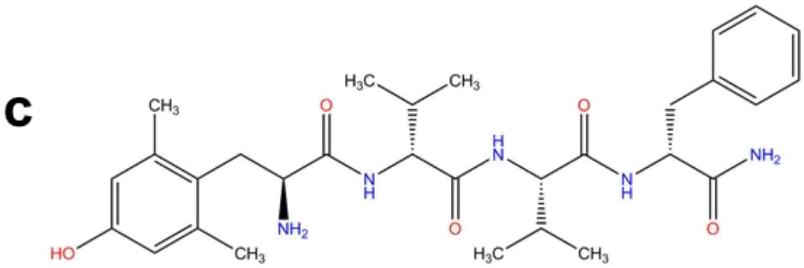

Bilorphin: H-(2,6-dimethyl-L-Tyr)-D-Val-Val-D-Phe-NH_2

Figure 5.1 Structures of the peptide ligands

2D structures of the peptide ligands used in this chapter; a) DAMGO, b) endomorphin-2, and c) bilorphin.

5.2 Materials & Methods

5.2.1 BRET assays

BRET assays for G_i activation and arrestin-3 recruitment were performed as described in Chapter 2 Section 2.2.4. For the arrestin assay, the $BRET^2$ configuration was used to measure arrestin-3 recruitment in HEK 293 cells expressing human MOPr-RlucII and arrestin-3-GFP.

Data analysis and curve fitting was performed in GraphPad Prism v7. For the G_i activation assay, BRET ratios were expressed as the percentage decrease from vehicle-treated control wells. For the arrestin-3 recruitment assays, data were expressed as the BRET ratio minus background from vehicle-treated control wells. Data were then fitted to log concentration – response curves with a Hill Slope of 1.0, and the minimum constrained to zero. The EC_{50} and maximum response (E_{Max}) values for each peptide were compared to DAMGO using one-way ANOVA with Dunnett's post-test.

Bias calculations were performed using the Black and Leff operational model to estimate log τ/K_A values for each agonist at each pathway (201, 314, 315), as detailed in Chapter 2 Section 2.2.5. DAMGO and endomorphin-2 were treated as full agonists, as the maximum response of these ligands were not significantly different (see Section 5.3.1), and bilorphin as a partial agonist in both assays. As suggested by *van der Westhuizen et al., (315),* the E_{max} values for each pathway were constrained to the maximum response of DAMGO, given in Table 5.1. DAMGO was the reference ligand. The resulting bias factors were compared by one-way ANOVA with Tukey's post-test.

5.2.2 Molecular modelling

Conformer generation of these highly flexible ligands and molecular docking with BUDE was carried out as detailed in Chapter 2 Section 2.1.3. Endomorphin-2 can exist as two isomers; with the Tyr^1-Pro^2 bond in the *trans* conformation or in the *cis* conformation (refer to Chapter 2 Figure 2.3). There are conflicting reports in the literature as to which is the bioactive conformation of endomorphin-2 (294-298, 345). I therefore performed molecular docking and molecular dynamics simulations with both isomers.

For DAMGO and bilorphin, this process yielded a single converged pose to be taken forward into MD simulations. These initial docked poses for DAMGO and bilorphin are shown in Figure 5.2.

For endomorphin-2, after docking to the MOPr using BUDE, 4 clusters of binding poses were found to be energetically favourable and meet the amine-D147$^{3.32}$ distance constraint; *cis* endomorphin-2 with Tyr^{1} orientated towards the intracellular side of the membrane (“Cis #1”; Figure 5.3a), *cis* endomorphin-2 with Tyr^{1} orientated towards the extracellular side of the membrane (“Cis #2”; Figure 5.3b), *trans* endomorphin-2 with Tyr^{1} orientated towards the extracellular side of the membrane (“Trans #1”; Figure 5.3c), and *trans* endomorphin-2 with Tyr^{1} orientated towards the intracellular side of the membrane (“Trans #2”; Figure 5.3d). Of these, Cis #1 and Trans #1 were the most populated clusters; representing 90 % and 88 % of each isomer’s 50 lowest energy poses, respectively. A 125 ns simulation of the MOPr bound to endomorphin-2 in each of these 4 poses was run and the final binding poses analysed to decide which endomorphin-2 conformation and binding pose to use in further simulations (Figure 5.3). All four conformers maintained the salt bridge with D147$^{3.32}$. However, only Cis #1 (Figure 5.3a) and Trans #2 (Figure 5.3d) were orientated such that the phenol group could interact with another important opioid binding residue, H297$^{6.52}$. RMSD calculations performed on the ligand showed that Cis #1 switched between two binding positions due to flexibility in Phe^{4} (inset, Figure 5.3a). Aside from this Phe^{4} flexibility, Cis#1, Cis #2 (Figure 5.3b) and Trans #2 (Figure 5.3d) were relatively stable in their binding positions, whereas Trans #1 deviated from its docked position markedly and failed to become stable during the 125 ns simulation time (Figure 5.3c). I therefore selected the Cis #1 conformer (Figure 5.3a) to use in further MD simulations, as it showed the most favourable ligand-residue interactions (over Cis #2 and Trans #1), had the lowest energy binding pose which was stable over the 125 ns simulation, and the most populated cluster from the BUDE docking procedure (over Trans #2).

After selecting the best docked poses for DAMGO, bilorphin and endomorphin-2, 1 µs MD simulations of all 3 membrane-embedded peptide-MOPr complexes were performed as described in Chapter 2 Section 2.1.5.

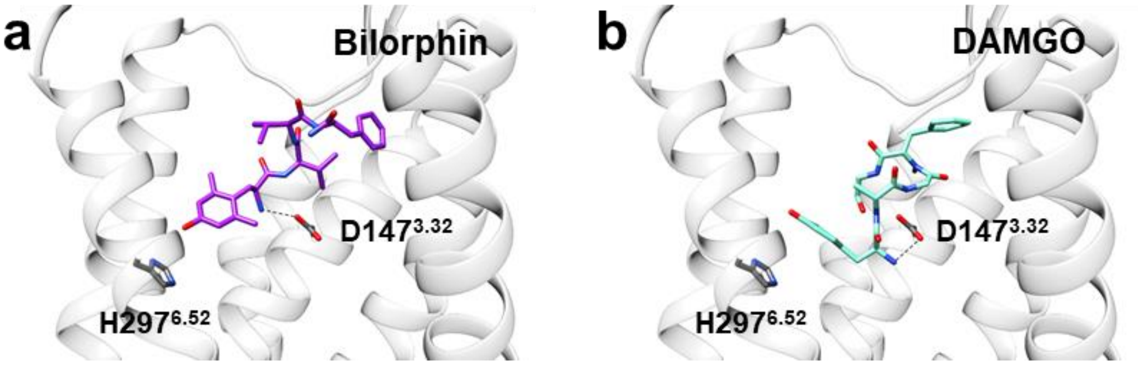

Figure 5.2 Initial docked poses of bilorphin and DAMGO

10,000 conformers of each peptide were docked using BUDE as outlined in Chapter 2 Section 2.1.3. The pose selected for MD simulations is shown above for a) bilorphin, and b) DAMGO.

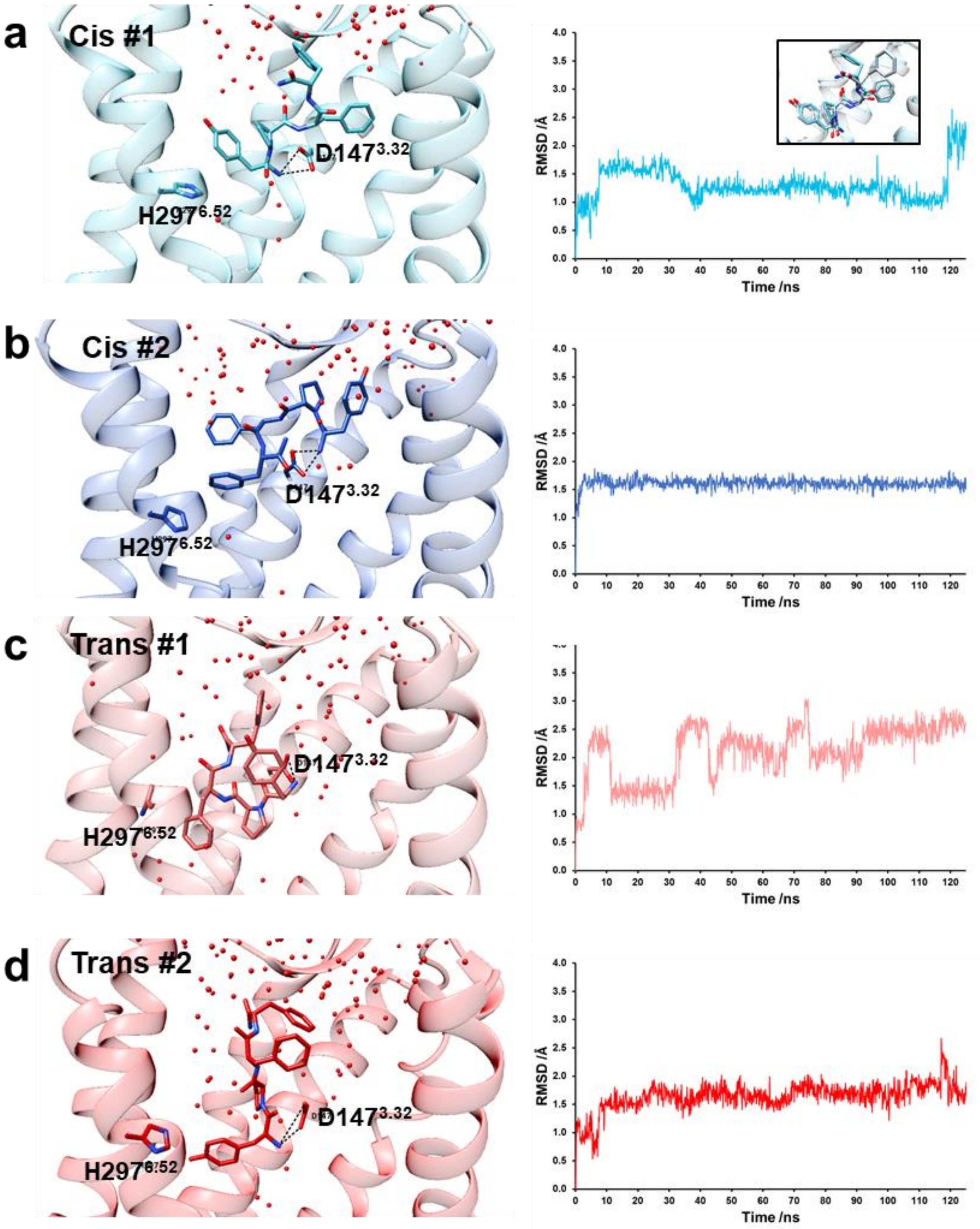

Figure 5.3 Final binding poses of the endomorphin-2 isomers after 125 ns MD simulations
10,000 conformers of a, b) *cis*-endomorphin-2 and c, d) *trans*-endomorphin-2 were docked using BUDE as outlined in Chapter 2 Section 2.1.3. Two poses of each isomer were selected for short 125 ns MD simulations to assess stability of the binding pose. For each pose, RMSD calculations were performed on the heavy atoms of the ligand compared to the atom positions in the first frame of the simulation, displayed in the right-hand panel of each figure. The inset in a) shows the flexibility of the Phe^4 side chain.

5.3 Results

5.3.1 Ligand-induced G protein activation and arrestin recruitment

BRET assays for G_i activation and arrestin-3 recruitment were performed with endomorphin-2 and bilorphin, with DAMGO as the reference ligand, to determine the signalling characteristics of these agonists and whether any bias could be detected.

Figure 5.4a shows concentration-response curves for each ligand in activating the G_i G protein. The maximum response for endomorphin-2 was not significantly different from DAMGO, making both peptides full agonists in this assay. In contrast, bilorphin was a partial agonist, reaching an E_{max} 79 % of the DAMGO response (Table 5.1). DAMGO had an EC_{50} of 0.4 ± 0.2 µM, whilst both the endomorphin-2 and bilorphin curves were right-shifted compared to DAMGO, with an EC_{50} of 0.8 ± 0.2 µM and 1.6 ± 0.6 µM, respectively (Table 5.1).

In the arrestin-3 recruitment assay (Figure 5.4b), both DAMGO and endomorphin-2 were full agonists, with similar micromolar EC_{50}s (Table 5.1). Bilorphin produced a much lower response in the arrestin-3 assay, with an E_{max} only 24 % of that elicited by DAMGO (Table 5.1). Compared to the G protein assay, DAMGO was approximately 12-fold less potent at recruiting arrestin-3 than activating G_i. Bilorphin was approximately 4-fold less potent in the arrestin assay, though this was accompanied with a lower maximum response. On the other hand, endomorphin-2 was only 2-fold less potent in the arrestin-3 assay, with a maximum response equal to that of DAMGO.

5.3.2 Bias calculations

Comparison of transduction ratios, as a quantification of the efficiency of an agonist to activate a particular signalling pathway, is a widely accepted method to characterise biased agonism from concentration-response data (201, 258, 346). Accordingly, the baseline-corrected concentration-response data in Figures 5.4a and 5.4b were fit to the Black and Leff operational model of agonism to estimate the transduction ratio (log τ/K_A) for each ligand in the G_i activation assay and the arrestin-3 recruitment assay (Table 5.2) (201, 314, 315). To remove any influence of system or observational bias, Δ log τ/K_A values for endomorphin-2 and bilorphin were calculated for each assay by subtracting the corresponding DAMGO value. Ligand bias was expressed as the difference in these DAMGO-subtracted transduction ratios at the G_i activation versus arrestin-3 pathways. The resulting bias factors are plotted in Figure 5.4c. As the reference balanced agonist, DAMGO by definition has a bias factor of zero, ligands biased towards G_i activation would have a bias factor greater than zero, whilst ligands biased towards arrestin-3 recruitment would have a bias factor less than zero.

Endomorphin-2 showed bias towards arrestin-3 recruitment over activation of G_i, a finding which is consistent with the previously reported bias profile of this peptide (240). In contrast, bilorphin displayed bias towards G_i activation over arrestin-3 recruitment, as reported by *Dekan et al.,* (344). The calculated bias factors for endomorphin-2 and bilorphin were significantly different between these oppositely biased peptides ($p < 0.05$, one-way ANOVA, Tukey's post-test).

Although neither of the bias factors for endomorphin-2 nor bilorphin were statistically different from the reference agonist DAMGO, looking at the concentration-response curves in Figures 5.4a and 5.4b, for endomorphin-2 there is a clear change in the order of potency between the G_i activation assay and the arrestin-3 recruitment assay. Endomorphin-2 is right shifted compared to DAMGO for G_i activation, but the curves overlie for arrestin-3 recruitment. In general, MOPr agonists activate Gi with greater potency than they recruit arrestin-3 (21, 243, 258). This lower fold change in endomorphin-2's potency for G_i versus arrestin pathways, along with the calculated bias factor trending towards arrestin recruitment, indicates that endomorphin-2 is arrestin-biased.

The relatively large error in estimating EC_{50} values for low efficacy ligands, such as bilorphin, combined with error terms being propagated through multiple calculations when quantifying ligand bias, makes determining accurate bias factors for partial agonists difficult (258). The low response of bilorphin in the arrestin-3 recruitment assay therefore makes determining whether bilorphin is truly G protein-biased, or in fact a low efficacy partial agonist, challenging. However, experiments performed by our collaborators showed that bilorphin is biased towards G protein activation (344).

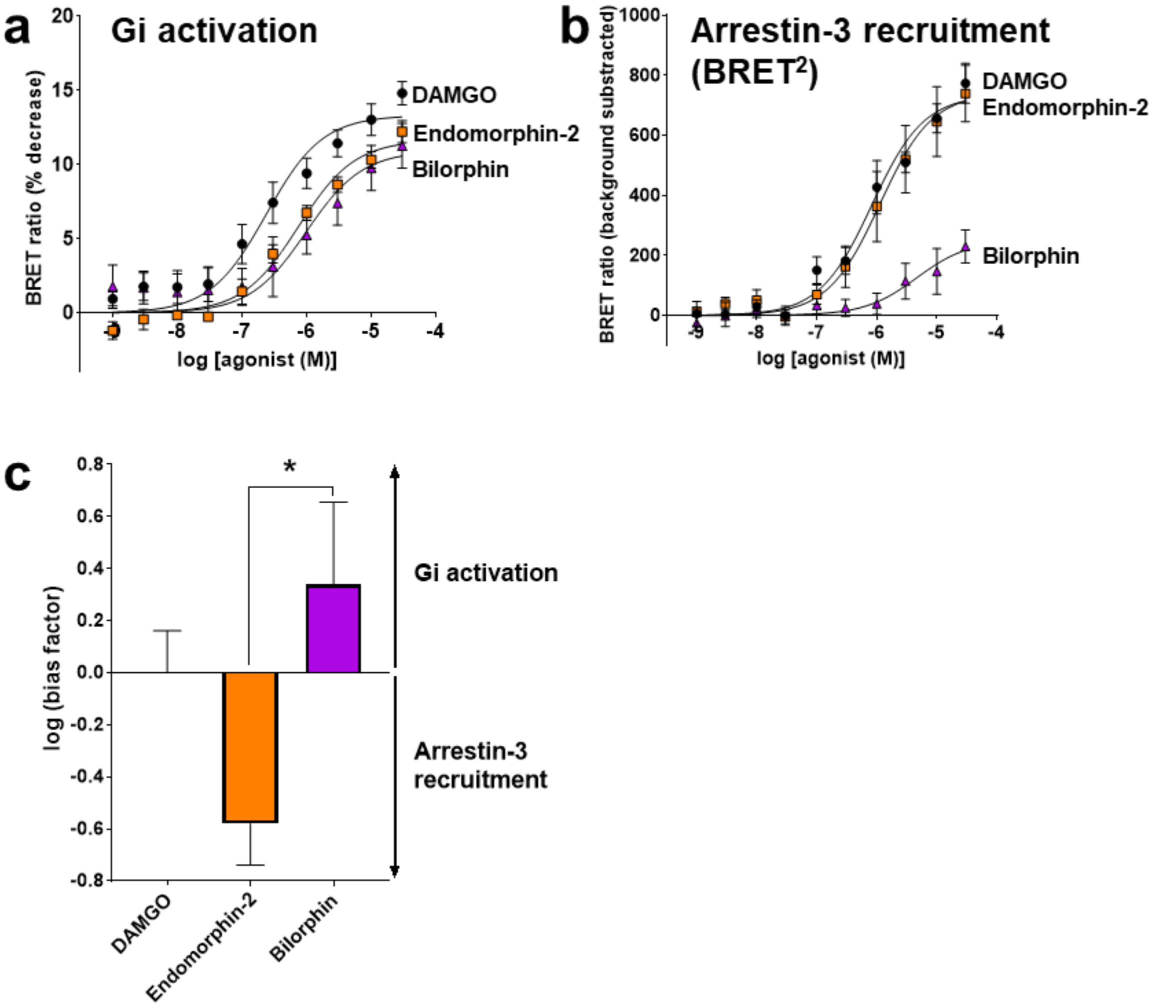

Figure 5.4 Ligand-induced G protein activation and arrestin recruitment

a) In HEK 293 cells expressing HA-MOPr, Gαi-RLucII and Gγ-GFP, DAMGO (black circles), endomorphin-2 (orange squares) and bilorphin (purple triangles) induced concentration-dependent activation of G_i, measured as a decrease in the BRET signal. b) In HEK 293 cells expressing MOPr-RLucII and arrestin-3-GFP, DAMGO (black circles) and endomorphin-2 (orange squares) induced concentration-dependent recruitment of arrestin-3 to the MOPr, measured as an increase in the BRET signal. Bilorphin (purple triangles) induced a much lower response. c) Calculated bias factors for endomorphin-2 (orange) and bilorphin (purple), using DAMGO as the reference balanced ligand. * $p < 0.05$, one-way ANOVA with Tukey's post-test. All data are expressed as mean ± SEM of 5 independent experiments.

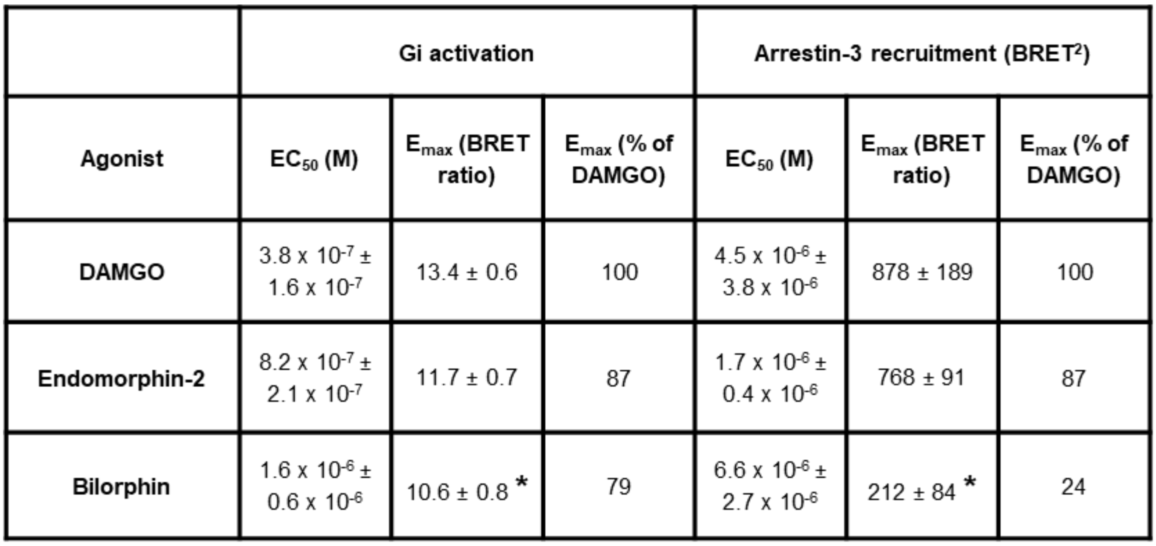

	Gi activation			Arrestin-3 recruitment ($BRET^2$)		
Agonist	EC_{50} (M)	E_{max} (BRET ratio)	E_{max} (% of DAMGO)	EC_{50} (M)	E_{max} (BRET ratio)	E_{max} (% of DAMGO)
DAMGO	$3.8 \times 10^{-7} \pm 1.6 \times 10^{-7}$	13.4 ± 0.6	100	$4.5 \times 10^{-6} \pm 3.8 \times 10^{-6}$	878 ± 189	100
Endomorphin-2	$8.2 \times 10^{-7} \pm 2.1 \times 10^{-7}$	11.7 ± 0.7	87	$1.7 \times 10^{-6} \pm 0.4 \times 10^{-6}$	768 ± 91	87
Bilorphin	$1.6 \times 10^{-6} \pm 0.6 \times 10^{-6}$	10.6 ± 0.8 *	79	$6.6 \times 10^{-6} \pm 2.7 \times 10^{-6}$	212 ± 84 *	24

Table 5.1 EC_{50} and maximum response values for DAMGO, endomorphin-2 and bilorphin in the G_i activation and arrestin-3 recruitment assays

Data are expressed as mean ± SEM, of 5 independent experiments. * $p < 0.05$, significantly different from the respective DAMGO value (one-way ANOVA with post-hoc Dunnett's test).

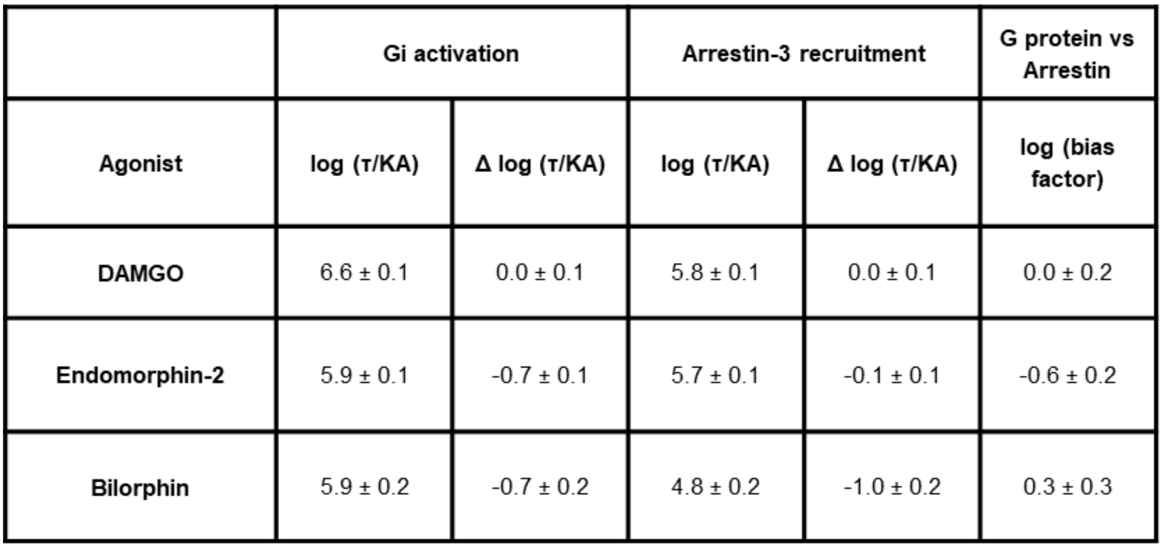

	Gi activation		Arrestin-3 recruitment		G protein vs Arrestin
Agonist	log (τ/KA)	Δ log (τ/KA)	log (τ/KA)	Δ log (τ/KA)	log (bias factor)
DAMGO	6.6 ± 0.1	0.0 ± 0.1	5.8 ± 0.1	0.0 ± 0.1	0.0 ± 0.2
Endomorphin-2	5.9 ± 0.1	-0.7 ± 0.1	5.7 ± 0.1	-0.1 ± 0.1	-0.6 ± 0.2
Bilorphin	5.9 ± 0.2	-0.7 ± 0.2	4.8 ± 0.2	-1.0 ± 0.2	0.3 ± 0.3

Table 5.2 Bias calculations for endomorphin-2 and bilorphin

DAMGO was used as the reference balanced full agonist. Data are expressed as mean ± SEM.

5.3.3 Peptide binding poses and residue interactions

After docking and selection of the best initial binding poses, 1 µs of MD data was collected for each peptide-MOPr complex. RMSD calculations (Figure 5.5) for the ligand and the MOPr helices were performed to determine how far each peptide deviated from its initial docked position, how stable the final binding pose was, and the deviation of the receptor helices from the inactive crystal structure.

For all peptide-MOPr complexes, the RMSD plots performed on the MOPr transmembrane domains quickly reached a plateau at approximately 1 Å. All 3 peptides remained bound to the orthosteric site during the simulation time, with only small deviations from the initial docked poses. Both bilorphin (Figure 5.5a) and DAMGO (Figure 5.5c) were stable in their binding poses, only shifting from the initial docked positions by approximately 2 Å. In contrast, the binding pose of endomorphin-2 appeared less stable (Figure 5.5b). However, the fluctuation in the RMSD plot can be attributed to the flexibility of the final C terminal Phe^4, as was also observed in the initial short simulations (see Section 5.2.2). The aromatic group of Phe^4 switched between 3 main positions, shown in the inset in Figure 5.5b.

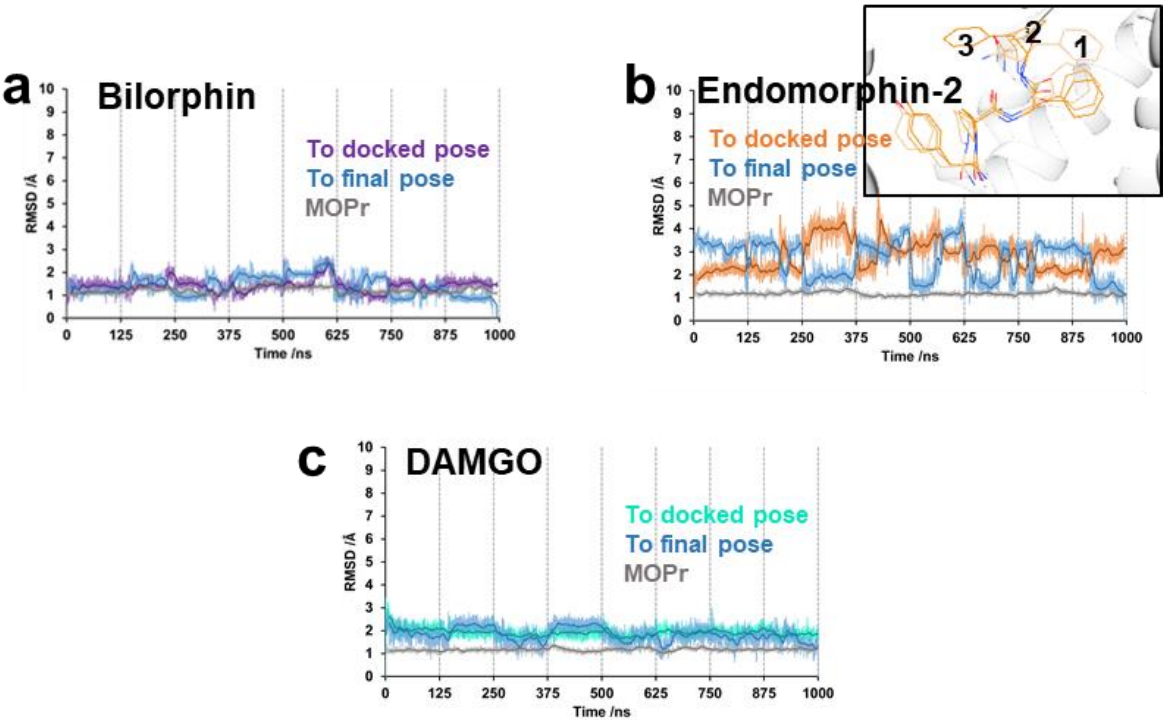

Figure 5.5 RMSD plots for the peptide ligand-MOPr complexes

a) RMSD calculations performed on the heavy atoms of bilorphin compared to the initial docked position (purple) or the final binding pose (light blue). b) RMSD calculations performed on the heavy atoms of endomorphin-2 compared to the initial docked position (orange) or the final binding pose (light blue). c) RMSD calculations performed on the heavy atoms of DAMGO compared to the initial docked position (turquoise) or the final binding pose (light blue).

RMSD calculations were also performed on the alpha carbons of the MOPr transmembrane domains, compared to the first frame of the MD simulation (light grey in each plot).

Inset in b): fluctuations of Phe^4 in endomorphin-2 during the MD simulation showing 3 different positions of Phe^4.

Data expressed as raw values (faded line) and moving average over 100 frames (10 ns) (bold line).

The final binding poses of each peptide are shown in Figure 5.6, and the ligand-residue interaction plots in Figure 5.7.

As these compounds are peptides, and therefore larger than the small molecule opioids studied in Chapter 4, they interacted with an extended binding site, contacting residues in the morphinan binding pocket as well as residues closer to the extracellular side of the receptor. In the morphinan binding site, all three peptides maintained interactions with residues on TM3 and TM6, including D147$^{3.32}$, Y148$^{3.33}$, N150$^{3.35}$, M151$^{3.36}$, W293$^{6.48}$, I296$^{6.51}$, H297$^{6.52}$ and V300$^{6.55}$, similar to the small molecule morphinan ligands (see Chapter 4 Section 4.3.2). Whilst all three peptides interacted with the essential opioid binding residue H297$^{6.52}$ via the N terminal phenol group, bilorphin was the only ligand to alternate between a direct interaction with this residue and hydrogen bonding via a bridging water molecule. The canonical amine-D147$^{3.32}$ salt bridge was strongly conserved for all three peptides throughout the simulation.

The ligand-residue interactions within this morphinan binding pocket were very similar for DAMGO, endomorphin-2 and bilorphin. However, these peptides differed in their interactions with the extended binding site. Both endomorphin-2 (Figure 5.6b) and DAMGO (Figure 5.6c) bound with the Tyr^{1} orientated to stack with His297$^{6.52}$ and the rest of the peptide backbone extending out towards the extracellular loops, contacting W133^{ECL1} in ECL1 and C217^{ECL2}, T218^{ECL2} and L219^{ECL2} in ECL2 (Figures 5.7b and 5.7c). In contrast, the tetrapeptide backbone of bilorphin extended towards the other side of the MOPr binding pocket, accessing an alternative binding site near TM1 and interacting with Y75$^{1.39}$. Strikingly, the interactions with the extracellular loops observed for DAMGO and endomorphin-2 were absent for this G protein-biased peptide. These differences in the orientation of the peptides is clearer when viewing the binding pocket from the extracellular side of the membrane (Figure 5.6d). The C terminal residues of DAMGO and endomorphin-2 are positioned to the left of the binding pocket, whereas bilorphin is positioned towards the right.

Moreover, the conformation of the microswitch, W293$^{6.48}$, differed between these peptides. The conformation of W293$^{6.48}$ is plotted as the χ2 dihedral in Figure 5.8. For the high efficacy agonist DAMGO, W293$^{6.48}$ adopted the “horizontal” conformation (Figure 5.8c), consistent with the other high efficacy ligands, norbuprenorphine and methadone, studied in Chapter 4. Endomorphin-2 and bilorphin both exhibit lower potency for G protein signalling than DAMGO (Section 5.3.1). With these lower efficacy peptides bound, the W293$^{6.48}$ rotamer favours the “vertical” conformation (Figures 5.8a and 5.8b) with the endomorphin-2-MOPr complex only engaging the W293$^{6.48}$ toggle switch once during the 1 μs simulation time, and bilorphin not at all.

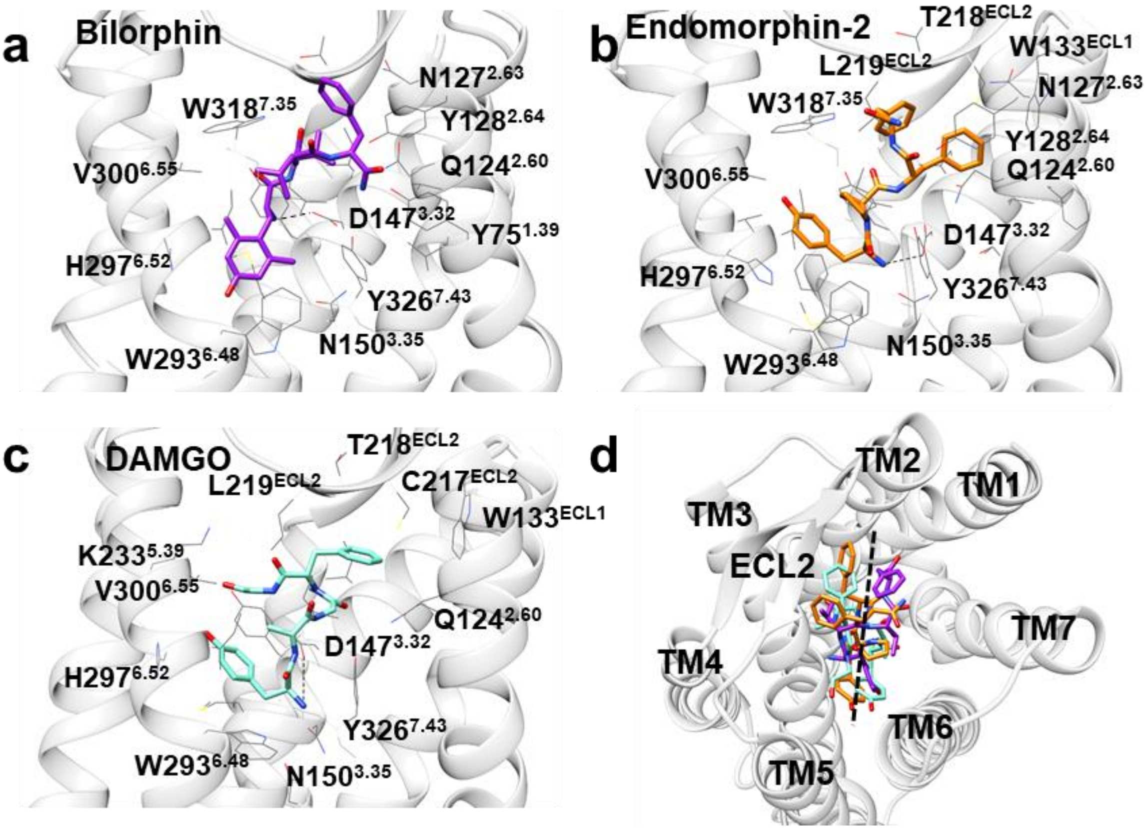

Figure 5.6 Final binding poses for the peptides

Final binding poses of the peptide ligands in the MOPr orthosteric site after 1 µs MD simulations. The MOPr helices are shown in light grey, with residues forming the ligand binding site as sticks. a) bilorphin is depicted in purple, b) endomorphin-2 depicted in orange, and c) DAMGO depicted in turquoise. d) Overlaid view of the three peptides in the orthosteric pocket, viewed from the extracellular side of the membrane. The peptides bind on opposite sides of the black dotted line; DAMGO (turquoise) and endomorphin-2 (orange) sit closer to ECL2, than bilorphin (purple) which binds closer to TM1 and 7.

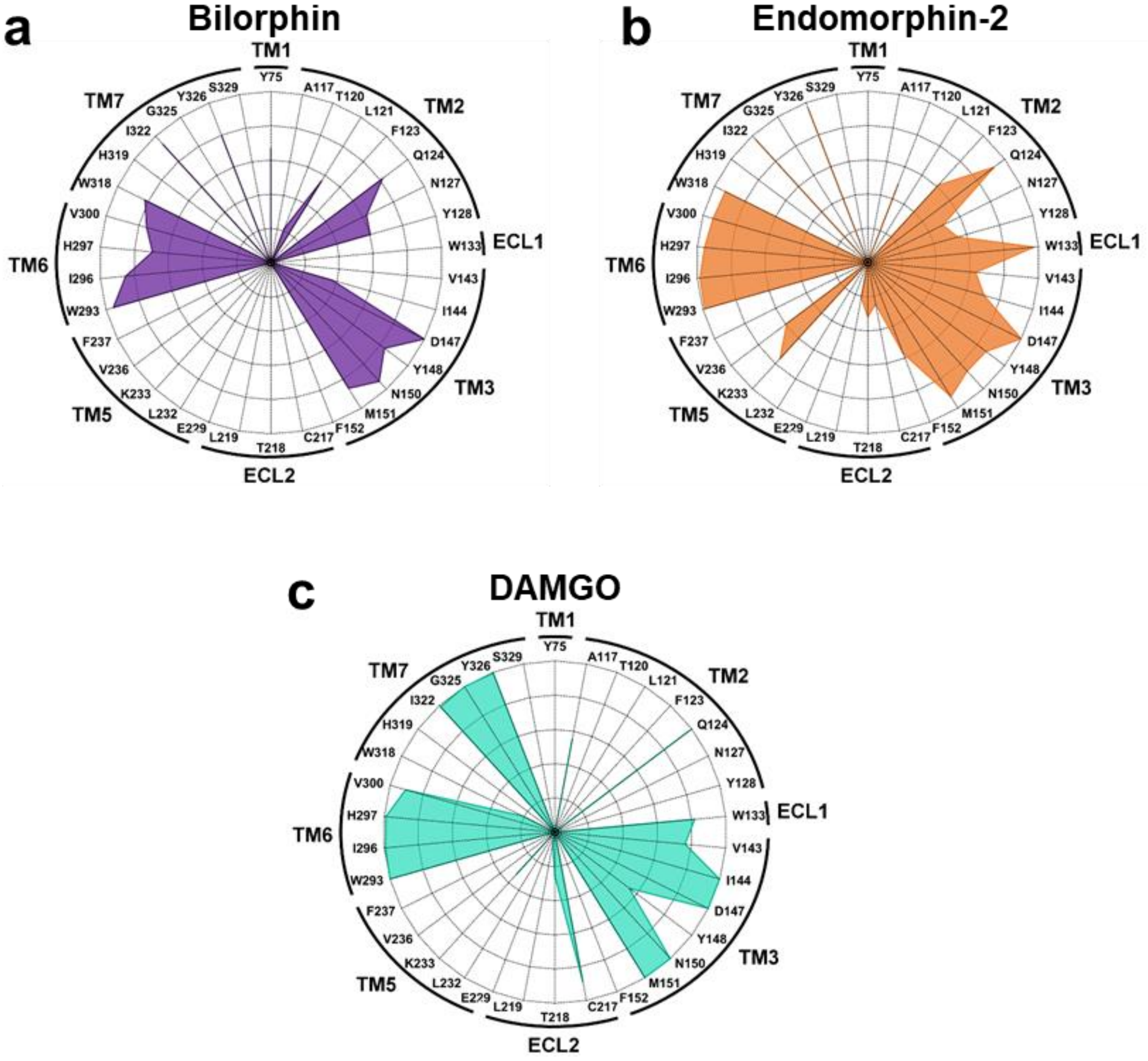

Figure 5.7 Ligand-residue interactions for the peptide ligand-MOPr complexes

a) Bilorphin, b) endomorphin-2, and c) DAMGO. Ligand-residue interactions are expressed as the percentage of simulation time each residue is within 4.5 Å of the ligand, with points radiating outwards from 0 to 100 % in 20 % increments.

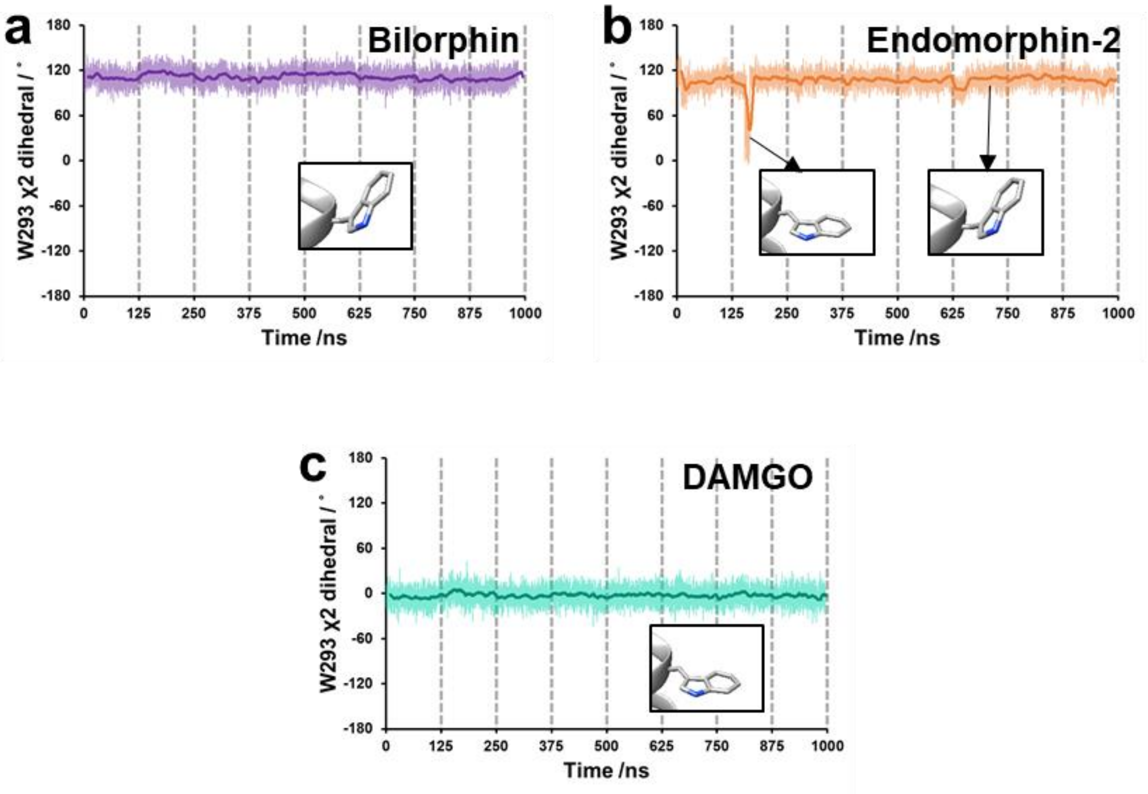

Figure 5.8 W293$^{6.48}$ rotamer toggle switch

The behaviour of the W293$^{6.48}$ rotamer toggle switch plotted as the χ2 dihedral angle over during 1 μs MD simulations of the MOPr bound to a) bilorphin, b) endomorphin-2, and c) DAMGO. Insets show how the dihedral angle relates to the conformation of the indole ring. Data expressed as raw values (faded line) and moving average over 100 frames (10 ns) (bold line).

5.3.4 Biased peptides stabilise distinct conformations of the MOPr

The conformational changes in the receptor transmembrane helices induced by the arrestin-biased peptide, endomorphin-2, or the G protein-biased peptide, bilorphin, were examined by principal component analysis. As described in Chapter 2 Section 2.1.7, after fitting to remove global rotation and translation of the system, the covariance matrix was generated using the alpha carbons of the receptor helices. The conformation of the MOPr at each time point was projected onto principal components (PC) 1 and 2 and plotted in Figure 5.9a. PC1 and PC2 accounted for 28.9 % and 10.9 % of the variance, respectively. PC2 described helix conformations common between the peptide-MOPr complexes, but in terms of PC1 the bilorphin-bound receptor clustered differently to the endomorphin-2-bound receptor. A pseudo-trajectory of PC1 was extracted to visualise these differences. As depicted in Figure 5.9b, PC1 primarily described alternative conformations in the extracellular region of the receptor close to the orthosteric binding site, and to a lesser extent differences in the intracellular portions of the helices. With bilorphin bound, there was a bulging of the middle portion of TM1 and a shift outward from the helix bundle, relative to the endomorphin-2-bound receptor. This movement of TM1 allowed bilorphin to occupy the alternative extended binding site (Section 5.3.3). There were also substantial movements of the extracellular ends of TMs 2, 6 and 7, and a kink formed in TM4 allowed the extracellular part of this helix to move towards TM3 with endomorphin-2 bound. A smaller movement of TM3 towards TM2 in the endomorphin-2-bound receptor, whereby M151$^{3.36}$ shifted ~1.7 Å from its initial position, is in agreement with the active conformation of TM3 observed in the agonist-bound crystal structure (22). On the intracellular side of the MOPr, PC1 described inward movements of TMs 5, 6 and 7 with endomorphin-2 bound, compared to the bilorphin-bound MOPr.

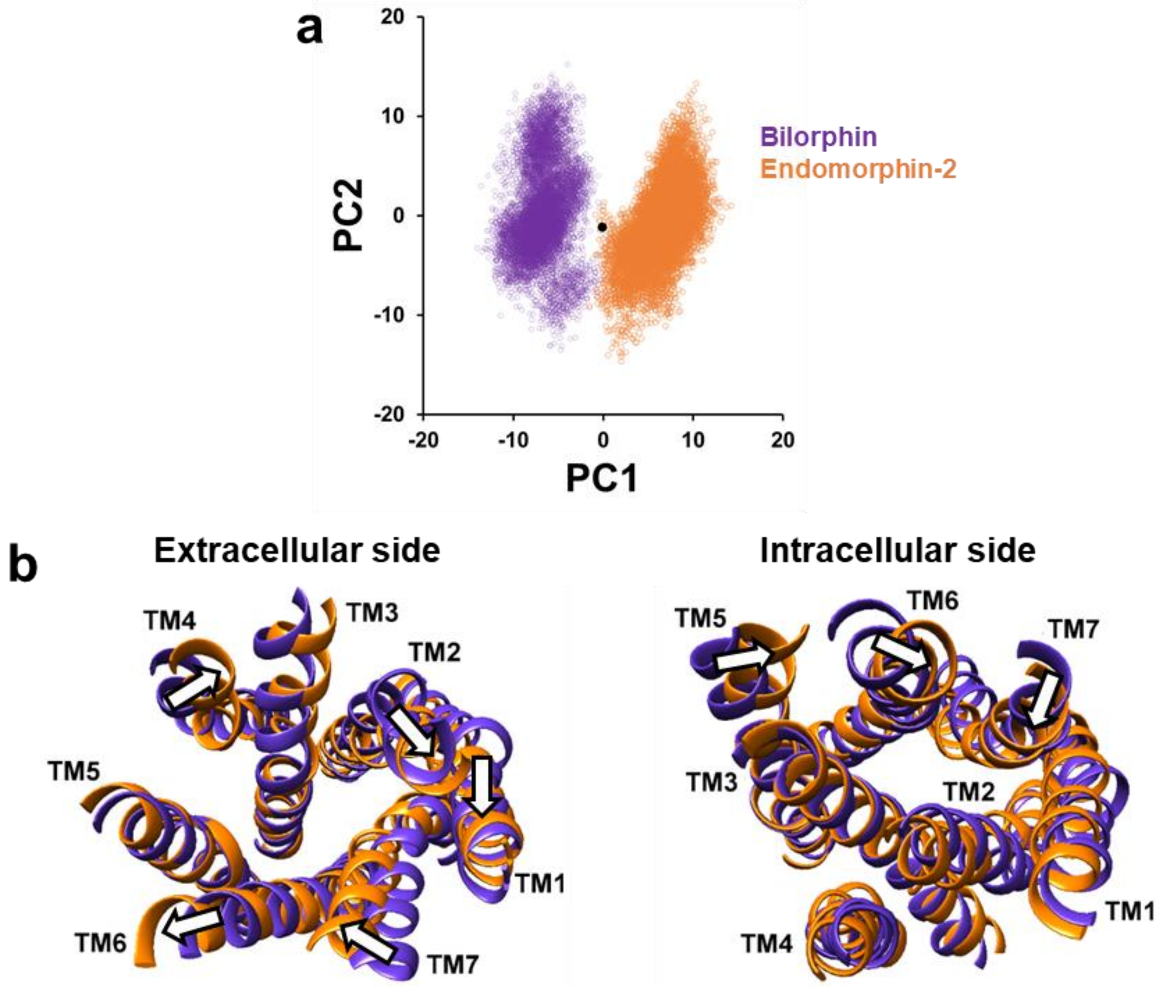

Figure 5.9 Principal component analysis reveals distinct MOPr conformations

a) Principal component analysis was performed on the alpha carbons of the receptor transmembrane domains, before projecting the receptor conformations at each simulation time point onto PC1 and PC2. The bilorphin-MOPr complex is in purple, the endomorphin-2-MOPr complex in orange, and the black point indicates the conformation of the inactive MOPr model.

b) Extracted structures representing the extremes of PC1 demonstrate the conformational differences between the bilorphin-MOPr complex (purple) and the endomorphin-2-MOPr complex (orange). Loops have been removed from the image to depict only the part of the receptor the principal component analysis was performed on. White arrows indicate conformational changes in the helices moving from bilorphin-bound to endomorphin-2-bound MOPr.

5.3.5 Molecular modelling of the DAMGO-MOPr complex agrees with the cryo-electron microscopy resolved structure

The molecular modelling data presented in this chapter was performed prior to the release of the cryo-electron microscopy structure of the MOPr-G_i complex bound to DAMGO (23). We used Chimera (293) to superimpose our final structure of the DAMGO-MOPr complex after 1 µs MD simulation onto the cryo-electron microscopy resolved receptor. Using all 281 Cα atoms in common, the RMSD between our MD model and the structure resolved by *Koehl et al.,* was 3.30 Å. This was largely due to the outward movement of TM6 in the cryo-electron structure which we did not capture in our MD simulations in the absence of a G protein, as with this helix removed from the analysis, the RMSD between the resolved structure and our model decreased to 2.1 Å.

The position of DAMGO itself was very similar in the resolved structure (Figure 5.10a) and our model (Figure 5.10b). *Koehl et al.,* reported poor resolution of the C terminal portion of DAMGO and high flexibility of this region in an MD simulation. With this flexible C terminal ethanolamine omitted, the RMSD between all heavy atoms of DAMGO in the cryo-electron microscopy structure and in our final pose after 1 µs MD was 2.83 Å. Due to the high degree of similarity between our predicted binding pose for DAMGO and that resolved by cryo-electron microscopy, the ligand-residue interactions in the resolved structure and in our model are near identical (Figure 5.10c). This includes interactions with residues in TM3, TM6, TM7 and the extracellular loops.

Additionally, the conformation of W293$^{6.48}$ in the newly resolved structure showed the indole ring in the “horizontal” position, predicted by our MD simulations (Figures 5.10a and 5.10b).

Overall, this provides excellent validation of our docking and MD strategy for not only DAMGO, but also the other peptides studied in this chapter, with the ligand-residue interactions we report here likely to be relevant to that occurring *in vivo*.

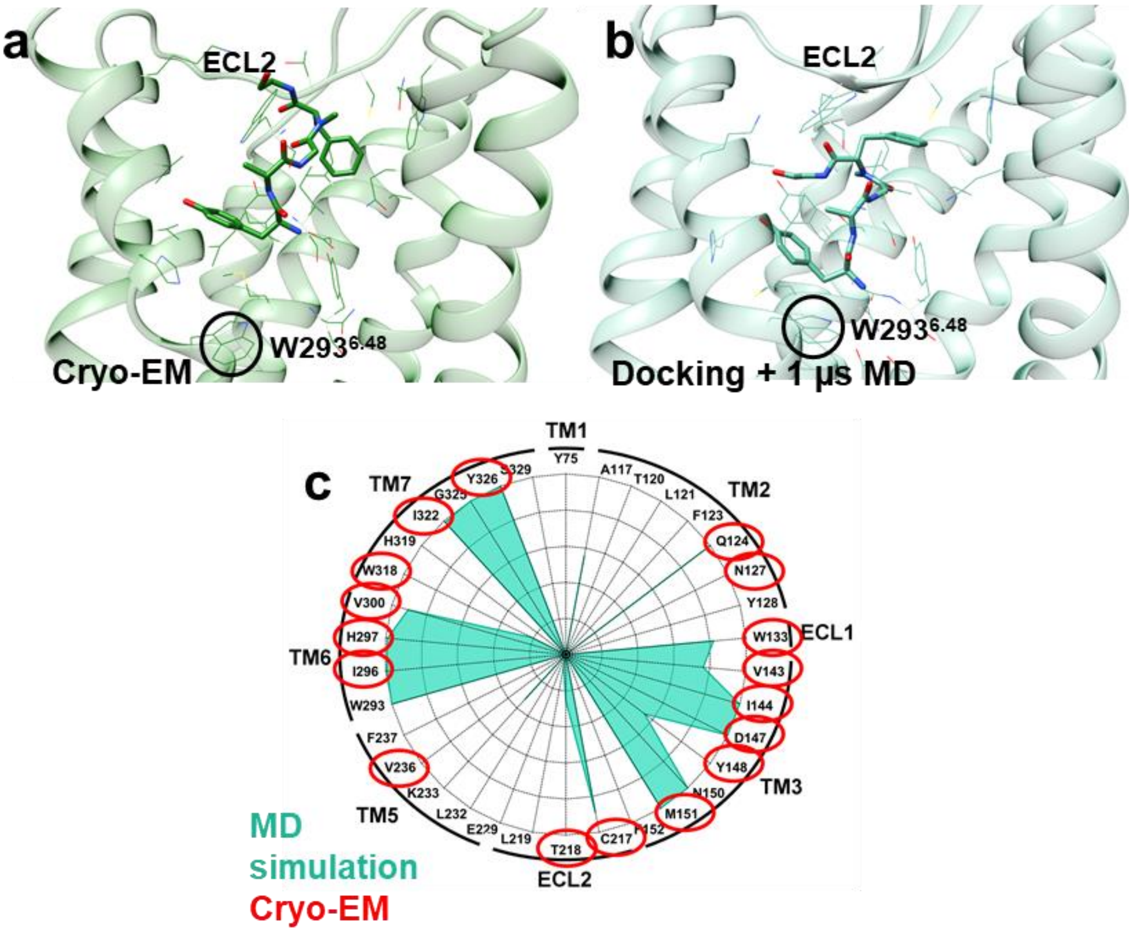

Figure 5.10 Comparison of the DAMGO-MOPr cryo-electron microscopy resolved structure with our DAMGO-MOPr model

a) The binding pose of DAMGO in the cryo-electron microscopy structure of the DAMGO-MOPr-G_i complex. b) The final binding pose of DAMGO after docking and 1 µs MD simulations. Extracellular loop 2 (ECL2) and the conformation of the W293$^{6.48}$ rotamer toggle switch are highlighted in both structures. c) The ligand-residue interactions in our modelled structure and the cryoEM structure are near identical; ligand-residue contacts identified in the MD simulation are shown in the turquoise radial plot (refer to Figure 5.7c) and those within the same distance cut-off in the cryo-electron microscopy structure are circled in red.

5.4 Discussion

In BRET assays for G_i activation and arrestin-3 recruitment, using DAMGO as the reference ligand, endomorphin-2 and bilorphin exhibited signalling properties in line with previous reports (21, 240, 344). Endomorphin-2 was a full agonist in both assays and biased towards arrestin-3 recruitment. In contrast, bilorphin was a partial agonist in both assays, with a markedly reduced ability to recruit arrestin-3, compared to endomorphin-2 and DAMGO. Whilst it is difficult to accurately determine bias factors for partial agonists using the transduction ratio method employed here, the bias factors calculated for bilorphin and endomorphin-2 are significantly different, indicating these peptides are oppositely biased. Moreover, *Dekan et al.,* used an alternative method to quantify bias by comparing E_{max} values in a system where all ligands behaved as partial agonists by inactivating a portion of available receptors. Under these conditions, bilorphin was biased towards G protein-mediated signalling over that initiated by arrestin recruitment (344).

MD simulations of the peptide-MOPr complexes revealed notable differences in how these peptides interact with the MOPr orthosteric site. Specifically, DAMGO and endomorphin-2 engaged an extended binding site, contacting residues in ECL1 and ECL2, whereas the C terminal residues of bilorphin occupied the opposite side of the MOPr pocket and did not interact with the extracellular loops. Interaction with a conserved hydrophobic residue in ECL2 ($L219^{ECL2}$ in the MOPr) has been proposed to dictate arrestin coupling and ligand residence time in 5HT receptors and other aminergic GPCRs (186, 187). ECL2 has been proposed to act as a “lid” in adenosine and muscarinic receptors, whereby upon ligand binding ECL2 closes over the orthosteric pocket (181, 182), which may stabilise the ligand in the binding site and hence increase residence time. Moreover, ligand residence time appears to correlate with efficacy in arrestin-mediated signalling for MOPr agonists (347). In the same study, bilorphin was found to have a fast dissociation rate relative to endomorphin-2 and DAMGO (347). It is tempting to speculate therefore, that bilorphin exhibits bias towards G protein signalling with a reduced ability to recruit arrestin-3 because it lacks this interaction with L219^{ECL2} and other residues in the extracellular loops, resulting in an enhanced off-rate compared to other opioid peptides. A larger test panel of biased compounds would be required to test these hypotheses.

Moreover, how these ligand-residue interactions with ECL2 translate to an allosteric effect on the conformation of the intracellular portion of the MOPr is yet to be elucidated. A computational study by *Schneider et al.,* used mutual information analysis to determine allosteric coupling between residues near the ligand binding site and the intracellular domains of the MOPr (263). They found that the residues most strongly correlated between these two regions were different between simulations with the MOPr bound to the G protein-biased compound oliceridine versus morphine. With oliceridine bound, residues in TMs 1, 3 and 7 contributed to this allosteric coupling, whereas with morphine bound there was a greater contribution of residues in TMs 2 and 6 (263). Similarly, in our MD simulations bilorphin binds on the opposite side of the extended binding pocket to endomorphin-2 and DAMGO, closer to TMs 1 and 7. As we have not modelled the binding pathway of these peptides, there may also be important differences in the initial interactions between the ligands and the MOPr which allosterically alter the resulting receptor conformation.

Principal component analysis revealed ligand-dependent differences primarily in the conformation of the extracellular side of the MOPr, likely due to the alternative extended binding pockets accessed by endomorphin-2 and bilorphin. In the absence of many high resolution structures of the MOPr bound to different intracellular signalling partners, it is challenging to associate these different ligand-induced receptor conformations with the subsequent preferential coupling to G proteins or arrestins (177, 348). However, we speculate that the differences captured in the present study may represent the initial changes induced by these oppositely biased peptides which eventually lead to alternative conformations on the intracellular surface of the MOPr. Indeed, comparison of our predicted DAMGO binding pose with that released by *Koehl et al.,* showed high similarity in both the binding position of DAMGO and the conformation of residues in the orthosteric site (23) (Section 5.3.5), but our MD did not capture the conformational changes observed on the intracellular side of the MOPr-G_i complex. This suggests that our molecular modelling protocol is able to sample the initial drug-induced changes around the binding site, prior to the receptor interacting with a specific intracellular protein. Although we did not capture the large conformational changes associated with receptor activation, the helix movements described by the principal component analysis showed the intracellular ends of the transmembrane domains adopting a more closed conformation, in towards the helix bundle, with endomorphin-2 bound compared to the bilorphin-MOPr complex. This closed conformation of the intracellular region is reminiscent of the "occluded state" stabilised by arrestin-biased ligands at the angiotensin II type I receptor (224), and may be the mechanism by which endomorphin-2 can recruit arrestin-3 more potently than other MOPr ligands.

As discussed in Chapter 4, the conformation of the conserved microswitch W293$^{6.48}$ appears to be dependent on the intrinsic efficacy of the bound ligand. The data described in the present chapter agrees with this previous hypothesis; DAMGO was a more potent agonist in the G_i activation assay than both endomorphin-2 and bilorphin (Section 5.3.1) and strongly induced the conformational change in W293$^{6.48}$, relative to the inactive MOPr model, whereas the lower potency peptides, endomorphin-2 and bilorphin, did not. Furthermore, the conformation of the W293$^{6.48}$ indole ring predicted by our MD simulations was also captured in the recently released cryo-electron microscopy structure of the fully activated DAMGO-MOPr-G_i complex (23).

5.5 Conclusions

In conclusion, in this chapter I have described the signalling characteristics of three MOPr-selective peptides; the balanced agonist DAMGO, the arrestin-biased agonist endomorphin-2, and the novel G protein-biased agonist bilorphin. MD simulations of the peptide-MOPr complexes revealed distinct interactions with the MOPr extended binding pocket which may confer the differing bias profiles of these compounds. DAMGO and endomorphin-2, which recruited arrestin-3, interacted with the extracellular loops, notably with the conserved hydrophobic residues on ECL2 suggested to be important for arrestin-bias and ligand kinetics (186, 187). Importantly, bilorphin did not engage these residues and instead interacted with a different extended binding site closer to TM1. Moreover, the MOPr sampled different conformational states in the presence of bilorphin versus endomorphin-2. These data add to the body of literature suggesting biased ligands can stabilise alternative GPCR conformations (222, 224, 262, 342, 343), and that these conformational changes are induced by unique ligand-residue interaction fingerprints. To our knowledge, this is the first study to identify structural differences between the binding of oppositely biased MOPr compounds.

Chapter 6: The effect of single point mutations on ligand-induced MOPr signalling

6.1 Introduction

The real power of any *in silico* study is when hypotheses based on MD simulation data can be tested and validated *in vitro,* or even *in vivo*. By analysing the full panel of ligand-MOPr simulation data described in Chapters 4 and 5, I identified residues of interest which may be important in encoding opioid ligand efficacy and bias. The positions of the two residues discussed in this chapter, W293$^{6.48}$ and L219^{ECL2}, are shown in Figure 6.1.

Firstly, the rotamer toggle switch W293$^{6.48}$, located at the base of the orthosteric pocket (Figure 6.1a), adopted distinct conformations depending on the bound ligand (152). In simulations with high efficacy agonists, such as DAMGO (Chapter 5 Section 5.3.3), norbuprenorphine or methadone (Chapter 4 Section 4.3.3), the indole ring of W293$^{6.48}$ favoured the “horizontal” conformation, whilst in the presence of the lower efficacy ligands, bilorphin (Chapter 5 Section 5.3.3), morphine, buprenorphine or diprenorphine (Chapter 4 Section 4.3.3) it favoured the “vertical” conformation. A tryptophan, or other aromatic residue, in position 6.48 (Ballesteros-Weinstein numbering (81)) is highly conserved across Class A GPCRs. Table 6.1 lists the residues at position 6.48 in all the currently crystallised Class A GPCRs (78). Out of these analysed sequences, 78 % contain a tryptophan and 96 % have an aromatic residue. W6.48 has been suggested to act as a microswitch for receptor activation (149, 349, 350) and mutations at this position drastically alter ligand binding and signalling across a range of GPCRs including cannabinoid, serotonin, ghrelin, adenosine and neuropeptide Y2 receptors (150, 151, 158-160). Moreover, by comparison of the available crystal structures of the MOPr, the conformation of W293$^{6.48}$ was highlighted as a key change between the inactive and active state receptor (22). However, to our knowledge, the effect of mutating W293$^{6.48}$ on ligand-induced signalling has not been reported for the MOPr.

Secondly, comparison of the oppositely biased peptides endomorphin-2 and bilorphin, and the reference agonist DAMGO (generally considered to be unbiased), highlighted differences in interactions with the extracellular loops. Peptides that robustly recruit arrestin interacted with W133^{ECL1}, C217^{ECL2}, T218^{ECL2} and L219^{ECL2}, but the G protein-biased peptide bilorphin did not (Chapter 5 Section 5.3.3). There is increasing interest in the role of the extracellular loops, particularly ECL2, in GPCR activation and bias (186, 187, 351). Notably, the presence of a hydrophobic residue at position 45.52 (numbering follows the nomenclature for loops described in (237)) in ECL2 (L219^{ECL2} in the MOPr, Figure 6.1) is reasonably conserved in Class A GPCRs; Table 6.1 shows that 54 % of the sequences analysed contain a hydrophobic residue at position 45.52 (78). From our MD simulations of the peptide-MOPr complexes, we hypothesised that ligand interaction with the extracellular loops, including L219^{ECL2}, may be important for arrestin recruitment to the MOPr (Chapter 5). Indeed, in the 5HT$_{2B}$ receptor mutation of this leucine residue to an alanine selectively reduced arrestin recruitment but did not alter G protein-mediated signalling (186). Furthermore, ligand interaction with the equivalent ECL2 residue (isoleucine) successfully predicted arrestin bias at the dopamine D$_2$ receptor (187). Based on this previous literature, along with observations from our MD simulations in Chapter 5, I sought to investigate the effect of the L219^{ECL2}A point mutation in MD simulations and in cell signalling assays.

In this chapter, I first perform MD simulations of the W293$^{6.48}$A and L219^{ECL2}A MOPr variants to determine the effect of these mutations on ligand binding poses and MOPr conformation. I then use site-directed mutagenesis by PCR to generate the single point mutations in the HA-rat MOPr construct to investigate if the effect predicted by the MD simulations translates to altered ligand-induced signal transduction in HEK 293 cells expressing the MOPr variants. I find that the W293$^{6.48}$A mutation causes the MOPr to favour an overall inactive conformation *in silico*, which did not respond to opioid agonists *in vitro*, whilst the L219^{ECL2}A mutation differentially modulates MOPr signalling in response to biased peptide agonists.

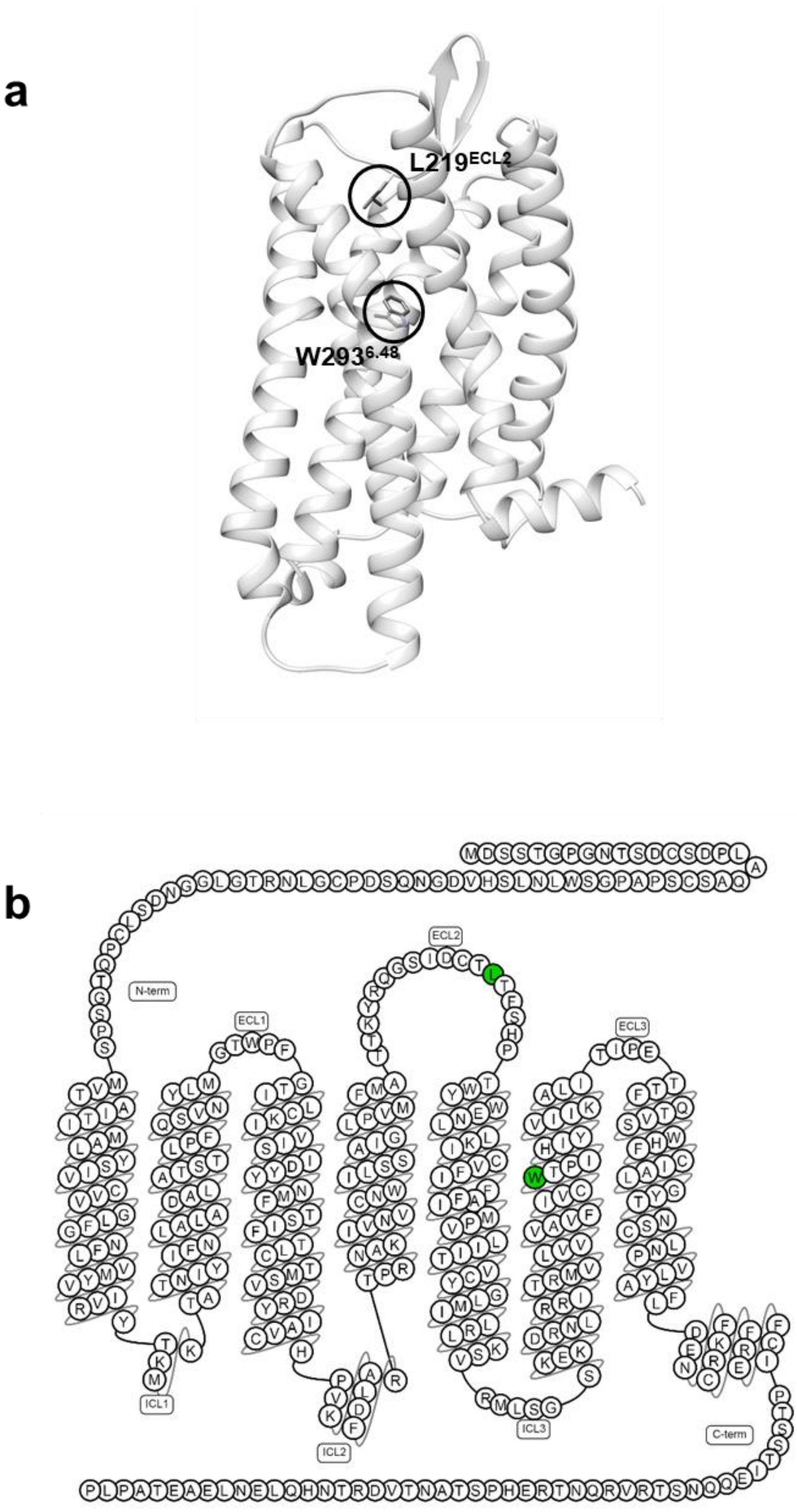

Figure 6.1 Position of the single point mutations characterised in this chapter

a) The residues are shown as dark grey sticks on the inactive MOPr model (ribbons). L219^{ECL2} is positioned in extracellular loop 2. W293$^{6.48}$ sits at the base of the orthosteric ligand binding site, on TM6. b) The same residues coloured in green on a snake plot of the rat MOPr (Figure made using the GPCRdb (78)).

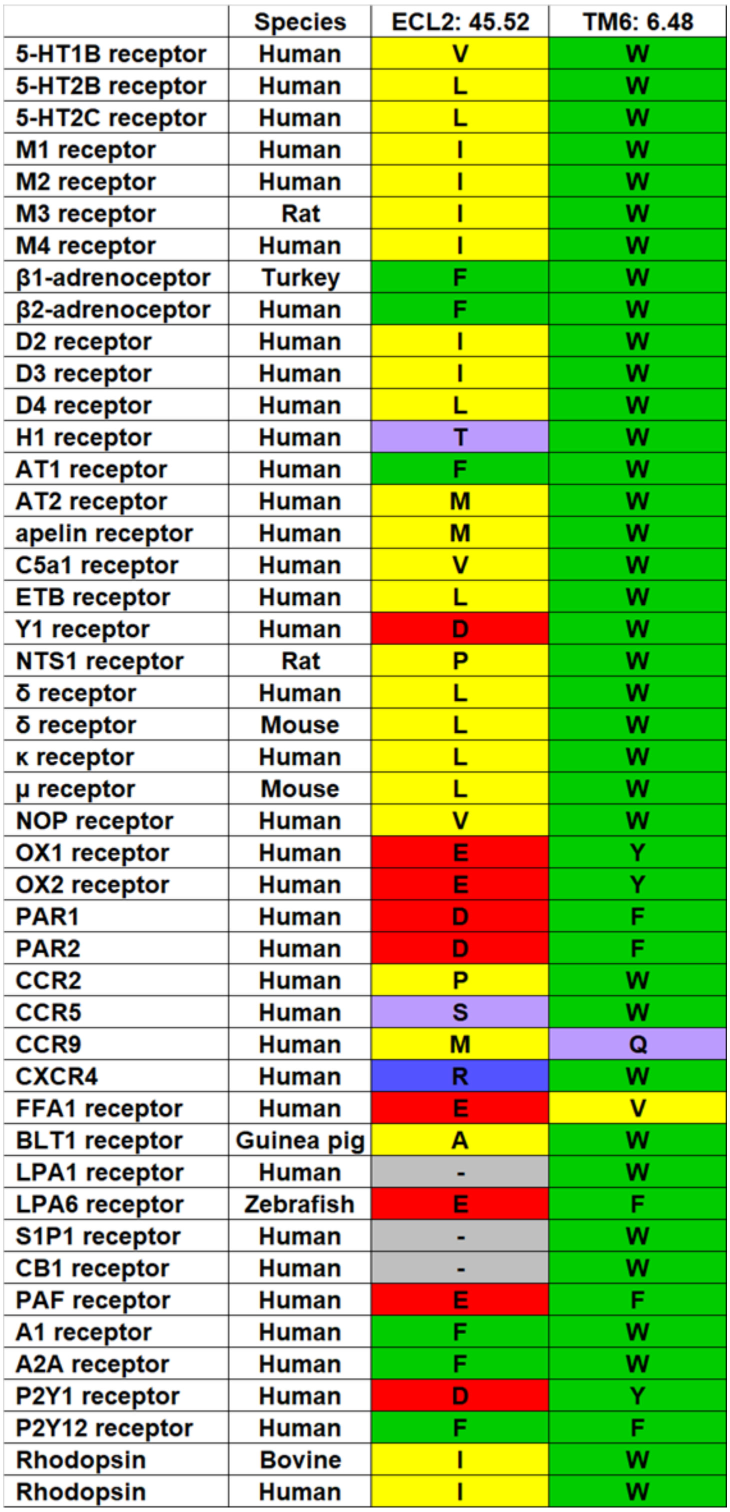

	Species	ECL2: 45.52	TM6: 6.48
5-HT1B receptor	Human	V	W
5-HT2B receptor	Human	L	W
5-HT2C receptor	Human	L	W
M1 receptor	Human	I	W
M2 receptor	Human	I	W
M3 receptor	Rat	I	W
M4 receptor	Human	I	W
β1-adrenoceptor	Turkey	F	W
β2-adrenoceptor	Human	F	W
D2 receptor	Human	I	W
D3 receptor	Human	I	W
D4 receptor	Human	L	W
H1 receptor	Human	T	W
AT1 receptor	Human	F	W
AT2 receptor	Human	M	W
apelin receptor	Human	M	W
C5a1 receptor	Human	V	W
ETB receptor	Human	L	W
Y1 receptor	Human	D	W
NTS1 receptor	Rat	P	W
δ receptor	Human	L	W
δ receptor	Mouse	L	W
κ receptor	Human	L	W
μ receptor	Mouse	L	W
NOP receptor	Human	V	W
OX1 receptor	Human	E	Y
OX2 receptor	Human	E	Y
PAR1	Human	D	F
PAR2	Human	D	F
CCR2	Human	P	W
CCR5	Human	S	W
CCR9	Human	M	Q
CXCR4	Human	R	W
FFA1 receptor	Human	E	V
BLT1 receptor	Guinea pig	A	W
LPA1 receptor	Human	-	W
LPA6 receptor	Zebrafish	E	F
S1P1 receptor	Human	-	W
CB1 receptor	Human	-	W
PAF receptor	Human	E	F
A1 receptor	Human	F	W
A2A receptor	Human	F	W
P2Y1 receptor	Human	D	Y
P2Y12 receptor	Human	F	F
Rhodopsin	Bovine	I	W
Rhodopsin	Human	I	W

Table 6.1 Amino acids at positions 45.52 in ECL2 and 6.48 in TM6 are conserved across Class A GPCRs

Sequences of all crystallised Class A GPCRs were analysed using the GPCRdb (78). Amino acids are colour-coded by side chain property; green = aromatic, yellow = hydrophobic, purple = polar, red = acidic, blue = basic.

6.2 Materials & Methods

6.2.1 *In silico* mutagenesis

Point mutations of the inactive MOPr model were generated by converting the residue of interest (W293$^{6.48}$ or L219^{ECL2}) to an alanine in Chimera (293). As alanine contains only a methyl group side chain, it was not necessary to optimise the rotamer position of the new residue. 250 ns MD simulations were performed of each membrane-embedded MOPr mutant bound to the ligands of interest. The initial pose of the bound ligand in each mutant was identical to that in the original wildtype simulations (see Chapter 4 Section 4.2.2 and Chapter 5 Section 5.2.2). For the W293$^{6.48}$A receptor, in order to determine the effect of the substitution on the ability of an agonist to induce an active-like state, simulations were performed with either the high efficacy agonist, norbuprenorphine, or the antagonist, diprenorphine, in the binding pocket. For the L219^{ECL2}A receptor, simulations were performed with the receptor bound to either the G protein-biased peptide, bilorphin, or the arrestin-biased peptide, endomorphin-2, as this substitution in the endomorphin-2 binding pocket was predicted to have a greater effect on endomorphin-2 than bilorphin.

MD simulations and subsequent analysis were performed as described in Chapter 2 Sections 2.1.5 and 2.1.7.

6.2.2 *In vitro* mutagenesis

To determine the effect of the W293$^{6.48}$A and L219^{ECL2}A point mutations on ligand-induced signalling, single point mutations were introduced to the MOPr constructs using mutagenic PCR, as described in Chapter 2 Section 2.2.6.

For each desired mutation, the aim was to introduce the variant into both the pcDNA3-HA-rMOPr and the pQCXIN-Myc-hMOPR-RlucII plasmids (see Chapter 2 Section 2.2.6), to use in the G protein and arrestin-3 BRET assays, respectively.

After the PCR reactions, the products were visualised by gel electrophoresis on 1 % agarose. Figure 6.2a shows the resulting gel for the pcDNA3-HA-rMOPr reactions, where both the W293$^{6.48}$A and L219^{ECL2}A reactions resulted in a band at the expected product size of 7 kb. E.Coli were transformed with these PCR products and the DNA extracted and purified as described in Chapter 2 Section 2.2.6. Figure 6.3 shows the DNA sequence of the mutagenized portion of the plasmid compared to the wildtype template plasmid for the W293$^{6.48}$A (Figure 6.3a) and L219^{ECL2}A (Figure 6.3b) reactions. Both mutations were successfully incorporated, with no other mis-matched bases elsewhere in the insert sequence. The full insert sequences are presented in the Appendix I and II.

Figure 6.2b shows a representative gel from the pQCXIN-Myc-hMOPR-RlucII reactions. Despite attempts to alter the PCR conditions for this larger plasmid, none of the reactions performed resulted in a detectable band at the expected size. E.Coli transformed with the PCR products failed to grow on ampicillin-containing agar, suggesting that the mutagenized plasmid had not formed correctly.

Cell signalling experiments were therefore performed with the pcDNA3-HA-rMOPr constructs. In the absence of successful mutation of the pQCXIN-Myc-hMOPR-RlucII plasmid, which contains the Renilla Luciferase essential for the arrestin-3 BRET assay, ligand-induced receptor internalisation measured by ELISA was used as a proxy for arrestin recruitment to the MOPr (6, 49, 72, 352).

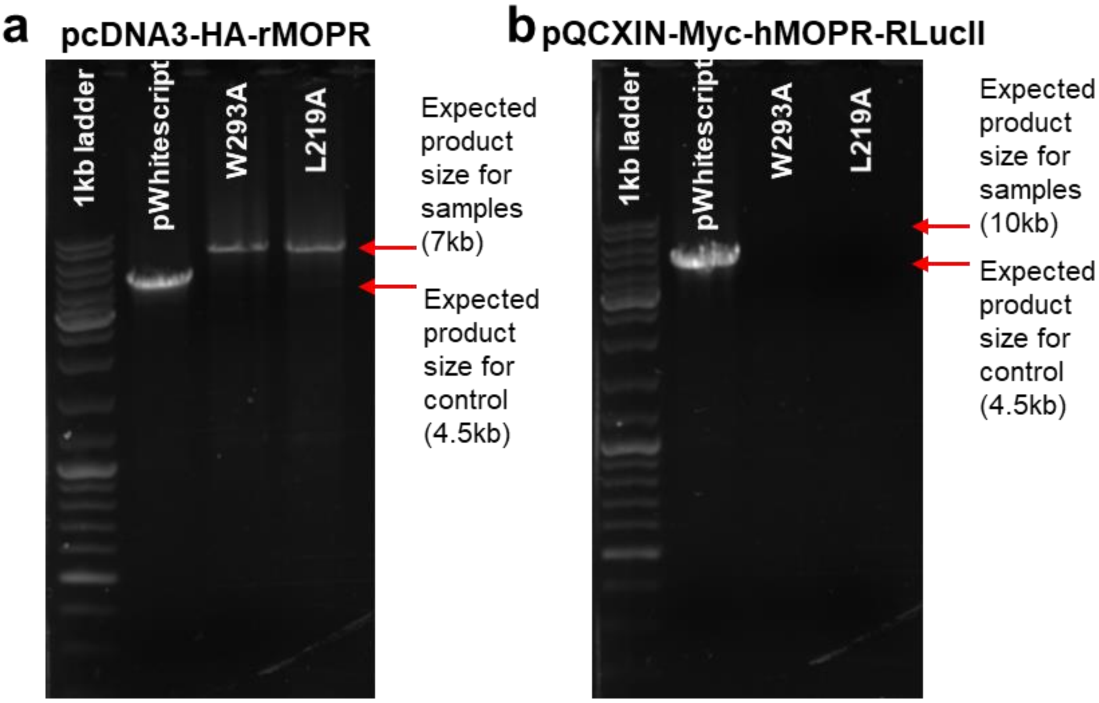

Figure 6.2 Gel electrophoresis of PCR products

PCR products, including the pWhitescript control reaction, were run on 1 % agarose gels to check bands were the correct size, and to check for any contaminants or primer-dimer formation. a) PCR products for the control reaction, W293$^{6.48}$A and L219^{ECL2}A reactions with the HA-rat MOPr construct. All reactions produced bands of the correct size, with no detectable contaminating bands. b) PCR products for the control reaction, W293$^{6.48}$A and L219^{ECL2}A reactions with the Myc-human MOPr-RLucII construct. The control reaction produced a band at the correct size, but neither the W293$^{6.48}$A nor L219^{ECL2}A reactions resulted in visible bands.

a

W293A vs wildtype

Insert sequence length: 1233
Sequence identity: 1230/1233 (99%)

```
W293A  841    AAAGAAAAGGACAGGAATCTGCGCAGGATCACCCGGATGGTGCTGGTGGTCGTGGCTGTA   900
              ||||||||||||||||||||||||||||||||||||||||||||||||||||||||||||
RMOPR  841    AAAGAAAAGGACAGGAATCTGCGCAGGATCACCCGGATGGTGCTGGTGGTCGTGGCTGTA   900

W293A  901    TTTATCGTCTGCGCCACCCCCATCCACATCTACGTCATCATCAAAGCGCTGATCACGATT   960
              ||||||||||||   |||||||||||||||||||||||||||||||||||||||||||||
RMOPR  901    TTTATCGTCTGCTGGACCCCCATCCACATCTACGTCATCATCAAAGCGCTGATCACGATT   960

W293A  961    CCAGAAACCACATTTCAGACCGTTTCCTGGCACTTCTGCATTGCTTTGGGTTACACGAAC   1020
              ||||||||||||||||||||||||||||||||||||||||||||||||||||||||||||
RMOPR  961    CCAGAAACCACATTTCAGACCGTTTCCTGGCACTTCTGCATTGCTTTGGGTTACACGAAC   1020
```

b

L219A vs wildtype

Insert sequence length: 1233
Sequence identity: 1231/1233 (99%)

```
L219A  601    GTCTGCAACTGGATCCTCTCTTCTGCCATCGGTCTGCCTGTAATGTTCATGGCAACCACA   660
              ||||||||||||||||||||||||||||||||||||||||||||||||||||||||||||
RMOPR  601    GTCTGCAACTGGATCCTCTCTTCTGCCATCGGTCTGCCTGTAATGTTCATGGCAACCACA   660

L219A  661    AAATACAGGCAGGGGTCCATAGATTGCACCGCCACGTTCTCCCACCCAACCTGGTACTGG   720
              ||||||||||||||||||||||||||||||  ||||||||||||||||||||||||||||
RMOPR  661    AAATACAGGCAGGGGTCCATAGATTGCACCCTCACGTTCTCCCACCCAACCTGGTACTGG   720

L219A  721    GAGAACCTGCTCAAAATCTGTGTCTTTATCTTCGCTTTCATCATGCCGATCCTCATCATC   780
              ||||||||||||||||||||||||||||||||||||||||||||||||||||||||||||
RMOPR  721    GAGAACCTGCTCAAAATCTGTGTCTTTATCTTCGCTTTCATCATGCCGATCCTCATCATC   780
```

Figure 6.3 Sequencing results for the obtained MOPr mutants

Purified DNA obtained from the site-directed mutagenesis protocol (see Chapter 2 Section 2.2.6) was sequenced by Source Bioscience, and the sequences aligned to the HA-rat MOPr template sequence. For both the a) W293$^{6.48}$A and b) the L219^{ECL2}A reactions, only the desired mutations were incorporated (yellow), with no mismatched bases elsewhere in the insert sequence. See Appendix I and II for full insert sequences.

6.2.3 Expression of the MOPr variants in HEK 293 cells

HEK 293 cells were transfected with either the HA-rat MOPr, W293A-MOPr or L219A-MOPr by lipofectamine transfection (see Chapter 2 Section 2.2.3). Surface expression of the wildtype and MOPr variants was determined 36 hours later by cell surface ELISA against the HA-tag, as described in Chapter 2 Section 2.2.7.

6.2.4 BRET assays

Using DNA ratios to produce approximately equal surface expression, as determined by ELISA, HEK 293 cells were transfected with either wildtype HA-rat MOPr, W293$^{6.48}$A-MOPr or L219^{ECL2}A-MOPr, along with Gαi-RlucII and Gγ-GFP. On the day of the assay, cells were counted and plated at equal cell densities for each variant, to allow comparison between the different plates of transfected cells.

Ligand-induced G protein activation was measured as described in Chapter 2 Section 2.2.4. For the single concentration experiments, all drugs were used at a concentration of 30 µM, except methadone which was used at 10 µM due to its off-target effects at high concentrations (353).

Statistical analysis was performed in GraphPad Prism version 7, comparing the ligand response in each MOPr variant to wildtype using two-way ANOVA with post-hoc Dunnett's test.

Full concentration-response curves were generated for DAMGO, endomorphin-2 and bilorphin at the wildtype HA-rat MOPr and the L219^{ECL2}A variant, and the resulting EC_{50} and maximum response values were compared by two-way ANOVA with post-hoc Sidak's test, for differences between wildtype and L219^{ECL2}A MOPr for each drug.

6.2.5 Receptor internalisation

Receptor internalisation in response to DAMGO, endomorphin-2 or bilorphin was measured by cell surface ELISA by pre-labelling receptors prior to incubation with drug, as described in Chapter 2 Section 2.2.8. All drugs were at added at a concentration of 30 µM and incubated with the cells for 30 minutes to produce maximal receptor internalisation (21, 39, 47, 315). Data analysis was performed in GraphPad Prism version 7, using two-way ANOVA with post-hoc Dunnett's test to test for differences in ligand response between the MOPr variant and wildtype.

6.3 Results

6.3.1 MD simulations of the W293$^{6.48}$A MOPr variant

The conserved tryptophan residue, W293$^{6.48}$, at the base of the orthosteric binding pocket has been previously described as a rotamer toggle switch for GPCR activation (22, 150-152, 334, 354). In Chapter 4 Section 4.3.3 and Chapter 5 Section 5.3.3 the rotameric state of W293$^{6.48}$ was assigned by measuring the χ2 dihedral; values around 80 - 120° indicated the indole ring was in the "vertical" conformation, whilst values between 0 - 60° were characteristic of the "horizontal" conformation. Plotting the average χ2 dihedral of W293$^{6.48}$ during the MD simulations of the ligand-bound wildtype receptor against the experimentally-derived values (21) for intrinsic efficacy in GTPγS binding assays (τ) showed that there was a significant strong negative correlation between the rotameric state of the W293$^{6.48}$ side chain and the efficacy of the bound ligand ($r = -0.85$, $p = 0.0165$, Pearson's correlation). Higher efficacy agonists induced a greater conformational change in this residue, from the "vertical" to "horizontal" position, than the lower efficacy ligands (Figure 6.4a). I therefore converted the tryptophan in position 293 to an alanine in the inactive MOPr model (Figure 6.4b), and 250 ns MD simulations were performed of the W293$^{6.48}$A variant receptor bound to either norbuprenorphine or diprenorphine, as examples of a high efficacy small molecule and an antagonist, respectively.

Principal component analysis comparing the wildtype and W293$^{6.48}$A simulations showed that in simulations of the wildtype receptor, the norbuprenorphine-bound complex clustered differently to the diprenorphine-bound complex, adopting a conformation consistent with an active intermediate (152) (see Chapter 4 Section 4.3.4). In simulations of the ligands bound to the W293$^{6.48}$A mutant, the clusters for both complexes overlapped with the diprenorphine-bound wildtype MOPr and the conformation of the inactive crystal structure (Figure 6.4c). This suggests that mutation of W293$^{6.48}$ to alanine reduced the probability of the receptor transitioning to an active state, even in the presence of the high efficacy agonist norbuprenorphine.

Extracting structures representing extremes of PC1 showed that these differences between the norbuprenorphine-MOPr structure and the norbuprenorphine- W293$^{6.48}$A receptor were mainly in the positions of the extracellular ends of the transmembrane domains (Figure 6.4d). In simulations of the W293$^{6.48}$A variant, TMs 2, 5 and 6 moved outwards away from the helix bundle, whilst TM3 and TM7 shifted inwards, compared to the norbuprenorphine-bound wildtype MOPr. These principal motions were very similar to those describing the differences between the high and low efficacy agonist-bound MOPr in Chapter 4, again suggesting that the W293$^{6.48}$A variant favours an inactive state.

As illustrated in Figure 6.4e, the binding pose of diprenorphine in the W293$^{6.48}$A mutant MOPr (yellow) essentially did not differ from its pose in simulations with the wildtype MOPr (grey). However, for norbuprenorphine, the conversion of W293$^{6.48}$ to alanine allowed the ligand to shift deeper into the receptor pore (green in Figure 6.4f) to adopt a binding pose which would clash with the indole ring of W293$^{6.48}$ in the wildtype receptor (grey in Figure 6.4f). In these simulations, the W293$^{6.48}$A mutation therefore altered the binding position of the high efficacy agonist norbuprenorphine, but not that of the antagonist diprenorphine.

These simulations of the W293$^{6.48}$A MOPr build on evidence that W293$^{6.48}$ is an important microswitch for GPCR activation and provides a strong rationale for investigating the effect of W293$^{6.48}$A mutation on opioid-induced signalling *in vitro*.

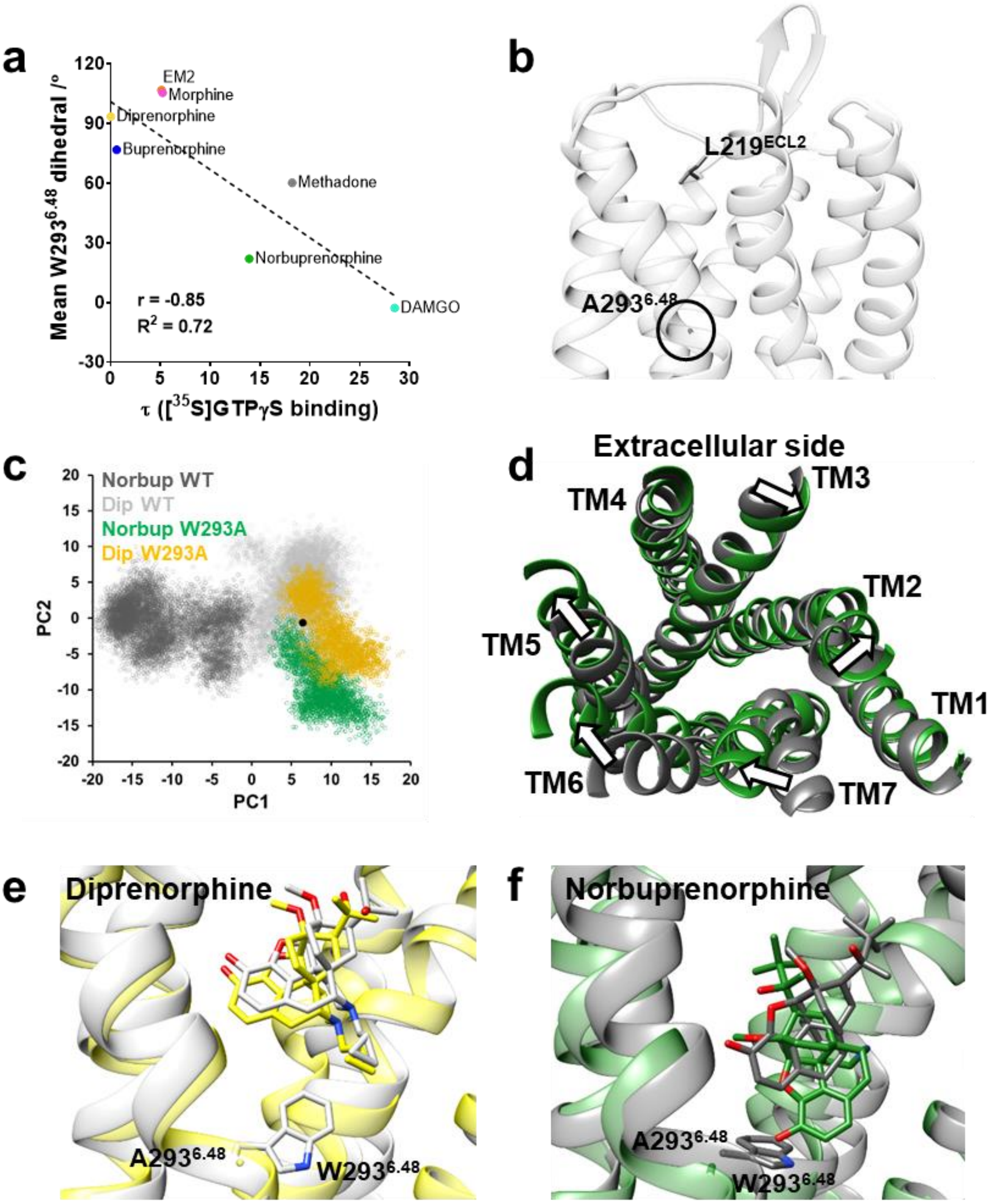

Figure 6.4 W293$^{6.48}$A *in silico* mutagenesis

a) The χ2 dihedral of W293$^{6.48}$ from the MD simulations correlates with experimental values of ligand efficacy for GTPγS binding (21) (Pearson's correlation). b) W293$^{6.48}$ was converted to alanine and 250 ns MD simulations were performed with the W293$^{6.48}$A-MOPr bound to norbuprenorphine or diprenorphine. c) Principal component analysis performed on the alpha carbons of the receptor transmembrane domains. Clusters for the 1 μs simulations of the wildtype MOPr bound to norbuprenorphine or diprenorphine are in dark grey or light grey, respectively. Data from the 250 ns simulations of the W293$^{6.48}$A MOPr mutant bound to either norbuprenorphine or diprenorphine are in green and yellow, respectively. The black point indicates the conformation of the inactive crystal structure. d) Extracting structures which represent extremes of PC1

[continued overleaf]

shows helix conformational changes primarily on the extracellular side of the MOPr. Loops have been removed from the image to just depict the part of the receptor on which the PCA was performed. White arrows indicate conformational changes in the helices moving from norbuprenorphine-bound wildtype MOPr (grey) to norbuprenorphine-bound W293$^{6.48}$A-MOPr (green). Final binding poses of e) diprenorphine (yellow) and f) norbuprenorphine (green) after MD simulation of the W293$^{6.48}$A receptor, compared to the ligands' poses in the wildtype MOPr (grey).

6.3.2 MD simulations of the L219^{ECL2}A MOPr variant

In Chapter 5, we observed differences in ligand interaction with residues in ECL2 through MD simulations of peptide-MOPr complexes. Endomorphin-2 and DAMGO both transiently interacted with residues in this extracellular loop, whereas the G protein-biased peptide bilorphin did not. A conserved hydrophobic residue in ECL2, L219^{ECL2} in the MOPr, has been suggested to play a role in arrestin-bias in Class A GPCRs (186, 187). Therefore, I mutated L219^{ECL2} to alanine *in silico* (Figure 6.5a) and performed 250 ns MD simulations of the L219^{ECL2}A receptor bound to either the arrestin-biased peptide endomorphin-2 or the G protein-biased peptide bilorphin.

A previous study of this conserved hydrophobic residue in the 5HT$_{2B}$ receptor showed that the leucine to alanine mutation resulted in greater flexibility of ECL2 (186). Figure 6.5b and 6.5c show the root mean square fluctuations (RMSF) of the alpha carbons of residues in ECL2 in simulations of the wildtype or L219^{ECL2}A MOPr bound to endomorphin-2 or bilorphin. In agreement with the study by *Wacker et al.*, in the L219^{ECL2}A variant the RMSF values for the ECL2 residues were generally higher than in simulations of the wildtype MOPr, suggesting that the L219^{ECL2}A mutation made this loop more flexible.

Figure 6.5d shows the results of the principal component analysis performed on the wildtype and L219^{ECL2}A simulations with the MOPr bound to bilorphin or endomorphin-2. Projecting the receptor conformations onto PC1 and PC2 showed that with either bilorphin or endomorphin-2 bound, the L219^{ECL2}A receptor adopted a conformation distinct from that stabilised by either peptide in the wildtype receptor. As both extracellular and intracellular loops were excluded from the analysis (see Chapter 2 Section 2.1.7), these alternative conformations must reflect a change in the positions of the transmembrane domains between the wildtype and L219^{ECL2}A simulations, which may have been induced by the mutation in ECL2. If so, this suggests that L219^{ECL2} can allosterically modulate the conformation of the MOPr helices.

Unexpectedly, in simulations of endomorphin-2 bound to the L219^{ECL2}A mutant there was a change in the rotameric state of W293$^{6.48}$ consistent with the active conformation of the MOPr (Figure 6.5e). This may be due to the slight change in the binding pose of endomorphin-2 in the L219^{ECL2}A receptor compared to the wildtype model, such that the N-terminal tyrosine of endomorphin-2 moved deeper into the receptor pore, engaging the W293$^{6.48}$ activation switch (Figure 6.5f, orange). In contrast, the binding pose of bilorphin shifted slightly away from W293$^{6.48}$ in the L219^{ECL2}A receptor (Figure 6.5g, purple) and the N-terminal dimethyl tyrosine maintained a favourable stacking interaction with the indole ring of W293$^{6.48}$, so the side chain remained in the "vertical", inactive position (Figure 6.5e).

This effect on the behaviour of a microswitch spatially distant from the L219^{ECL2}A mutation suggests that L219^{ECL2} may play an important role in signal transduction for endomorphin-2. Together with the increasing literature on the role of extracellular loops in GPCR activation (181, 182, 186, 187, 191, 351), the impact of mutating this residue warrants further investigation in *in vitro* cell signalling assays.

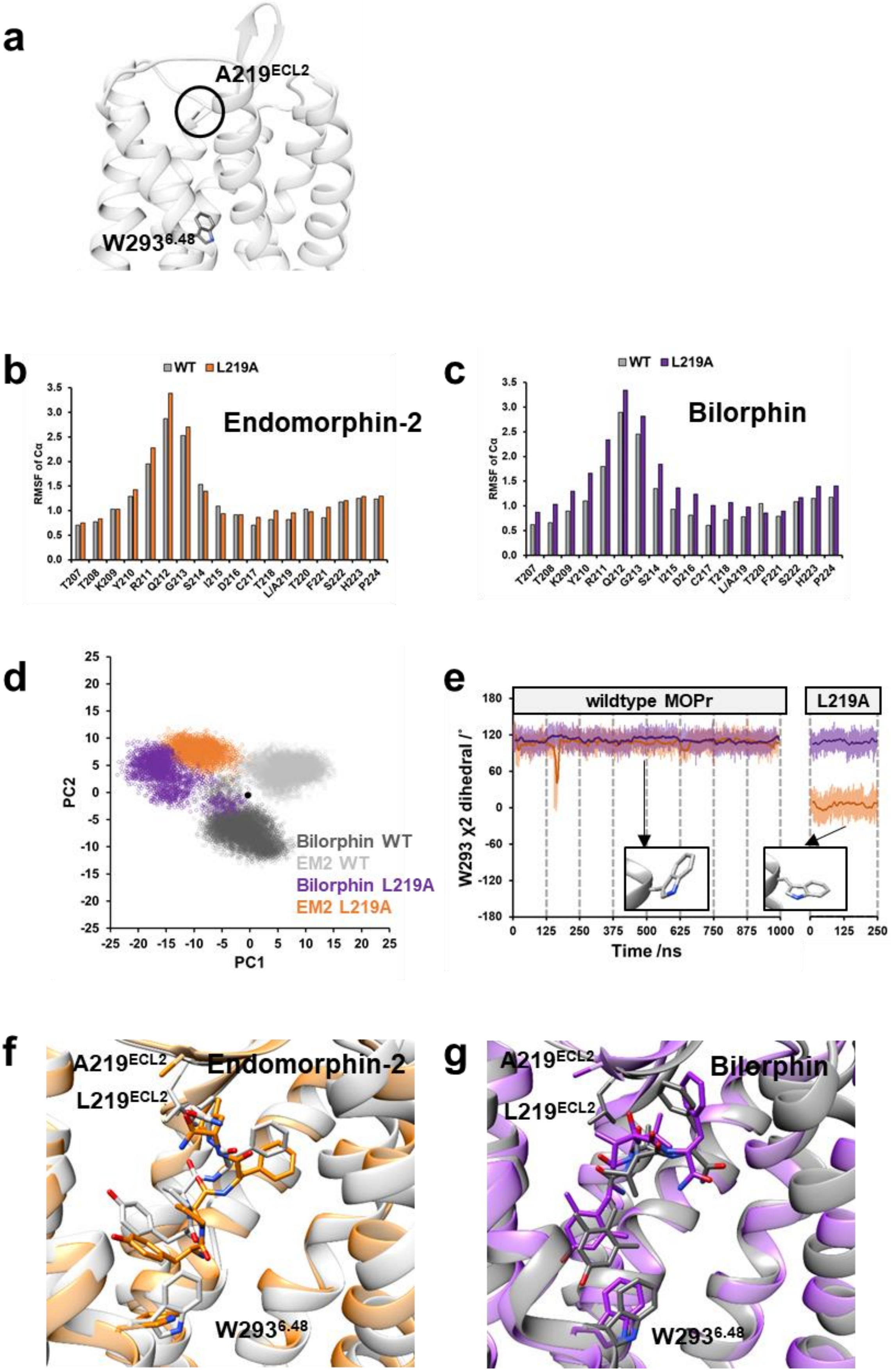

Figure 6.5 L219^{ECL2}A *in silico* mutagenesis

[continued overleaf]

a) L219^{ECL2} was converted to alanine and 250 ns MD simulations were performed with the L219^{ECL2}A-MOPr bound to bilorphin or endomorphin-2. RMSF calculations performed on the alpha carbons of ECL2 residues in simulations with the L219^{ECL2}A variant bound to b) endomorphin-2 and c) bilorphin, compared to the wildtype MOPr (grey). d) Principal component analysis performed on the alpha carbons of the receptor transmembrane domains. Clusters for the 1 μs simulations of the wildtype MOPr bound to bilorphin or endomorphin-2 are in dark grey or light grey, respectively. Data from the 250 ns simulations of the L219^{ECL2}A MOPr mutant bound to either bilorphin or endomorphin-2 are in purple and orange, respectively. The black point indicates the conformation of the inactive crystal structure. e) The rotamer angle of W293$^{6.48}$ with bilorphin (purple) or endomorphin-2 (orange) bound in the wildtype receptor, and in the L219^{ECL2}A mutant. Data expressed as raw values (faded line) and moving average over 100 frames (10 ns) (bold line). Final binding poses of f) endomorphin-2 (orange) and g) bilorphin (purple) after MD simulation of the L219^{ECL2}A receptor, compared to the ligands' poses in the wildtype MOPr (faded).

6.3.3 Surface expression of the MOPr variants in HEK 293 cells

To investigate the effect of these MOPr variants on ligand-induced MOPr signalling *in vitro*, the W293$^{6.48}$A and L219^{ECL2}A point mutations were introduced to the HA-rat MOPr construct by PCR site-directed mutagenesis (see Section 6.2.2).

Cell surface ELISAs were performed to confirm whether the MOPr variants reached the plasma membrane. Initially, separate dishes of HEK 293 cells were transfected with equal (5 µg) amounts of either wildtype HA-rat MOPr, W293$^{6.48}$A MOPr or L219^{ECL2}A MOPr DNA, and ELISA against the HA-tag performed 36 hours post-transfection (Section 6.2.5). With this 1:1:1 ratio of WT:W293A:L219A DNA, although there was no significant difference in the level of receptor at the surface, by eye there appeared to be more of the wildtype HA-rat MOPr on the cell surface than the two variants (Figure 6.6a). For the subsequent cell signalling experiments it was important to have the MOPr variants expressed at equal levels to the wildtype construct so that any differences in ligand response could be attributed to the single point mutation and not different expression of the receptors which could lead to changes in observed agonist potency. Cells were therefore transfected with different amounts of DNA (2.5 µg of wildtype HA-rat MOPr, 5 µg of W293$^{6.48}$A MOPr, or 10 µg of L219^{ECL2}A MOPr), which resulted in approximately equal, if not higher, levels of surface expression of each MOPr variant compared to wildtype (Figure 6.6b). This 1:2:4 ratio of WT:W293A:L219A DNA was used for all subsequent cell signalling experiments.

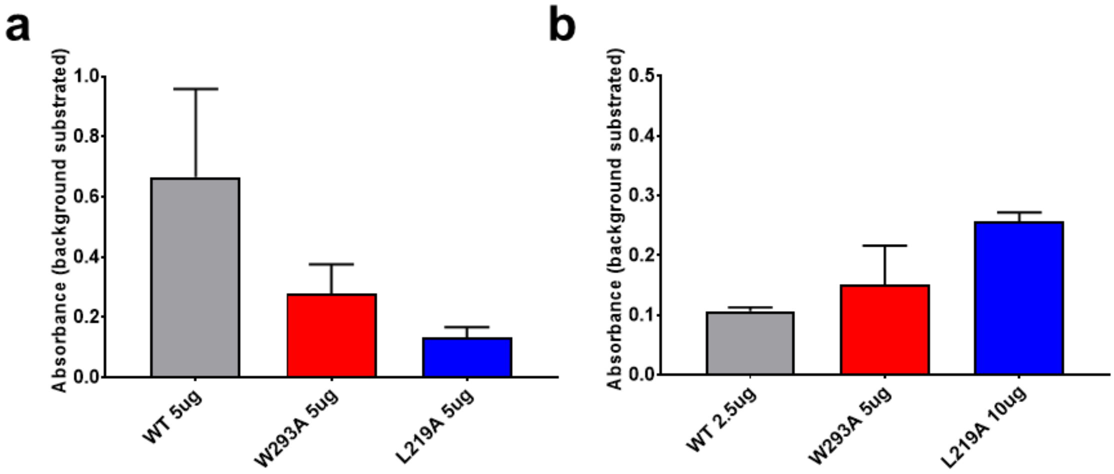

Figure 6.6 Surface expression of the MOPr mutants

Surface expression of the W293$^{6.48}$A and L219^{ECL2}A HA-rat MOPr constructs was measured by ELISA and compared to the wildtype HA-rat MOPr construct. a) Surface expression of HA-tagged receptors in HEK 293 cells transfected with 5 µg of receptor DNA (1:1:1 ratio). b) Surface expression of HA-tagged receptors in HEK 293 cells transfected with 2.5 µg of HA-rat MOPr, 5 µg of W293$^{6.48}$A mutant or 10 µg of L219^{ECL2}A mutant (1:2:4 ratio of WT:W293A:L219A). Data expressed as mean ± SEM of 3 independent experiments. Surface expression of the MOPr mutants was not significantly different from wildtype HA-rat MOPr in either case (one-way ANOVA, post-hoc Dunnett’s test).

6.3.4 Ligand-induced G protein activation

To determine the effect of the W293$^{6.48}$A and L219^{ECL2}A point mutations on MOPr signalling, ligand-induced G$_i$ activation was measured in cells expressing the wildtype HA-rat MOPr or the MOPr variants (Figure 6.7). The BRET signal in response to a single high concentration of opioid agonist (30 µM for all drugs, except methadone 10 µM) was compared in cells expressing the wildtype HA-rat receptor, or the W293$^{6.48}$A variant (Figure 6.7a), or the L219^{ECL2}A variant (Figure 6.7b). Strikingly, the W293$^{6.48}$A mutation clearly abolished G$_i$ activation in response to all opioid ligands tested (Figure 6.7a), even at these maximal concentrations. In contrast, the L219^{ECL2}A mutation had no significant effect on the G protein BRET signal in response to a single high concentration of agonist (Figure 6.7b).

Next, full concentration-response curves for the peptide opioid agonists were performed in cells expressing either the wildtype or L219^{ECL2}A MOPr in order to determine if the mutation had an effect on the agonist potency (Figures 6.7c-e). The maximum response and EC$_{50}$ values calculated for each peptide at the wildtype and L219^{ECL2}A receptors are given in Table 6.2. As suggested by the initial single concentration experiments, the maximum response was not significantly changed for any of the peptide agonists between wildtype and L219^{ECL2}A. DAMGO exhibited a small rightward shift of the curve for the L219^{ECL2}A variant (Figure 6.7c), although the EC$_{50}$ values were not significantly different between wildtype (0.8 ± 0.2 µM) and L219^{ECL2}A (1.4 ± 0.5 µM) expressing cells (Table 6.2). The curve for endomorphin-2 at the L219^{ECL2}A MOPr was significantly right-shifted compared to wildtype (Figure 6.7d), resulting in endomorphin-2 displaying over 3-fold lower potency at activating G$_i$ through the L219^{ECL2}A variant compared to wildtype, with an EC$_{50}$ of 3.3 ± 0.7 µM and 1.0 ± 0.1 µM, respectively (Table 6.2). Bilorphin had almost identical potency in activating G$_i$ through both the wildtype and L219^{ECL2}A MOPr (Figure 6.7e).

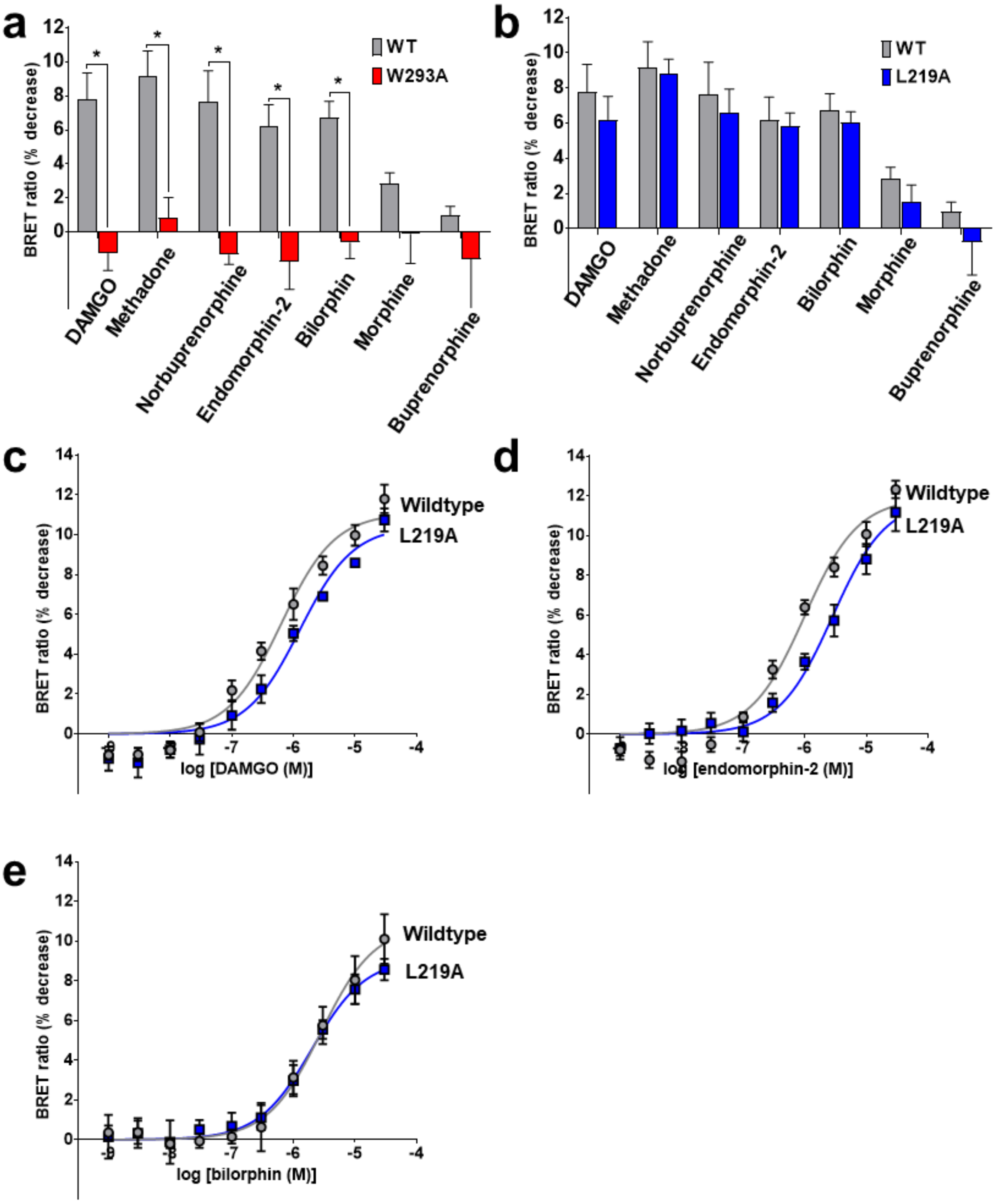

Figure 6.7 Ligand-induced G_i activation in the MOPr mutants

Ligand-induced G_i activation was measured by BRET assay in HEK 293 cells expressing Gαi-RLucII, Gγ-GFP, and either HA-rat MOPr (grey bars), HA-W293$^{6.48}$A (red bars) or HA-L219^{ECL2}A (blue bars). All drugs at 30 µM, except methadone 10 µM. a) The W293$^{6.48}$A mutation abolished G_i activation in response to opioid agonist. b) For the L219^{ECL2}A variant there was no significant effect on the level of G_i activation in response to a single high concentration of opioid agonist, compared to the wildtype receptor. Data expressed as mean ± SEM, of 3 independent experiments. * $p < 0.05$, two-way ANOVA, post-hoc Dunnett's test for differences in ligand response between the MOPr variant and wildtype. Concentration response curves for c) DAMGO, d) endomorphin-2 and e) bilorphin in cells expressing Gαi-RLucII, Gγ-GFP, and either HA-rat MOPr (grey) or HA-L219^{ECL2}A (blue). Data expressed as mean ± SEM, of 5 independent experiments.

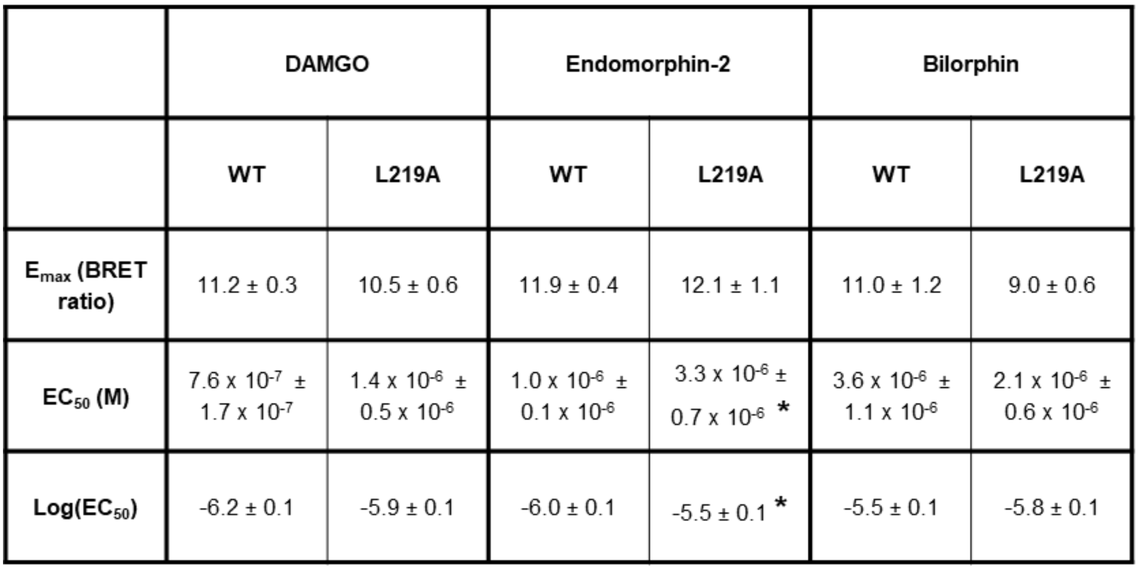

	DAMGO		Endomorphin-2		Bilorphin	
	WT	**L219A**	**WT**	**L219A**	**WT**	**L219A**
E_{max} (BRET ratio)	11.2 ± 0.3	10.5 ± 0.6	11.9 ± 0.4	12.1 ± 1.1	11.0 ± 1.2	9.0 ± 0.6
EC_{50} (M)	$7.6 \times 10^{-7} \pm 1.7 \times 10^{-7}$	$1.4 \times 10^{-6} \pm 0.5 \times 10^{-6}$	$1.0 \times 10^{-6} \pm 0.1 \times 10^{-6}$	$3.3 \times 10^{-6} \pm 0.7 \times 10^{-6}$ *	$3.6 \times 10^{-6} \pm 1.1 \times 10^{-6}$	$2.1 \times 10^{-6} \pm 0.6 \times 10^{-6}$
$Log(EC_{50})$	-6.2 ± 0.1	-5.9 ± 0.1	-6.0 ± 0.1	-5.5 ± 0.1 *	-5.5 ± 0.1	-5.8 ± 0.1

Table 6.2 Maximum response and EC_{50} values for peptide agonists in the G_i activation assay in HEK 293 cells expressing wildtype HA-rMOPR or $L219^{ECL2}A$ variant receptors

Data are expressed as mean ± SEM, of 5 independent experiments. * $p < 0.05$, significantly different from the respective WT value (two-way ANOVA, post-hoc Sidak's test for differences in ligand response between $L219^{ECL2}A$ and wildtype).

6.3.5 MOPr internalisation

In the absence of MOPr-RlucII BRET constructs containing the desired mutations (see Section 6.2.2), MOPr internalisation in response to opioids was used as a proxy for arrestin recruitment. GPCR internalisation following arrestin recruitment is a well-documented phenomenon, and the ability of MOPr agonists to induce internalisation generally correlates with efficacy in arrestin recruitment assays (6, 21, 355).

HEK 293 cells expressing either the wildtype HA-rat MOPr, or the W293$^{6.48}$A or L219^{ECL2}A variants were prelabelled with HA-antibody and then incubated with 30 µM DAMGO, endomorphin-2, bilorphin or vehicle for 30 minutes. Cell surface receptor ELISAs were then performed as described in Chapter 2 Section 2.2.8. Receptor internalisation was expressed as the percentage decrease in absorbance compared to vehicle-treated cells. As with the previous ELISAs (Section 6.3.3), in vehicle-treated cells the surface expression of the MOPr variants was approximately equal to wildtype (Figure 6.8a), suggesting that not only was the surface expression of the MOPr unaffected by the point mutations, but that the level of constitutive receptor internalisation, if any, was also not altered in the W293$^{6.48}$A or L219^{ECL2}A variants.

In agreement with previous reports (21, 240), at the wildtype receptor DAMGO and endomorphin-2 both induced robust internalisation of the MOPr (grey bars, Figure 6.8b); 30 µM DAMGO induced 47.3 ± 3.0 % loss of the MOPr from the cell surface, whilst the same concentration of endomorphin-2 resulted in 30.7 ± 5.6 % internalisation. In contrast, at the wildtype receptor bilorphin induced a very low internalisation response, 6-fold lower than that of DAMGO, with only an 8.0 ± 5.7 % loss of receptor from the plasma membrane (grey bars, Figure 6.8b). This lack of efficacy for bilorphin in inducing MOPr internalisation agrees with the report by *Dekan et al.,* describing bilorphin as a non-internalising, G protein-biased agonist (344).

There was no detectable internalisation of the W293$^{6.48}$A MOPr in response to any of the three peptide agonists tested (red bars, Figure 6.8b).

Both DAMGO and endomorphin-2 induced internalisation of the L219^{ECL2}A receptor, with neither response significantly different from wildtype (blue bars, Figure 6.8b). Unexpectedly, the L219^{ECL2}A mutation converted the non-internalising G protein-biased ligand, bilorphin, into an agonist for MOPr internalisation. 30 µM bilorphin induced 29.7 ± 8.9 % internalisation of the L219^{ECL2}A receptor (blue bars, Figure 6.8b), significantly higher than the wildtype response and similar in magnitude to that of endomorphin-2 (Figure 6.8b).

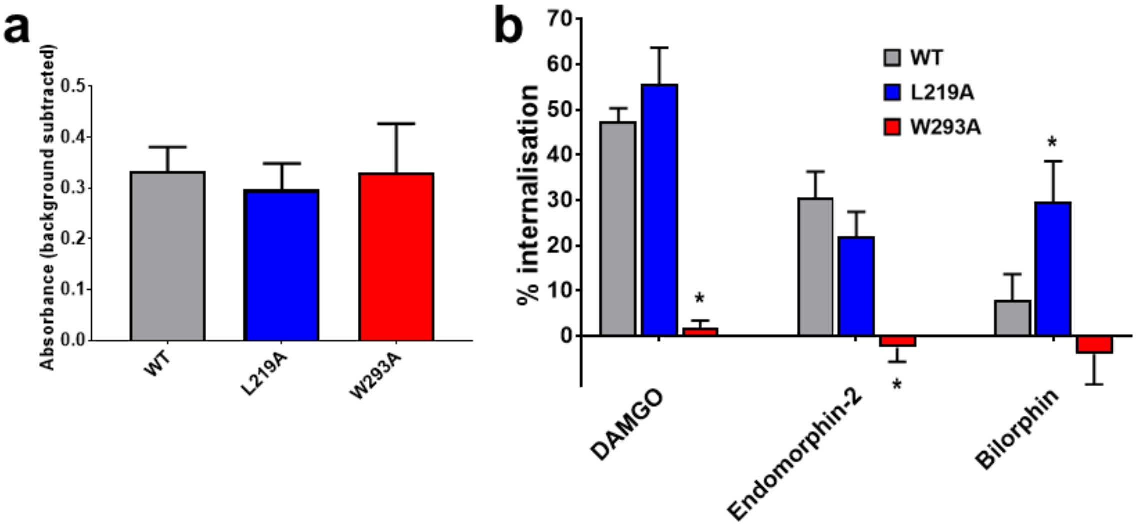

Figure 6.8 Ligand-induced receptor internalisation in the MOPr mutants

Ligand-induced receptor internalisation was measured by surface receptor ELISA in HEK 293 cells expressing either HA-rat MOPr (grey bars), HA-L219^{ECL2}A (blue bars) or HA-W293$^{6.48}$A (red bars). a) In cells treated with vehicle, surface expression of the L219^{ECL2}A and W293$^{6.48}$A MOPr variants was equal to wildtype HA-rat MOPr. b) Loss of receptor from the cell surface in response to 30 µM DAMGO, endomorphin-2 or bilorphin was expressed as the percentage decrease in absorbance compared to vehicle-treated cells. All data are expressed as mean ± SEM, of 5 independent experiments. * $p < 0.05$, two-way ANOVA, post-hoc Dunnett's test for differences in ligand response between the MOPr variant and wildtype.

6.4 Discussion

Using evidence from the MD simulations of ligand-MOPr complexes from Chapters 4 and 5, we hypothesised firstly that, as has been shown in other GPCRs, W293$^{6.48}$ is a key residue in translating the binding of an agonist to MOPr activation. Secondly, MD simulations of the peptide-MOPr complexes suggested that interactions with the conserved hydrophobic residue L219^{ECL2} may be a predictor of efficacy for arrestin recruitment. In this chapter, I used both *in silico* and *in vitro* mutagenesis to test these hypotheses by molecular modelling and in cell signalling assays.

MD simulations of the W293$^{6.48}$A MOPr model suggested this mutation produces a receptor incapable of being activated. Whilst the binding pose and overall protein conformation of the antagonist- (diprenorphine) bound receptor was not significantly altered in the W293$^{6.48}$A variant compared to wildtype, for the high efficacy agonist norbuprenorphine this single amino acid change was sufficient to alter both the ligand binding pose and the conformational state of the receptor. This finding demonstrates that as in other GPCRs (349, 350, 356), the activation of the MOPr is coupled to the behaviour of this important residue.

This prediction of the effect of this W293$^{6.48}$A mutation was reflected in the cell signalling results; the W293$^{6.48}$A MOPr variant was expressed on the cell surface but did not activate the G_i G protein nor internalise in response to a high concentration of any opioid agonist tested. However, this is in contrast to results reported for the DOPr where a W6.48L mutation selectively abrogated arrestin recruitment in response to the peptide agonist DADLE, but only had a modest effect on G protein-mediated signalling (161). It is also interesting that in the MOPr the W293$^{6.48}$A mutation completely abolished ligand-induced signalling for all opioids used in this study. In a study of the 5HT$_4$ receptor although there was an almost 30-fold difference in the EC$_{50}$ values, 5HT still invoked an agonist response in a cAMP assay with the W6.48A mutant (160), whereas for the 5HT$_4$ receptor-selective agonist BIMU8 the W6.48A mutation substantially affected agonist activity. In contrast, the data presented in this chapter suggests that for the MOPr the lack of signalling in the W293$^{6.48}$A variant is independent of the opioid agonist used.

However, it is important to note that this lack of response could be due to ligands having a reduced affinity for the W293$^{6.48}$A variant compared to wildtype. W293$^{6.48}$ is located in the orthosteric binding site and all 8 opioids investigated in this thesis interacted with W293$^{6.48}$ in the MD simulations (see Chapter 4 Section 4.3.2 and Chapter 5 Section 5.3.3). Indeed, the equivalent mutation in the angiotensin II AT1 receptor resulted in a 7-fold reduction in the binding of angiotensin, whilst in the muscarinic M_3 receptor the W6.48A mutation reduced the binding affinity of all ligands tested by up to 24-fold (155, 156). However, in the DOPr, mutating W6.48 had variable effects on ligand binding, reducing the affinity of some ligands but enhancing that of others (157). In the only published report of a W6.48 point mutation in the MOPr, substituting W6.48 for a cysteine residue reduced diprenorphine binding 3-fold, but did not abolish binding completely (357). No functional data was reported in this study. To more fully characterise the W293$^{6.48}$A MOPr variant described in this chapter, it will be important in due course to perform radioligand binding studies to determine the binding affinity of tritiated diprenorphine, and whether the W293$^{6.48}$A mutation has divergent effects on the binding of agonists versus antagonists. The MD simulation data presented here would suggest that agonist binding may be more adversely affected than antagonist binding.

The data presented in this chapter, therefore, supports the role of W293$^{6.48}$ as an important microswitch in transducing agonist binding to the subsequent activation of the MOPr, as in both the MD simulations and the cell signalling studies the W293$^{6.48}$A mutation produced an inactive receptor.

The MD simulation data for the L219^{ECL2}A variant were more difficult to interpret. The binding pose of endomorphin-2 appeared more altered by this mutation than that for bilorphin, however it is difficult to determine whether this relatively small change was due to the L219^{ECL2}A substitution or merely differences between two independent sets of simulations occurring by chance. Intriguingly, we also observed a change in the rotameric state of W293$^{6.48}$ in the endomorphin-2-bound L219^{ECL2}A receptor, which may indicate an important allosteric link between L219^{ECL2} and this microswitch.

In HEK 293 cells, the L219^{ECL2}A variant also reached the cell surface and responded to opioid agonists to both signal through G protein and internalise. However, the L219^{ECL2}A variant had divergent effects on the ligand-induced signalling by different agonists. For the reference agonist DAMGO there was no significant difference between the wildtype and L219^{ECL2}A responses in either the G_i activation assay or in the receptor internalisation assay. In contrast, the arrestin-biased peptide endomorphin-2 had a small (3-fold decrease in potency) yet significantly right-shifted G_i activation curve for the L219^{ECL2}A mutant compared to wildtype, but no significant difference in the level of internalisation induced by a receptor-saturating concentration of agonist was observed. There was no difference in the ability of the G protein-biased agonist bilorphin to activate G_i in wildtype or L219^{ECL2}A MOPr, but the L219^{ECL2}A mutation converted bilorphin to an internalising agonist, producing a similar level of receptor internalisation to endomorphin-2. This result was unexpected and suggests an important role of L219^{ECL2}, or more broadly ECL2, in modulating MOPr signalling. In the absence of full concentration-response curves in an arrestin recruitment assay it is difficult to comment on the effect of the L219^{ECL2}A mutation on the bias profile of endomorphin-2. However, for bilorphin the ability of this G protein-biased peptide to induce robust MOPr internalisation at the L219^{ECL2}A receptor suggests that this mutation may have abolished the bias profile of this ligand such that at the L219^{ECL2}A MOPr bilorphin becomes an un-biased agonist. To test this hypothesis further it would be necessary to conduct full concentration-response curves in an arrestin recruitment or receptor internalisation assay to allow calculation of bias factors. In addition, as discussed for the W293$^{6.48}$A variant, radioligand binding studies would confirm whether the affinity of these ligands was affected by the L219^{ECL2}A mutation.

These data on the effect of the L219^{ECL2}A mutation on arrestin-mediated signalling do not correspond to previous work on aminergic receptors, where the equivalent mutations abolished arrestin recruitment (186, 187). These divergent effects of ECL2 point mutations suggest that the role of ECL2 in ligand binding and receptor function is not a universally conserved mechanism across GPCRs. As discussed in Chapter 4, the MOPr is endogenously a peptide receptor, and therefore it may be unsurprising that the precise mechanisms of receptor activation and modulation of signalling responses do not correspond to those seen in GPCRs which are primarily activated by small molecules.

However, one finding in this chapter which does agree with the study by *Wacker et al.*, concerns the movement of ECL2. The behaviour of GPCR extracellular loops has been proposed to affect ligand kinetics (181, 186, 191, 358) and in our MD studies we observed enhanced flexibility of ECL2 in the L219^{ECL2}A variant compared to wildtype. Similarly, both ECL2 flexibility and ligand off-rate were enhanced by the L209^{ECL2}A mutation in the 5HT$_{2B}$ receptor (186). It would be interesting to investigate the binding kinetics of opioid ligands at the L219^{ECL2}A MOPr variant to determine if the effect of mutating this ECL2 residue is conserved in Class A GPCRs, and therefore whether this points to a more general role of ECL2 in ligand binding kinetics.

It must be noted that conclusions drawn from any mutagenesis study come with certain caveats. Firstly, single point mutations may change the protein structure beyond just the one residue of interest. For instance, mutations which substitute one amino acid for another with very different side chain properties may alter protein folding and packing between helices. However, as both MOPr variants described in this chapter were expressed on the cell surface, it is likely that the receptor is folded correctly. Additionally, differences observed between a receptor variant and wildtype may not be due to the specific residue substitution itself but may alter the behaviour of other nearby residues due to the disruption or formation of important contacts between side chains. In this study, the effect of the W293$^{6.48}$A mutation could be directly due to the loss of the tryptophan itself or removing this bulky residue may impact the conformation of other residues, for instance those in the nearby allosteric sodium ion binding site, PIF motif, or orthosteric binding pocket. Similarly, in the MD simulations the L219^{ECL2}A mutation increased the mobility of residues throughout ECL2, and so it is difficult to delineate whether the changes we observe are due to the loss of the leucine or the downstream effect this point mutation has on other parts of the receptor. An interesting example of this are the crystal structures of two adenosine A_{2A} receptor variants; D52$^{2.50}$N and S91$^{3.39}$A. Both mutations are in the allosteric sodium site, but the resolved structures displayed alternative conformations of the spatially distant NPxxY motif (137), demonstrating an allosteric link between the mutation sites and this motif. As our MD simulations do not capture the fully active state of the MOPr (as discussed in Chapter 4 Section 4.4 and Chapter 5 Section 5.4), I could not determine the effect of either point mutation on the conformation of activation motifs far from the orthosteric binding site.

6.5 Conclusions

Using both MD simulations and *in vitro* cell signalling assays, in this chapter I have shown that W293$^{6.48}$ is a crucial residue for ligand-induced activation of the MOPr. Whether this is primarily due to an effect on ligand affinity, or the ability of an agonist to induce the MOPr active state once bound, is yet to be determined. Nevertheless, this work highlights the key role of this W293$^{6.48}$ microswitch in MOPr function and demonstrates that hypotheses based on computational models can be validated *in vitro*.

Furthermore, I have characterised the L219^{ECL2}A MOPr variant both in MD simulations and in cell signalling assays. These data so far suggest that L219^{ECL2} is able to modulate MOPr function, possibly by affecting the behaviour of the W293$^{6.48}$ microswitch, and differentially modulates the signalling properties of oppositely biased MOPr agonists. Intriguingly, the G protein-biased agonist, bilorphin, exhibited enhanced internalisation of the L219^{ECL2}A receptor, a finding which was unexpected and may point towards an important role of L219^{ECL2} and ECL2 in the molecular mechanism of MOPr biased agonism.

Chapter 7: General Discussion

7.1 Research summary

GPCRs are important drug targets and the wealth of new structural data in recent years has improved our understanding of how these biologically important receptors function. The MOPr is a GPCR of great clinical and societal importance, due to its role in analgesia and drug abuse. Yet, relatively little is understood about how different opioids interact with the MOPr binding pocket and how different ligand-receptor interactions lead to different signalling outcomes. This thesis sought to use MD simulations combined with cell signalling assays to identify molecular mechanisms of agonist efficacy and agonist bias at the MOPr.

Using MD simulations, the interactions between a panel of 8 different opioid ligands and the MOPr orthosteric site were characterised. These compounds span the full spectrum of opioid activity, from antagonists to full agonists, and small molecule and peptide ligands. These *in silico* studies have modelled different MOPr conformations and highlighted residues which may be important in conveying opioid ligand efficacy and bias. *In vitro* cell signalling studies have characterised these same opioid ligands in BRET assays to detect G protein activation and arrestin recruitment. Furthermore, the expression of single point MOPr mutants in HEK 293 cells has translated the *in silico* findings to effects on ligand-induced MOPr signalling *in vitro*.

Firstly, MD simulations of the unliganded MOPr revealed that sodium will spontaneously bind to the conserved allosteric site of the inactive MOPr, whereas, sodium did not bind to the same site in the active state MOPr, where this allosteric pocket is collapsed.

Secondly, to investigate a potential molecular mechanism for opioid ligand efficacy, a series of small molecule opioid ligands of varying efficacy were docked to the MOPr and MD simulations performed. These MD simulations showed that although opioid ligands may share the same chemical scaffold, they can adopt distinct binding poses and thus interact with different subsets of residues (152). Moreover, the conformation of the W293$^{6.48}$ rotamer toggle switch was dependent on the bound ligand; higher efficacy ligands induced a greater rotameric change in this residue than the lower efficacy compounds. Conformational changes in the MOPr transmembrane helices also differentiated high and low efficacy ligands, with the norbuprenorphine-bound receptor occupying a different conformational cluster to the buprenorphine- or diprenorphine-bound receptor. The alternative ligand binding pose, W293$^{6.48}$ rotamer and helix conformations induced by norbuprenorphine were reversed in the presence of an allosteric sodium ion, suggesting a molecular mechanism for the negative modulatory effect of sodium at opioid receptors (115, 121, 152).

Thirdly, a structural basis for MOPr biased agonism was also investigated using the oppositely biased peptides, bilorphin and endomorphin-2. MD simulations predicted that whilst endomorphin-2 and DAMGO interacted with the MOPr ECLs, the G protein-biased peptide bilorphin did not (344). Moreover, these oppositely biased peptides stabilised different conformations of the MOPr, with the endomorphin-2-bound receptor favouring a more occluded conformation of the intracellular domain than the bilorphin-bound receptor.

Finally, these *in silico* findings were tested in *in vitro* cell signalling assays by producing the relevant single point mutations of the MOPr. Corroborating the MD simulation data, the W293$^{6.48}$A receptor did not respond to opioid agonist in *in vitro* cell signalling assays. The L219^{ECL2}A receptor subtly modulated the biased signalling of the MOPr peptides, such that the G protein-biased agonist bilorphin was able to produce greater internalisation of the L219^{ECL2}A receptor compared to wildtype.

This thesis therefore provides insight into several aspects of the molecular pharmacology of the MOPr. Namely, the allosteric modulation of the MOPr by sodium ions, how different small molecule and peptide MOPr ligands interact with the orthosteric binding pocket, the role of the W293$^{6.48}$ microswitch in agonist-induced MOPr activation, and the different binding modes of biased MOPr peptides.

7.2 Sodium modulation of MOPr function

In Chapter 3, using MD simulations of the unliganded (apo) MOPr, the binding of a sodium ion to the conserved allosteric sodium binding site in the inactive state receptor was observed. Both the binding pathway (via the extracellular vestibule and orthosteric site) and the residues involved in the coordination of the sodium ion in the allosteric site were in agreement with the position of sodium in high resolution crystal structures of other GPCRs (122-125) and other computational studies modelling the binding of sodium to Class A GPCRs (323-325, 359).

The negative modulatory effect of sodium ions on the MOPr appears to be due to interplay between the allosteric and orthosteric sites, as well as modulation of the W293$^{6.48}$ rotamer toggle switch (Figure 7.1a). The MD simulations presented in Chapter 4 suggest that high efficacy agonists may disrupt sodium binding, as norbuprenorphine favoured a deeper binding pose close to the allosteric site and high efficacy agonists induced a conformational change in the W293$^{6.48}$ microswitch which would be incompatible with a bound sodium ion. On the other hand, the presence of a sodium ion in the allosteric site disrupted this deeper binding pose of norbuprenorphine and stabilised the W293$^{6.48}$ indole ring in the inactive, vertical position. This is similar to MD simulations of the dopamine D_2 receptor, where the entrance of a sodium ion into the helix bundle was coupled to the toggle motion of W6.48 (359).

Therefore, there appears to be allosteric communication between the orthosteric agonist and sodium binding sites, with occupation of either site modulating the other, possibly via the rotameric state of W293$^{6.48}$. Indeed, disruption of the sodium site may be a general mechanism for agonist activation of the MOPr and other GPCRs. As discussed in Chapter 1 Section 1.2.3.3, the positive allosteric modulation of the MOPr by BMS-986122 has been suggested to be due to disruption of sodium binding (135), thus releasing the brake on receptor activation. Recently, a putative novel binding site for the agonist acetylcholine at muscarinic M_3 and M_4 receptors was identified using MD simulations; this new binding site is in fact the allosteric sodium site (286). Moreover, an inverse agonist of the leukotriene B4 receptor exerts its activity-quenching effect by occupying the allosteric sodium site, mimicking a bound sodium ion, and thereby stabilising the inactive state (360). Conversely, our group has recently performed MD simulations of the active state MOPr bound to fentanyl, suggesting that the ligand's phenethyl group binds within the second coordination shell of the allosteric sodium site, allowing fentanyl to exert its highly potent agonist effect, presumably by disrupting sodium binding (361). In their review of the mechanism of sodium modulation of GPCRs, *Katritch et al.,* elegantly argue not only that disruption of the bound sodium may be an activation mechanism in Class A GPCRs, but also that the egress of sodium from the allosteric site into the cytoplasm may provide an energy source for GPCR signalling (138). Whilst the MD simulations in this thesis did not sample a sodium ion relocating to the intracellular side of the membrane, the data do support a mechanism for agonist disruption of sodium binding.

The MD simulations presented in this thesis, and the other cited reports, were carried out in the absence of an electrochemical gradient across the bilayer. Physiologically, the drive for sodium ions to bind from the extracellular side of the MOPr, and potentially relocate to the cytoplasm, would be even greater due to the concentration and potential difference across the membrane. The propensity for sodium ions to bind to the MOPr may even be influenced by the membrane potential. Indeed, MD simulations of the DOPr under a membrane potential have shown voltage-sensitivity of sodium binding (140). The MOPr is primarily expressed on excitable tissue where the membrane potential changes subject to neurotransmission. Other Class A GPCRs have been shown to be voltage-sensitive (141-145), and some authors have argued that GPCR voltage sensitivity may be mediated by the movement of cations, such as sodium, within the transmembrane helix bundle (140). It is tempting to speculate therefore, that for GPCRs expressed on neurons there is an important physiological role of sodium ion modulation of receptor function to fine-tune GPCR signalling. Perhaps, drugs acting on the allosteric sodium binding site of the MOPr may be a strategy for specifically targeting opioid receptors expressed on overactive neurones in pain states. In any case, it is important to understand how physiological concentrations of sodium alter ligand binding and MOPr function.

7.3 Opioids exhibit distinct binding poses

The main purpose of this thesis was to characterise the binding modes of a series of opioid ligands with the MOPr orthosteric binding pocket. A central theme throughout is that despite sharing similar chemical structures, opioid ligands are predicted adopt distinct binding poses (152).

The work presented in this thesis highlights the importance of using both molecular docking and MD simulations to predict ligand binding poses. For instance, in Chapter 4 docking alone would not have revealed the deeper binding pose of norbuprenorphine compared to its analogues, buprenorphine and diprenorphine. Using both docking and MD simulations, norbuprenorphine was found to adopt a pose close to the allosteric sodium ion binding site, interacting with different residues and causing the rotameric change in the W293$^{6.48}$ microswitch (152). These differences in ligand binding pose may explain norbuprenorphine's higher efficacy compared to the lower efficacy yet structurally similar ligands.

Moreover, in Chapter 5, although endomorphin-2 and bilorphin are both tetrapeptides with an N-terminal tyrosine (or tyrosine-like) residue, they adopted different poses in the orthosteric site. Bilorphin, probably due to its unusual stereochemistry of alternating L and D amino acids, extended towards the opposite side of the MOPr pocket compared to endomorphin-2 and DAMGO. Bilorphin thus accessed the alternative extended binding pocket and contacted TM1 (344). These different binding poses may provide an explanation for the different bias profiles of these compounds and will be discussed further in Section 7.5.

The observation that structurally similar compounds can nevertheless adopt different binding positions is not unique to the MOPr. For instance, comparison of the x-ray crystal structures of the $5HT_{2B}$ receptor bound to LSD or ergotamine revealed that ergotamine could rotate around the amine-D3.32 salt bridge to adopt a deeper binding position than its analogue LSD (186). This has obvious parallels with the norbuprenorphine work presented in Chapter 4, where norbuprenorphine also pivoted around the amine-D147$^{3.32}$ interaction (152). Moreover, distinct ligand-receptor interaction fingerprints, such as those reported in Chapters 4 and 5, have been successfully used in structure-based discovery efforts to find new compounds targeting GPCRs and to predict ligand activity (339, 362-367).

One caveat to the MD simulation data described here is that, as detailed in Chapter 2 Section 2.1.3.2, the molecular docking protocol used just the extracellular portion of the MOPr as the search space, meaning that binding poses outside of this region were not evaluated. Binding pose selection was then rationalised partly based on the presence of the canonical interaction between the opioid amine and D147$^{3.32}$, as this residue has been highlighted as an essential residue of opioid ligand binding in mutagenesis studies (95, 111-113). However, the reliance on this interaction as a determining factor for selecting a binding pose may mean that other alternative binding modes may have been missed.

However, these caveats notwithstanding, we can be reasonably confident in the predicted binding poses reported here, due to the similarities between our modelled DAMGO-MOPr complex (Chapter 5) and the subsequently reported cryoEM structure of DAMGO bound to the G_i-coupled MOPr (23). As DAMGO is a pentapeptide, it is one of the most flexible ligands studied in this thesis, and therefore potentially more difficult to accurately model. However, the binding position, conformation of key residues (such as W293$^{6.48}$) and the conformation of DAMGO itself were very similar between our model and the cryoEM structure.

The MOPr has a remarkably deep orthosteric binding pocket compared to other Class A GPCRs, and it may be this larger available volume which gives rise to the different binding modes observed here. As discussed in Chapter 1 Section 1.5, this could be because the MOPr has evolved to respond to peptides rather than small molecule ligands.

7.4 The W293$^{6.48}$ activation switch

The data in this thesis supports the hypothesis that W293$^{6.48}$ serves as a link translating agonist binding to activation-related MOPr conformational changes (Figure 7.1a). In Chapters 4 and 6, ligand efficacy for G protein signalling correlated with W293$^{6.48}$ conformation in the MD simulations, as agonists with higher efficacy for G protein signalling, such as DAMGO, norbuprenorphine and methadone, elicited greater rotameric changes in the W293$^{6.48}$ side chain than lower efficacy ligands, such as diprenorphine, buprenorphine and morphine. This finding is in agreement with both experimental studies and other computational work. One of the first studies to identify the W6.48 toggle switch used NMR spectroscopy of rhodopsin to show spectral changes around W6.48 in the light verses dark state (368). Whilst MD simulations of the adenosine A_3 receptor and β_2 adrenoceptor have correlated the W6.48 rotameric state with ligand efficacy (356, 369, 370). Furthermore, in this thesis the conformational change in W293$^{6.48}$ could be prevented by addition of an allosteric sodium ion, which, as discussed above, has a negative modulatory effect on MOPr function (Section 7.2).

In the simplified model depicted in Figure 7.1a, in the presence of an antagonist or a high sodium concentration, the W293$^{6.48}$ side chain is stabilised in the inactive, vertical state. The binding of an agonist induces the movement of the W293$^{6.48}$ indole ring, causing sodium to relocate to the intracellular side of the membrane, and initiating conformational changes in the helices to promote G protein coupling.

However, it should be noted that this correlation between the W293$^{6.48}$ dihedral and ligand efficacy was largely influenced by DAMGO and norbuprenorphine which both induced the greatest change in the W293$^{6.48}$ dihedral. Ligands such as endomorphin-2 and morphine, which do have reasonable efficacy in activating G_i (21), did not stabilise the horizontal conformation of W293$^{6.48}$. These discrepancies suggest that whilst W293$^{6.48}$ is an important residue for MOPr activation, there are likely other mechanisms which can also translate agonist binding to activation of the receptor. For instance, the PIF motif is also adjacent to the ligand binding site and has been implicated in receptor activation, primarily in aminergic receptors but also the MOPr (22, 162, 165). Alternatively, with lower efficacy ligands bound, the probability of the W293$^{6.48}$ conformational change may be lower and therefore is not sampled within the simulation times achieved here.

Moreover, the W6.48 rotamer toggle switch is likely to work in concert with other GPCR activation mechanisms. For example, *Yuan et al.*, suggest that rotameric changes in W6.48 allow for hydration of the GPCR helix bundle (371). The influx of water would alter the hydrogen bond network from the orthosteric site to the intracellular domain and hence lead to conformational changes in the G protein coupling region. An NMR spectroscopy study of the adenosine A_{2A} receptor and the D2.50A variant showed interplay between W6.48 and D2.50 of the allosteric sodium ion binding site (349). The authors suggest a model whereby agonist-induced conformational changes in W6.48 are transmitted to D2.50 which then causes conformational changes in the GPCR intracellular domain.

In Chapter 6, mutagenesis of W293$^{6.48}$ to alanine both in the molecular modelling and in *in vitro* experiments supported the hypothesis that W293$^{6.48}$ is a critical residue for MOPr activation. In the MD simulations, with either norbuprenorphine or diprenorphine bound, the W293$^{6.48}$A receptor did not sample the alternative active-like conformation observed in the norbuprenorphine-bound wildtype receptor. This suggested that W293$^{6.48}$ is required for the conformational changes in the MOPr helices associated with receptor activation, and therefore the W293$^{6.48}$A mutation produces a receptor incapable of being activated. This was reflected in the cell signalling studies, where the W293$^{6.48}$A mutant did not signal through the G_i G protein or internalise in response to opioid agonist. Clearly, W293$^{6.48}$ is required for agonist-induced MOPr signalling, either as an “efficacy switch” between the orthosteric site and the intracellular cavity, or as a critical residue for ligand binding, or a combination of effects on both ligand affinity and efficacy. Similarly, in the adenosine A_3 receptor, mutation of W6.48 resulted in a receptor which still bound ligand but did not signal (372), whereas, at the neuropeptide Y2 receptor, a W6.48 mutation only reduced agonist potency and interestingly, this effect could be rescued using agonists containing a bulky aromatic group to mimic the indole ring of W6.48 (159). Adding further complexity, *Stoddart et al.,* showed that a W6.48F mutation of the adenosine A_3 receptor impaired G protein signalling of both agonists tested, but had differential, ligand-dependent effects on receptor internalisation (158). Together, these studies and the data in this thesis suggest an important role for W6.48 in GPCR activation, but that the precise nature of how W6.48 modulates receptor function is dependent on the receptor and the ligand in question. For the MOPr, the data in this thesis suggests that mutation of W6.48 appears to abolish either the binding or ligand-induced signalling of any opioid agonist, indiscriminately.

To our knowledge, this is the first study which has reported functional data for a $W293^{6.48}$ mutation in the MOPr, which alongside the computational data, contributes to our understanding of how agonists promote GPCR activation via the $W293^{6.48}$ microswitch. This study also serves as another example of how MD simulations can successfully model and predict the behaviour of biological molecules (see Chapter 1 Section 1.4.3). Furthermore, the observation that the position of the $W293^{6.48}$ indole ring in the MD simulations corresponded to agonist efficacy in an experimental system has potentially useful implications for future *in silico* screening efforts for the discovery of new MOPr compounds. Lower efficacy MOPr agonists, notably buprenorphine and oliceridine, have been reported to be safer yet still therapeutically efficacious analgesics (261, 373, 374), whilst new MOPr antagonists which can reverse opioid overdose may be required to combat the rising fentanyl epidemic (375). With these applications in mind, monitoring the conformation of $W293^{6.48}$ could serve as a predictor of efficacy in structure-based drug design.

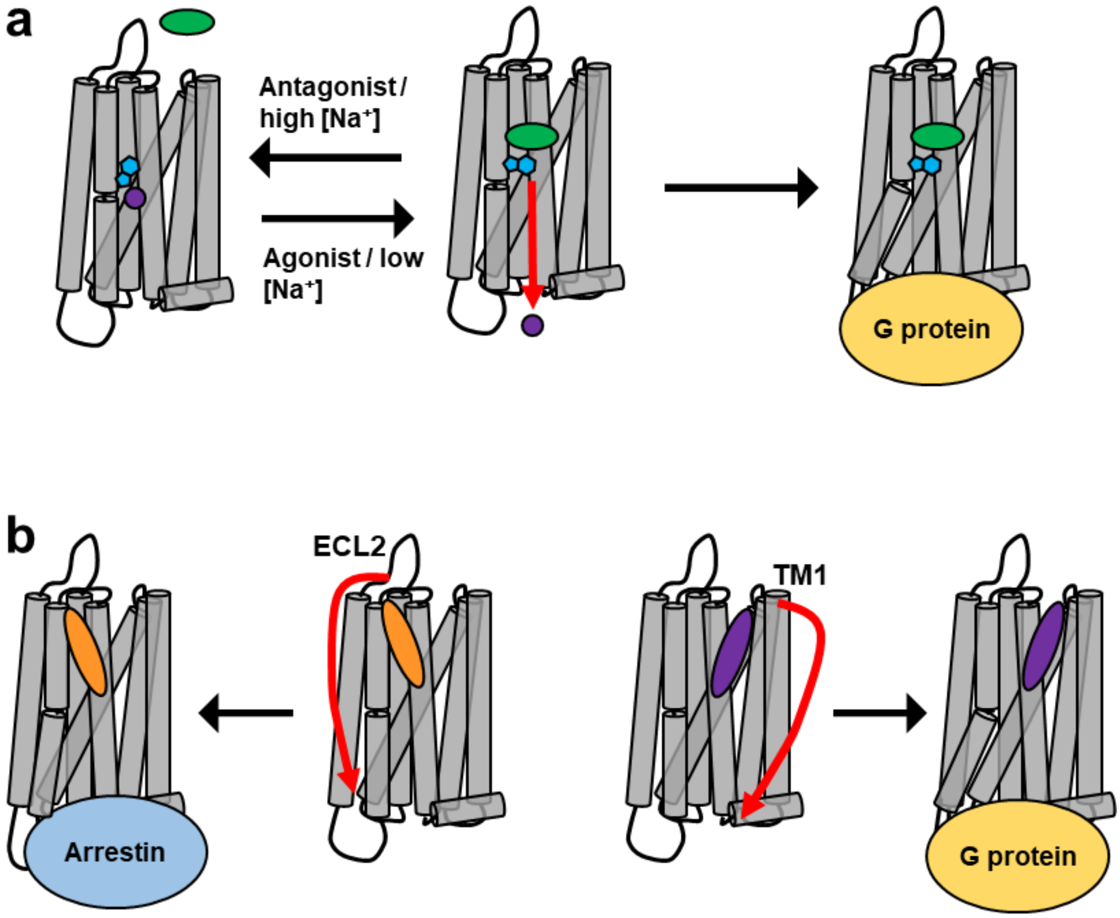

Figure 7.1 Proposed model for agonist efficacy and bias at the MOPr

a) In the inactive state, a sodium ion (purple) is bound in the allosteric site, maintaining W293$^{6.48}$ (blue) in the vertical conformation. In this conformation, agonist binding is unfavourable. Upon agonist binding (green), W293$^{6.48}$ switches to the horizontal conformation, disrupting sodium binding so that the ion moves into the cytoplasm. W293$^{6.48}$ is coupled to conformational changes in the MOPr helices, allowing binding of a G protein (yellow) to the intracellular cavity.

b) An arrestin-biased agonist (orange) contacts or modulates residues in the extracellular loops, which translates to conformational changes on the intracellular side so that the MOPr adopts the “occluded” conformation capable of binding arrestin (blue). A G protein-biased agonist (purple) contacts or modulates residues in TM1, translating to the more “open” conformation of the intracellular cavity so that the MOPr can couple to a G protein.

7.5 Molecular mechanisms of MOPr ligand bias

To investigate a molecular mechanism for biased agonism at the MOPr, in Chapter 5 two oppositely biased agonists, endomorphin-2 and bilorphin, along with the reference agonist DAMGO were docked to the MOPr and MD simulations performed. Analysis of the MD simulation data revealed that these peptides adopted different binding poses with respect to their interactions with the extended binding pocket (Figure 7.1b). As depicted in the model in Figure 7.1b, the peptides which recruit arrestin, endomorphin-2 and DAMGO, interacted with the ECLs, whereas the G protein-biased agonist, bilorphin, did not. Instead bilorphin, uniquely amongst the ligands studied in this thesis, contacted residues in TM1.

Similarly, an *in silico* study modelling agonist binding and allosteric communication between the orthosteric site and the G protein binding cavity found that the weakly G protein-biased MOPr agonist, oliceridine, utilised residues in TM1 to transfer information to the intracellular domain (263). Interestingly, another computational study attempting to identify regions of allosteric communication between the binding site and intracellular region also identified the extracellular end of TM1 as important for allosteric communication when the DOPr was bound to a G protein-biased agonist (376). Furthermore, the cryoEM-resolved structure of the G protein-biased peptide, ExP5, bound to the GLP-1 receptor revealed interactions between the ligand and TM1 (108). Together, these studies and the data presented in this thesis suggest that TM1 may be an important hub for G protein bias.

The current well-accepted model for the molecular mechanism of agonist bias is the stabilisation of distinct GPCR conformations which have different affinities for intracellular signalling partners (221, 377). The data presented in Chapter 5 support this hypothesis, as principal component analysis of the ligand-MOPr simulations showed that the biased peptides stabilised different conformations of the MOPr helices. Specifically, with endomorphin-2 bound the receptor favoured a more closed conformation of the intracellular domain, compared to the bilorphin-bound MOPr. This is perhaps similar to the “occluded” arrestin-biased conformations of the angiotensin II type I receptor and the MOPr reported in DEER and NMR spectroscopy studies (224, 262).

However, the question of exactly how the presence or absence of ligand contact with the ECLs or TM1 translates to different conformations of the MOPr intracellular domain is yet to be determined. GPCRs are allosteric machines, evolved to transduce the signal of a ligand binding to the extracellular portion of the protein through to a conformational change of the intracellular domain, nearly 30 Å away from the orthosteric site. It is perhaps unsurprising therefore, that the primary differences between biased and unbiased agonists which have been captured so far are in the interactions and movements of the ECLs and extracellular ends of the transmembrane helices. How these changes are translated to the intracellular cavity may eventually be resolved with more structures of GPCR-effector complexes bound to different biased agonists.

As L219^{ECL2} was one of the residues contacted by endomorphin-2 and DAMGO, but not bilorphin, and has been previously identified as important for encoding bias and ligand residence time in aminergic receptors (186, 187), in Chapter 6 I produced a single point mutation of this residue to determine the effect on MOPr signalling. Unlike the W293$^{6.48}$A mutation, the L219^{ECL2}A mutant had a subtle effect on ligand-induced MOPr signalling. In the G protein BRET assay, DAMGO and endomorphin-2 exhibited a small decrease in potency compared to the wildtype receptor, whilst in the receptor internalisation assay, the L219^{ECL2}A mutation converted bilorphin to an internalising agonist. Hence, it could conceivably be hypothesised that L219^{ECL2} can modulate bias between G protein and arrestin pathways, as at the L219^{ECL2}A mutant bilorphin is unlikely to be G protein-biased.

However, these results should be interpreted with caution, as without full concentration-response curves in an arrestin assay it cannot be definitively concluded whether the bias profile of bilorphin had been altered by the L219^{ECL2}A mutation. Moreover, based on a MD simulation data a greater effect of the L219^{ECL2}A substitution may have been expected, particularly on the potency of endomorphin-2. In the MD simulations of the L219^{ECL2}A receptor, endomorphin-2 induced greater rotameric changes in the W293$^{6.48}$ rotamer toggle switch than at the wildtype MOPr, but this did not translate to increased potency of endomorphin-2 in the G protein BRET assay. In fact, the opposite was evident. Other residues in the alternative extended binding pockets may have a more profound effect on the signalling profiles of these peptides. For example, W133^{ECL1}, T218^{ECL2} and Y75$^{1.39}$.

Another mechanism of biased agonism has been proposed whereby ligand residence time is linked with arrestin recruitment, as in general, MOPr agonists with a slower off-rate show greater efficacy for arrestin recruitment (347). Similarly, in the 5HT$_{2B}$ receptor, interactions between LSD and ECL2 controlled both ligand dissociation rate and arrestin recruitment (186). Whilst conventional MD simulations cannot determine ligand binding kinetics, it is possible that the lack of interaction between bilorphin and the ECLs results in the faster off-rate and minimal arrestin recruitment stimulated by this biased ligand (344, 347).

Overall, the data presented here add to the body of literature proposing that agonist bias is due to the stabilisation of different receptor conformations (162, 221, 222, 224, 262, 343, 377). Moreover, for the two biased compounds studied, differential interactions with the ECLs and TM1 may be the mechanism by which these alternative MOPr states are achieved.

7.6 Future directions

To more fully test the hypotheses presented in this thesis, it would be necessary to use a greater panel of opioid ligands to determine if for instance, changes in the W293$^{6.48}$ rotamer are conserved across different opioid agonists, or whether interaction with the ECLs is a common differentiator between opioids of opposing bias profiles. Furthermore, with a much larger test set of ligands, machine learning approaches (378-380) could be utilised to analyse the MD simulation data to identify conserved ligand-residue interactions, pharmacophores and conformational signatures associated with different signalling outcomes.

To establish whether the lack of agonist-induced signalling at the W293$^{6.48}$A mutant is due to an effect on agonist binding or agonist efficacy, radioligand binding studies need to be conducted to measure the binding of the MOPr antagonist ^{3}H-diprenorphine and its displacement by opioid agonists. If agonist binding is unimpaired at this MOPr variant, it would be interesting to determine whether the lack of the W293$^{6.48}$ activation switch prevents formation of the agonist-bound and G protein-coupled high affinity state (381, 382). The MD simulations presented in Chapter 6 predict that the W293$^{6.48}$A mutation would cause the MOPr to adopt an inactive conformation, and therefore would not exhibit a G protein-coupled high affinity state.

Building on the work using the L219^{ECL2}A MOPr variant, it would be interesting to examine the trafficking of this mutant. When stimulated with DAMGO or endomorphin-2 the L219^{ECL2}A receptor was internalised, presumably via the canonical arrestin-dependent mechanism (383). When stimulated with bilorphin, unlike the wildtype MOPr, the L219^{ECL2}A mutant was internalised. This may be arrestin-mediated or via an arrestin-independent mechanism. Similarly, the naturally occurring single nucleotide polymorphism (SNP), L83$^{1.47}$I, unlike the wildtype MOPr, internalises in response to morphine, but with no corresponding increase in DAMGO-induced internalisation (317). *Cooke et al.*, found morphine-induced internalisation of this SNP to be GRK2-dependent, but with no change in the levels of S375 phosphorylation or arrestin recruitment, concluding that the enhanced internalisation in response to morphine may be via a novel endocytic process (317). It would be interesting to conduct the same kind of study with the L219^{ECL2}A mutant to determine if there are any parallels in the agonist-induced trafficking of these MOPr variants.

The MD simulation data presented in this thesis also identifies other residues which may be important for encoding ligand efficacy or bias at the MOPr. For instance, residues in the ECLs other than L219^{ECL2} were contacted by DAMGO and endomorphin-2 but not bilorphin, notably W133^{ECL1}, whereas Y75$^{1.39}$ formed part of the extended binding pocket for bilorphin. As well as W293$^{6.48}$, other residues in the allosteric sodium site are likely to affect ligand efficacy, for instance D114$^{2.50}$ and N150$^{3.35}$. Further research could also be conducted to determine the effect of a single point mutation of one or more of these residues, and others, on ligand binding and ligand-induced MOPr signalling.

Although the molecular modelling approach used here provides insight into the binding position of the opioid ligands within the orthosteric site, it does not capture the means of access or egress of the ligand between the extracellular milieu and the MOPr helix bundle. The use of advanced MD approaches, such as coarse grained or steered MD, could be employed to model the binding pathway of a ligand, as this may reveal further ligand-receptor interactions which can modulate MOPr conformation. In particular, the unusually slow dissociation rate of buprenorphine (333) may be explained by identification of another metastable binding site along the dissociation pathway. Moreover, in the sphingosine-1-phosphate, cannabinoid CB2 and PAR1 receptors, lipophilic ligands have been predicted to bind through the lipid bilayer via a channel in the receptor transmembrane domains (284, 285, 384). The fentanyls are highly potent and lipophilic MOPr agonists (385), and it is tempting to speculate that they may also exhibit such a binding mode.

7.7 Conclusion

The MD simulations presented in this thesis predict that opioid ligands adopt distinct binding poses in the MOPr orthosteric site. These ligands therefore interact with different subsets of residues, and these distinct ligand-residue interactions appear to translate to different conformations of the MOPr and hence different signalling outcomes. Through these simulations I also propose a mechanism for sodium ion negative modulation of MOPr function, via destabilisation of agonist binding and prevention of the conformational changes in the W293$^{6.48}$ microswitch and the MOPr helices. Using both MD simulations and expression of the W293$^{6.48}$A mutant in HEK 293 cells, the data in this thesis has shown that, like other Class A GPCRs, W293$^{6.48}$ is important for ligand-induced MOPr activation. Moreover, using the same techniques, I have characterised the binding modes of the MOPr biased agonists, endomorphin-2 and bilorphin. These MD simulation data, alongside expression of the L219^{ECL2}A MOPr variant, have demonstrated that for these peptides, interaction with the MOPr ECLs may modulate opioid ligand bias.

References

1. Curtis HJ, Croker R, Walker AJ, Richards GC, Quinlan J, Goldacre B. Opioid prescribing trends and geographical variation in England, 1998-2018: a retrospective database study. Lancet Psychiatry. 2019;6(2):140-50.

2. Benyamin R, Trescot AM, Datta S, Buenaventura R, Adlaka R, Sehgal N, et al. Opioid complications and side effects. Pain Physician. 2008;11(2 Suppl):S105-20.

3. Kolodny A, Courtwright DT, Hwang CS, Kreiner P, Eadie JL, Clark TW, et al. The prescription opioid and heroin crisis: a public health approach to an epidemic of addiction. Annu Rev Public Health. 2015;36:559-74.

4. Corbett AD, Henderson G, McKnight AT, Paterson SJ. 75 years of opioid research: the exciting but vain quest for the Holy Grail. British journal of pharmacology. 2006;147 Suppl 1:S153-62.

5. Stanczyk MA, Kandasamy R. Biased agonism: the quest for the analgesic holy grail. Pain Rep. 2018;3(3):e650.

6. Williams JT, Ingram SL, Henderson G, Chavkin C, von Zastrow M, Schulz S, et al. Regulation of mu-opioid receptors: desensitization, phosphorylation, internalization, and tolerance. Pharmacological reviews. 2013;65(1):223-54.

7. Waldhoer M, Bartlett SE, Whistler JL. Opioid receptors. Annu Rev Biochem. 2004;73:953-90.

8. Mollereau C, Parmentier M, Mailleux P, Butour JL, Moisand C, Chalon P, et al. ORL1, a novel member of the opioid receptor family. Cloning, functional expression and localization. FEBS Lett. 1994;341(1):33-8.

9. Pasternak GW, Pan YX. Mu opioids and their receptors: evolution of a concept. Pharmacological reviews. 2013;65(4):1257-317.

10. Inturrisi CE. Clinical pharmacology of opioids for pain. Clin J Pain. 2002;18(4 Suppl):S3-13.

11. Stoeber M, Jullie D, Lobingier BT, Laeremans T, Steyaert J, Schiller PW, et al. A Genetically Encoded Biosensor Reveals Location Bias of Opioid Drug Action. Neuron. 2018;98(5):963-76 e5.

12. Gomes I, Gupta A, Filipovska J, Szeto HH, Pintar JE, Devi LA. A role for heterodimerization of mu and delta opiate receptors in enhancing morphine analgesia. Proceedings of the National Academy of Sciences of the United States of America. 2004;101(14):5135-9.

13. George SR, Fan T, Xie Z, Tse R, Tam V, Varghese G, et al. Oligomerization of mu- and delta-opioid receptors. Generation of novel functional properties. The Journal of biological chemistry. 2000;275(34):26128-35.

14. Charles AC, Mostovskaya N, Asas K, Evans CJ, Dankovich ML, Hales TG. Coexpression of delta-opioid receptors with mu receptors in GH3 cells changes the functional response to micro agonists from inhibitory to excitatory. Molecular pharmacology. 2003;63(1):89-95.

15. Matthes HW, Maldonado R, Simonin F, Valverde O, Slowe S, Kitchen I, et al. Loss of morphine-induced analgesia, reward effect and withdrawal symptoms in mice lacking the mu-opioid-receptor gene. Nature. 1996;383(6603):819-23.

16. Hughes J, Smith TW, Kosterlitz HW, Fothergill LA, Morgan BA, Morris HR. Identification of two related pentapeptides from the brain with potent opiate agonist activity. Nature. 1975;258(5536):577-80.

17. Goldstein A, Fischli W, Lowney LI, Hunkapiller M, Hood L. Porcine pituitary dynorphin: complete amino acid sequence of the biologically active

heptadecapeptide. Proceedings of the National Academy of Sciences of the United States of America. 1981;78(11):7219-23.

18. Li CH, Chung D. Isolation and structure of an untriakontapeptide with opiate activity from camel pituitary glands. Proceedings of the National Academy of Sciences of the United States of America. 1976;73(4):1145-8.

19. Zadina JE, Hackler L, Ge LJ, Kastin AJ. A potent and selective endogenous agonist for the mu-opiate receptor. Nature. 1997;386(6624):499-502.

20. Handa BK, Land AC, Lord JA, Morgan BA, Rance MJ, Smith CF. Analogues of beta-LPH61-64 possessing selective agonist activity at mu-opiate receptors. European journal of pharmacology. 1981;70(4):531-40.

21. McPherson J, Rivero G, Baptist M, Llorente J, Al-Sabah S, Krasel C, et al. mu-opioid receptors: correlation of agonist efficacy for signalling with ability to activate internalization. Molecular pharmacology. 2010;78(4):756-66.

22. Huang W, Manglik A, Venkatakrishnan AJ, Laeremans T, Feinberg EN, Sanborn AL, et al. Structural insights into mu-opioid receptor activation. Nature. 2015;524(7565):315-21.

23. Koehl A, Hu H, Maeda S, Zhang Y, Qu Q, Paggi JM, et al. Structure of the mu-opioid receptor-Gi protein complex. Nature. 2018;558(7711):547-52.

24. Kurose H, Katada T, Amano T, Ui M. Specific uncoupling by islet-activating protein, pertussis toxin, of negative signal transduction via alpha-adrenergic, cholinergic, and opiate receptors in neuroblastoma x glioma hybrid cells. The Journal of biological chemistry. 1983;258(8):4870-5.

25. Raffa RB, Martinez RP, Connelly CD. G-protein antisense oligodeoxyribonucleotides and mu-opioid supraspinal antinociception. European journal of pharmacology. 1994;258(1-2):R5-7.

26. Carter BD, Medzihradsky F. Go mediates the coupling of the mu opioid receptor to adenylyl cyclase in cloned neural cells and brain. Proceedings of the National Academy of Sciences of the United States of America. 1993;90(9):4062-6.

27. Nagi K, Pineyro G. Kir3 channel signaling complexes: focus on opioid receptor signaling. Front Cell Neurosci. 2014;8:186.

28. Ikeda K, Kobayashi T, Kumanishi T, Niki H, Yano R. Involvement of G-protein-activated inwardly rectifying K (GIRK) channels in opioid-induced analgesia. Neurosci Res. 2000;38(1):113-6.

29. Montandon G, Ren J, Victoria NC, Liu H, Wickman K, Greer JJ, et al. G-protein-gated Inwardly Rectifying Potassium Channels Modulate Respiratory Depression by Opioids. Anesthesiology. 2016;124(3):641-50.

30. Williams JT, Egan TM, North RA. Enkephalin opens potassium channels on mammalian central neurones. Nature. 1982;299(5878):74-7.

31. North RA, Williams JT. On the potassium conductance increased by opioids in rat locus coeruleus neurones. J Physiol. 1985;364:265-80.

32. Schroeder JE, Fischbach PS, Zheng D, McCleskey EW. Activation of mu opioid receptors inhibits transient high- and low-threshold Ca2+ currents, but spares a sustained current. Neuron. 1991;6(1):13-20.

33. Seward E, Hammond C, Henderson G. Mu-opioid-receptor-mediated inhibition of the N-type calcium-channel current. Proc Biol Sci. 1991;244(1310):129-35.

34. Collier HO, Roy AC. Hypothesis: Inhibition of E prostaglandin-sensitive adenyl cyclase as the mechanism of morphine analgesia. Prostaglandins. 1974;7(5):361-76.

35. Levine JD, Taiwo YO. Involvement of the mu-opiate receptor in peripheral analgesia. Neuroscience. 1989;32(3):571-5.

36. Gutstein HB, Rubie EA, Mansour A, Akil H, Woodgett JR. Opioid effects on mitogen-activated protein kinase signaling cascades. Anesthesiology. 1997;87(5):1118-26.

37. Belcheva MM, Vogel Z, Ignatova E, Avidor-Reiss T, Zippel R, Levy R, et al. Opioid modulation of extracellular signal-regulated protein kinase activity is ras-dependent and involves Gbetagamma subunits. Journal of neurochemistry. 1998;70(2):635-45.

38. Kam AY, Chan AS, Wong YH. Phosphatidylinositol-3 kinase is distinctively required for mu-, but not kappa-opioid receptor-induced activation of c-Jun N-terminal kinase. Journal of neurochemistry. 2004;89(2):391-402.

39. Johnson EA, Oldfield S, Braksator E, Gonzalez-Cuello A, Couch D, Hall KJ, et al. Agonist-selective mechanisms of mu-opioid receptor desensitization in human embryonic kidney 293 cells. Molecular pharmacology. 2006;70(2):676-85.

40. Montandon G, Horner R. CrossTalk proposal: The preBotzinger complex is essential for the respiratory depression following systemic administration of opioid analgesics. J Physiol. 2014;592(6):1159-62.

41. Fields HL, Margolis EB. Understanding opioid reward. Trends Neurosci. 2015;38(4):217-25.

42. Mann A, Illing S, Miess E, Schulz S. Different mechanisms of homologous and heterologous mu-opioid receptor phosphorylation. British journal of pharmacology. 2015;172(2):311-6.

43. Kelly E. The subtleties of m-opioid receptor phosphorylation. British journal of pharmacology. 2011;164:294-7.

44. Doll C, Konietzko J, Pöll F, Koch T, Höllt V, Schulz S. Agonist-selective patterns of m-opioid receptor phosphorylation revealed by phosphosite-specific antibodies. British journal of pharmacology. 2011;164:298-307.

45. El Kouhen R, Burd AL, Erickson-Herbrandson LJ, Chang CY, Law PY, Loh HH. Phosphorylation of Ser363, Thr370, and Ser375 residues within the carboxyl tail differentially regulates mu-opioid receptor internalization. The Journal of biological chemistry. 2001;276(16):12774-80.

46. Chen YJ, Oldfield S, Butcher AJ, Tobin AB, Saxena K, Gurevich VV, et al. Identification of phosphorylation sites in the COOH-terminal tail of the mu-opioid receptor. Journal of neurochemistry. 2013;124(2):189-99.

47. Just S, Illing S, Trester-Zedlitz M, Lau EK, Kotowski SJ, Miess E, et al. Differentiation of opioid drug effects by hierarchical multi-site phosphorylation. Molecular pharmacology. 2013;83(3):633-9.

48. Lau EK, Trester-Zedlitz M, Trinidad JC, Kotowski SJ, Krutchinsky AN, Burlingame AL, et al. Quantitative Encoding of the Effect of a Partial Agonist on Individual Opioid Receptors by Multisite Phosphorylation and Threshold Detection. Science Signalling. 2011;4(185).

49. Miess E, Gondin AB, Yousuf A, Steinborn R, Mosslein N, Yang Y, et al. Multisite phosphorylation is required for sustained interaction with GRKs and arrestins during rapid mu-opioid receptor desensitization. Sci Signal. 2018;11(539).

50. Komolov KE, Benovic JL. G protein-coupled receptor kinases: Past, present and future. Cell Signal. 2018;41:17-24.

51. Doll C, Poll F, Peuker K, Loktev A, Gluck L, Schulz S. Deciphering mu-opioid receptor phosphorylation and dephosphorylation in HEK 293 cells. British journal of pharmacology. 2012;167(6):1259-70.

52. Lowe JD, Sanderson HS, Cooke AE, Ostovar M, Tsisanova E, Withey SL, et al. Role of G Protein-Coupled Receptor Kinases 2 and 3 in mu-Opioid Receptor Desensitization and Internalization. Molecular pharmacology. 2015;88(2):347-56.

53. Bailey CP, Oldfield S, Llorente J, Caunt CJ, Teschemacher AG, Roberts L, et al. Involvement of PKC alpha and G-protein-coupled receptor kinase 2 in agonist-selective desensitization of mu-opioid receptors in mature brain neurons. British journal of pharmacology. 2009;158(1):157-64.

54. Bailey CP, Kelly E, Henderson G. Protein kinase C activation enhances morphine-induced rapid desensitization of mu-opioid receptors in mature rat locus ceruleus neurons. Molecular pharmacology. 2004;66(6):1592-8.

55. Melief EJ, Miyatake M, Bruchas MR, Chavkin C. Ligand-directed c-Jun N-terminal kinase activation disrupts opioid receptor signaling. Proceedings of the National Academy of Sciences of the United States of America. 2010;107(25):11608-13.

56. Schattauer SS, Land BB, Reichard KL, Abraham AD, Burgeno LM, Kuhar JR, et al. Peroxiredoxin 6 mediates Galphai protein-coupled receptor inactivation by cJun kinase. Nature communications. 2017;8(1):743.

57. Dang VC, Napier IA, Christie MJ. Two distinct mechanisms mediate acute mu-opioid receptor desensitization in native neurons. J Neurosci. 2009;29(10):3322-7.

58. Polakiewicz RD, Schieferl SM, Dorner LF, Kansra V, Comb MJ. A mitogen-activated protein kinase pathway is required for mu-opioid receptor desensitization. The Journal of biological chemistry. 1998;273(20):12402-6.

59. Schmidt H, Schulz S, Klutzny M, Koch T, Handel M, Hollt V. Involvement of mitogen-activated protein kinase in agonist-induced phosphorylation of the mu-opioid receptor in HEK 293 cells. Journal of neurochemistry. 2000;74(1):414-22.

60. Koch T, Kroslak T, Mayer P, Raulf E, Hollt V. Site mutation in the rat mu-opioid receptor demonstrates the involvement of calcium/calmodulin-dependent protein kinase II in agonist-mediated desensitization. Journal of neurochemistry. 1997;69(4):1767-70.

61. Hull LC, Llorente J, Gabra BH, Smith FL, Kelly E, Bailey C, et al. The effect of protein kinase C and G protein-coupled receptor kinase inhibition on tolerance induced by mu-opioid agonists of different efficacy. The Journal of pharmacology and experimental therapeutics. 2010;332(3):1127-35.

62. Terman GW, Jin W, Cheong YP, Lowe J, Caron MG, Lefkowitz RJ, et al. G-protein receptor kinase 3 (GRK3) influences opioid analgesic tolerance but not opioid withdrawal. British journal of pharmacology. 2004;141(1):55-64.

63. Hill R, Dewey WL, Kelly E, Henderson G. Oxycodone-induced tolerance to respiratory depression: reversal by ethanol, pregabalin and protein kinase C inhibition. British journal of pharmacology. 2018;175(12):2492-503.

64. Withey SL, Hill R, Lyndon A, Dewey WL, Kelly E, Henderson G. Effect of Tamoxifen and Brain-Penetrant Protein Kinase C and c-Jun N-Terminal Kinase Inhibitors on Tolerance to Opioid-Induced Respiratory Depression in Mice. The Journal of pharmacology and experimental therapeutics. 2017;361(1):51-9.

65. Bohn LM, Gainetdinov RR, Lin FT, Lefkowitz RJ, Caron MG. Mu-opioid receptor desensitization by beta-arrestin-2 determines morphine tolerance but not dependence. Nature. 2000;408(6813):720-3.

66. Kliewer A, Schmiedel F, Sianati S, Bailey A, Bateman JT, Levitt ES, et al. Phosphorylation-deficient G-protein-biased mu-opioid receptors improve analgesia and diminish tolerance but worsen opioid side effects. Nature communications. 2019;10(1):367.

67. Arttamangkul S, Heinz DA, Bunzow JR, Song X, Williams JT. Cellular tolerance at the mu-opioid receptor is phosphorylation dependent. eLife. 2018;7.

68. Hauser AS, Attwood MM, Rask-Andersen M, Schioth HB, Gloriam DE. Trends in GPCR drug discovery: new agents, targets and indications. Nat Rev Drug Discov. 2017;16(12):829-42.

69. Justus CR, Dong L, Yang LV. Acidic tumor microenvironment and pH-sensing G protein-coupled receptors. Front Physiol. 2013;4:354.

70. Lam RM, Chesler AT. Shear elegance: A novel screen uncovers a mechanosensitive GPCR. J Gen Physiol. 2018;150(7):907-10.

71. Shukla AK, Xiao K, Lefkowitz RJ. Emerging paradigms of beta-arrestin-dependent seven transmembrane receptor signaling. Trends Biochem Sci. 2011;36(9):457-69.

72. Groer CE, Schmid CL, Jaeger AM, Bohn LM. Agonist-directed interactions with specific beta-arrestins determine mu-opioid receptor trafficking, ubiquitination, and dephosphorylation. The Journal of biological chemistry. 2011;286(36):31731-41.

73. Sriram K, Insel PA. G Protein-Coupled Receptors as Targets for Approved Drugs: How Many Targets and How Many Drugs? Molecular pharmacology. 2018;93(4):251-8.

74. Ghosh E, Kumari P, Jaiman D, Shukla AK. Methodological advances: the unsung heroes of the GPCR structural revolution. Nature reviews Molecular cell biology. 2015;16(2):69-81.

75. Palczewski K, Kumasaka T, Hori T, Behnke CA, Motoshima H, Fox BA, et al. Crystal structure of rhodopsin: A G protein-coupled receptor. Science. 2000;289(5480):739-45.

76. Manglik A, Kruse AC, Kobilka TS, Thian FS, Mathiesen JM, Sunahara RK, et al. Crystal structure of the mu-opioid receptor bound to a morphinan antagonist. Nature. 2012;485(7398):321-6.

77. Safdari HA, Pandey S, Shukla AK, Dutta S. Illuminating GPCR Signaling by Cryo-EM. Trends Cell Biol. 2018;28(8):591-4.

78. Pandy-Szekeres G, Munk C, Tsonkov TM, Mordalski S, Harpsoe K, Hauser AS, et al. GPCRdb in 2018: adding GPCR structure models and ligands. Nucleic Acids Res. 2018;46(D1):D440-D6.

79. Attwood TK, Findlay JB. Fingerprinting G-protein-coupled receptors. Protein Eng. 1994;7(2):195-203.

80. Hu GM, Mai TL, Chen CM. Visualizing the GPCR Network: Classification and Evolution. Sci Rep. 2017;7(1):15495.

81. Ballesteros JA, Weinstein H. Integrated methods for the construction of three-dimensional models and computational probing of structure-function relations in G protein-coupled receptors. Methods Neurosci 1995;25:366–428.

82. Venkatakrishnan AJ, Deupi X, Lebon G, Heydenreich FM, Flock T, Miljus T, et al. Diverse activation pathways in class A GPCRs converge near the G-protein-coupling region. Nature. 2016;536(7617):484-7.

83. Rosenbaum DM, Zhang C, Lyons JA, Holl R, Aragao D, Arlow DH, et al. Structure and function of an irreversible agonist-beta(2) adrenoceptor complex. Nature. 2011;469(7329):236-40.

84. Carpenter B, Nehme R, Warne T, Leslie AG, Tate CG. Structure of the adenosine A(2A) receptor bound to an engineered G protein. Nature. 2016;536(7614):104-7.

85. Scheerer P, Park JH, Hildebrand PW, Kim YJ, Krauss N, Choe HW, et al. Crystal structure of opsin in its G-protein-interacting conformation. Nature. 2008;455(7212):497-502.

86. Rasmussen SG, DeVree BT, Zou Y, Kruse AC, Chung KY, Kobilka TS, et al. Crystal structure of the beta2 adrenergic receptor-Gs protein complex. Nature. 2011;477(7366):549-55.

87. Kruse AC, Ring AM, Manglik A, Hu J, Hu K, Eitel K, et al. Activation and allosteric modulation of a muscarinic acetylcholine receptor. Nature. 2013;504(7478):101-6.

88. DeVree BT, Mahoney JP, Velez-Ruiz GA, Rasmussen SG, Kuszak AJ, Edwald E, et al. Allosteric coupling from G protein to the agonist-binding pocket in GPCRs. Nature. 2016;535(7610):182-6.

89. Nygaard R, Zou Y, Dror RO, Mildorf TJ, Arlow DH, Manglik A, et al. The dynamic process of beta(2)-adrenergic receptor activation. Cell. 2013;152(3):532-42.

90. Isogai S, Deupi X, Opitz C, Heydenreich FM, Tsai CJ, Brueckner F, et al. Backbone NMR reveals allosteric signal transduction networks in the beta-adrenergic receptor. Nature. 2016.

91. Manglik A, Kim TH, Masureel M, Altenbach C, Yang Z, Hilger D, et al. Structural Insights into the Dynamic Process of beta2-Adrenergic Receptor Signaling. Cell. 2015;161(5):1101-11.

92. Sounier R, Mas C, Steyaert J, Laeremans T, Manglik A, Huang W, et al. Propagation of conformational changes during mu-opioid receptor activation. Nature. 2015;524(7565):375-8.

93. Rasmussen SG, Jensen AD, Liapakis G, Ghanouni P, Javitch JA, Gether U. Mutation of a highly conserved aspartic acid in the beta2 adrenergic receptor:

constitutive activation, structural instability, and conformational rearrangement of transmembrane segment 6. Molecular pharmacology. 1999;56(1):175-84.

94. Alewijnse AE, Timmerman H, Jacobs EH, Smit MJ, Roovers E, Cotecchia S, et al. The effect of mutations in the DRY motif on the constitutive activity and structural instability of the histamine H(2) receptor. Molecular pharmacology. 2000;57(5):890-8.

95. Li J, Huang P, Chen C, de Riel JK, Weinstein H, Liu-Chen LY. Constitutive activation of the mu opioid receptor by mutation of D3.49(164), but not D3.32(147): D3.49(164) is critical for stabilization of the inactive form of the receptor and for its expression. Biochemistry. 2001;40(40):12039-50.

96. Valentin-Hansen L, Groenen M, Nygaard R, Frimurer TM, Holliday ND, Schwartz TW. The arginine of the DRY motif in transmembrane segment III functions as a balancing micro-switch in the activation of the beta2-adrenergic receptor. The Journal of biological chemistry. 2012;287(38):31973-82.

97. Zhu SZ, Wang SZ, Hu J, el-Fakahany EE. An arginine residue conserved in most G protein-coupled receptors is essential for the function of the m1 muscarinic receptor. Molecular pharmacology. 1994;45(3):517-23.

98. Jones PG, Curtis CA, Hulme EC. The function of a highly-conserved arginine residue in activation of the muscarinic M1 receptor. European journal of pharmacology. 1995;288(3):251-7.

99. Barak LS, Oakley RH, Laporte SA, Caron MG. Constitutive arrestin-mediated desensitization of a human vasopressin receptor mutant associated with nephrogenic diabetes insipidus. Proceedings of the National Academy of Sciences of the United States of America. 2001;98(1):93-8.

100. Ballesteros JA, Jensen AD, Liapakis G, Rasmussen SG, Shi L, Gether U, et al. Activation of the beta 2-adrenergic receptor involves disruption of an ionic lock

between the cytoplasmic ends of transmembrane segments 3 and 6. The Journal of biological chemistry. 2001;276(31):29171-7.

101. Tehan BG, Bortolato A, Blaney FE, Weir MP, Mason JS. Unifying family A GPCR theories of activation. Pharmacol Ther. 2014;143(1):51-60.

102. Weis WI, Kobilka BK. The Molecular Basis of G Protein-Coupled Receptor Activation. Annu Rev Biochem. 2018;87:897-919.

103. Farrens DL, Altenbach C, Yang K, Hubbell WL, Khorana HG. Requirement of rigid-body motion of transmembrane helices for light activation of rhodopsin. Science. 1996;274(5288):768-70.

104. Huang P, Li J, Chen C, Visiers I, Weinstein H, Liu-Chen LY. Functional role of a conserved motif in TM6 of the rat mu opioid receptor: constitutively active and inactive receptors result from substitutions of Thr6.34(279) with Lys and Asp. Biochemistry. 2001;40(45):13501-9.

105. Kang Y, Kuybeda O, de Waal PW, Mukherjee S, Van Eps N, Dutka P, et al. Cryo-EM structure of human rhodopsin bound to an inhibitory G protein. Nature. 2018;558(7711):553-8.

106. Draper-Joyce CJ, Khoshouei M, Thal DM, Liang YL, Nguyen ATN, Furness SGB, et al. Structure of the adenosine-bound human adenosine A1 receptor-Gi complex. Nature. 2018;558(7711):559-63.

107. Garcia-Nafria J, Nehme R, Edwards PC, Tate CG. Cryo-EM structure of the serotonin 5-HT1B receptor coupled to heterotrimeric Go. Nature. 2018;558(7711):620-3.

108. Liang YL, Khoshouei M, Glukhova A, Furness SGB, Zhao P, Clydesdale L, et al. Phase-plate cryo-EM structure of a biased agonist-bound human GLP-1 receptor-Gs complex. Nature. 2018;555(7694):121-5.

109. Van Eps N, Altenbach C, Caro LN, Latorraca NR, Hollingsworth SA, Dror RO, et al. Gi- and Gs-coupled GPCRs show different modes of G-protein binding. Proceedings of the National Academy of Sciences of the United States of America. 2018;115(10):2383-8.

110. Liu X, Xu X, Hilger D, Aschauer P, Tiemann JKS, Du Y, et al. Structural Insights into the Process of GPCR-G Protein Complex Formation. Cell. 2019.

111. Surratt CK, Johnson PS, Moriwaki A, Seidleck BK, Blaschak CJ, Wang JB, et al. -mu opiate receptor. Charged transmembrane domain amino acids are critical for agonist recognition and intrinsic activity. The Journal of biological chemistry. 1994;269(32):20548-53.

112. Mansour A, Taylor LP, Fine JL, Thompson RC, Hoversten MT, Mosberg HI, et al. Key residues defining the mu-opioid receptor binding pocket: a site-directed mutagenesis study. Journal of neurochemistry. 1997;68(1):344-53.

113. Li JG, Chen C, Yin J, Rice K, Zhang Y, Matecka D, et al. ASP147 in the third transmembrane helix of the rat mu opioid receptor forms ion-pairing with morphine and naltrexone. Life Sci. 1999;65(2):175-85.

114. Spivak CE, Beglan CL, Seidleck BK, Hirshbein LD, Blaschak CJ, Uhl GR, et al. Naloxone activation of mu-opioid receptors mutated at a histidine residue lining the opioid binding cavity. Molecular pharmacology. 1997;52(6):983-92.

115. Pert CB, Snyder SH. Opiate receptor binding of agonists and antagonists affected differentially by sodium. Molecular pharmacology. 1974;10(6):868-79.

116. Gao ZG, Melman N, Erdmann A, Kim SG, Muller CE, AP IJ, et al. Differential allosteric modulation by amiloride analogues of agonist and antagonist binding at A(1) and A(3) adenosine receptors. Biochem Pharmacol. 2003;65(4):525-34.

117. Neve KA. Regulation of dopamine D2 receptors by sodium and pH. Molecular pharmacology. 1991;39(4):570-8.

118. Kong H, Raynor K, Yasuda K, Bell GI, Reisine T. Mutation of an aspartate at residue 89 in somatostatin receptor subtype 2 prevents Na+ regulation of agonist binding but does not alter receptor-G protein association. Molecular pharmacology. 1993;44(2):380-4.

119. Quitterer U, AbdAlla S, Jarnagin K, Muller-Esterl W. Na+ ions binding to the bradykinin B2 receptor suppress agonist-independent receptor activation. Biochemistry. 1996;35(41):13368-77.

120. Pert CB, Pasternak G, Snyder SH. Opiate agonists and antagonists discriminated by receptor binding in brain. Science. 1973;182(4119):1359-61.

121. Selley DE, Cao CC, Liu Q, Childers SR. Effects of sodium on agonist efficacy for G-protein activation in mu-opioid receptor-transfected CHO cells and rat thalamus. British journal of pharmacology. 2000;130(5):987-96.

122. Liu W, Chun E, Thompson AA, Chubukov P, Xu F, Katritch V, et al. Structural basis for allosteric regulation of GPCRs by sodium ions. Science. 2012;337(6091):232-6.

123. Miller-Gallacher JL, Nehme R, Warne T, Edwards PC, Schertler GF, Leslie AG, et al. The 2.1 A resolution structure of cyanopindolol-bound beta1-adrenoceptor identifies an intramembrane Na+ ion that stabilises the ligand-free receptor. PloS one. 2014;9(3):e92727.

124. Fenalti G, Giguere PM, Katritch V, Huang XP, Thompson AA, Cherezov V, et al. Molecular control of delta-opioid receptor signalling. Nature. 2014;506(7487):191-6.

125. Zhang C, Srinivasan Y, Arlow DH, Fung JJ, Palmer D, Zheng Y, et al. High-resolution crystal structure of human protease-activated receptor 1. Nature. 2012;492(7429):387-92.

126. Barbhaiya H, McClain R, Ijzerman A, Rivkees SA. Site-directed mutagenesis of the human A1 adenosine receptor: influences of acidic and hydroxy residues in the first four transmembrane domains on ligand binding. Molecular pharmacology. 1996;50(6):1635-42.

127. Horstman DA, Brandon S, Wilson AL, Guyer CA, Cragoe EJ, Jr., Limbird LE. An aspartate conserved among G-protein receptors confers allosteric regulation of alpha 2-adrenergic receptors by sodium. The Journal of biological chemistry. 1990;265(35):21590-5.

128. Ceresa BP, Limbird LE. Mutation of an aspartate residue highly conserved among G-protein-coupled receptors results in nonreciprocal disruption of alpha 2-adrenergic receptor-G-protein interactions. A negative charge at amino acid residue 79 forecasts alpha 2A-adrenergic receptor sensitivity to allosteric modulation by monovalent cations and fully effective receptor/G-protein coupling. The Journal of biological chemistry. 1994;269(47):29557-64.

129. Li B, Nowak NM, Kim SK, Jacobson KA, Bagheri A, Schmidt C, et al. Random mutagenesis of the M3 muscarinic acetylcholine receptor expressed in yeast: identification of second-site mutations that restore function to a coupling-deficient mutant M3 receptor. The Journal of biological chemistry. 2005;280(7):5664-75.

130. Tao Q, Abood ME. Mutation of a highly conserved aspartate residue in the second transmembrane domain of the cannabinoid receptors, CB1 and CB2, disrupts G-protein coupling. The Journal of pharmacology and experimental therapeutics. 1998;285(2):651-8.

131. Rosenberg EM, Jr., Harrison RES, Tsou LK, Drucker N, Humphries B, Rajasekaran D, et al. Characterization, Dynamics, and Mechanism of CXCR4 Antagonists on a Constitutively Active Mutant. Cell Chem Biol. 2019.

132. Tsai BS, Lefkowitz RJ. Agonist-specific effects of monovalent and divalent cations on adenylate cyclase-coupled alpha adrenergic receptors in rabbit platelets. Molecular pharmacology. 1978;14(4):540-8.

133. Ye L, Neale C, Sljoka A, Lyda B, Pichugin D, Tsuchimura N, et al. Mechanistic insights into allosteric regulation of the A2A adenosine G protein-coupled receptor by physiological cations. Nature communications. 2018;9(1):1372.

134. Valentin-Hansen L, Frimurer TM, Mokrosinski J, Holliday ND, Schwartz TW. Biased Gs Versus Gq Proteins and beta-Arrestin Signaling in the NK1 Receptor Determined by Interactions in the Water Hydrogen Bond Network. The Journal of biological chemistry. 2015;290(40):24495-508.

135. Livingston KE, Traynor JR. Disruption of the Na+ ion binding site as a mechanism for positive allosteric modulation of the mu-opioid receptor. Proceedings of the National Academy of Sciences of the United States of America. 2014;111(51):18369-74.

136. Burford NT, Traynor JR, Alt A. Positive allosteric modulators of the mu-opioid receptor: a novel approach for future pain medications. British journal of pharmacology. 2015;172(2):277-86.

137. White KL, Eddy MT, Gao ZG, Han GW, Lian T, Deary A, et al. Structural Connection between Activation Microswitch and Allosteric Sodium Site in GPCR Signaling. Structure. 2018;26(2):259-69 e5.

138. Katritch V, Fenalti G, Abola EE, Roth BL, Cherezov V, Stevens RC. Allosteric sodium in class A GPCR signaling. Trends Biochem Sci. 2014;39(5):233-44.

139. Gutierrez-de-Teran H, Massink A, Rodriguez D, Liu W, Han GW, Joseph JS, et al. The role of a sodium ion binding site in the allosteric modulation of the A(2A) adenosine G protein-coupled receptor. Structure. 2013;21(12):2175-85.

140. Vickery ON, Machtens JP, Tamburrino G, Seeliger D, Zachariae U. Structural Mechanisms of Voltage Sensing in G Protein-Coupled Receptors. Structure. 2016;24(6):997-1007.

141. Rinne A, Birk A, Bunemann M. Voltage regulates adrenergic receptor function. Proceedings of the National Academy of Sciences of the United States of America. 2013;110(4):1536-41.

142. Ben Chaim Y, Bochnik S, Parnas I, Parnas H. Voltage affects the dissociation rate constant of the m2 muscarinic receptor. PloS one. 2013;8(9):e74354.

143. Navarro-Polanco RA, Moreno Galindo EG, Ferrer-Villada T, Arias M, Rigby JR, Sanchez-Chapula JA, et al. Conformational changes in the M2 muscarinic receptor induced by membrane voltage and agonist binding. J Physiol. 2011;589(Pt 7):1741-53.

144. Rinne A, Mobarec JC, Mahaut-Smith M, Kolb P, Bunemann M. The mode of agonist binding to a G protein-coupled receptor switches the effect that voltage changes have on signaling. Sci Signal. 2015;8(401):ra110.

145. Martinez-Pinna J, Tolhurst G, Gurung IS, Vandenberg JI, Mahaut-Smith MP. Sensitivity limits for voltage control of P2Y receptor-evoked Ca2+ mobilization in the rat megakaryocyte. J Physiol. 2004;555(Pt 1):61-70.

146. Shi L, Liapakis G, Xu R, Guarnieri F, Ballesteros JA, Javitch JA. Beta2 adrenergic receptor activation. Modulation of the proline kink in transmembrane 6 by a rotamer toggle switch. The Journal of biological chemistry. 2002;277(43):40989-96.

147. Katritch V, Cherezov V, Stevens RC. Structure-function of the G protein-coupled receptor superfamily. Annu Rev Pharmacol Toxicol. 2013;53:531-56.

148. Nygaard R, Frimurer TM, Holst B, Rosenkilde MM, Schwartz TW. Ligand binding and micro-switches in 7TM receptor structures. Trends in pharmacological sciences. 2009;30(5):249-59.

149. Schwartz TW, Frimurer TM, Holst B, Rosenkilde MM, Elling CE. Molecular mechanism of 7TM receptor activation--a global toggle switch model. Annu Rev Pharmacol Toxicol. 2006;46:481-519.

150. Holst B, Nygaard R, Valentin-Hansen L, Bach A, Engelstoft MS, Petersen PS, et al. A conserved aromatic lock for the tryptophan rotameric switch in TM-VI of seven-transmembrane receptors. The Journal of biological chemistry. 2010;285(6):3973-85.

151. McAllister SD, Rizvi G, Anavi-Goffer S, Hurst DP, Barnett-Norris J, Lynch DL, et al. An aromatic microdomain at the cannabinoid CB(1) receptor constitutes an agonist/inverse agonist binding region. Journal of medicinal chemistry. 2003;46(24):5139-52.

152. Sutcliffe KJ, Henderson G, Kelly E, Sessions RB. Drug Binding Poses Relate Structure with Efficacy in the mu Opioid Receptor. Journal of molecular biology. 2017;429(12):1840-51.

153. Bhattacharya S, Hall SE, Vaidehi N. Agonist-induced conformational changes in bovine rhodopsin: insight into activation of G-protein-coupled receptors. Journal of molecular biology. 2008;382(2):539-55.

154. Deupi X, Standfuss J. Structural insights into agonist-induced activation of G-protein-coupled receptors. Curr Opin Struct Biol. 2011;21(4):541-51.

155. Yamano Y, Ohyama K, Kikyo M, Sano T, Nakagomi Y, Inoue Y, et al. Mutagenesis and the molecular modeling of the rat angiotensin II receptor (AT1). The Journal of biological chemistry. 1995;270(23):14024-30.

156. Wess J, Nanavati S, Vogel Z, Maggio R. Functional role of proline and tryptophan residues highly conserved among G protein-coupled receptors studied by mutational analysis of the m3 muscarinic receptor. EMBO J. 1993;12(1):331-8.

157. Befort K, Tabbara L, Kling D, Maigret B, Kieffer BL. Role of aromatic transmembrane residues of the delta-opioid receptor in ligand recognition. The Journal of biological chemistry. 1996;271(17):10161-8.

158. Stoddart LA, Kellam B, Briddon SJ, Hill SJ. Effect of a toggle switch mutation in TM6 of the human adenosine A(3) receptor on Gi protein-dependent signalling and Gi-independent receptor internalization. British journal of pharmacology. 2014;171(16):3827-44.

159. Kaiser A, Hempel C, Wanka L, Schubert M, Hamm HE, Beck-Sickinger AG. G Protein Preassembly Rescues Efficacy of W(6.48) Toggle Mutations in Neuropeptide Y2 Receptor. Molecular pharmacology. 2018;93(4):387-401.

160. Pellissier LP, Sallander J, Campillo M, Gaven F, Queffeulou E, Pillot M, et al. Conformational toggle switches implicated in basal constitutive and agonist-induced activated states of 5-hydroxytryptamine-4 receptors. Molecular pharmacology. 2009;75(4):982-90.

161. Sun X, Laroche G, Wang X, Agren H, Bowman GR, Giguere PM, et al. Propagation of the Allosteric Modulation Induced by Sodium in the delta-Opioid Receptor. Chemistry. 2017;23(19):4615-24.

162. Wacker D, Wang C, Katritch V, Han GW, Huang X, Vardy E, et al. Structural Features for Functional Selectivity at Serotonin Receptors. Science. 2013;340:615-9.

163. Rasmussen SG, Choi HJ, Fung JJ, Pardon E, Casarosa P, Chae PS, et al. Structure of a nanobody-stabilized active state of the beta(2) adrenoceptor. Nature. 2011;469(7329):175-80.

164. Standfuss J, Edwards PC, D'Antona A, Fransen M, Xie G, Oprian DD, et al. The structural basis of agonist-induced activation in constitutively active rhodopsin. Nature. 2011;471(7340):656-60.

165. Peng Y, McCorvy JD, Harpsoe K, Lansu K, Yuan S, Popov P, et al. 5-HT2C Receptor Structures Reveal the Structural Basis of GPCR Polypharmacology. Cell. 2018;172(4):719-30 e14.

166. Manglik A, Kruse AC. Structural Basis for G Protein-Coupled Receptor Activation. Biochemistry. 2017;56(42):5628-34.

167. Erlandson SC, McMahon C, Kruse AC. Structural Basis for G Protein-Coupled Receptor Signaling. Annu Rev Biophys. 2018.

168. Ragnarsson L, Andersson A, Thomas WG, Lewis RJ. Mutations in the NPxxY motif stabilize pharmacologically distinct conformational states of the alpha1B- and beta2-adrenoceptors. Sci Signal. 2019;12(572).

169. Gabilondo AM, Krasel C, Lohse MJ. Mutations of Tyr326 in the beta 2-adrenoceptor disrupt multiple receptor functions. European journal of pharmacology. 1996;307(2):243-50.

170. Liu R, Nahon D, le Roy B, Lenselink EB, AP IJ. Scanning mutagenesis in a yeast system delineates the role of the NPxxY(x)(5,6)F motif and helix 8 of the adenosine A(2B) receptor in G protein coupling. Biochem Pharmacol. 2015;95(4):290-300.

171. Borroto-Escuela DO, Romero-Fernandez W, Garcia-Negredo G, Correia PA, Garriga P, Fuxe K, et al. Dissecting the conserved NPxxY motif of the M3 muscarinic

acetylcholine receptor: critical role of Asp-7.49 for receptor signaling and multiprotein complex formation. Cell Physiol Biochem. 2011;28(5):1009-22.

172. Fritze O, Filipek S, Kuksa V, Palczewski K, Hofmann KP, Ernst OP. Role of the conserved NPxxY(x)5,6F motif in the rhodopsin ground state and during activation. Proceedings of the National Academy of Sciences of the United States of America. 2003;100(5):2290-5.

173. Kapoor A, Martinez-Rosell G, Provasi D, de Fabritiis G, Filizola M. Dynamic and Kinetic Elements of micro-Opioid Receptor Functional Selectivity. Sci Rep. 2017;7(1):11255.

174. Roth CL, Ludwig M, Woelfle J, Fan ZC, Brumm H, Biebermann H, et al. A novel melanocortin-4 receptor gene mutation in a female patient with severe childhood obesity. Endocrine. 2009;36(1):52-9.

175. Bonnefond A, Clement N, Fawcett K, Yengo L, Vaillant E, Guillaume JL, et al. Rare MTNR1B variants impairing melatonin receptor 1B function contribute to type 2 diabetes. Nat Genet. 2012;44(3):297-301.

176. Tello JA, Newton CL, Bouligand J, Guiochon-Mantel A, Millar RP, Young J. Congenital hypogonadotropic hypogonadism due to GnRH receptor mutations in three brothers reveal sites affecting conformation and coupling. PloS one. 2012;7(6):e38456.

177. Carpenter B, Tate CG. Active state structures of G protein-coupled receptors highlight the similarities and differences in the G protein and arrestin coupling interfaces. Curr Opin Struct Biol. 2017;45:124-32.

178. Kang Y, Zhou XE, Gao X, He Y, Liu W, Ishchenko A, et al. Crystal structure of rhodopsin bound to arrestin by femtosecond X-ray laser. Nature. 2015;523(7562):561-7.

179. Shi L, Javitch JA. The second extracellular loop of the dopamine D2 receptor lines the binding-site crevice. Proceedings of the National Academy of Sciences of the United States of America. 2004;101(2):440-5.

180. Zhao MM, Hwa J, Perez DM. Identification of critical extracellular loop residues involved in alpha 1-adrenergic receptor subtype-selective antagonist binding. Molecular pharmacology. 1996;50(5):1118-26.

181. Unal H, Jagannathan R, Bhat MB, Karnik SS. Ligand-specific conformation of extracellular loop-2 in the angiotensin II type 1 receptor. The Journal of biological chemistry. 2010;285(21):16341-50.

182. Avlani VA, Gregory KJ, Morton CJ, Parker MW, Sexton PM, Christopoulos A. Critical role for the second extracellular loop in the binding of both orthosteric and allosteric G protein-coupled receptor ligands. The Journal of biological chemistry. 2007;282(35):25677-86.

183. Jakubik J, Randakova A, Zimcik P, El-Fakahany EE, Dolezal V. Binding of N-methylscopolamine to the extracellular domain of muscarinic acetylcholine receptors. Sci Rep. 2017;7:40381.

184. Massotte D, Kieffer BL. The second extracellular loop: a damper for G protein-coupled receptors? Nature structural & molecular biology. 2005;12(4):287-8.

185. Klco JM, Wiegand CB, Narzinski K, Baranski TJ. Essential role for the second extracellular loop in C5a receptor activation. Nature structural & molecular biology. 2005;12(4):320-6.

186. Wacker D, Wang S, McCorvy JD, Betz RM, Venkatakrishnan AJ, Levit A, et al. Crystal Structure of an LSD-Bound Human Serotonin Receptor. Cell. 2017;168(3):377-89 e12.

187. McCorvy JD, Butler KV, Kelly B, Rechsteiner K, Karpiak J, Betz RM, et al. Structure-inspired design of beta-arrestin-biased ligands for aminergic GPCRs. Nature chemical biology. 2018;14(2):126-34.

188. Nawaratne V, Leach K, Felder CC, Sexton PM, Christopoulos A. Structural determinants of allosteric agonism and modulation at the M4 muscarinic acetylcholine receptor: identification of ligand-specific and global activation mechanisms. The Journal of biological chemistry. 2010;285(25):19012-21.

189. Dror RO, Green HF, Valant C, Borhani DW, Valcourt JR, Pan AC, et al. Structural basis for modulation of a G-protein-coupled receptor by allosteric drugs. Nature. 2013;503(7475):295-9.

190. Shihoya W, Nishizawa T, Okuta A, Tani K, Dohmae N, Fujiyoshi Y, et al. Activation mechanism of endothelin ETB receptor by endothelin-1. Nature. 2016;537(7620):363-8.

191. Wheatley M, Wootten D, Conner MT, Simms J, Kendrick R, Logan RT, et al. Lifting the lid on GPCRs: the role of extracellular loops. British journal of pharmacology. 2012;165(6):1688-703.

192. Dror RO, Pan AC, Arlow DH, Borhani DW, Maragakis P, Shan Y, et al. Pathway and mechanism of drug binding to G-protein-coupled receptors. Proceedings of the National Academy of Sciences of the United States of America. 2011;108(32):13118-23.

193. Gonzalez A, Perez-Acle T, Pardo L, Deupi X. Molecular basis of ligand dissociation in beta-adrenergic receptors. PloS one. 2011;6(9):e23815.

194. Xue JC, Chen C, Zhu J, Kunapuli SP, de Riel JK, Yu L, et al. The third extracellular loop of the mu opioid receptor is important for agonist selectivity. The Journal of biological chemistry. 1995;270(22):12977-9.

195. Dietrich G, Gaibelet G, Capeyrou R, Butour JL, Pontet F, Emorine LJ. Implication of the first and third extracellular loops of the mu-opioid receptor in the formation of the ligand binding site: a study using chimeric mu-opioid/angiotensin receptors. Journal of neurochemistry. 1998;70(5):2106-11.

196. Minami M, Onogi T, Nakagawa T, Katao Y, Aoki Y, Katsumata S, et al. DAMGO, a mu-opioid receptor selective ligand, distinguishes between mu-and kappa-opioid receptors at a different region from that for the distinction between mu- and delta-opioid receptors. FEBS Lett. 1995;364(1):23-7.

197. Onogi T, Minami M, Katao Y, Nakagawa T, Aoki Y, Toya T, et al. DAMGO, a mu-opioid receptor selective agonist, distinguishes between mu- and delta-opioid receptors around their first extracellular loops. FEBS Lett. 1995;357(1):93-7.

198. Lipinski PFJ, Kosson P, Matalinska J, Roszkowski P, Czarnocki Z, Jaronczyk M, et al. Fentanyl Family at the Mu-Opioid Receptor: Uniform Assessment of Binding and Computational Analysis. Molecules. 2019;24(4).

199. Marmolejo-Valencia AF, Martinez-Mayorga K. Allosteric modulation model of the mu opioid receptor by herkinorin, a potent not alkaloidal agonist. J Comput Aided Mol Des. 2017;31(5):467-82.

200. Kenakin T. Biased Receptor Signaling in Drug Discovery. Pharmacological reviews. 2019;71(2):267-315.

201. Kenakin T, Watson C, Muniz-Medina V, Christopoulos A, Novick S. A simple method for quantifying functional selectivity and agonist bias. ACS Chem Neurosci. 2012;3(3):193-203.

202. Lorenzen E, Ceraudo E, Berchiche YA, Rico CA, Furstenberg A, Sakmar TP, et al. G protein subtype-specific signaling bias in a series of CCR5 chemokine analogs. Sci Signal. 2018;11(552).

203. Bolognini D, Moss CE, Nilsson K, Petersson AU, Donnelly I, Sergeev E, et al. A Novel Allosteric Activator of Free Fatty Acid 2 Receptor Displays Unique Gi-functional Bias. The Journal of biological chemistry. 2016;291(36):18915-31.

204. Weston C, Winfield I, Harris M, Hodgson R, Shah A, Dowell SJ, et al. Receptor Activity-modifying Protein-directed G Protein Signaling Specificity for the Calcitonin Gene-related Peptide Family of Receptors. The Journal of biological chemistry. 2016;291(42):21925-44.

205. Pradhan AA, Perroy J, Walwyn WM, Smith ML, Vicente-Sanchez A, Segura L, et al. Agonist-Specific Recruitment of Arrestin Isoforms Differentially Modify Delta Opioid Receptor Function. J Neurosci. 2016;36(12):3541-51.

206. Zidar DA, Violin JD, Whalen EJ, Lefkowitz RJ. Selective engagement of G protein coupled receptor kinases (GRKs) encodes distinct functions of biased ligands. Proceedings of the National Academy of Sciences of the United States of America. 2009;106(24):9649-54.

207. Wisler JW, DeWire SM, Whalen EJ, Violin JD, Drake MT, Ahn S, et al. A unique mechanism of beta-blocker action: carvedilol stimulates beta-arrestin signaling. Proceedings of the National Academy of Sciences of the United States of America. 2007;104(42):16657-62.

208. Kopecky SL. Effect of beta blockers, particularly carvedilol, on reducing the risk of events after acute myocardial infarction. Am J Cardiol. 2006;98(8):1115-9.

209. Carr R, 3rd, Schilling J, Song J, Carter RL, Du Y, Yoo SM, et al. beta-arrestin-biased signaling through the beta2-adrenergic receptor promotes cardiomyocyte contraction. Proceedings of the National Academy of Sciences of the United States of America. 2016;113(28):E4107-16.

210. Mores KL, Cummins BR, Cassell RJ, van Rijn RM. A Review of the Therapeutic Potential of Recently Developed G Protein-Biased Kappa Agonists. Front Pharmacol. 2019;10:407.

211. Gaveriaux-Ruff C, Kieffer BL. Delta opioid receptor analgesia: recent contributions from pharmacology and molecular approaches. Behav Pharmacol. 2011;22(5-6):405-14.

212. Schattauer SS, Kuhar JR, Song A, Chavkin C. Nalfurafine is a G-protein biased agonist having significantly greater bias at the human than rodent form of the kappa opioid receptor. Cell Signal. 2017;32:59-65.

213. White KL, Robinson JE, Zhu H, DiBerto JF, Polepally PR, Zjawiony JK, et al. The G protein-biased kappa-opioid receptor agonist RB-64 is analgesic with a unique spectrum of activities in vivo. The Journal of pharmacology and experimental therapeutics. 2015;352(1):98-109.

214. Brust TF, Morgenweck J, Kim SA, Rose JH, Locke JL, Schmid CL, et al. Biased agonists of the kappa opioid receptor suppress pain and itch without causing sedation or dysphoria. Sci Signal. 2016;9(456):ra117.

215. Violin JD, DeWire SM, Yamashita D, Rominger DH, Nguyen L, Schiller K, et al. Selectively engaging beta-arrestins at the angiotensin II type 1 receptor reduces blood pressure and increases cardiac performance. The Journal of pharmacology and experimental therapeutics. 2010;335(3):572-9.

216. Felker GM, Butler J, Collins SP, Cotter G, Davison BA, Ezekowitz JA, et al. Heart failure therapeutics on the basis of a biased ligand of the angiotensin-2 type 1 receptor. Rationale and design of the BLAST-AHF study (Biased Ligand of the Angiotensin Receptor Study in Acute Heart Failure). JACC Heart Fail. 2015;3(3):193-201.

217. Boerrigter G, Soergel DG, Violin JD, Lark MW, Burnett JC, Jr. TRV120027, a novel beta-arrestin biased ligand at the angiotensin II type I receptor, unloads the heart and maintains renal function when added to furosemide in experimental heart failure. Circ Heart Fail. 2012;5(5):627-34.

218. Pang PS, Butler J, Collins SP, Cotter G, Davison BA, Ezekowitz JA, et al. Biased ligand of the angiotensin II type 1 receptor in patients with acute heart failure: a randomized, double-blind, placebo-controlled, phase IIB, dose ranging trial (BLAST-AHF). Eur Heart J. 2017;38(30):2364-73.

219. Zhou L, Bohn LM. Functional selectivity of GPCR signaling in animals. Curr Opin Cell Biol. 2014;27:102-8.

220. Ehrlich AT, Semache M, Gross F, Da Fonte DF, Runtz L, Colley C, et al. Biased Signaling of the Mu Opioid Receptor Revealed in Native Neurons. iScience. 2019;14:47-57.

221. Reiter E, Ahn S, Shukla AK, Lefkowitz RJ. Molecular mechanism of beta-arrestin-biased agonism at seven-transmembrane receptors. Annu Rev Pharmacol Toxicol. 2012;52:179-97.

222. Kahsai AW, Xiao K, Rajagopal S, Ahn S, Shukla AK, Sun J, et al. Multiple ligand-specific conformations of the beta2-adrenergic receptor. Nature chemical biology. 2011;7(10):692-700.

223. Ye L, Van Eps N, Zimmer M, Ernst OP, Prosser RS. Activation of the A2A adenosine G-protein-coupled receptor by conformational selection. Nature. 2016;533(7602):265-8.

224. Wingler LM, Elgeti M, Hilger D, Latorraca NR, Lerch MT, Staus DP, et al. Angiotensin Analogs with Divergent Bias Stabilize Distinct Receptor Conformations. Cell. 2019;176(3):468-78 e11.

225. Sleno R, Devost D, Petrin D, Zhang A, Bourque K, Shinjo Y, et al. Conformational biosensors reveal allosteric interactions between heterodimeric AT1 angiotensin and prostaglandin F2alpha receptors. The Journal of biological chemistry. 2017;292(29):12139-52.

226. Bourque K, Petrin D, Sleno R, Devost D, Zhang A, Hebert TE. Distinct Conformational Dynamics of Three G Protein-Coupled Receptors Measured Using FlAsH-BRET Biosensors. Front Endocrinol (Lausanne). 2017;8:61.

227. Zhao LH, Ma S, Sutkeviciute I, Shen DD, Zhou XE, de Waal PW, et al. Structure and dynamics of the active human parathyroid hormone receptor-1. Science. 2019;364(6436):148-53.

228. Krishna Kumar K, Shalev-Benami M, Robertson MJ, Hu H, Banister SD, Hollingsworth SA, et al. Structure of a Signaling Cannabinoid Receptor 1-G Protein Complex. Cell. 2019;176(3):448-58 e12.

229. Liang YL, Khoshouei M, Deganutti G, Glukhova A, Koole C, Peat TS, et al. Cryo-EM structure of the active, Gs-protein complexed, human CGRP receptor. Nature. 2018;561(7724):492-7.

230. Maeda S, Qu Q, Robertson MJ, Skiniotis G, Kobilka BK. Structures of the M1 and M2 muscarinic acetylcholine receptor/G-protein complexes. Science. 2019;364(6440):552-7.

231. Zhou XE, Gao X, Barty A, Kang Y, He Y, Liu W, et al. X-ray laser diffraction for structure determination of the rhodopsin-arrestin complex. Sci Data. 2016;3:160021.

232. Zhou XE, He Y, de Waal PW, Gao X, Kang Y, Van Eps N, et al. Identification of Phosphorylation Codes for Arrestin Recruitment by G Protein-Coupled Receptors. Cell. 2017;170(3):457-69 e13.

233. Zhou XE, Melcher K, Xu HE. Understanding the GPCR biased signaling through G protein and arrestin complex structures. Curr Opin Struct Biol. 2017;45:150-9.

234. Cabana J, Holleran B, Leduc R, Escher E, Guillemette G, Lavigne P. Identification of Distinct Conformations of the Angiotensin-II Type 1 Receptor Associated with the Gq/11 Protein Pathway and the beta-Arrestin Pathway Using Molecular Dynamics Simulations. The Journal of biological chemistry. 2015;290(25):15835-54.

235. Zhang Y, Sun B, Feng D, Hu H, Chu M, Qu Q, et al. Cryo-EM structure of the activated GLP-1 receptor in complex with a G protein. Nature. 2017;546(7657):248-53.

236. Wang C, Jiang Y, Ma J, Wu H, Wacker D, Katritch V, et al. Structural basis for molecular recognition at serotonin receptors. Science. 2013;340(6132):610-4.

237. de Graaf C, Foata N, Engkvist O, Rognan D. Molecular modeling of the second extracellular loop of G-protein coupled receptors and its implication on structure-based virtual screening. Proteins. 2008;71(2):599-620.

238. McCorvy JD, Wacker D, Wang S, Agegnehu B, Liu J, Lansu K, et al. Structural determinants of 5-HT2B receptor activation and biased agonism. Nature structural & molecular biology. 2018;25(9):787-96.

239. Fowler JC, Bhattacharya S, Urban JD, Vaidehi N, Mailman RB. Receptor conformations involved in dopamine D(2L) receptor functional selectivity induced by selected transmembrane-5 serine mutations. Molecular pharmacology. 2012;81(6):820-31.

240. Rivero G, Llorente J, McPherson J, Cooke A, Mundell SJ, McArdle CA, et al. Endomorphin-2: a biased agonist at the mu-opioid receptor. Molecular pharmacology. 2012;82(2):178-88.

241. Thompson GL, Lane JR, Coudrat T, Sexton PM, Christopoulos A, Canals M. Biased Agonism of Endogenous Opioid Peptides at the mu-Opioid Receptor. Molecular pharmacology. 2015;88(2):335-46.

242. Frolich N, Dees C, Paetz C, Ren X, Lohse MJ, Nikolaev VO, et al. Distinct pharmacological properties of morphine metabolites at G(i)-protein and beta-arrestin signaling pathways activated by the human mu-opioid receptor. Biochem Pharmacol. 2011;81(10):1248-54.

243. Molinari P, Vezzi V, Sbraccia M, Gro C, Riitano D, Ambrosio C, et al. Morphine-like opiates selectively antagonize receptor-arrestin interactions. The Journal of biological chemistry. 2010;285(17):12522-35.

244. Bohn LM, Lefkowitz RJ, Gainetdinov RR, Peppel K, Caron MG, Lin FT. Enhanced Morphine Analgesia in Mice Lacking Beta-Arrestin 2. Science. 1999;286:2495-8.

245. Raehal KM, Walker JK, Bohn LM. Morphine side effects in beta-arrestin 2 knockout mice. The Journal of pharmacology and experimental therapeutics. 2005;314(3):1195-201.

246. Schmid CL, Kennedy NM, Ross NC, Lovell KM, Yue Z, Morgenweck J, et al. Bias Factor and Therapeutic Window Correlate to Predict Safer Opioid Analgesics. Cell. 2017;171(5):1165-75 e13.

247. DeWire SM, Yamashita DS, Rominger DH, Liu G, Cowan CL, Graczyk TM, et al. A G protein-biased ligand at the mu-opioid receptor is potently analgesic with

reduced gastrointestinal and respiratory dysfunction compared with morphine. The Journal of pharmacology and experimental therapeutics. 2013;344(3):708-17.

248. Singla N, Minkowitz HS, Soergel DG, Burt DA, Subach RA, Salamea MY, et al. A randomized, Phase IIb study investigating oliceridine (TRV130), a novel micro-receptor G-protein pathway selective (mu-GPS) modulator, for the management of moderate to severe acute pain following abdominoplasty. J Pain Res. 2017;10:2413-24.

249. Soergel DG, Subach RA, Burnham N, Lark MW, James IE, Sadler BM, et al. Biased agonism of the mu-opioid receptor by TRV130 increases analgesia and reduces on-target adverse effects versus morphine: A randomized, double-blind, placebo-controlled, crossover study in healthy volunteers. Pain. 2014;155(9):1829-35.

250. Austin Zamarripa C, Edwards SR, Qureshi HN, Yi JN, Blough BE, Freeman KB. The G-protein biased mu-opioid agonist, TRV130, produces reinforcing and antinociceptive effects that are comparable to oxycodone in rats. Drug Alcohol Depend. 2018;192:158-62.

251. Negus SS, Freeman KB. Abuse Potential of Biased Mu Opioid Receptor Agonists. Trends in pharmacological sciences. 2018;39(11):916-9.

252. Manglik A, Lin H, Aryal DK, McCorvy JD, Dengler D, Corder G, et al. Structure-based discovery of opioid analgesics with reduced side effects. Nature. 2016;537(7619):185-90.

253. Hill R, Disney A, Conibear A, Sutcliffe K, Dewey W, Husbands S, et al. The novel mu-opioid receptor agonist PZM21 depresses respiration and induces tolerance to antinociception. British journal of pharmacology. 2018;175(13):2653-61.

254. Varadi A, Marrone GF, Palmer TC, Narayan A, Szabo MR, Le Rouzic V, et al. Mitragynine/Corynantheidine Pseudoindoxyls As Opioid Analgesics with Mu Agonism and Delta Antagonism, Which Do Not Recruit beta-Arrestin-2. Journal of medicinal chemistry. 2016;59(18):8381-97.

255. Groer CE, Tidgewell K, Moyer RA, Harding WW, Rothman RB, Prisinzano TE, et al. An opioid agonist that does not induce mu-opioid receptor--arrestin interactions or receptor internalization. Molecular pharmacology. 2007;71(2):549-57.

256. Lamb K, Tidgewell K, Simpson DS, Bohn LM, Prisinzano TE. Antinociceptive effects of herkinorin, a MOP receptor agonist derived from salvinorin A in the formalin test in rats: new concepts in mu opioid receptor pharmacology: from a symposium on new concepts in mu-opioid pharmacology. Drug Alcohol Depend. 2012;121(3):181-8.

257. Piekielna-Ciesielska J, Ferrari F, Calo G, Janecka A. Cyclopeptide Dmt-[D-Lys-p-CF3-Phe-Phe-Asp]NH2, a novel G protein-biased agonist of the mu opioid receptor. Peptides. 2018;101:227-33.

258. Kelly E. Efficacy and ligand bias at the mu-opioid receptor. British journal of pharmacology. 2013;169(7):1430-46.

259. Thompson GL, Kelly E, Christopoulos A, Canals M. Novel GPCR paradigms at the mu-opioid receptor. British journal of pharmacology. 2015;172(2):287-96.

260. Yudin Y, Rohacs T. The G protein-biased agents PZM21 and TRV130 are partial agonists of mu-opioid receptor-mediated signaling to ion channels. British journal of pharmacology. 2019.

261. Ehrlich AT, Darcq E. Recommending buprenorphine for pain management. Pain Manag. 2019;9(1):13-6.

262. Okude J, Ueda T, Kofuku Y, Sato M, Nobuyama N, Kondo K, et al. Identification of a Conformational Equilibrium That Determines the Efficacy and Functional Selectivity of the mu-Opioid Receptor. Angewandte Chemie. 2015.

263. Schneider S, Provasi D, Filizola M. How Oliceridine (TRV-130) Binds and Stabilizes a mu-Opioid Receptor Conformational State That Selectively Triggers G Protein Signaling Pathways. Biochemistry. 2016;55(46):6456-66.

264. Hothersall JD, Torella R, Humphreys S, Hooley M, Brown A, McMurray G, et al. Residues W320 and Y328 within the binding site of the mu-opioid receptor influence opiate ligand bias. Neuropharmacology. 2017;118:46-58.

265. Heydenreich FM, Vuckovic Z, Matkovic M, Veprintsev DB. Stabilization of G protein-coupled receptors by point mutations. Front Pharmacol. 2015;6:82.

266. Chun E, Thompson AA, Liu W, Roth CB, Griffith MT, Katritch V, et al. Fusion partner toolchest for the stabilization and crystallization of G protein-coupled receptors. Structure. 2012;20(6):967-76.

267. Manglik A, Kobilka BK, Steyaert J. Nanobodies to Study G Protein-Coupled Receptor Structure and Function. Annu Rev Pharmacol Toxicol. 2017;57:19-37.

268. Maeda S, Koehl A, Matile H, Hu H, Hilger D, Schertler GFX, et al. Development of an antibody fragment that stabilizes GPCR/G-protein complexes. Nature communications. 2018;9(1):3712.

269. Neilan CL, Husbands SM, Breeden S, Ko MC, Aceto MD, Lewis JW, et al. Characterization of the complex morphinan derivative BU72 as a high efficacy, long-lasting mu-opioid receptor agonist. European journal of pharmacology. 2004;499(1-2):107-16.

270. Latorraca NR, Venkatakrishnan AJ, Dror RO. GPCR Dynamics: Structures in Motion. Chem Rev. 2017;117(1):139-55.

271. Basith S, Cui M, Macalino SJY, Park J, Clavio NAB, Kang S, et al. Exploring G Protein-Coupled Receptors (GPCRs) Ligand Space via Cheminformatics Approaches: Impact on Rational Drug Design. Front Pharmacol. 2018;9:128.

272. Becker OM, Marantz Y, Shacham S, Inbal B, Heifetz A, Kalid O, et al. G protein-coupled receptors: in silico drug discovery in 3D. Proceedings of the National Academy of Sciences of the United States of America. 2004;101(31):11304-9.

273. Jacobson KA. New paradigms in GPCR drug discovery. Biochem Pharmacol. 2015;98(4):541-55.

274. Shaw DE, Deneroff MM, Dror RO, Kuskin JS, Larson RH, Salmon JK, et al. Anton, A Special-Purpose Machine For Molecular Dynamics Simulation. Communications of the ACM. 2008;51(7):91-7.

275. Bernardi RC, Melo MCR, Schulten K. Enhanced sampling techniques in molecular dynamics simulations of biological systems. Biochim Biophys Acta. 2015;1850(5):872-7.

276. Dawaliby R, Trubbia C, Delporte C, Masureel M, Van Antwerpen P, Kobilka BK, et al. Allosteric regulation of G protein-coupled receptor activity by phospholipids. Nature chemical biology. 2015.

277. Thomsen ARB, Plouffe B, Cahill TJ, 3rd, Shukla AK, Tarrasch JT, Dosey AM, et al. GPCR-G Protein-beta-Arrestin Super-Complex Mediates Sustained G Protein Signaling. Cell. 2016;166(4):907-19.

278. Strohman MJ, Maeda S, Hilger D, Masureel M, Du Y, Kobilka BK. Local membrane charge regulates β2 adrenergic receptor coupling to Gi3. Nature communications. 2019;10(1):2234.

279. Kruse AC, Hu J, Pan AC, Arlow DH, Rosenbaum DM, Rosemond E, et al. Structure and dynamics of the M3 muscarinic acetylcholine receptor. Nature. 2012;482(7386):552-6.

280. Haga K, Kruse AC, Asada H, Yurugi-Kobayashi T, Shiroishi M, Zhang C, et al. Structure of the human M2 muscarinic acetylcholine receptor bound to an antagonist. Nature. 2012;482(7386):547-51.

281. Korczynska M, Clark MJ, Valant C, Xu J, Moo EV, Albold S, et al. Structure-based discovery of selective positive allosteric modulators of antagonists for the M2 muscarinic acetylcholine receptor. Proceedings of the National Academy of Sciences of the United States of America. 2018;115(10):E2419-E28.

282. Shang Y, Yeatman HR, Provasi D, Alt A, Christopoulos A, Canals M, et al. Proposed Mode of Binding and Action of Positive Allosteric Modulators at Opioid Receptors. ACS Chem Biol. 2016;11(5):1220-9.

283. Bartuzi D, Kaczor AA, Matosiuk D. Interplay between Two Allosteric Sites and Their Influence on Agonist Binding in Human mu Opioid Receptor. Journal of chemical information and modeling. 2016;56(3):563-70.

284. Bokoch MP, Jo H, Valcourt JR, Srinivasan Y, Pan AC, Capponi S, et al. Entry from the Lipid Bilayer: A Possible Pathway for Inhibition of a Peptide G Protein-Coupled Receptor by a Lipophilic Small Molecule. Biochemistry. 2018;57(39):5748-58.

285. Hurst DP, Grossfield A, Lynch DL, Feller S, Romo TD, Gawrisch K, et al. A lipid pathway for ligand binding is necessary for a cannabinoid G protein-coupled receptor. The Journal of biological chemistry. 2010;285(23):17954-64.

286. Chan HCS, Wang J, Palczewski K, Filipek S, Vogel H, Liu ZJ, et al. Exploring a new ligand binding site of G protein-coupled receptors. Chem Sci. 2018;9(31):6480-9.

287. Dror RO, Arlow DH, Maragakis P, Mildorf TJ, Pan AC, Xu H, et al. Activation mechanism of the beta2-adrenergic receptor. Proceedings of the National Academy of Sciences of the United States of America. 2011;108(46):18684-9.

288. Landin EJB, Lovera S, de Fabritiis G, Kelm S, Mercier J, McMillan D, et al. The Aminotriazole Antagonist Cmpd-1 Stabilises a Distinct Inactive State of the Adenosine 2A Receptor. Angewandte Chemie. 2019.

289. Cheng JX, Cheng T, Li WH, Liu GX, Zhu WL, Tang Y. Computational insights into the G-protein-biased activation and inactivation mechanisms of the mu opioid receptor. Acta Pharmacol Sin. 2018;39(1):154-64.

290. Maier JA, Martinez C, Kasavajhala K, Wickstrom L, Hauser KE, Simmerling C. ff14SB: Improving the Accuracy of Protein Side Chain and Backbone Parameters from ff99SB. Journal of Chemical Theory and Computation. 2015;11(8):3696-713.

291. Jorgensen WL, Chandrasekhar J, Madura JD, Impey RW, Klein ML. Comparison of simple potential functions for simulating liquid water. The Journal of Chemical Physics. 1983;79(2):926-35.

292. Wang J, Wolf RM, Caldwell JW, Kollman PA, Case DA. Development and testing of a general amber force field. J Comput Chem. 2004;25(9):1157-74.

293. Pettersen EF, Goddard TD, Huang CC, Couch GS, Greenblatt DM, Meng EC, et al. UCSF Chimera--a visualization system for exploratory research and analysis. J Comput Chem. 2004;25(13):1605-12.

294. Fenalti G, Zatsepin NA, Betti C, Giguere P, Han GW, Ishchenko A, et al. Structural basis for bifunctional peptide recognition at human delta-opioid receptor. Nature structural & molecular biology. 2015;22(3):265-8.

295. Keller M, Boissard C, Patiny L, Chung NN, Lemieux C, Mutter M, et al. Pseudoproline-containing analogues of morphiceptin and endomorphin-2: evidence for a cis Tyr-Pro amide bond in the bioactive conformation. Journal of medicinal chemistry. 2001;44(23):3896-903.

296. Leitgeb B, Otvos F, Toth G. Conformational analysis of endomorphin-2 by molecular dynamics methods. Biopolymers. 2003;68(4):497-511.

297. Okada Y, Fujita Y, Motoyama T, Tsuda Y, Yokoi T, Li T, et al. Structural studies of [2',6'-dimethyl-L-tyrosine1]endomorphin-2 analogues: enhanced activity and cis orientation of the Dmt-Pro amide bond. Bioorganic & medicinal chemistry. 2003;11(9):1983-94.

298. Shao X, Gao Y, Zhu C, Liu X, Yao J, Cui Y, et al. Conformational analysis of endomorphin-2 analogs with phenylalanine mimics by NMR and molecular modeling. Bioorganic & medicinal chemistry. 2007;15(10):3539-47.

299. Wu H, Wacker D, Mileni M, Katritch V, Han GW, Vardy E, et al. Structure of the human kappa-opioid receptor in complex with JDTic. Nature. 2012;485(7398):327-32.

300. Roe DR, Cheatham TE, 3rd. PTRAJ and CPPTRAJ: Software for Processing and Analysis of Molecular Dynamics Trajectory Data. J Chem Theory Comput. 2013;9(7):3084-95.

301. McIntosh-Smith S, Price J, Sessions RB, Ibarra AA. High performance in silico virtual drug screening on many-core processors. The international journal of high performance computing applications. 2015;29(2):119-34.

302. Jo S, Kim T, Iyer VG, Im W. CHARMM-GUI: a web-based graphical user interface for CHARMM. J Comput Chem. 2008;29(11):1859-65.

303. Mondal M, Mesmin B, Mukherjee S, Maxfield FR. Sterols are mainly in the cytoplasmic leaflet of the plasma membrane and the endocytic recycling compartment in CHO cells. Molecular biology of the cell. 2009;20(2):581-8.

304. Pankov R, Markovska T, Antonov P, Ivanova L, Momchilova A. The plasma membrane lipid composition affects fusion between cells and model membranes. Chemico-biological interactions. 2006;164(3):167-73.

305. Calderon RO, Attema B, DeVries GH. Lipid composition of neuronal cell bodies and neurites from cultured dorsal root ganglia. Journal of neurochemistry. 1995;64(1):424-9.

306. Dickson CJ, Madej BD, Skjevik AA, Betz RM, Teigen K, Gould IR, et al. Lipid14: The Amber Lipid Force Field. J Chem Theory Comput. 2014;10(2):865-79.

307. Kappel K, Miao Y, McCammon JA. Accelerated molecular dynamics simulations of ligand binding to a muscarinic G-protein-coupled receptor. Quarterly reviews of biophysics. 2015;48(4):479-87.

308. Humphrey W, Dalke A, Schulten K. VMD: visual molecular dynamics. Journal of molecular graphics. 1996;14(1):33-8, 27-8.

309. Gasiunaite G, University of B. Galanin receptor dimerisation 2017.

310. Namkung Y, Le Gouill C, Lukashova V, Kobayashi H, Hogue M, Khoury E, et al. Monitoring G protein-coupled receptor and beta-arrestin trafficking in live cells using enhanced bystander BRET. Nature communications. 2016;7:12178.

311. Vezzi V, Onaran HO, Molinari P, Guerrini R, Balboni G, Calo G, et al. Ligands raise the constraint that limits constitutive activation in G protein-coupled opioid receptors. The Journal of biological chemistry. 2013;288(33):23964-78.

312. Molinari P, Casella I, Costa T. Functional complementation of high-efficiency resonance energy transfer: a new tool for the study of protein binding interactions in living cells. The Biochemical journal. 2008;409(1):251-61.

313. Hamdan FF, Percherancier Y, Breton B, Bouvier M. Monitoring protein-protein interactions in living cells by bioluminescence resonance energy transfer (BRET). Current protocols in neuroscience. 2006;Chapter 5:Unit 5.23.

314. Black JW, Leff P. Operational models of pharmacological agonism. Proc R Soc Lond B Biol Sci. 1983;220(1219):141-62.

315. van der Westhuizen ET, Breton B, Christopoulos A, Bouvier M. Quantification of ligand bias for clinically relevant beta2-adrenergic receptor ligands: implications for drug taxonomy. Molecular pharmacology. 2014;85(3):492-509.

316. Daunt DA, Hurt C, Hein L, Kallio J, Feng F, Kobilka BK. Subtype-specific intracellular trafficking of alpha2-adrenergic receptors. Molecular pharmacology. 1997;51(5):711-20.

317. Cooke AE, Oldfield S, Krasel C, Mundell SJ, Henderson G, Kelly E. Morphine-induced internalization of the L83I mutant of the rat mu-opioid receptor. British journal of pharmacology. 2015;172(2):593-605.

318. Keith DE, Anton B, Murray SR, Zaki PA, Chu PC, Lissin DV, et al. mu-Opioid receptor internalization: opiate drugs have differential effects on a conserved endocytic mechanism in vitro and in the mammalian brain. Molecular pharmacology. 1998;53(3):377-84.

319. Moraes I, Evans G, Sanchez-Weatherby J, Newstead S, Stewart PD. Membrane protein structure determination - the next generation. Biochim Biophys Acta. 2014;1838(1 Pt A):78-87.

320. Cheng Y. Membrane protein structural biology in the era of single particle cryo-EM. Curr Opin Struct Biol. 2018;52:58-63.

321. Topiol S. X-ray structural information of GPCRs in drug design: what are the limitations and where do we go? Expert Opin Drug Discov. 2013;8(6):607-20.

322. Ciancetta A, Jacobson KA. Breakthrough in GPCR Crystallography and Its Impact on Computer-Aided Drug Design. Methods Mol Biol. 2018;1705:45-72.

323. Shang Y, LeRouzic V, Schneider S, Bisignano P, Pasternak GW, Filizola M. Mechanistic insights into the allosteric modulation of opioid receptors by sodium ions. Biochemistry. 2014;53(31):5140-9.

324. Yuan S, Vogel H, Filipek S. The role of water and sodium ions in the activation of the mu-opioid receptor. Angewandte Chemie. 2013;52(38):10112-5.

325. Selvam B, Shamsi Z, Shukla D. Universality of the Sodium Ion Binding Mechanism in Class A G-Protein-Coupled Receptors. Angewandte Chemie. 2018;57(12):3048-53.

326. Hu X, Wang Y, Hunkele A, Provasi D, Pasternak GW, Filizola M. Kinetic and thermodynamic insights into sodium ion translocation through the mu-opioid receptor from molecular dynamics and machine learning analysis. PLoS Comput Biol. 2019;15(1):e1006689.

327. Livingston KE, Mahoney JP, Manglik A, Sunahara RK, Traynor JR. Measuring ligand efficacy at the mu-opioid receptor using a conformational biosensor. eLife. 2018;7.

328. Toll L, Berzetei-Gurske IP, Polgar WE, Brandt SR, Adapa ID, Rodriguez L, et al. Standard binding and functional assays related to medications development division testing for potential cocaine and opiate narcotic treatment medications. NIDA research monograph. 1998;178:440-66.

329. Huang P, Kehner GB, Cowan A, Liu-Chen LY. Comparison of Pharmacological Activities of Buprenorphine and Norbuprenorphine: Norbuprenorphine Is a Potent Opioid Agonist. The Journal of pharmacology and experimental therapeutics. 2001.

330. Cone EJ, Gorodetzky CW, Yousefnejad D, Buchwald WF, Johnson RE. The metabolism and excretion of buprenorphine in humans. Drug metabolism and disposition: the biological fate of chemicals. 1984;12(5):577-81.

331. Brown SM, Campbell SD, Crafford A, Regina KJ, Holtzman MJ, Kharasch ED. P-glycoprotein is a major determinant of norbuprenorphine brain exposure and antinociception. The Journal of pharmacology and experimental therapeutics. 2012;343(1):53-61.

332. Cui X, Yeliseev A, Liu R. Ligand interaction, binding site and G protein activation of the mu opioid receptor. European journal of pharmacology. 2013;702(1-3):309-15.

333. Virk MS, Arttamangkul S, Birdsong WT, Williams JT. Buprenorphine is a weak partial agonist that inhibits opioid receptor desensitization. J Neurosci. 2009;29(22):7341-8.

334. Singh R, Hurst DP, Barnett-Norris J, Lynch DL, Reggio PH, Guarnieri F. Activation of the cannabinoid CB1 receptor may involve a W6 48/F3 36 rotamer toggle switch. J Pept Res. 2002;60(6):357-70.

335. Amadei A, Linssen AB, Berendsen HJ. Essential dynamics of proteins. Proteins. 1993;17(4):412-25.

336. Pierce LC, Salomon-Ferrer R, Augusto FdOC, McCammon JA, Walker RC. Routine Access to Millisecond Time Scale Events with Accelerated Molecular Dynamics. J Chem Theory Comput. 2012;8(9):2997-3002.

337. Shim J, Coop A, MacKerell AD, Jr. Consensus 3D model of mu-opioid receptor ligand efficacy based on a quantitative Conformationally Sampled Pharmacophore. The journal of physical chemistry B. 2011;115(22):7487-96.

338. Shim J, Coop A, MacKerell AD, Jr. Molecular details of the activation of the mu opioid receptor. The journal of physical chemistry B. 2013;117(26):7907-17.

339. Chan HC, Filipek S, Yuan S. The Principles of Ligand Specificity on beta-2-adrenergic receptor. Sci Rep. 2016;6:34736.

340. Masureel M, Zou Y, Picard LP, van der Westhuizen E, Mahoney JP, Rodrigues J, et al. Structural insights into binding specificity, efficacy and bias of a beta2AR partial agonist. Nature chemical biology. 2018;14(11):1059-66.

341. Viscusi ER, Webster L, Kuss M, Daniels S, Bolognese JA, Zuckerman S, et al. A randomized, phase 2 study investigating TRV130, a biased ligand of the mu-opioid receptor, for the intravenous treatment of acute pain. Pain. 2016;157(1):264-72.

342. Devost D, Sleno R, Petrin D, Zhang A, Shinjo Y, Okde R, et al. Conformational Profiling of the AT1 Angiotensin II Receptor Reflects Biased Agonism, G Protein Coupling, and Cellular Context. The Journal of biological chemistry. 2017;292(13):5443-56.

343. Liu JJ, Horst R, Katritch V, Stevens RC, Wuthrich K. Biased signaling pathways in beta2-adrenergic receptor characterized by 19F-NMR. Science. 2012;335(6072):1106-10.

344. Dekan Z, Sianati S, Yousuf A, Sutcliffe KJ, Gillis A, Mallet C, et al. A novel tetrapeptide class of biased analgesics from an Australian fungus targets the mu-opioid receptor. Proceedings of the National Academy of Sciences of the United States of America. 2019;116(44):22353-8.

345. Wu YC, Jaglinski T, Hsieh JY, Chiu JJ, Chiang TY, Hwang CC. Four-component pharmacophore model for endomorphins toward mu opioid receptor subtypes. J Mol Model. 2012;18(2):825-34.

346. Kenakin T, Christopoulos A. Signalling bias in new drug discovery: detection, quantification and therapeutic impact. Nat Rev Drug Discov. 2013;12(3):205-16.

347. Sianati S. µ-Opioid receptor signalling mechanisms: quantifying bias and kinetics: University of Sydney; 2014.

348. Hilger D, Masureel M, Kobilka BK. Structure and dynamics of GPCR signaling complexes. Nature structural & molecular biology. 2018;25(1):4-12.

349. Eddy MT, Lee MY, Gao ZG, White KL, Didenko T, Horst R, et al. Allosteric Coupling of Drug Binding and Intracellular Signaling in the A2A Adenosine Receptor. Cell. 2018;172(1-2):68-80 e12.

350. Lin SW, Sakmar TP. Specific tryptophan UV-absorbance changes are probes of the transition of rhodopsin to its active state. Biochemistry. 1996;35(34):11149-59.

351. Bermudez M, Bock A. Does Divergent Binding Pocket Closure Drive Ligand Bias for Class A GPCRs? Trends in pharmacological sciences. 2019.

352. Shenoy SK, Lefkowitz RJ. beta-Arrestin-mediated receptor trafficking and signal transduction. Trends in pharmacological sciences. 2011;32(9):521-33.

353. Rodriguez-Martin I, Braksator E, Bailey CP, Goodchild S, Marrion NV, Kelly E, et al. Methadone: does it really have low efficacy at mu-opioid receptors? Neuroreport. 2008;19(5):589-93.

354. Wess J. Molecular basis of muscarinic acetylcholine receptor function. Trends in pharmacological sciences. 1993;14(8):308-13.

355. Zhang J, Ferguson SS, Barak LS, Bodduluri SR, Laporte SA, Law PY, et al. Role for G protein-coupled receptor kinase in agonist-specific regulation of mu-opioid receptor responsiveness. Proceedings of the National Academy of Sciences of the United States of America. 1998;95(12):7157-62.

356. Hallmen C, Wiese M. Molecular dynamics simulation of the human adenosine A3 receptor: agonist induced conformational changes of Trp243. J Comput Aided Mol Des. 2006;20(10-11):673-84.

357. Xu W, Li J, Chen C, Huang P, Weinstein H, Javitch JA, et al. Comparison of the amino acid residues in the sixth transmembrane domains accessible in the binding-site crevices of mu, delta, and kappa opioid receptors. Biochemistry. 2001;40(27):8018-29.

358. Akal-Strader A, Khare S, Xu D, Naider F, Becker JM. Residues in the first extracellular loop of a G protein-coupled receptor play a role in signal transduction. The Journal of biological chemistry. 2002;277(34):30581-90.

359. Selent J, Sanz F, Pastor M, De Fabritiis G. Induced effects of sodium ions on dopaminergic G-protein coupled receptors. PLoS Comput Biol. 2010;6(8).

360. Hori T, Okuno T, Hirata K, Yamashita K, Kawano Y, Yamamoto M, et al. Na(+)-mimicking ligands stabilize the inactive state of leukotriene B4 receptor BLT1. Nature chemical biology. 2018;14(3):262-9.

361. Bancroft S, Sutcliffe KJ, Kelly E, Sessions RB. Molecular dynamics simulations reveal a novel binding mode of fentanyl at the mu opioid receptor. In preparation

362. de Graaf C, Kooistra AJ, Vischer HF, Katritch V, Kuijer M, Shiroishi M, et al. Crystal structure-based virtual screening for fragment-like ligands of the human histamine H(1) receptor. Journal of medicinal chemistry. 2011;54(23):8195-206.

363. Kooistra AJ, Vischer HF, McNaught-Flores D, Leurs R, de Esch IJ, de Graaf C. Function-specific virtual screening for GPCR ligands using a combined scoring method. Sci Rep. 2016;6:28288.

364. Sirci F, Goracci L, Rodriguez D, van Muijlwijk-Koezen J, Gutierrez-de-Teran H, Mannhold R. Ligand-, structure- and pharmacophore-based molecular fingerprints: a case study on adenosine A(1), A (2A), A (2B), and A (3) receptor antagonists. J Comput Aided Mol Des. 2012;26(11):1247-66.

365. Wacker D, Stevens RC, Roth BL. How Ligands Illuminate GPCR Molecular Pharmacology. Cell. 2017;170(3):414-27.

366. Ngo T, Ilatovskiy AV, Stewart AG, Coleman JL, McRobb FM, Riek RP, et al. Orphan receptor ligand discovery by pickpocketing pharmacological neighbors. Nature chemical biology. 2017;13(2):235-42.

367. Vass M, Kooistra AJ, Ritschel T, Leurs R, de Esch IJ, de Graaf C. Molecular interaction fingerprint approaches for GPCR drug discovery. Curr Opin Pharmacol. 2016;30:59-68.

368. Crocker E, Eilers M, Ahuja S, Hornak V, Hirshfeld A, Sheves M, et al. Location of Trp265 in metarhodopsin II: implications for the activation mechanism of the visual receptor rhodopsin. Journal of molecular biology. 2006;357(1):163-72.

369. Bhattacharya S, Hall SE, Li H, Vaidehi N. Ligand-stabilized conformational states of human beta(2) adrenergic receptor: insight into G-protein-coupled receptor activation. Biophys J. 2008;94(6):2027-42.

370. Plazinska A, Plazinski W, Luchowski R, Wnorowski A, Grudzinski W, Gruszecki WI. Ligand-induced action of the W286(6.48) rotamer toggle switch in the beta2-adrenergic receptor. Phys Chem Chem Phys. 2017;20(1):581-94.

371. Yuan S, Hu Z, Filipek S, Vogel H. W246(6.48) opens a gate for a continuous intrinsic water pathway during activation of the adenosine A2A receptor. Angewandte Chemie. 2015;54(2):556-9.

372. Gao ZG, Chen A, Barak D, Kim SK, Muller CE, Jacobson KA. Identification by site-directed mutagenesis of residues involved in ligand recognition and activation of the human A3 adenosine receptor. The Journal of biological chemistry. 2002;277(21):19056-63.

373. Khanna IK, Pillarisetti S. Buprenorphine - an attractive opioid with underutilized potential in treatment of chronic pain. J Pain Res. 2015;8:859-70.

374. Singla NK, Skobieranda F, Soergel DG, Salamea M, Burt DA, Demitrack MA, et al. APOLLO-2: A Randomized, Placebo and Active-Controlled Phase III Study Investigating Oliceridine (TRV130), a G Protein-Biased Ligand at the mu-Opioid Receptor, for Management of Moderate to Severe Acute Pain Following Abdominoplasty. Pain Pract. 2019.

375. Tomassoni AJ, Hawk KF, Jubanyik K, Nogee DP, Durant T, Lynch KL, et al. Multiple Fentanyl Overdoses - New Haven, Connecticut, June 23, 2016. MMWR Morb Mortal Wkly Rep. 2017;66(4):107-11.

376. Nivedha AK, Tautermann CS, Bhattacharya S, Lee S, Casarosa P, Kollak I, et al. Identifying Functional Hotspot Residues for Biased Ligand Design in G-Protein-Coupled Receptors. Molecular pharmacology. 2018;93(4):288-96.

377. Kenakin T. Functional selectivity and biased receptor signaling. The Journal of pharmacology and experimental therapeutics. 2011;336(2):296-302.

378. Lavecchia A, Di Giovanni C. Virtual screening strategies in drug discovery: a critical review. Curr Med Chem. 2013;20(23):2839-60.

379. Vamathevan J, Clark D, Czodrowski P, Dunham I, Ferran E, Lee G, et al. Applications of machine learning in drug discovery and development. Nat Rev Drug Discov. 2019;18(6):463-77.

380. Plante A, Shore DM, Morra G, Khelashvili G, Weinstein H. A Machine Learning Approach for the Discovery of Ligand-Specific Functional Mechanisms of GPCRs. Molecules. 2019;24(11).

381. De Lean A, Stadel JM, Lefkowitz RJ. A ternary complex model explains the agonist-specific binding properties of the adenylate cyclase-coupled beta-adrenergic receptor. The Journal of biological chemistry. 1980;255(15):7108-17.

382. Warne T, Edwards PC, Dore AS, Leslie AGW, Tate CG. Molecular basis for high-affinity agonist binding in GPCRs. Science. 2019;364(6442):775-8.

383. Tian X, Kang DS, Benovic JL. beta-arrestins and G protein-coupled receptor trafficking. Handb Exp Pharmacol. 2014;219:173-86.

384. Hanson MA, Roth CB, Jo E, Griffith MT, Scott FL, Reinhart G, et al. Crystal structure of a lipid G protein-coupled receptor. Science. 2012;335(6070):851-5.

385. Comer SD, Cahill CM. Fentanyl: Receptor pharmacology, abuse potential, and implications for treatment. Neurosci Biobehav Rev. 2018.

Appendices

Appendix I

W293$^{6.48}$A MOPr

Sequence alignment between the wildtype template HA-rat MOPr plasmid and the W293$^{6.48}$A mutant. Base changes are highlighted in yellow.

```
W293A 1     TACCCATACGATGTGCCCGACTATGCTCTGGTGCCGCGGGACAGCAGCACCGGCCCAGGG  60
            ||||||||||||||||||||||||||||||||||||||||||||||||||||||||||||
RMOPR 1     TACCCATACGATGTGCCCGACTATGCTCTGGTGCCGCGGGACAGCAGCACCGGCCCAGGG  60

W293A 61    AACACCAGCGACTGCTCAGACCCCTTAGCTCAGGCAAGTTGCTCCCCAGCACCTGGCTCC  120
            ||||||||||||||||||||||||||||||||||||||||||||||||||||||||||||
RMOPR 61    AACACCAGCGACTGCTCAGACCCCTTAGCTCAGGCAAGTTGCTCCCCAGCACCTGGCTCC  120

W293A 121   TGGCTCAACTTGTCCCACGTTGATGGCAACCAGTCCGATCCATGCGGTCTGAACCGCACC  180
            ||||||||||||||||||||||||||||||||||||||||||||||||||||||||||||
RMOPR 121   TGGCTCAACTTGTCCCACGTTGATGGCAACCAGTCCGATCCATGCGGTCTGAACCGCACC  180

W293A 181   GGGCTTGGCGGGAACGACAGCCTGTGCCCTCAGACCGGCAGCCCTTCCATGGTCACAGCC  240
            ||||||||||||||||||||||||||||||||||||||||||||||||||||||||||||
RMOPR 181   GGGCTTGGCGGGAACGACAGCCTGTGCCCTCAGACCGGCAGCCCTTCCATGGTCACAGCC  240

W293A 241   ATTACCATCATGGCCCTCTACTCTATCGTGTGTGTAGTGGGCCTCTTCGGAAACTTCCTG  300
            ||||||||||||||||||||||||||||||||||||||||||||||||||||||||||||
RMOPR 241   ATTACCATCATGGCCCTCTACTCTATCGTGTGTGTAGTGGGCCTCTTCGGAAACTTCCTG  300

W293A 301   GTCATGTATGTGATTGTAAGATACACCAAAATGAAGACTGCCACCAACATCTACATTTTC  360
            ||||||||||||||||||||||||||||||||||||||||||||||||||||||||||||
RMOPR 301   GTCATGTATGTGATTGTAAGATACACCAAAATGAAGACTGCCACCAACATCTACATTTTC  360

W293A 361   AACCTTGCTCTGGCAGACGCCTTAGCGACCAGTACACTGCCCTTTCAGAGTGTCAACTAC  420
            ||||||||||||||||||||||||||||||||||||||||||||||||||||||||||||
RMOPR 361   AACCTTGCTCTGGCAGACGCCTTAGCGACCAGTACACTGCCCTTTCAGAGTGTCAACTAC  420

W293A 421   CTGATGGGAACATGGCCCTTCGGAACCATCCTCTGCAAGATCGTGATCTCAATAGATTAC  480
            ||||||||||||||||||||||||||||||||||||||||||||||||||||||||||||
RMOPR 421   CTGATGGGAACATGGCCCTTCGGAACCATCCTCTGCAAGATCGTGATCTCAATAGATTAC  480

W293A 481   TACAACATGTTCACCAGCATATTCACCCTCTGCACCATGAGCGTGGACCGCTACATTGCT  540
            ||||||||||||||||||||||||||||||||||||||||||||||||||||||||||||
RMOPR 481   TACAACATGTTCACCAGCATATTCACCCTCTGCACCATGAGCGTGGACCGCTACATTGCT  540
```

```
W293A 541  GTCTGCCACCCAGTCAAAGCCCTGGATTTCCGTACCCCCCGAAATGCCAAAATCGTCAAC  600
           ||||||||||||||||||||||||||||||||||||||||||||||||||||||||||||
RMOPR 541  GTCTGCCACCCAGTCAAAGCCCTGGATTTCCGTACCCCCCGAAATGCCAAAATCGTCAAC  600

W293A 601  GTCTGCAACTGGATCCTCTCTTCTGCCATCGGTCTGCCTGTAATGTTCATGGCAACCACA  660
           ||||||||||||||||||||||||||||||||||||||||||||||||||||||||||||
RMOPR 601  GTCTGCAACTGGATCCTCTCTTCTGCCATCGGTCTGCCTGTAATGTTCATGGCAACCACA  660

W293A 661  AAATACAGGCAGGGGTCCATAGATTGCACCCTCACGTTCTCCCACCCAACCTGGTACTGG  720
           ||||||||||||||||||||||||||||||||||||||||||||||||||||||||||||
RMOPR 661  AAATACAGGCAGGGGTCCATAGATTGCACCCTCACGTTCTCCCACCCAACCTGGTACTGG  720

W293A 721  GAGAACCTGCTCAAAATCTGTGTCTTTATCTTCGCTTTCATCATGCCGATCCTCATCATC  780
           ||||||||||||||||||||||||||||||||||||||||||||||||||||||||||||
RMOPR 721  GAGAACCTGCTCAAAATCTGTGTCTTTATCTTCGCTTTCATCATGCCGATCCTCATCATC  780

W293A 781  ACTGTGTGTTACGGCCTGATGATCTTACGACTCAAGAGCGTTCGCATGCTATCGGGCTCC  840
           ||||||||||||||||||||||||||||||||||||||||||||||||||||||||||||
RMOPR 781  ACTGTGTGTTACGGCCTGATGATCTTACGACTCAAGAGCGTTCGCATGCTATCGGGCTCC  840

W293A 841  AAAGAAAAGGACAGGAATCTGCGCAGGATCACCCGGATGGTGCTGGTGGTCGTGGCTGTA  900
           ||||||||||||||||||||||||||||||||||||||||||||||||||||||||||||
RMOPR 841  AAAGAAAAGGACAGGAATCTGCGCAGGATCACCCGGATGGTGCTGGTGGTCGTGGCTGTA  900

W293A 901  TTTATCGTCTGCGCCACCCCCATCCACATCTACGTCATCATCAAAGCGCTGATCACGATT  960
           ||||||||||||   |||||||||||||||||||||||||||||||||||||||||||||
RMOPR 901  TTTATCGTCTGCTGGACCCCCATCCACATCTACGTCATCATCAAAGCGCTGATCACGATT  960

W293A 961  CCAGAAACCACATTTCAGACCGTTTCCTGGCACTTCTGCATTGCTTTGGGTTACACGAAC 1020
           ||||||||||||||||||||||||||||||||||||||||||||||||||||||||||||
RMOPR 961  CCAGAAACCACATTTCAGACCGTTTCCTGGCACTTCTGCATTGCTTTGGGTTACACGAAC 1020

W293A 1021 AGCTGCCTGAATCCAGTTCTTTACGCCTTCCTGGATGAAAACTTCAAGCGATGCTTCAGA 1080
           ||||||||||||||||||||||||||||||||||||||||||||||||||||||||||||
RMOPR 1021 AGCTGCCTGAATCCAGTTCTTTACGCCTTCCTGGATGAAAACTTCAAGCGATGCTTCAGA 1080

W293A 1081 GAGTTCTGCATCCCAACCTCGTCCACGATCGAACAGCAAAACTCCACTCGAGTCCGTCAG 1140
           ||||||||||||||||||||||||||||||||||||||||||||||||||||||||||||
RMOPR 1081 GAGTTCTGCATCCCAACCTCGTCCACGATCGAACAGCAAAACTCCACTCGAGTCCGTCAG 1140

W293A 1141 AACACTAGGGAACATCCCTCCACGGCTAATACAGTGGATCGAACTAACCACCAGCTAGAA 1200
           ||||||||||||||||||||||||||||||||||||||||||||||||||||||||||||
RMOPR 1141 AACACTAGGGAACATCCCTCCACGGCTAATACAGTGGATCGAACTAACCACCAGCTAGAA 1200
```

```
W293A 1201 AATCTGGAGGCAGAAACTGCTCCATTGCCCTAA  1233
           |||||||||||||||||||||||||||||||||
RMOPR 1201 AATCTGGAGGCAGAAACTGCTCCATTGCCCTAA  1233
```

Appendix II

L219^{ECL2}A MOPr

Sequence alignment between the wildtype template HA-rat MOPr plasmid and the L219^{ECL2}A mutant. Base changes are highlighted in yellow.

```
L219A 1    TACCCATACGATGTGCCCGACTATGCTCTGGTGCCGCGGGACAGCAGCACCGGCCCAGGG  60
           ||||||||||||||||||||||||||||||||||||||||||||||||||||||||||||
RMOPR 1    TACCCATACGATGTGCCCGACTATGCTCTGGTGCCGCGGGACAGCAGCACCGGCCCAGGG  60

L219A 61   AACACCAGCGACTGCTCAGACCCCTTAGCTCAGGCAAGTTGCTCCCCAGCACCTGGCTCC  120
           ||||||||||||||||||||||||||||||||||||||||||||||||||||||||||||
RMOPR 61   AACACCAGCGACTGCTCAGACCCCTTAGCTCAGGCAAGTTGCTCCCCAGCACCTGGCTCC  120

L219A 121  TGGCTCAACTTGTCCCACGTTGATGGCAACCAGTCCGATCCATGCGGTCTGAACCGCACC  180
           ||||||||||||||||||||||||||||||||||||||||||||||||||||||||||||
RMOPR 121  TGGCTCAACTTGTCCCACGTTGATGGCAACCAGTCCGATCCATGCGGTCTGAACCGCACC  180

L219A 181  GGGCTTGGCGGGAACGACAGCCTGTGCCCTCAGACCGGCAGCCCTTCCATGGTCACAGCC  240
           ||||||||||||||||||||||||||||||||||||||||||||||||||||||||||||
RMOPR 181  GGGCTTGGCGGGAACGACAGCCTGTGCCCTCAGACCGGCAGCCCTTCCATGGTCACAGCC  240

L219A 241  ATTACCATCATGGCCCTCTACTCTATCGTGTGTGTAGTGGGCCTCTTCGGAAACTTCCTG  300
           ||||||||||||||||||||||||||||||||||||||||||||||||||||||||||||
RMOPR 241  ATTACCATCATGGCCCTCTACTCTATCGTGTGTGTAGTGGGCCTCTTCGGAAACTTCCTG  300

L219A 301  GTCATGTATGTGATTGTAAGATACACCAAAATGAAGACTGCCACCAACATCTACATTTTC  360
           ||||||||||||||||||||||||||||||||||||||||||||||||||||||||||||
RMOPR 301  GTCATGTATGTGATTGTAAGATACACCAAAATGAAGACTGCCACCAACATCTACATTTTC  360

L219A 361  AACCTTGCTCTGGCAGACGCCTTAGCGACCAGTACACTGCCCTTTCAGAGTGTCAACTAC  420
           ||||||||||||||||||||||||||||||||||||||||||||||||||||||||||||
RMOPR 361  AACCTTGCTCTGGCAGACGCCTTAGCGACCAGTACACTGCCCTTTCAGAGTGTCAACTAC  420

L219A 421  CTGATGGGAACATGGCCCTTCGGAACCATCCTCTGCAAGATCGTGATCTCAATAGATTAC  480
           ||||||||||||||||||||||||||||||||||||||||||||||||||||||||||||
RMOPR 421  CTGATGGGAACATGGCCCTTCGGAACCATCCTCTGCAAGATCGTGATCTCAATAGATTAC  480

L219A 481  TACAACATGTTCACCAGCATATTCACCCTCTGCACCATGAGCGTGGACCGCTACATTGCT  540
           ||||||||||||||||||||||||||||||||||||||||||||||||||||||||||||
RMOPR 481  TACAACATGTTCACCAGCATATTCACCCTCTGCACCATGAGCGTGGACCGCTACATTGCT  540
```

```
L219A 541  GTCTGCCACCCAGTCAAAGCCCTGGATTTCCGTACCCCCCGAAATGCCAAAATCGTCAAC  600
           ||||||||||||||||||||||||||||||||||||||||||||||||||||||||||||
RMOPR 541  GTCTGCCACCCAGTCAAAGCCCTGGATTTCCGTACCCCCCGAAATGCCAAAATCGTCAAC  600

L219A 601  GTCTGCAACTGGATCCTCTCTTCTGCCATCGGTCTGCCTGTAATGTTCATGGCAACCACA  660
           ||||||||||||||||||||||||||||||||||||||||||||||||||||||||||||
RMOPR 601  GTCTGCAACTGGATCCTCTCTTCTGCCATCGGTCTGCCTGTAATGTTCATGGCAACCACA  660

L219A 661  AAATACAGGCAGGGGTCCATAGATTGCACCGCCACGTTCTCCCACCCAACCTGGTACTGG  720
           ||||||||||||||||||||||||||||||  ||||||||||||||||||||||||||||
RMOPR 661  AAATACAGGCAGGGGTCCATAGATTGCACCCTCACGTTCTCCCACCCAACCTGGTACTGG  720

L219A 721  GAGAACCTGCTCAAAATCTGTGTCTTTATCTTCGCTTTCATCATGCCGATCCTCATCATC  780
           ||||||||||||||||||||||||||||||||||||||||||||||||||||||||||||
RMOPR 721  GAGAACCTGCTCAAAATCTGTGTCTTTATCTTCGCTTTCATCATGCCGATCCTCATCATC  780

L219A 781  ACTGTGTGTTACGGCCTGATGATCTTACGACTCAAGAGCGTTCGCATGCTATCGGGCTCC  840
           ||||||||||||||||||||||||||||||||||||||||||||||||||||||||||||
RMOPR 781  ACTGTGTGTTACGGCCTGATGATCTTACGACTCAAGAGCGTTCGCATGCTATCGGGCTCC  840

L219A 841  AAAGAAAAGGACAGGAATCTGCGCAGGATCACCCGGATGGTGCTGGTGGTCGTGGCTGTA  900
           ||||||||||||||||||||||||||||||||||||||||||||||||||||||||||||
RMOPR 841  AAAGAAAAGGACAGGAATCTGCGCAGGATCACCCGGATGGTGCTGGTGGTCGTGGCTGTA  900

L219A 901  TTTATCGTCTGCTGGACCCCCATCCACATCTACGTCATCATCAAAGCGCTGATCACGATT  960
           ||||||||||||||||||||||||||||||||||||||||||||||||||||||||||||
RMOPR 901  TTTATCGTCTGCTGGACCCCCATCCACATCTACGTCATCATCAAAGCGCTGATCACGATT  960

L219A 961  CCAGAAACCACATTTCAGACCGTTTCCTGGCACTTCTGCATTGCTTTGGGTTACACGAAC 1020
           ||||||||||||||||||||||||||||||||||||||||||||||||||||||||||||
RMOPR 961  CCAGAAACCACATTTCAGACCGTTTCCTGGCACTTCTGCATTGCTTTGGGTTACACGAAC 1020

L219A 1021 AGCTGCCTGAATCCAGTTCTTTACGCCTTCCTGGATGAAAACTTCAAGCGATGCTTCAGA 1080
           ||||||||||||||||||||||||||||||||||||||||||||||||||||||||||||
RMOPR 1021 AGCTGCCTGAATCCAGTTCTTTACGCCTTCCTGGATGAAAACTTCAAGCGATGCTTCAGA 1080

L219A 1081 GAGTTCTGCATCCCAACCTCGTCCACGATCGAACAGCAAAACTCCACTCGAGTCCGTCAG 1140
           ||||||||||||||||||||||||||||||||||||||||||||||||||||||||||||
RMOPR 1081 GAGTTCTGCATCCCAACCTCGTCCACGATCGAACAGCAAAACTCCACTCGAGTCCGTCAG 1140

L219A 1141 AACACTAGGGAACATCCCTCCACGGCTAATACAGTGGATCGAACTAACCACCAGCTAGAA 1200
           ||||||||||||||||||||||||||||||||||||||||||||||||||||||||||||
RMOPR 1141 AACACTAGGGAACATCCCTCCACGGCTAATACAGTGGATCGAACTAACCACCAGCTAGAA 1200
```

```
L219A 1201 AATCTGGAGGCAGAAACTGCTCCATTGCCCTAA  1233
           |||||||||||||||||||||||||||||||||
RMOPR 1201 AATCTGGAGGCAGAAACTGCTCCATTGCCCTAA  1233
```